Per mill level control of the Fabry-Perot cavity optical system for precision Compton polarimetry

M. Jacquet

ORSAY
n° d'ordre :

LAL 09-210
Juillet 2009

Mémoire d'Habilitation à Diriger des Recherches

Per mill level control of the Fabry-Perot cavity optical system for precision Compton polarimetry

Marie Jacquet

Habilitation soutenue le vendredi 10 juillet 2009, devant la commission d'examen :

MM.	M.E. Couprie	rapporteur
	G. Moortgat-Pick	rapporteur
	C. Rizzo	rapporteur
	P. Walter	
	G. Wormser	président
	F. Zomer	

Remerciements

Avant tout, je tiens à remercier Marie-Emmanuelle Couprie, Gudrid Moortgat-Pick et Carlo Rizzo d'avoir pris le temps d'être rapporteurs de ce document, ainsi que Philippe Walter et Guy Wormser d'avoir accepté de faire partie du jury.

Je souhaite remercier particulièrement Fabian Zomer, qui m'a guidée tout au long de ces années, et qui a toujours été là qu'il s'agisse de physique ou d'amitié.

Merci à Christian Pascaud, Jean-Claude Bizot et Ronic Chiche pour tout ce qu'il m'ont appris, pour les réponses qu'ils ont apportées à mes nombreuses questions, toujours avec simplicité et dans une ambiance amicale.

Merci à Viktor Soskov pour toutes les heures passées à "bougerfaisceau.vi" ...

Je remercie également tous ceux avec qui j'ai travaillé sur le projet du polarimètre: Mourad Ait-Mohand, Ties Behnke, Sylvestre Baudrand, Matthew Beckingham, Roger Bernier, Violette Brisson, Thierry Caceres, Nicola Coppola, Christophe De la Taille, Yorck Holler, Sergey Kurbasov, Gang Li, Michel Lintz, Joerg Ludwig, Rodolphe Marie, Norbert Meyners, Yannick Queinec, André Reboux, Claude Vallée et Zhiqing Zhang.

Je voudrais dire toute ma sympathie à l'ensemble des administratifs, techniciens et ingénieurs du laboratoire et les remercier pour tous les bons moments passés au voisinage de la machine à café ou ailleurs ... Je tiens à remercier particulièrement Jocelyne Brosselard pour sa présence chaleureuse, ainsi que Patricia Chémali et Françoise Marechal pour la relecture de mon document.

Enfin, merci à Emmanuel et à mes enfants, Nathan, Salomé, Manon, Albertine, merci d'être là. Et une pensée pour ma mère qui a pu vivre un de ses derniers moments de joie à l'occasion de ma soutenance de thèse en décembre 1995 dans ce même auditorium.

Contents

Liste de notations

IP	interaction point
LPOL	HERA longitudinal polarimeter
POLCA	HERA Fabry-Perot cavity polarimeter
TPOL	HERA transverse polarimeter
ρ	HERA bending radius
a	electron gyromagnetic anomaly
γ	Lorentz factor
r_0	classical electron radius
λ_c	reduced electron Compton wavelength
P_{ST}	Sokolov-Ternov asymptotic polarisation
E_γ	Compton scattered photon energy
S_γ	degree of circular polarisation of the laser light
σ_c	Compton cross section
σ_0	non-polarised Compton cross section
σ_L	longitudinal Compton cross section
σ_T	transverse Compton cross section
P_e	electron(positron) beam longitudinal polarisation
P_c	light power at the Compton IP or light power inside the Fabry-Perot cavity at the resonance
λ	laser wavelength
ν	laser frequency
n_γ	number of scattered photons per bunch
ΔP_e	electron(positron) beam longitudinal polarisation uncertainty

R	intensity reflection coefficient of the cavity mirrors
T	intensity transmission coefficient of the cavity mirrors
P	energy absorbed and scattered in the cavity mirrors (in ppm)
A_{ref}	field reflected by the cavity
A_{circ}	field circulating inside the cavity
A_{tr}	field transmitted by the cavity
qwp	quater wave plate
L	cavity length
α_c	laser beam-electron beam crossing angle
R_M	cavity mirror radius of curvature
FSR	cavity free spectral range
FWMH	cavity full width of the resonance
$\mathcal{F}$	finesse of the cavity
P_{circ}	power circulating inside the cavity in stationary regime
P_{las}	incident laser beam power
P_{inc}	incident laser beam power coupled with the cavity
P_{dec}	power circulating inside the cavity in transient regime
G	cavity gain
G_{max}	maximum cavity gain
T_d	cavity decay time
DOCP ($\equiv S_\gamma$)	Degree Of Circular Polarisation of the laser light
χ_P, ϕ_P	angles characterising the polarisation of the laser beam
pd_0, pd_1, pd_2	ellipsometer photodiodes
I_0, I_1, I_2	pd_0, pd_1, pd_2 photodiode signals
ϵ_x, ϵ_y	Wollaston prism ellipticity parameters
$\mathbf{n}$	normal to the surface of a perfectly aligned qwp
$\mathbf{k_{in}}$	initial wave vector of the laser wave
θ_{inc}	angle of incidence between the laser beam and a qwp in case the plate is perfectly aligned
ϕ	azimuthal angle of an ellipsometer qwp
$\mathbf{n_{desal}}$	normal to the surace of a misaligned qwp

δ_x	small tilt of a qwp plane around the y_{lab} axis
e	thickness of a qwp at the level of the laser light impact point
e_0	thickness of a qwp at the level of the plate azimuthal rotation axis
d_{cm}	mechanical center misalignment parameter of a qwp
ϕ_{cm}	azimuthal angle maximizing the thickness variations $e - e_0$ of a qwp
pl_1, pl_2	order 1/2 and order 5 qwp's
e_1^{nom}, e_2^{nom}	thickness nominal values, for pl_1 and pl_2 plates
N_o, N_e	textbook ordinary and extraordinary quartz optical indices
n_o, n_e	ordinary and extraordinary quartz optical indices
Δn_o	parameter characterising the difference between n_o and N_o
θ_{turn}	angle corresponding to one turn of the ellipsometer qwp rotating stage screw around the x axis
N_{turn}	number of screw turns done to generated the incident angle θ_{inc}
θ	angle of incidence between the laser beam and an ellipsometer qwp
Δe_1, Δe_2	differences of the real thicknesses with respect to nominal values, for pl_1 and pl_2 plates
ϕ_{0_1}, ϕ_{0_2}	differences between ϕ and the position of the qwp optical axis, for pl_1 and pl_2 plates
δ_{x_1}, δ_{x_2}	as δ_x, for pl_1 and pl_2 plates
d_{cm_i}, i=1,6	as d_{cm}, for the six D_i data files
ϕ_{cm_1}, ϕ_{cm_2}	as ϕ_{cm}, for pl_1 and pl_2 plates
"moco qwp"	entrance beam line qwp
pd_{ent}	entrance beam line photodiode
I_{diode}	pd_{ent} photodiode signal
ϕ_{moco}	"moco qwp" azimuthal angle
ϕ_{bir}	parasitic birefringence angle
ϕ_G	glan azimuthal angle
$DOCP_{in}$	DOCP at the entrance of the ellipsometer
$DOCP_{cc}$	DOCP at the exit of the cavity
$DOCP_{moc}$	DOCP just after the "moco qwp"
$DOCP_{ent}$	DOCP before the entrance cavity mirror

Introduction

This document aims at giving an overview of the fast and precise Fabry-Perot Compton polarimeter which has been installed in 2003 in the tunnel of HERA [1]. HERA is an electron(positron)-proton collider located at the DESY laboratory in Hamburg where, since 2001, leptons are longitudinally polarised around the two experiments H1 [2, 3] and ZEUS [4]. The lepton polarisation at HERA ring reaches about 50%. This longitudinal polarisation allows some quantities of the standard model in the electroweak sector (as the right charged current cross sections, the mass of the W propagator, or the vectorial and axial couplings of the quarks u and d to the Z boson) to be measured or constrained. To cover accurately the physics program [5], a project to upgrade the longitudinal polarimeter was proposed and accepted in 2000. This new polarimeter is devoted to increase the accuracy of the lepton polarisation measurement to reach a stastitical uncertainty of 1% per bunch and per minute and a systematic uncertainty below the percent. This precision is necessary to achieve precise cross section measurements in H1 and ZEUS.

In the first chapter, basic principles of the polarisation build up in storage rings are described and polarisation measurement principles at HERA are presented. The second chapter is devoted to describe the whole Fabry-Perot polarimeter system and to present the main results of its functionment in the HERA tunnel up to the end of the HERA experiment in summer 2007.

One essential point to reach the per mill level on the systematic uncertainties on the lepton polarisation is the precise control of the optical system, and more precisely the precise knowledge of the laser beam polarisation. The characterisation of our optical setup is the main subject of this document and is described in Chapters 3, 4, 5 and 6.

In Chapter 3, the ellipsometer, *i.e.* the optical system used to characterise the light polarisation state, is presented. Some precise and dedicated studies performed with this ellipsometer in the laboratory environment at Orsay are described in Chapter 4. The characterisation of the optical system and the measurement of the laser beam polarisation in the HERA tunnel are presented in Chapter 5. Chapter 6 is devoted to check the global coherence of the light polarisation along the optical line.

Finally, in the annex, the formalism of a wave propagating in an anisotropic medium is developped to obtain the expression of the field transmitted by such a medium. Indeed, one of the most critical components of our optical system being a quartz quater wave plate, a model as complete as possible has been used to simulate our ellipsometer measurements described in Chapters 4 and 5 and to extract the main parameters of our optical system.

Chapter 1

Polarisation at HERA

HERA is a high energy electron(positron)-proton collider of the Deutsches Elektronen-Synchrotron Laboratory (DESY) in Hamburg [1]. The machine has provided luminosity since 1992. The electron(positron) beam is accelerated to an energy of 27.5 GeV and since 1998 the proton beam energy is 920 GeV. HERA has four experimental regions: the detectors H1 [2, 3] and ZEUS [4] (located at North and South interaction points respectively) where the unpolarised lepton and proton beams collide head-on, the HERMES detector [6] located at the East straight section of the ring which uses since 1995 the longitudinally polarised electron(position) beam in collision with a polarised gas fixed target, and the HERA B detector [7] which is located in the West straight section which use the proton beam halo interacting with a wire target (HERA B has taken data from 1998 to 2001).

Since 1992 the transverse polarisation of the lepton beam is measured with the transverse polarimeter TPOL located in the West area. Before the year 2000, HERA operated with two spin rotators around the HERMES experiment where the longitudinal polarisation was measured with the longitudinal polarimeter LPOL. Since 2001, HERA has started its second phase: HERA II. During the machine upgrade [5, 8, 9], two pairs of spin rotators have been installed, one around H1 and one around ZEUS, providing a longitudinally polarised lepton beam at the two interaction point (IP) regions. Also, during the machine upgrade, a second longitudinal polarimeter using a Fabry-Perot cavity (POLCA) has been tested and installed in the HERMES area during the summer 2003. A schematic view of the HERA collider showing the four experiment areas and the three polarimeters is presented in Figure 1.1.

This chapter is devoted to a description of the lepton beam polarisation build up in storage rings and to polarisation measurements with the different HERA polarimeters. We will also see why it was decided to build another longitudinal polarimeter (the Fabry-Perot cavity) during the upgrade of the year 2000.

1.1 Lepton beam polarisation

1.1.1 Definition and description of polarisation

The spin of a particle is represented by the quantum vectorial operator $\widehat{\mathbf{S}}$:

$$\widehat{\mathbf{S}} = \left\{ \widehat{\mathbf{S}}_{\mathrm{x}}, \widehat{\mathbf{S}}_{\mathrm{y}}, \widehat{\mathbf{S}}_{\mathrm{z}} \right\} \ .$$

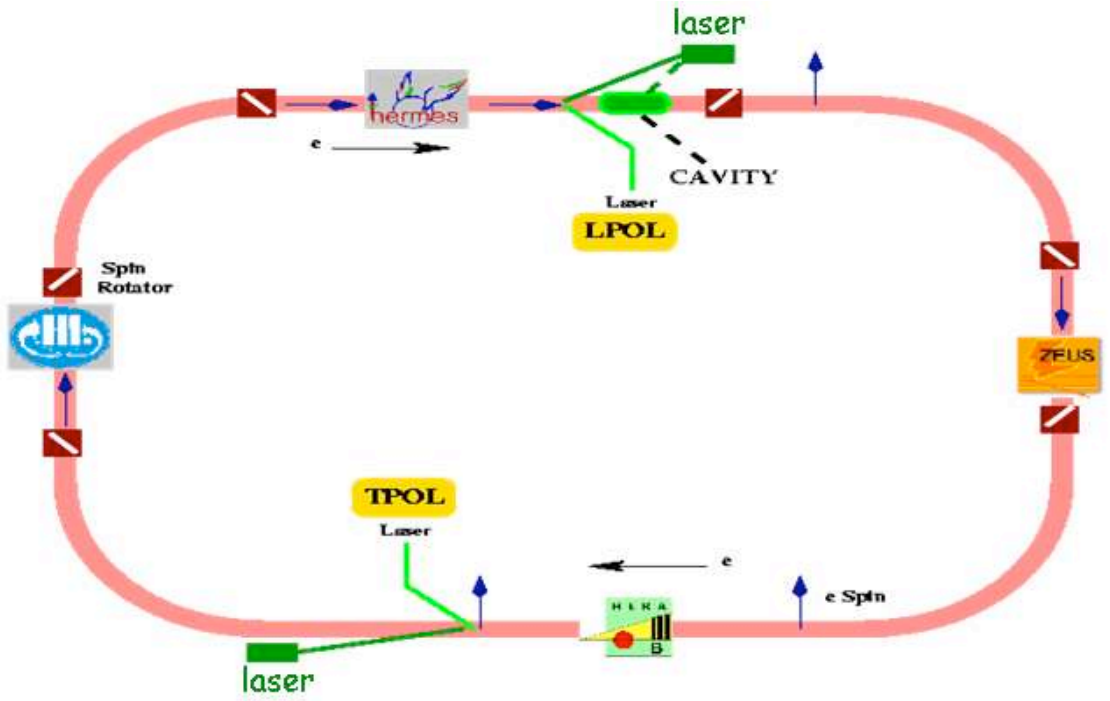

Figure 1.1: Drawing of HERA showing the four experiment locations H1, ZEUS, HERMES and HERA B, and the three polarimeter (TPOL, LPOL and POLCA) areas. The spin rotators located around H1, HERMES and ZEUS to turn the transverse polarisation of the electron beam into a longitudinal polarisation are aslo shown.

Considering a quantum system at one single particle characterised by its quantum state $\mid \phi_k >$, the polarisation vector is the quantum average of the spin operator $\widehat{\mathbf{S}}$ [10]:

$$\mathbf{P} =< \phi_k \mid \widehat{\mathbf{S}} \mid \phi_k > ,$$

and, in the semi-classical description of the spin dynamics, $\mathbf{P}$ is by convention named the spin vector $\mathbf{S}$.

For a quantum system containing a large number k of identical particles, the probability $d\mathcal{P}$ to have a single particle in the state $\mid \phi_k >$ is defined by:

$$d\mathcal{P} \; = \; \mathcal{P}(\phi_k) \; dk \; = \; p_k \; dk \; ,$$

and the polarisation vector is the statistical average of individual spin vectors, *i.e.* the statistical and quantum average of the spin quantum operator $\widehat{\mathbf{S}}$. It is written as:

$$\mathbf{P} = \sum_k p_k < \phi_k \mid \widehat{\mathbf{S}} \mid \phi_k > \; .$$

The value P of the polarisation (or the degree of polarisation) is the modulus of the vector $\mathbf{P}$. A beam is unpolarised ($P = 0$) if the spin vectors point to all directions isotropically. It is fully polarised ($P = \pm 1$) if all the particles are in the same spin state.

Although spin effects are necessarily quantum mechanical, it is possible to derive most of the equations and results semi-classically by starting with an effective Hamiltonian that includes a term describing the interaction between the spin and the electromagnetic field. According to the general rules of quantum mechanics, polarisation of electrons (*i.e.* the quantum average of $\widehat{\mathbf{S}}$) behaves classically (Ehrenfest theorem [11]). Although polarisation can be described in terms of spinors, Schrödinger equation for spinors is equivalent to a classical equation for the polarisation vector $\mathbf{P}$ [12]. Thus, there is no need for use of such spinors and a classical description of polarisation is exact and allows a concrete motion to be shown.

1.1.2 Time evolution of the polarisation

The spin of a particle interacts with an electromagnetic field through the magnetic moment associated with the spin. For non-relativistic and non-radiating particles, the motion of the spin of a particle in a static magnetic field $\mathbf{B}$ is established by applying the kinetic moment theorem of the fundamental law of classical mechanics:

$$\frac{\mathrm{d}\mathbf{S}}{\mathrm{dt}} = \mu \times \mathbf{B} \quad , \quad \text{with} \qquad \mu = \frac{\mathrm{g}}{2}\frac{\mathrm{e}}{\mathrm{m}_0}\mathbf{S} \; . \tag{1.1}$$

μ is the magnetic moment vector of the particle associated to the spining particle and proportional to its spin vector $\mathbf{S}$. e and m_0 are respectively the electric charge and the mass of the particle. g is the gyromagnetic ratio. Equation (1.1) can be rewritten as:

$$\frac{\mathrm{d}\mathbf{S}}{\mathrm{dt}} = \mathbf{\Omega_L} \times \mathbf{S} \quad , \quad \text{with} \qquad \mathbf{\Omega_L} = \frac{\mathrm{g}}{2}\frac{\mathrm{e}}{\mathrm{m}_0}\mathbf{B} \; . \tag{1.2}$$

(1.2) is the equation of a rotation (precession) of the spin vector around the direction defined by the rotation vector $\mathbf{\Omega_L}$ collinear to $\mathbf{B}$. The modulus of $\mathbf{\Omega_L}$ is the Larmor frequency.

Equation (1.2) describes the precession for a stationary electron and we need now an equation for a relativistic electron moving in an electromagnetic field $\mathbf{E}$ and $\mathbf{B}$. When particles are accelerated and are relativistic, electromagnetic fields have to be transformed from the laboratory to the accelerated rest frame of the particles. After applying the appropriated Lorentz transformations [13, 14], the spin evolution time follows the same law than (1.2) but with a different rotation vector [10]:

$$\frac{\mathrm{d}\mathbf{S}}{\mathrm{dt}} = \mathbf{\Omega_{BMT}} \times \mathbf{S} \tag{1.3}$$

with

$$\begin{aligned} \mathbf{\Omega_{BMT}} = -\frac{\mathrm{e}}{\mathrm{m}_0\gamma} \Bigg[\; & (1+\mathrm{a}\gamma)\; \mathbf{B} - \frac{\mathrm{a}(\gamma-1)}{\mathrm{v}^2}\,(\mathbf{v}\cdot\mathbf{B})\mathbf{v} \\ & + \left(\mathrm{a} + \frac{1}{\gamma+1}\right)\frac{\gamma}{\mathrm{c}^2}\;\mathbf{E}\times\mathbf{v} \Bigg] \; . \end{aligned} \tag{1.4}$$

$\mathrm{a} = (\mathrm{g}-2)/2$ is the gyromagnetic anomaly, γ is the lorentz factor, and $\mathbf{v}$ is the particle velocity. Equation (1.3) is known as the Bargmann-Michel-Telegdi (BMT) equation [15]. Let us note from the BMT equation that spin rotation in an electric field of 3×10^8 V/m or in a magnetic field of 1 Tesla is of the same order of magnitude. Supplied electric

fields in accelerators are in general smaller and their effect on the spin negligible [10]. We therefore assume $\mathbf{E} = 0$ in the following.

In Figure 1.2, a naive drawing illustrates the spin precession described by (1.4). In case the magnetic field is a purely transverse field perpendicular to the plane of motion ($\mathbf{v}\cdot\mathbf{B} = 0$ and $\mathbf{B} \equiv \mathbf{B}_\perp$), the direction of the spin vector changes but not its projection along the transverse direction y (Figure 1.2(a)), whilst when the magnetic field is a purely longitudinal field ($\mathbf{v}\times\mathbf{B} = 0$ and $\mathbf{B} \equiv \mathbf{B}_{||}$), the projection of $\mathbf{S}$ along the transverse direction varies in time (Figure 1.2(b)).

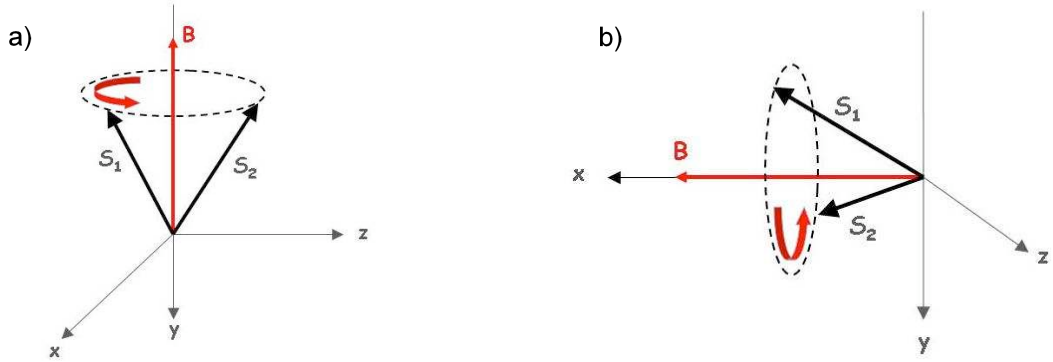

Figure 1.2: Basic scheme illustrating the precession of the spin vector. (a): the magnetic field $\mathbf{B}$ is normal to the particle plane of motion. (b): $\mathbf{B}$ is in the plane of motion and perpendicular to the particle direction. $\mathbf{S_1}$ and $\mathbf{S_2}$ schematize two positions of the spin vector that precesses around $\mathbf{B}$.

According to (1.4), in the coordinate system that rotates with the ideal electron with z along the electron velocity, x the horizontal direction, and the precession axis along the vertical axis y, the difference in frequency of spin and velocity precessions in a transverse magnetic field $\mathbf{B}_\perp$ is γa times larger than the relativistic cyclotron frequency $\Omega_c = e\mathbf{B}_\perp/(m_0\gamma)$: as the electron completes one revolution of a ring, the coordinate system rotates by 2π and the spin has precessed around y by an angle $2\pi a\gamma$. The spin tune is defined by:

$$\text{spin tune} \;=\; a\gamma \tag{1.5}$$

For electrons, $a = 1.159652 \times 10^{-3}$, and thus at HERA for 27 GeV electrons, the spin tune is around 60.

1.1.3 Spin dependence synchrotron radiation and spontaneous polarisation build up

Because of their small mass, electrons and positrons, subject in storage rings to the central acceleration of the guide field, radiate energy. The probability for an electron to emit a photon depends slightly on the initial spin state of the electron [16]. Sokolov and Ternov [17] have calculated the rate of photon emission for a given electron with a given initial and final spin states in the direction of the magnetic field. By introducing the parameter S specifying the initial spin state of the electron ($S = 1$ or $S = -1$ corresponding to the spin being parallel or anti-parallel respectively to the magnetic field), the no-spin-flip rate w_{nsf} (*i.e.* the photon emission rate where the spin state of the initial electron is identical

to the spin state of the final electron) and the spin-flip rate w_{sf} (*i.e.* the photon emission rate where the initial and final electron spin states are different) are written as [10, 14]:

$$\begin{aligned} w_{nsf} &= \left(\tfrac{5\sqrt{3}}{6}\right)\left(\frac{r_0\ \gamma\ c}{\rho\ \lambda_c}\right)\left[1-\left(\tfrac{16\sqrt{3}}{45}\right)\xi+\left(\tfrac{25}{18}\right)\xi^2-\tfrac{1}{5}\ S\left(1-\tfrac{20\sqrt{3}}{9}\xi\right)\xi\right]\ , \\ w_{sf} &= \left(\tfrac{5\sqrt{3}}{6}\right)\left(\frac{r_0\ \gamma\ c}{\rho\ \lambda_c}\right)\left[\tfrac{1}{6}\ \xi^2\ \left(1-S\ \tfrac{8\sqrt{3}}{15}\right)\right]\ , \end{aligned} \tag{1.6}$$

where $\gamma = E/m_e$ is the electron Lorentz factor, ρ is the storage ring bending radius, r_0 is the classical electron radius:

$$r_0 = \frac{e^2}{4\pi\ \epsilon_0\ m_e\ c^2} = 2.8179 \times 10^{-15} m\ ,$$

λ_c is the reduced electron Compton wavelength:

$$\lambda_c = \frac{\hbar}{m_e c} = 3.8616 \times 10^{-13} m\ ,$$

and ξ is the critical photon energy divided by the electron energy:

$$\xi\ =\ \frac{\hbar\omega_c}{m_e c^2\ \gamma}\ =\ \frac{3}{2}\ \frac{\lambda_c}{\rho}\ \gamma^2\ .$$

The parameter ξ is usually very small. For instance, an electron storage ring of 25 GeV energy with a bending radius ρ of 700 m would have $\xi \sim 2 \times 10^{-6}$. Formula (1.6) shows that there are quantum emission asymmetries related to the initial and final spin states of the electron. Second formula of (1.6) is the spin-flip contribution leading to the famous Sokolov-Ternov effect. w_{nsf} being of first order in ξ and w_{sf} of second order in ξ, the majority of photon emissions does not involve spin flip.

By noting $w_{\uparrow\downarrow}$ ($w_{\downarrow\uparrow}$) the rate w_{sf} for $S = 1$ (respectively for $S = -1$), *i.e.* the probability for a spin flip from a parallel (respectively anti-parallel) state to an anti-parallel (respectively parallel) state, w_{sf} of formula (1.6) can be rewritten as:

$$\begin{aligned} w_{\uparrow\downarrow} &= \tfrac{5\sqrt{3}}{16}\ \left(1+\tfrac{8}{5\sqrt{3}}\right) c\ \lambda_c\ r_0\ \frac{\gamma^5}{\rho^3}\ , \\ w_{\downarrow\uparrow} &= \tfrac{5\sqrt{3}}{16}\ \left(1-\tfrac{8}{5\sqrt{3}}\right) c\ \lambda_c\ r_0\ \frac{\gamma^5}{\rho^3}\ . \end{aligned} \tag{1.7}$$

This implies that starting from an unpolarised beam, after a certain time, synchrotron radiation induces a transverse polarisation: electrons are polarised anti-parallel to the guide magnetic field, whereas positrons are polarised parallel to the guide magnetic field (Figure 1.3).

In a uniform magnetic field and provided the very small electron(positron) recoil is neglected, the dynamics of the polarisation build up may thus be calculated: considering for instance electrons, if at a given time there are respectively $n_\uparrow$ and $n_\downarrow$ electrons in each spin state, the polarisation level of the beam and its time derivative are defined by:

$$P = \frac{n_\uparrow - n_\downarrow}{n} \qquad , \qquad \frac{dP}{dt} = \frac{1}{n}\left(\frac{dn_\uparrow}{dt} - \frac{dn_\downarrow}{dt}\right)\ ,$$

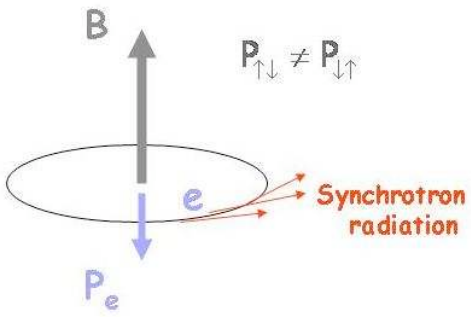

Figure 1.3: Scheme of the Sokolov-Ternov effect responsible for the build up of electron polarisation in a storage ring: $P_{\uparrow\downarrow}$ (respectively $P_{\downarrow\uparrow}$) is the probability of the transition of an electron spin down (respectively spin up) in an electron spin up (respectively spin down).

where $n = n_\uparrow + n_\downarrow$ is the total number of electrons. The time derivative of the rates $n_\uparrow$ and $n_\downarrow$ can be expressed as function of the transition probabilities $w_{\uparrow\downarrow}$ and $w_{\downarrow\uparrow}$ as:

$$\frac{dn_\uparrow}{dt} = n_\downarrow\, w_{\downarrow\uparrow} - n_\uparrow\, w_{\uparrow\downarrow} \quad , \quad \frac{dn_\downarrow}{dt} = n_\uparrow\, w_{\uparrow\downarrow} - n_\downarrow\, w_{\downarrow\uparrow} \quad .$$

These equations lead to:

$$\frac{dP}{dt} = (w_{\downarrow\uparrow} - w_{\uparrow\downarrow}) - (w_{\downarrow\uparrow} + w_{\uparrow\downarrow})\, P \quad , \tag{1.8}$$

where $w_{\uparrow\downarrow}$ and $w_{\downarrow\uparrow}$ are given by (1.7). The time integration of (1.8) leads to:

$$P(t) = P_{ST} \; + \; (P_0 - P_{ST}) \left[1 - e^{\frac{-(t-t_0)}{\tau_P}} \right] \quad , \tag{1.9}$$

$$\text{with} \quad \begin{cases} P_{ST} & = & \dfrac{w_{\downarrow\uparrow} - w_{\uparrow\downarrow}}{w_{\uparrow\downarrow} + w_{\downarrow\uparrow}} = \frac{8}{5\sqrt{3}} \quad , \\ \tau_P & = & \dfrac{1}{w_{\uparrow\downarrow} + w_{\downarrow\uparrow}} = \left(\frac{5\sqrt{3}}{8}\; c\; \lambda_c\; r_0\; \dfrac{\gamma^5}{\rho^3} \right)^{-1} \quad , \\ P_0 & = & P(t = t_0) \quad . \end{cases} \tag{1.10}$$

P_{ST} is the asymptotic polarisation of Sokolov-Ternov and is equal to 92.4%. The characteristic time τ_P [s] $= 2.83\ 10^{18}\ (\rho^3/\gamma^5)$ is a constant characteristic of the polarisation rise. At HERA where E $\sim$ 27 GeV and $\rho \sim$ 700 m, τ_P is around 40 min. This very long time compared to the time interval between two photon emissions ($\sim \rho\lambda_c/c\gamma r_0 \sim 10^{-8}$ sec) is due to the very small spin-flip probability. This time decreases very rapidly as the energy increases due to the very fast increase of radiation rate that counteracts the small spin flip probability in photon emission.

1.1.4 Depolarisation effects

The previous expressions (1.10) of τ_P and P_{ST} are valid for an ideal machine, *i.e.* if the magnetic field is homogeneous and if leptons follow the designed trajectory exactly and

stay on their perfect circular orbit (named the closed orbit) after some radiation emission. In that case, as discussed in Section 1.1.2, each spin precess around the vertical direction y and the net beam polarisation direction $\mathbf{n}$ is along y. The rate of spin precession is equal to $a\gamma$ (see (1.5)) and corresponds to the number of rotations in a single turn around the ring on the closed orbit. The assumption that all electrons follow the designed trajectory is of course never fulfilled because the beam distribution has a finite spatial size and a non zero energy width, and also because accelerator error fields (*i.e.* magnet misalignments) cause excursions in particle motions. Thus, in reality, there are several depolarising effects which contribute to the deterioration of the lepton beam polarisation.

Integer and sidebands resonances

One of the depolarising processes is due to "integer resonances": if, for instance, an electron sees a perturbing horizontal magnetic field, it can easily be shown [18] that a cosine factor $\mathbf{n}\cdot\mathbf{y}$ between the vertical axis y and the net beam polarisation axis appears. This factor is proportional to $\sin(\pi a\gamma)$ and it follows that the beam polarisation vanishes ($\mathbf{n}\cdot\mathbf{y} = 0$) when the spin tune $a\gamma$ is equal to an integer. With typical magnet misalignments (few hundred micrometers at HERA), the width of such a resonance being much narrower than the spacing between the integer resonances, integer depolarisation resonances are easy to avoid.

Other depolarising processes (called "sidebands resonance depolarisations") arise when a particle undergoes betatron and/or synchrotron oscillations [19, 20]. Betatron oscillations are lateral (radial and vertical) motions executed by electrons due to focussing fields driving all electrons toward the ideal closed orbit. Individual electrons oscillate also in longitudinal position and in energy (relative to an ideal reference particle at the bunch centre) due to the periodic accelerating field. These motions are called synchrotron oscillations. Because of these particle oscillation motions, the spin precession angle $2\pi a\gamma$ acquires an additional term proportional to the betatron and/or synchrotron amplitudes and oscillating with the betatron and/or synchrotron tune of the machine [10]. By calling ν_x and ν_y the horizontal and vertical betatron tunes, and ν_s the synchrotron tune, the spin motion is seriously influenced by the perturbation if $a\gamma \pm \nu_x$ and/or $a\gamma \pm \nu_y$ and/or $a\gamma \pm \nu_s$ are equal to an integer [21].

Once the system deviates from the ideal case, the situation rapidly becomes complicated and the study of these effects case by case is impossible [22]. The knowledge of the storage ring fields including the error fields and the associated closed-orbit distortions are needed to obtain a formal description and calculate the expected polarisation [23, 24, 26].

Synchrotron radiation emission

Whereas the synchrotron radiation emission is responsible for the build up of the polarisation, it can also enhance the depolarisation resonance effect. Indeed, after a synchrotron photon is emitted, a particle deviates from its orbit and jumps to another. A spin is then sensitive to a magnetic field component in the quadrupole to which it would not have been sensitive in the absence of photon emission, and according to (1.4) its precession is changed. Let us give the order of magnitude of the time scales of the process: we consider an electron following the closed orbit with its spin polarised along a unit vector $\mathbf{n}$, as schematized by the first line in Figure 1.4. The second line in Figure 1.4 represents the

state just after the photon emission: the phase space coordinates of the particles change due to the photon emission and the particle starts to execute betatron and synchrotron oscillations (typical periods in the HERA collider are $\sim 10^{-6}$ sec and $\sim 10^{-4}$ sec for betatron and synchrotron oscillations respectively [14, 25]). Along the new trajectory, the spin motion is slightly different, precessing about a new axis $\mathbf{n}$ tilted with respect to the initial spin direction with a polar angle $|\mathrm{dn}|$. The third line in Figure 1.4 shows the evolution of the particle motion within a few transverse damping times ($\sim 3\rho^2/\mathrm{cr}_0\gamma^3$ [14, 19], *i.e.* a few miliseconds at HERA): the excited orbital oscillations are damped by the well-known damping mechanism [19]. Damping is a slow process compared to spin precession. Therefore the initial spin closed solution is restored but spin continues to precess around it with the polar angle $|\mathrm{dn}|$ when the orbital coordinates have been restored. The horizontal component of the spin precesses in a stochastic way as photon are emitted and its average over all particles of the beam vanishes. The remaining polarisation is the projection of the initial polarisation vector onto the spin axis tilted by the photon emission of an angle $|\mathrm{dn}|$.

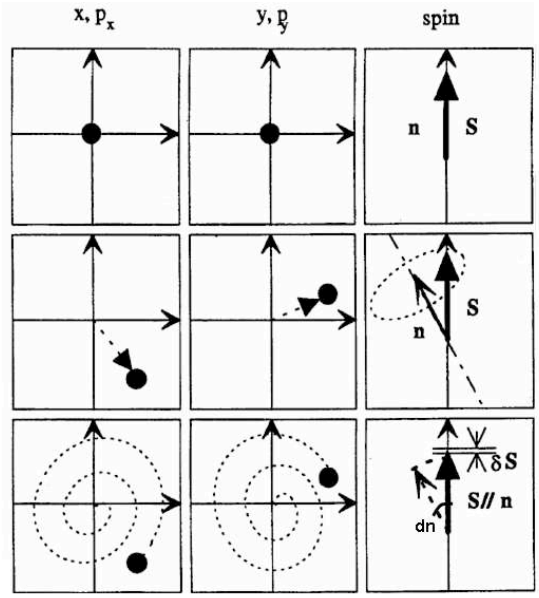

Figure 1.4: Evolution of the phase space and spin coordinates of a reference particle which emits a photon. From [10]. First line: an electron following the closed orbit. 2nd line: electron state just after a photon emission. 3rd line: electron motion within a few damping time.

This simple scheme of depolarisation due to quantum photon emission arises because of the very large difference between time constants of the relevant processes: around 10^{-7} sec for one spin precession ($\sim 2\pi\rho/\mathrm{c}\gamma\mathrm{a}$), a few milliseconds for the damping of the orbital coordinate and the gradual change of $\mathbf{n}$, and several tens of minutes for the Sokolov-Ternov polarising mechanism. All these times have also to be compared to the time scale for synchrotron emission $\sim 10^{-8}$ s. Photons are thus constantly emitted in a stochastic way and an electron bunch is in fact made up of a superposition of a large number of orbits. The asymptotic polarisation of a given bunch is thus reduced with respect to the asymptotic value $\mathrm{P_{ST}}$ of formula (1.10). To guarantee a good polarisation, the depolarisation time must be smaller than the polarisation time. For this one must stay far away from the sideband resonances so that synchrotron radiation does not enhance sideband depolarisation resonances.

Beam-beam effect

Beam-beam collisions are also a cause of particle orbit deviations leading to depolarisation effect. This is due to the effect of the proton beam charge which can be viewed as a quadrupole magnet by the electron beam. In addition, the electromagnetic field of one beam causes a precession of the spins of the particles in the second beam. The Luminosity Upgrade design for HERA II has been optimised for the highest improvement in luminosity but is not optimal for polarisation. Since the beam-beam force is highly nonlinear, it is very difficult to make analytical calculations on its effect for the lepton beams, and even more difficult to make analytical estimations of the effect on the polarisation. Calculations on depolarisation due to beam-beam effects [27] could not deliver convincing results for the upgraded optics and there is no clear statement about the importance of this depolarisation effect. They can nevertheless be estimated on the basis of the pre-Upgrade observations to be around 10% [28].

Polarisation predictions can be made using machine simulation (PETROS code [29]) and spin tracking simulation (SITROS code [26]). However, since the polarisation is very sensitive to the exact distortion of the machine and since this distortion cannot be measured with sufficient accuracy, theoretical predictions serve rather as a guide when setting up the machine and in correcting the orbit to minimise the depolarising effects. Let us make finally an important remark: the polarisation build up characteristic time ($\sim$ 40 min at HERA) being much larger than all other depolarising process time scales, the polarisation is varying very slowly and is the same in absolute value all over the ring.

1.1.5 Spin rotators

Spin rotators are special ensembles of magnets which allow the $\mathbf{n}$ vector to be rotated [25, 30]. As it was described previously, the Sokolov-Ternov effect polarises the beam vertically. Thus to obtain a longitudinal polarisation around the H1 and ZEUS areas, two pairs of spin rotators have been installed on both sides of the two experiments. The principle of a spin rotator is to use a set of magnetic fields to transform a transverse polarisation to a longitudinal polarisation. Because the requirement of a longitudinal spin is incompatible with the Sokolov-Ternov polarising mechanism, the polarisation must remain vertical in the arcs, where most of the synchrotron radiation is emitted. Therefore, in order not to depolarise the beam, longitudinal polarisation has to be transformed back to transverse polarisation before reaching the arcs of HERA. This is why spin rotators are always used in pairs. The rotators installed at HERA are the so-called "Mini-Rotators", whose design was developed by Buon and Steffen [31]. A single mini-rotator consists of a sandwich of horizontally and vertically bending magnets, as schematized in Figure 1.5.

Spin diffusion can be strong in a ring containing spin rotators. The reason is that between a pair of rotators, the average spin direction $\mathbf{n}$ can be considered to be maximally tilted with respect to the vertical direction since the spin precesses around the axis perpendicular to the vertical natural equilibrium direction. In this configuration, the vertical quadrupole fields may cause a large spin diffusion. Also, when spin is longitudinal, synchrotron radiation emitted in the rotators excite vertical orbital oscillations which are sources of depolarisation.

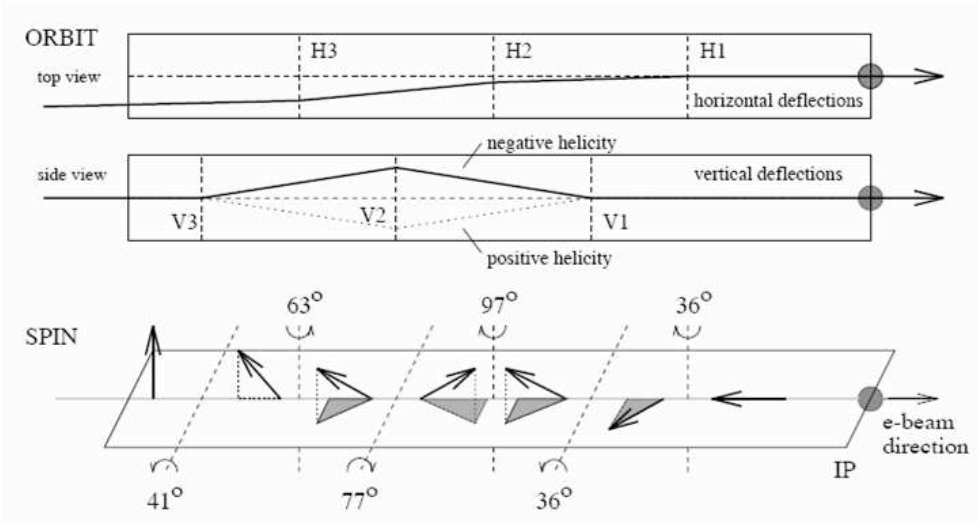

Figure 1.5: Spin rotator installed at HERA. From [25]. Horizontal and vertical orbital motions are shown on the two top drawings and spin direction on the bottom drawing. "V" and "H" refer to vertical and horizontal bending magnets respectively. The length of the device is approximately 56 m.

1.2 Polarisation measurement principles

Several methods exist for measuring electron beam polarisation [32] (the Mott polarimetry [33, 34], the Møller polarimetry [35], the Compton polarimetry [36]). At the HERA energy, the most accurate is Compton polarimetry because it gives a non destructive measurement and thus polarisation measurements can be done simultaneously with the experimental data taking. In this section the principle of Compton polarimetry is presented.

1.2.1 Compton scattering cross section

The principle of Compton polarimetry is the Compton scattering process e $\gamma \rightarrow$ e γ [37, 38, 39]. At HERA, the lepton beam interacts with a circularly polarised laser beam and the scattered Compton photons detected in a calorimeter allow the lepton beam polarisation to be determined. A basic drawing of the Compton process is presented in Figure 1.6.

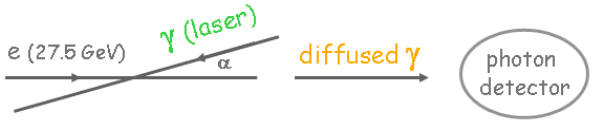

Figure 1.6: Basic drawing of the Compton scattering process.

We won't enter in the details of the kinematics and angular distribution of the scattered photons. They are described in detail in [40, 41]. The main point is that with a high energy electron beam, the photons are scattered within a cone of a few hundred of microradians in the direction of the electron beam. Therefore the energy of an ensemble of scattered photons coming from interactions with a laser beam can be measured completely within a small calorimeter.

Let us consider now a polarised electron beam interacting with a circularly polarised laser beam under the assumption that the crossing angle is null. In the laboratory rest

frame, electrons and photons propagate along the z direction in opposite direction as schematized in Figure 1.7.

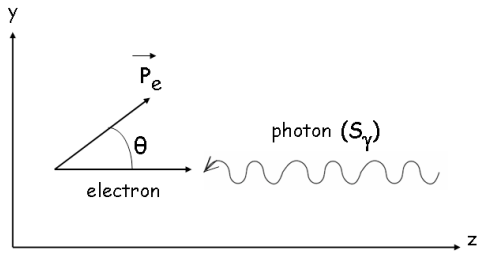

Figure 1.7: Interaction between a polarised electron and a circular polarised photon schematized in the laboratory rest frame.

In this Figure, $\vec{P}_e$ represents the polarisation vector of electrons and is oriented by an angle θ with respect to the z axis. S_γ is the circular polarisation of the laser beam. With:

- E and m the energy and the mass of the incident electron,
- k_γ the energy of the incident photon (*i.e* of the laser beam),
- θ_γ the polar angle of the scattered photon,
- ϕ_γ the azimuthal angle of the scattered photon with respect to the (yOz) plane,
- E_γ the energy of the scattered photon,

the differential Compton cross section can be written as [39]:

$$\frac{d^2\sigma_c^{\pm}}{d\rho_\gamma\, d\phi_\gamma} = \frac{d^2\sigma_0}{d\rho_\gamma\, d\phi_\gamma} - P_e\, S_\gamma \left(\cos\theta \frac{d^2\sigma_L}{d\rho_\gamma\, d\phi_\gamma} + \sin\theta\, \cos\phi_\gamma \frac{d^2\sigma_T}{d\rho_\gamma\, d\phi_\gamma} \right) \tag{1.11}$$

where the parameter ρ_γ is defined by:

$$\rho_\gamma \equiv \frac{E_\gamma}{E_\gamma^{max}} = \left[1 + \left(\frac{1}{1 + \frac{4k_\gamma E}{m^2}} \right) \left(\frac{\theta_\gamma E}{m} \right)^2 \right]^{-1} ,$$

E_γ^{max} being the maximal energy of the scattered photon (reached for $\theta_\gamma = 0$). In (1.11), σ_0, σ_L and σ_T are respectively the non-polarised, the the longitudinal and the transverse Compton cross sections. σ_0, σ_L and σ_T are three functions of ρ_γ (*i.e.* of the energy of the scattered photon), of the incident lepton energy and mass E and m respectively, and of the incident laser photon energy k_γ (the complete expressions of these three functions can be found in [41]). The differential Compton cross section after integration over the variable ϕ_γ is written as:

$$\frac{d\sigma_c^{\pm}}{d\rho_\gamma} = \frac{d\sigma_0}{d\rho_\gamma} - P_{e||}\, S_\gamma \left(\frac{d\sigma_L}{d\rho_\gamma} \right) \tag{1.12}$$

where $P_{e||} = P_e \cos\theta$ is the longitudinal component of the electron beam polarisation.

The transverse cross section appears in (1.11) through the term ($\cos\phi_\gamma$). Indeed, the transverse component of the electron polarisation breaks the azimuthal symmetry in the scattering process. Therefore, to determine the transverse polarisation, both the energy and the azimuth angle ϕ_γ of scattered photons have to be measured [42, 43]. The electron longitudinal polarisation can be determined from the scattered photon energy only, after integrating over the azimuth angle ϕ_γ. An accurate measurement of the longitudinal polarisation is therefore easier to perform.

1.2.2 HERA polarimeter measurement modes

At HERA, three polarimeters are used to measure the polarisation of the 27.5 GeV electron or positron beams [44]. All instruments are laser scattering Compton devices. The first is the transverse polarimeter TPOL located in the west area of HERA. It measures the transverse beam polarisation by detecting the angular asymmetry of the scattered Compton photons with respect to the orbital plane of the lepton beam [36, 45]. The second is the longitudinal polarimeter LPOL which measures the longitudinal lepton polarisation between the two spin rotators located around the HERMES experiment (see Figure 1.1). The longitudinal polarisation component along the beam direction is measured by detecting an asymmetry in the energy spectra of the Compton photons [46, 47]. Up to the year 2001, only the TPOL and the LPOL were in operation. During the upgrade of 2001, a third longitudinal polarimeter, the cavity polarimeter POLCA, has been constructed and installed on the HERA ring between the HERMES spin rotators just behind the LPOL. Because they have the same scattered Compton photon beam line, both longitudinal polarimeters LPOL and POLCA were used in turn during the HERA II phase.

The number of scattered photons

The HERA polarimeters do not have the same measurement mode: the average numbers of scattered photons n_γ per laser-electron bunch crossing may be different by several orders of magnitude. n_γ firstly depends on the laser beam-electron beam crossing rate which is determined by the laser choice (pulsed laser or continuous wave laser) and the HERA frequency (in the HERA ring, 220 bunches of electrons/positrons are stored, each one time spaced by 96 nsec). n_γ depends also on the laser beam-electron beam luminosity $\mathcal{L}_{e\gamma}$. Assuming a gaussian shape for the electron beam and the laser beam intensities, the expression of $\mathcal{L}_{e\gamma}$ (calculated in [40] for instance) integrated over the space variables is written as:

$$\mathcal{L}_{e\gamma} = \frac{1}{\sqrt{2\pi}} \frac{I_e}{ec} \frac{P_c \lambda}{hc} \frac{1}{\sigma_{ex}^2 + \sigma_\gamma^2} \frac{1+\cos\alpha_c}{\sin\alpha_c} \quad , \tag{1.13}$$

where σ_{ex} and σ_γ are the transverse electron and laser beam radius along the x axis (the z dependance of the sigmas has been neglected and the the plane of interaction of the electron and laser beams is assumed to be vertical), P_c is the light power at the Compton IP, λ is the laser wavelength, I_e is the electron beam current, and α_c is the electron-laser beam crossing angle. Therefore, in a storage ring where lepton bunches are separated by Δt in time, the number of scattered photons per bunch can be written as:

$$n_\gamma/\text{bunch} = \Delta t \; \mathcal{L}_{e\gamma} \sigma_c \quad . \tag{1.14}$$

n_γ for TPOL and LPOL

Table 1.1 gives the main parameters of the TPOL and the LPOL devices and in particular the number of scattered photons resulting from Compton interactions. The TPOL employs an Ar-ion laser delivering a 10 W continuous-wave beam at a wavelength of 515.5 nm. The frequency of the electron beam-laser beam crossing is 10 MHz (corresponding to the HERA bunch spacing frequency). The number of scattered photon per bunch is small (around 0.001). This measurement mode where $n_\gamma \ll 1$ is called "single photon

	LPOL	TPOL
Laser	10 W pulsed (100 mJ/pulse, 100 Hz)	10 W CW laser
e–γ crossing	100 Hz	10 MHz
n_γ	$\sim$1000 γ/pulse	$\sim$0.001 γ/bunch [45] [1]
ΔP_e(stat)	3%/bunch/20min [47]	1%–4%/allbunches/min [48]

Table 1.1: Main parameters of the transverse and longitudinal polarimeters TPOL and LPOL.

mode". The LPOL employs a frequency-doubled pulsed YAG laser which produces 3 ns long pulses and which can be operated with variable repetition rate from single shot up to 100 Hz, and with pulse energies from 1 to 250 mJ. To minimise pulse-to-pulse intensity fluctuations, the LPOL laser is operated at a fixed energy of 100 mJ per pulse. A large number of Compton photons (about 1000 photons) is produced each time a laser pulse interacts with an electron bunch. This mode is called the "multi photon mode".

For the TPOL, because of the single photon measurement mode, the average of all the HERA bunches is necessary to obtain a statistical uncertainty of 1% up to 4% per minute (1% at the beginning of a HERA fill when electron current is maximum, and 4% at the end of the fill). An example of TPOL lepton polarisation measurements and the corresponding statistical uncertainties is presented in Figure 1.8.

For the LPOL running in the multi photon mode, twenty minutes are necessary to obtain a statistical uncertainty on the lepton polarisation of 3% per bunch. The LPOL could also run in the single photon mode if the laser pulse intensity is drastically reduced. But in this case a beam polarisation measurement with a statistical accuracy of 1% should take about 2.5 hours. In multi photon mode, the LPOL laser pulses are very energetic but the repetition rate of 100 Hz does not allow a better statistical accuracy to be obtained. To illustrate the muti photon and the single photon modes, experimental distributions taken by the LPOL are shown in Figures 1.9 and 1.10.

In the single photon mode, the energy of each individual Compton photon is analysed. The advantage of this mode is that one can calibrate absolutely the calorimeter by using the shape of the photon distribution. The disadvantage of this mode is the low statistics. In the case of large background levels, the signal may also be too diluted and thereby the polarisation measurement accuracy deteriorated.

In the multi photon mode one measures the total energy deposited in the detector. When the background level is large, or when the polarisation needs to be known after a single bunch crossing (as linear colliders for instance), high energy pulsed lasers are used. The longitudinal polarisation is linearly proportional to the difference between the two distributions (such as those in Figure 1.9) obtained with a left and right circularly polarised laser beam. The disadvantage of this mode is the very high energy (a total energy up to 10 TeV [49]) seen by the calorimeter. Since the energy calibration of the calorimeter is done using low energy beam electrons, the polarisation measurement is affected by a large systematic uncertainty difficult to control. Another difference between this mode and the single mode is that one cannot extract the polarisation without combining the

[1] this number 0.001 comes from a rescaling of the number in [45] taking into account the upgrade of the HERA luminosity

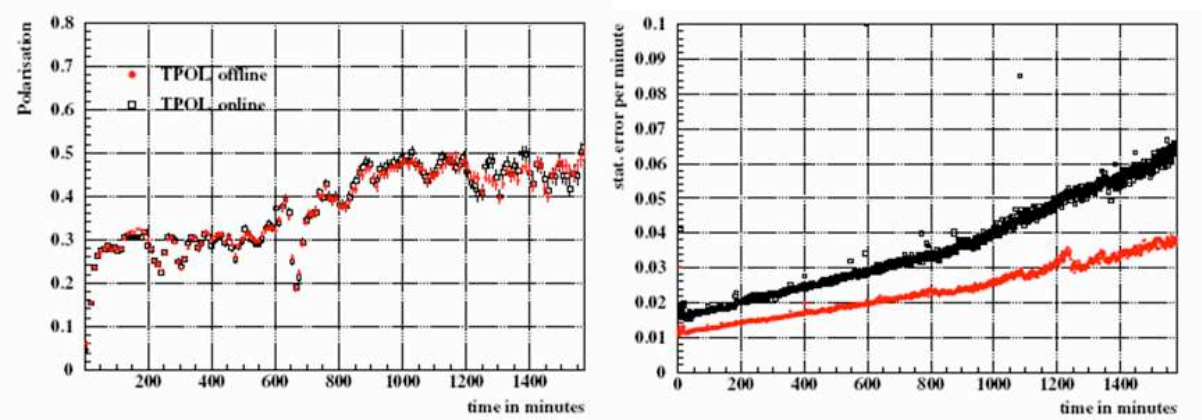

Figure 1.8: HERA-TPOL polarisation measurements (left plot) and statistical errors (right plot). From [48].

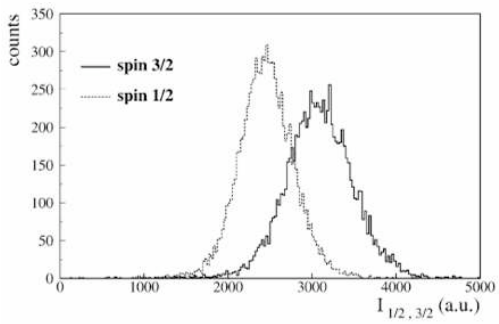

Figure 1.9: HERA-LPOL energy spectra collected in multi photon mode for $S_\gamma = +1$ (spin 3/2 in the plot) and $S_\gamma = -1$ (spin 1/2 in the plot). From [47].

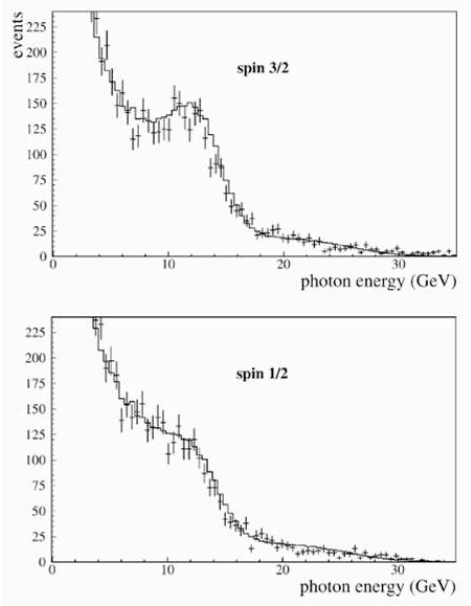

Figure 1.10: HERA-LPOL energy spectra collected in single photon mode for $S_\gamma = +1$ (spin 3/2 in the plot) and $S_\gamma = -1$ (spin 1/2 in the plot). The solid line is the result of a simulation. From [47].

two photon energy spectra corresponding to the two laser helicities. Finally, the statistic is also limited by the laser pulse frequency.

For all these reasons, the "few photon mode", *i.e.* a measurement mode where the number of scattered photons n_γ is around the unity, appears to be a good compromise between the single and the multi photon modes. The cavity polarimeter instrument POLCA has been designed to operate in this mode in order to reach the few per mill level on the statistical and systematic accuracies on the longitudinal lepton polarisation measurement. Before describing the instrument itself, let us give a more precise description of the few photon mode measurement procedure and an estimation of the expected statistical accuracy.

1.3 Polarisation extraction in the few photon mode

1.3.1 Principle

For a longitudinal polarised electron beam, the Compton scattering cross section in the laboratory rest frame as a function of the scattered photon energy is given by (1.12). By replacing the dimensionless variable ρ_γ by the scattering photon energy E_γ and the longitudinal lepton polarisation $P_{e||}$ by P_e, (1.12) is written as:

$$\frac{d\sigma_c^{\pm}}{dE_\gamma} = \frac{d\sigma_0}{dE_\gamma} - P_e\, S_\gamma \left(\frac{d\sigma_L}{dE_\gamma}\right) \tag{1.15}$$

In the few photon mode, the signal consists of about one scattered photon per electron bunch (220 bunches turn in HERA, with an electron beam current of 40 mA). Sources of background are the following. We just give the list of the background sources without too much details. This subject has been largely treated in [50].

- **Bremsstrahlung photons**: photons are produced by the electron beam hitting the residual gas in the vacuum pipe. The expression of the differential cross section $d\sigma(e+g \to e+g+\gamma)$ (where g stands for the residual gas) can be found in [51, 52]. The Bremsstrahlung background rate is expected to be of order of 0.1 photons per bunch.

- **Blackbody photons**: these photons are produced by collisions between electrons and photons emitted from the 310 K hot beam pipe walls [53]. The rate is expected to be ~ 0.06 photon per bunch and the maximum energy to amount ~ 3 GeV.

- **Synchrotron radiation**: the calorimeter is illuminating by synchrotron radiation from a bending magnets (BH90 magnet) located between the Compton IP and the calorimeter. Synchrotron background from this magnet is made of a large number of low energy photons and the total reaches ~ 2 TeV per bunch [49]. A lead shielding is located in front of the calorimeter so that only 100 MeV is expected in the detector.

The energy spectra of the scattered photons for left and right circular polarised laser photons are shown in Figure 1.11 where the dominant background spectra from bremsstrahlung photons and blackbody photons are also represented.

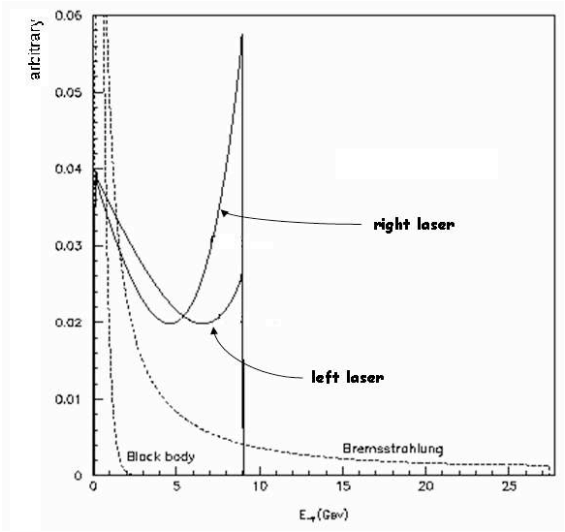

Figure 1.11: Compton scattered energy spectra for left and right polarised laser light. Also shown are the black body radiation spectrum and the dominant background spectrum coming from electron beam - gas bremsstrahlung for an electron beam energy of 27.5 GeV. Relative normalisation between Compton, bremsstrahlung and blackbody spectra are arbitrary and no detector effect has been taken into account. From [54].

Calorimeter signals are measured by setting alternalively $S_\gamma = +1$ (right circularly polarised photons) and $S_\gamma = -1$ (left circularly polarised photons). One calorimeter acquisition is made for each electron bunch turning in HERA. To extract the longitudinal polarisation of a lepton bunch, an adjustment is performed with the two measured energy spectra ($S_\gamma = \pm 1$). Contrary to the multi photon mode measurement, in the single or few photon modes the shape of the energy distribution is exploited to determine the numbers of signal and background events in the same time with the detector parameters. Because physical processes which produce photons are independent, the adjustment is performed to the sum of bremsstrahlung, blackbody, synchrotron radiation and Compton photon spectra: after one period of acquisition with the calorimeter (which lasts typically 20 seconds, corresponding to $\sim$ 400.000 entries in each one of the two energy spectrum histograms), average numbers of events of energy between E and E + ΔE are computed according to the theoretical energy distributions of synchrotron radiation, Bremsstrahlung, blackbody background and Compton processes. A statistical estimator is then constructed and a minimisation is performed to extract the numbers of signal and background photons per bunch and then the lepton bunch polarisation. All mathematical expressions of this procedure are given in [55, 50].

1.3.2 Numerical studies

To get an idea of the statistical uncertainty of the lepton polarisation expected in the few photon mode, a set of Monte Carlo studies have been performed by varying the number of scattered photons n_γ. For this study, the laser is a continuous wave laser of wavelength $\lambda = 1.064$ nm, the lepton beam energy is 27.5 GeV, the lepton beam polarisation is 0.5, the crossing angle between the lepton beam and the laser beam is 58 mrad and the acquisition time per histogram is 6 seconds. The absolute statistical accuracy obtained from this analysis is presented in Figure 1.12 for two bremsstrahlung background rates describing the range presently observed in the HERA-LPOL area.

For $n_\gamma \sim 1$ one sees that a statistical accuracy of a few per mill per bunch and per minute is reached. From the expression (1.13) of the electron beam-laser beam luminosity, one finds that for a crossing angle of 58 mrad, one scattered photon corresponds to a laser power of $\approx$ 70 KW for an electron beam current of 1 mA (or a laser power of $\approx$ 1.8 KW

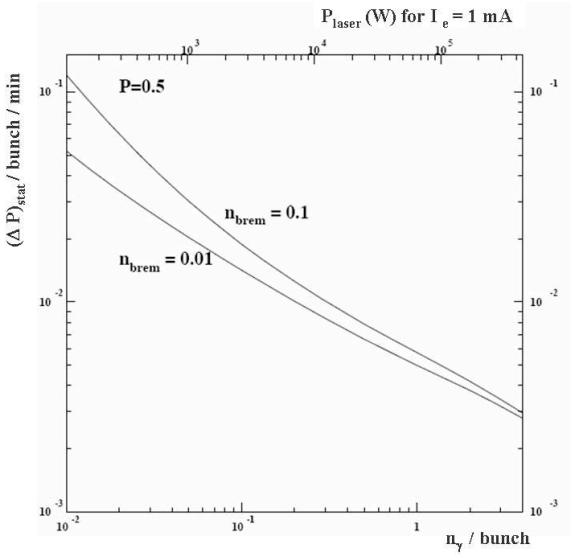

Figure 1.12: Statistical uncertainty of the polarisation per bunch and per minute as a function of the number of scattered photon n_γ. Two curves are shown for different bremsstrahlung background levels of 1% and 10%. Also shown is the laser power needed to obtain a given number of scattered photons, assuming a crossing angle of 58 mrad. From [56].

for the HERA lepton beam current of 40 mA). The technical solution to obtain such a power with a continuous wave laser is then to use an optical amplifier. This is the idea of the Fabry-Perot cavity polarimeter.

Chapter 2

The Fabry-Perot polarimeter setup

In Chapter 1, the lepton beam polarisation build up and the basic principles of its measurement at HERA have been described. We have also seen why it has been decided to build a new polarimeter using a Fabry-Perot cavity and why this instrument can improve significantly the accuracy of the lepton polarisation measurements. This chapter describes the Fabry-Perot cavity installed in the HERA tunnel. Firstly, basic principles of a Fabry-Perot resonator will be introduced. Then, the cavity system itself and the photon detection system will be described. Finally, we will show some results concerning the laser/cavity coupling and some measured photon energy spectra with their corresponding theoretical distributions used to extract the lepton beam polarisation.

2.1 Basic principles

2.1.1 Fabry-Perot resonator principle

In its simplest version, a Fabry-Perot cavity consists of two mirrors located opposite to each other. By applying the energy conservation principle and by taking into account the losses, a mirror (supposed to be flat[1]) is characterised by:

- its reflection coefficient in field amplitude r,
- its transmission coefficient in field amplitude t,
- its losses P (*i.e.* absorbed and scattered energy in ppm).

The corresponding energy reflection and transmission coefficients are written as: $R = |r|^2$ and $T = |t|^2$ respectively. Only two of the three parameters P, R and T are independent and they are related by:

$$P + R + T = 1 \; . \tag{2.1}$$

When an incident wave of amplitude A_{inc} arrives at a mirror interface, the relations between the incident wave amplitude A_{inc}, the reflected wave amplitude A_{ref} and the

[1]If the mirror is not flat but has a radius of curvature very large relative to a light beam size, it can be still considered as a plane mirror.

transmitted wave amplitude A_{tr} are (by convention) written as:

$$\begin{cases} A_{ref} = r\ A_{inc} \\ \\ A_{tr} = i\ t\ A_{inc} \end{cases} \tag{2.2}$$

Let us consider the cavity schematized in Figure 2.1 where L is the distance between two identical mirrors of reflection and transmission coefficients r and t respectively.

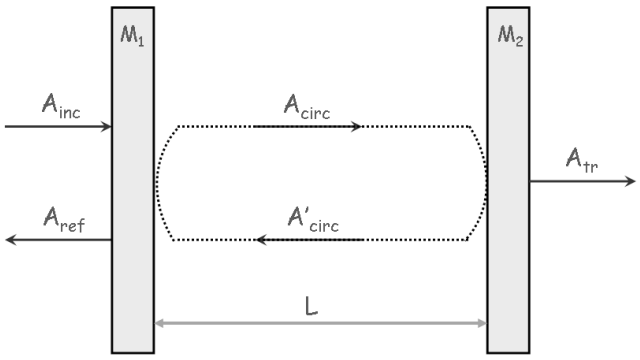

Figure 2.1: Basic drawing of an optical Fabry-Perot cavity made of two plane mirrors M_1 and M_2 separated by a distance L.

When an incident wave arrives on the cavity, the amplitudes A_{ref}, A_{circ} and A_{tr} of the fields reflected by the cavity, circulating inside the cavity and transmitted by the cavity in stationary regime can be obtained from (2.2):

$$\begin{cases} A_{ref} &= r\ A_{inc} + i\ t\ A'_{circ} \\ \\ A_{circ} &= i\ t\ A_{inc} + r\ A'_{circ} \\ \\ A_{tr} &= i\ t\ e^{-i\Delta\phi}\ A_{circ} \end{cases} \tag{2.3}$$

$$\text{with :}\ \ A'_{circ} = r\ e^{-2i\Delta\phi}\ A_{circ}\ .$$

$\Delta\phi$ is the phase shift induced during the passage of the light from one cavity mirror to the other. These amplitudes are then written as:

$$\begin{aligned} A_{ref} &= r\left(1 - t^2\ \frac{e^{-2i\Delta\phi}}{1 - r^2\ e^{-2i\Delta\phi}}\right)\ A_{inc}\ , \\ \\ A_{circ} &= \frac{i\ t}{1 - r^2\ e^{-2i\Delta\phi}}\ A_{inc}\ , \\ \\ A_{tr} &= \frac{-\ t^2\ e^{-i\Delta\phi}}{1 - r^2\ e^{-2i\Delta\phi}}\ A_{inc}\ . \end{aligned} \tag{2.4}$$

2.1.2 Gaussian laser beam

In practice, laser beams are usually almost Gaussian beams. Their intensity distributions are concentrated near the axis of propagation, and their wave fronts are curved. Let us consider a gaussian field E of a coherent laser light travelling along the z axis. By calling

E_0 the laser field intensity, this field, solution of the Maxwell equations, can be written in the paraxial approximation[2] as:

$$E = E_0 \, \psi(x,y,z) \, e^{-ikz} \quad , \tag{2.5}$$

where ψ satisfies the paraxiale wave equation:

$$\frac{\partial^2 \psi}{\partial x^2} + \frac{\partial^2 \psi}{\partial y^2} - 2ik \frac{\partial \psi}{\partial z} = 0 \, . \tag{2.6}$$

ψ is a complex function which could represent the difference between a laser beam and a plane wave (the non-uniformity of the intensity distribution and the curvature of the wave fronts). The eigensolutions to (2.6) can be given as a complete set of functions called the Hermite-Gauss functions and have the form [57, 58, 59]:

$$\psi_{nm}(x,y,z) = H_n\left(\frac{\sqrt{2}\,x}{w(z)}\right) H_m\left(\frac{\sqrt{2}\,y}{w(z)}\right) e^{i\Phi_{nm}(z)} \; e^{-r^2\left[\frac{1}{w^2(z)} + \frac{ik}{2R(z)}\right]} \tag{2.7}$$

where:

- H_n is the Hermite polynomial[3] of order n,
- n and m are the transverse mode numbers,
- $r^2 = x^2 + y^2$,
- w(z) is the transverse radius of the field and is written as:

$$w^2(z) = w_0^2 \left[1 + \left(\frac{\lambda z}{\pi w_0^2}\right)^2\right] \, , \tag{2.8}$$

  where $w_0 \equiv w(0)$ is the laser beam waist and λ the laser wavelength. For the fundamental mode ($n = m = 0$), at a given position z, w is the distance at which the field amplitude is 1/e times that on the z axis.

- R(z) is the radius of curvature of the wavefront:

$$R(z) = z \left[1 + \left(\frac{\pi w_0^2}{\lambda z}\right)^2\right] \, . \tag{2.9}$$

- Φ_{nm} is the phase shift which depends on the mode numbers m and n and of the Guoy phase $\phi_{Guoy}(z)$:

$$\begin{cases} \Phi_{nm}(z) = (n + m + 1) \; \phi_{Guoy}(z) \\ \\ \phi_{Guoy}(z) = \arctan\left(\dfrac{\lambda z}{\pi w_0^2}\right) \quad . \end{cases} \tag{2.10}$$

  Equation (2.10) expresses the fact that the phase velocity of a wave increases with the mode number.

[2]The paraxial approximation supposes a small divergence ($\lesssim 30^o$) of the beam with respect to its propagation axis.

[3]Hermite polynomials of low orders are: $H_0(x) = 1$, $H_1(x) = x$, $H_2(x) = 4x^2 - 2$, $H_3(x) = 8x^3 - 12x$.

Figure 2.2 shows the expansion of a beam in its fundamental mode according to (2.8) and (2.9). The beam contour w(z) is a hyperbola with asymptotes inclined to the axis at an angle $\theta = \lambda/(\pi w_0)$. The gaussian beam "contracts" and, in a certain plane of the propagation axis, it passes by a minimum size w_0 (the waist).

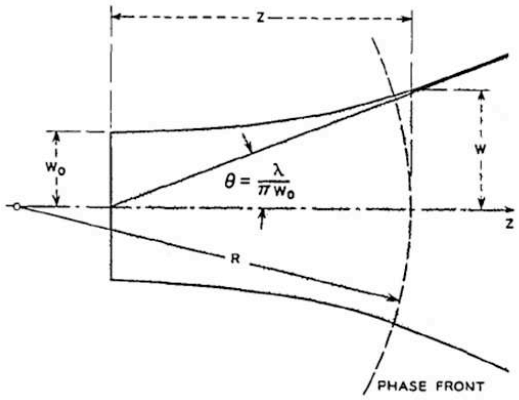

Figure 2.2: Profile and main characteristics of a gaussian beam. From [57].

From the field expression (2.7), the intensity pattern in a cross section of a beam of order (n,m) can be derived. It is described by the product of Hermite and Gaussian functions. Pictures of intensity patterns of lowest order modes are shown in Figure 2.3.

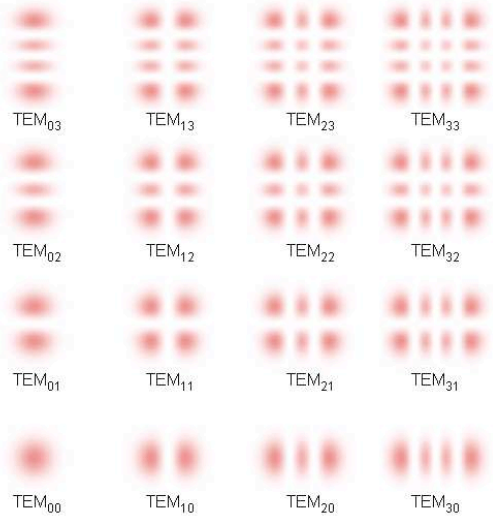

Figure 2.3: Intensity profiles of the lowest order Hermite-Gaussian modes. The number of zeros in one direction is equal to the corresponding mode number. From [60].

In the fundamental mode (obtained by taking n = m = 0), equation (2.5) has a pure gaussian form: the intensity distribution is then gaussian in every beam cross section and the width of that gaussian intensity profile changes as the beam propagates along its axis.

2.1.3 Laser/cavity resonance conditions

A mode resonator is defined as a self-consistent field configuration: if a mode can be represented by a wave propagating between the mirrors, the beam parameters must be the same after one complete round trip of the beam in order to propagate inside the cavity. Hence, for a cavity of length L and made of two identical spherical mirrors (whose

sizes are large compared to the spot size of the beam), the waist of the beam must be in the centre of the cavity, and the beam radius of curvature on the mirror M and the mirror radius of curvature must be the same in order to conserve the same waist size after a reflection by this mirror. Taking z = 0 at the cavity centre, this boundary condition leads to:

$$R(z = \frac{L}{2}) = R_M \quad , \tag{2.11}$$

where R_M is the radius of curvature of the cavity mirrors. Using formula (2.9) results in a condition on the waist: w_0 has to be matched to the parameters L and R_M of the cavity by the relation [57]:

$$w_0^2 \; = \; \frac{\lambda}{2\pi} \sqrt{L\,(2R_M - L)} \; . \tag{2.12}$$

This resonant condition is independent of the mode number and thus is the same for all the laser modes.

In addition to the waist condition, a phase condition has to be fulfilled to keep the cavity at a resonance. Indeed a resonance occurs when the amplitude of the field circulating inside the cavity is maximal. From (2.4), one sees that A_{circ} is maximal when $2\Delta\phi = 2q\pi$ (where q is an integer called the longitudinal mode number), *i.e.* when the phase shift of a wave from one cavity mirror to the other is an integer multiple of π. From formula (2.5) and (2.10) of the phase of a Hermite-Gaussian wave, this condition leads to:

$$\left[k \times \frac{L}{2} \; - \; \Phi_{nm}\left(\frac{L}{2}\right) \right] \; - \; \left[- \, k \times \frac{L}{2} \; - \; \Phi_{nm}\left(-\frac{L}{2}\right) \right] \; = \; q \; \pi \quad . \tag{2.13}$$

From (2.10) and (2.12) and after a small calculation, the resonance frequency ν_{nm} of a mode of order (n,m) is given by:

$$\nu_{nm} \; = \; FSR \left[\, q + \frac{1}{\pi} \, (n + m + 1) \arccos\left(1 - \frac{L}{R_M}\right) \right] \quad , \tag{2.14}$$

where $FSR = c/(2L)$ is the free spectral range of the cavity, *i.e.* the frequency distance between two longitudinal modes of the cavity.

So, in order to propagate a Hermite-Gaussian mode of order (n,m) in a cavity of length L with two mirrors of equal radius of curvature R_M, the laser frequency must satisfy the condition (2.14) and the laser waist w_0 must be located at the centre of the cavity and satisfy the condition (2.12).

2.1.4 Cavity geometry

The principle of the implementation of a cavity around an electron beam pipe is to introduce the cavity mirrors near the electron beam pipe and put the laser and all other optical components on an optical table under the cavity, as schematized in Figure 2.4. To avoid synchrotron radiation which is focused in the electron orbit plane, the laser beam must cross the electron beam in the vertical plane, *i.e.* along the y axis. Since the mirrors are located inside an ultra high vacuum region, it would not have been convenient to use actuators to adjust the cavity length. A monolithic cavity design has therefore been chosen (in this case the laser frequency must be adjusted on a resonant cavity frequency). This experimental setup had already been operated successfully at Jefferson Laboratory on the CEBAF accelerator [62, 63, 64, 65].

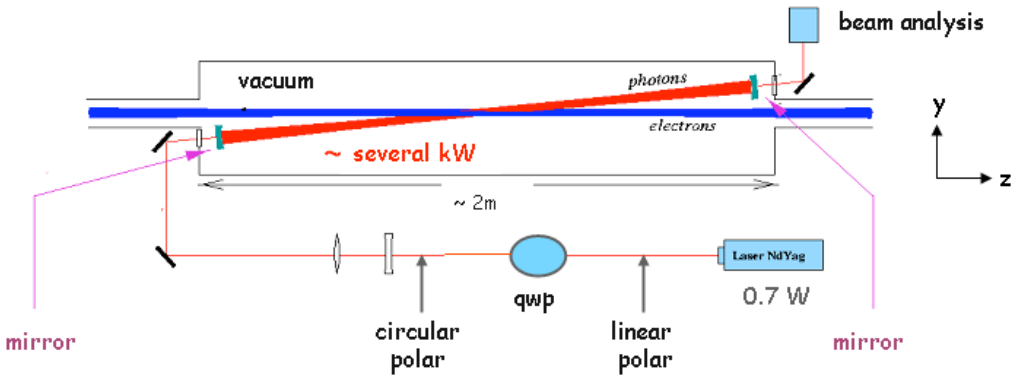

Figure 2.4: Simplified scheme of the Fabry-Perot cavity implemented in an electron beam pipe. From [61]. "qwp" is a quater wave plate which turn the polarisation of the laser light (see Section 2.2.2).

The exact geometry of the cavity is determined by the distance of the two mirrors, the radius of curvature of the mirrors and the crossing angle α_c between the laser beam and the lepton beam. This angle has to be minimal to maximise the laser beam-lepton beam luminosity (see equation (1.13)). At HERA, the minimum distance d_{min} between the electron beam axis and the edge of the mirror is 4.5 cm (2 cm for machine requirements and 2.5 cm for mechanical reasons).

Hence, in the same way as in Section 1.3.2, numerical studies has been performed to estimate the Compton event rate as function of the cavity geometry parameters. The distance d_{min} being fixed, the Compton event rate can be determined as function of the cavity length (or in an equivalent way of the crossing angle α_c) and of the light power inside the cavity. This rate is shown in Figure 2.5 for an 1 mA electron beam current. The yellow hatched area indicates the scattered photon rate of 0.025 to 0.05 photons per bunch (*i.e.* the rate of 1 to 2 photon per bunch for the HERA lepton beam currents of 40 mA). One sees in this figure that the required scattered photon rate is obtained with a 2 m long cavity in which the light power is of a few kW, or with a 30 m long cavity in which the light power is around of 500 W. Obviously the first solution has been adopted.

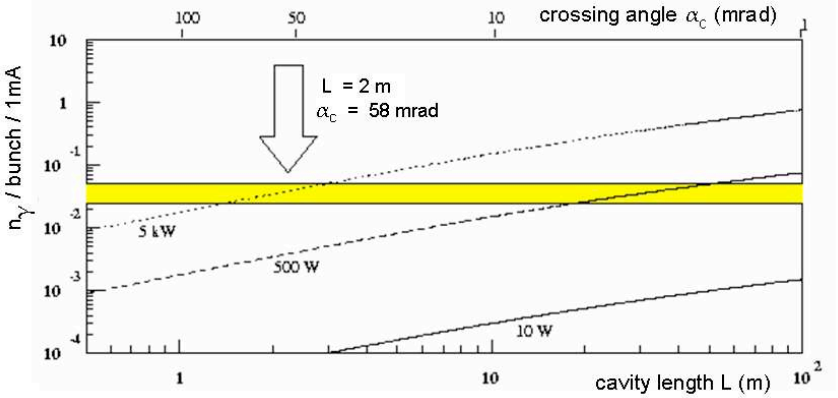

Figure 2.5: Scattered photon event rate per bunch for an electron current of 1 mA as a function of the cavity length L (bottom scale) and equivalently as a function of the laser-electron crossing angle α_c (top scale), for a fixed distance d_{min} = 4.5 cm between the electron beam axis and the cavity mirror edges, and for different light power inside the cavity. The arrow indicates the adopted solution.

Hence, our cavity is an almost 2 m long monolithic cavity, made of two spherical mirrors with a radius of curvature of 2 m. The choice of a confocal cavity design ($L \approx R_M$) has been made because of its better mechanical stability as schematized in Figure 2.6.

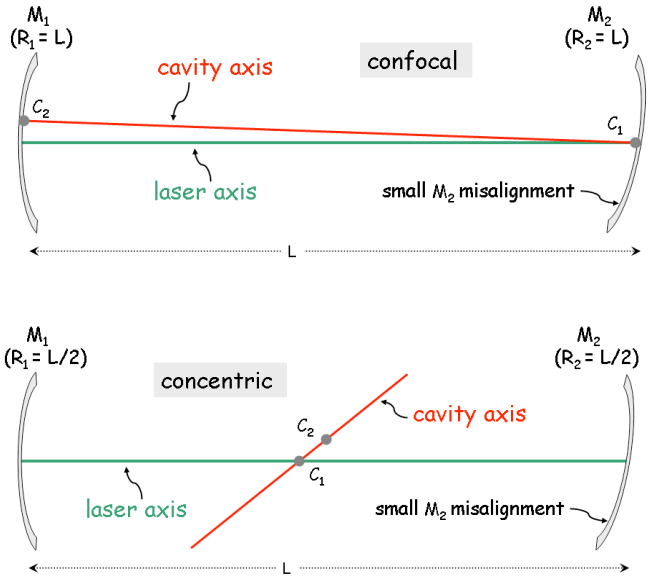

Figure 2.6: Two examples of two-mirror optical cavities illustrating the stability of a confocal cavity: a confocal scheme (up) and a concentric scheme (bottom). C_1 and C_2 are the mirror centres. In the confocal scheme, a little misalignment leads to a small mismatching between the cavity axis and the laser axis, whereas in the concentric scheme it leads to a large mismatching.

In fact, the cavity length is not exactly equal to the radius of curvature of the mirrors in order to avoid degeneracy in the transverse mode frequencies (see Section 2.1.5). Hence, the ratio L/R_M is a little larger than the unity, and is written as:

$$\frac{L}{R_M} \equiv 1 - \Delta_L \qquad \text{with} \qquad \Delta L = -0.0075 \ . \tag{2.15}$$

This value $\Delta L = -0.0075$ (which has been arbitrarly choosen) corresponds to a cavity lenght $L = 2.015$ m and allows the transverse mode frequencies to be sufficently spaced. The spherical cavity mirrors have been coated at the SMA/IN2P3 Laboratory of Lyon. They are dielectric mirrors made of a pure silica substrate (SiO_2, of optical indice $n = 1.47$ and absorption coefficient 1 ppm/cm) of a 6 mm tickness and of diameter 2.5 cm. The mirror coating is made of dielectric SiO_2/Ta_2O_5 ($n = 1.47$) quater wave stacks. The size of the coating on the substrate is 10 mm. The loss is ≈ 40 ppm (absorption plus scattering) and the transmission ≈ 100 ppm, leading to a reflectivity larger than 99.98%. The laser injected in the cavity is a continuous wave Nd:YAG laser ($\lambda = 1.064$ μm) of power 0.7 W and tunable frequency [66]. We will see in Section 2.1.5 that these mirror parameters associated with the laser power are sufficient to obtain the few kilowatts required inside the cavity.

2.1.5 Mode structure and resonance: orders of magnitude

Cavity mode pattern

Because the phase shift depends on the Hermite-Gaussian mode number, the transverse modes may have different resonant frequencies. The choice of not using an exact confocal

scheme but a nearly confocal scheme was made to avoid a degeneracy of these resonant frequencies. Indeed, in an exact confocal scheme, one sees from (2.14) where $L = R_M$ that all the even mode frequencies (*i.e.* when n+m is even) coincide exactly with a TEM_{00} frequency $\nu_{00} \pm$ qFSR, and all the odd modes (*i.e.* when n+m is odd) are halfway between two longitudinal modes, *i.e.* have frequencies which coincide with a $\nu_{00} + \text{FSR}/2 \pm$ qFSR (where q is an integer). This degeneracy is suppressed using a nearly confocal cavity. Using our design cavity described above, from formula (2.14) and (2.15) the resonant frequency spectra becomes:

$$\nu_{nm} = \text{FSR}\left[\, q + (n+m+1)\,\frac{1+\delta}{2}\,\right], \text{ with } \quad \delta = \frac{2\Delta_L}{\pi}, \tag{2.16}$$

and determines the transverse mode pattern illustrated in Figure 2.7:

- The modes TEM_{nm} with n+m = 2 are located at $\delta \times \text{FSR} \sim 360$ KHz from a TEM_{00} mode and all other even modes are shifted from each other by $\delta \times$ FSR.
- The modes TEM_{nm} with n+m = 1 are located at $(1-\delta) \times \text{FSR}/2 \sim 37.32$ MHz from a TEM_{00} mode and all other odd modes are shifted from each other by $\delta \times$ FSR.

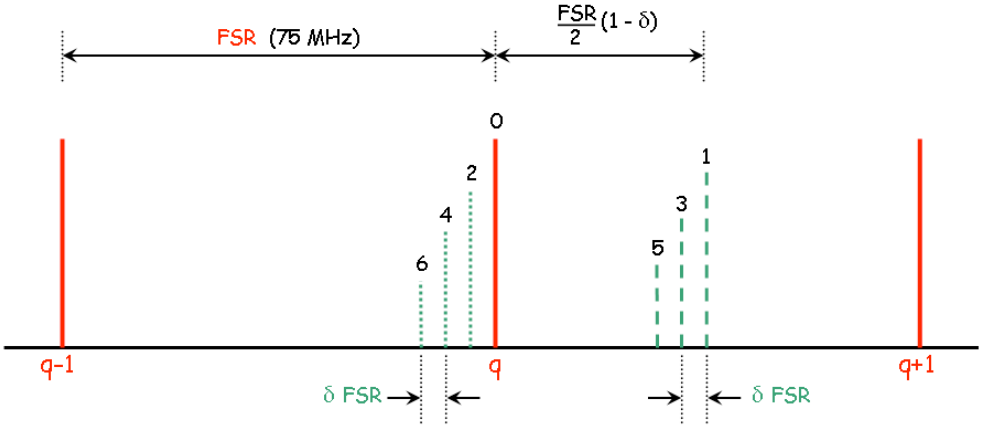

Figure 2.7: Transverse mode frequencies of a nearly confocal cavity. Numbers 0,1,2 ... correspond to the n+m mode number. In our design: FSR = 75 MHz and $\delta = 0.0048$.

Frequency matching

The beam intensity inside the cavity can be written from the expression of the anplitude field A_{circ} circulating inside the cavity as: $P_{circ} = A^*_{circ}\, A_{circ}$ where A^*_{circ} is the complex conjugate of A_{circ}. Considering a laser beam of frequency ν propagating in a two mirror cavity, the power inside the cavity in the stationary regime can be calculated from (2.4) and is written as:

$$P_{circ} = \frac{T}{(1-R)^2}\,\frac{1}{1 + \left(\frac{2\mathcal{F}}{\pi}\right)^2 \sin^2\left(\frac{2\pi L}{c}\Delta\nu\right)}\,P_{inc} \equiv P_{inc} \times G\ , \tag{2.17}$$

where

$$\mathcal{F} = \frac{\pi \sqrt{\mathrm{R}}}{1-\mathrm{R}} \tag{2.18}$$

is the finesse of the cavity, $\Delta\nu = \nu - \nu_{\mathrm{nm}}$ is the difference between the laser frequency and a cavity mode frequency ν_{nm}, $\mathrm{P_{inc}}$ is the incident laser power coupled with the cavity, R and T are the intensity reflection and transmission cavity mirror coefficients and G is the gain of the cavity. In Figure 2.33, the gain is represented as a function of $\Delta\nu$ for the cavity described in Section 2.1.4. At the resonance, the gain value is around 10^4 and leads to a power inside the cavity of the order of a few kW. The full width at half maximum FWHM of the resonance peak (*i.e.* the bandwidth of the cavity) calculated from (2.17) is $\approx$ 3 KHz. Thus for a Nd:YAG laser ($\lambda = 1.064$ μm) entering in such a cavity, one gets:

$$\frac{\mathrm{FWHM}}{\nu} \sim \frac{3 \text{ KHz}}{(\mathrm{c}/1.064\ \mu\mathrm{m})} \sim 10^{-11} \quad .$$

In consequence, to keep such a cavity at the resonance condition, the laser frequency and the cavity length should be matched at the 10^{-11} level. A fast feedback system is required in order to ensure this condition.

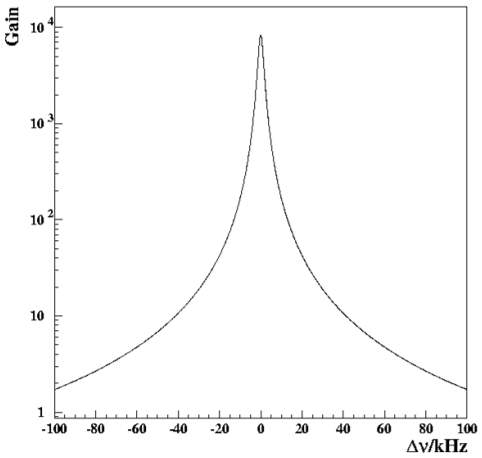

Figure 2.8: Gain of a 2 m long cavity made of two mirrors having reflection and transmission coefficients of $\approx$ 0.9998 and 100 ppm respectively, as a function of the difference between the laser frequency and a cavity resonance frequency.

The finesse (2.18) can be also expressed as the ratio between the free spectral range and the bandwidth of the cavity:

$$\mathcal{F} = \frac{\mathrm{FSR}}{\mathrm{FWMH}} \quad . \tag{2.19}$$

2.2 Description of the system installed in the HERA tunnel

The overall system is shown in Figure 2.9. The lepton beam line crosses the laser beam and scattered Compton photons reach a calorimeter at about 60 m from the cavity interaction point. In this section we will describe the system both in its technical aspects and in its experimental ones once installed in the HERA tunnel.

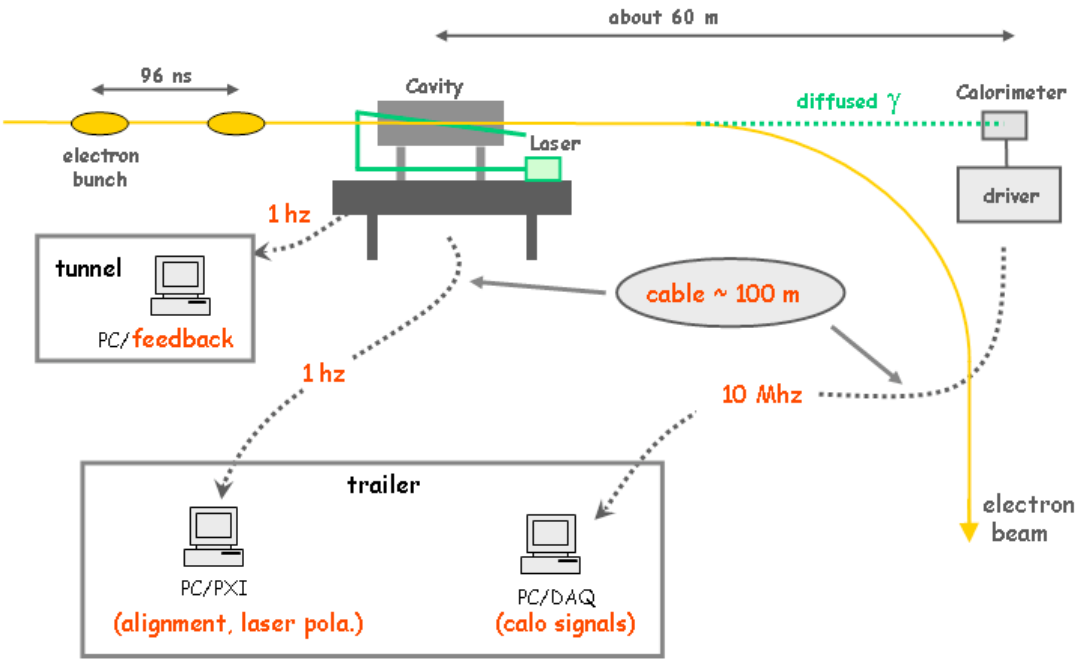

Figure 2.9: Overview of the area of the cavity polarimeter installed in the HERA tunnel.

2.2.1 Mechanical design for the HERA tunnel environment

The cavity and the beam pipe

The mechanical scheme of the cavity is shown in Figure 2.10. All components are made of stainless-steel. The cavity consists of a cylindrical vacuum vessel surrounding a beam pipe section. The propagation of the wake-field [68, 69] inside the cavity (*i.e.* high frequency modes from the passing electron beam) is suppressed by the introduction of a 15 mm diameter tube (soldered to the beam pipe) around the laser beam. The design of this tube, conceived at the Laboratoire de l'Accélérateur Linéaire (LAL) is shown in the bottom sketch in Figure 2.10. To reduce the vibrations coming from the beam pipe, the beam pipe inside the cavity, attached to the two cavity end flanges, is isolated from the rest of the HERA beam pipe by two standard HERA bellows, and from the cavity vessel by two other big bellows. The vessel is mounted on the table via two pairs of passive absorbers. Finally, the optical table is isolated from the ground with passive absorbers: the feet are equipped with elastomer isolators cutting vibrations from the tunnel ground. Main dimensions of this mechanical design are visible in Figure 2.11. Inside the cavity, the vacuum is maintained by two 160 ℓ ion pumps (the two blue cubes in Figure 2.10) isolated from the optical table by passive absorbers. Pressure is measured by a vacuum gauge located on the top of the cavity vessel. The residual pressure is of 10^{-9} Torr and fits the HERA requirements. Pictures of the cavity and of the beam pipe with its soldered tube for wake-field reduction are shown in Figures 2.12 and 2.13 respectively.

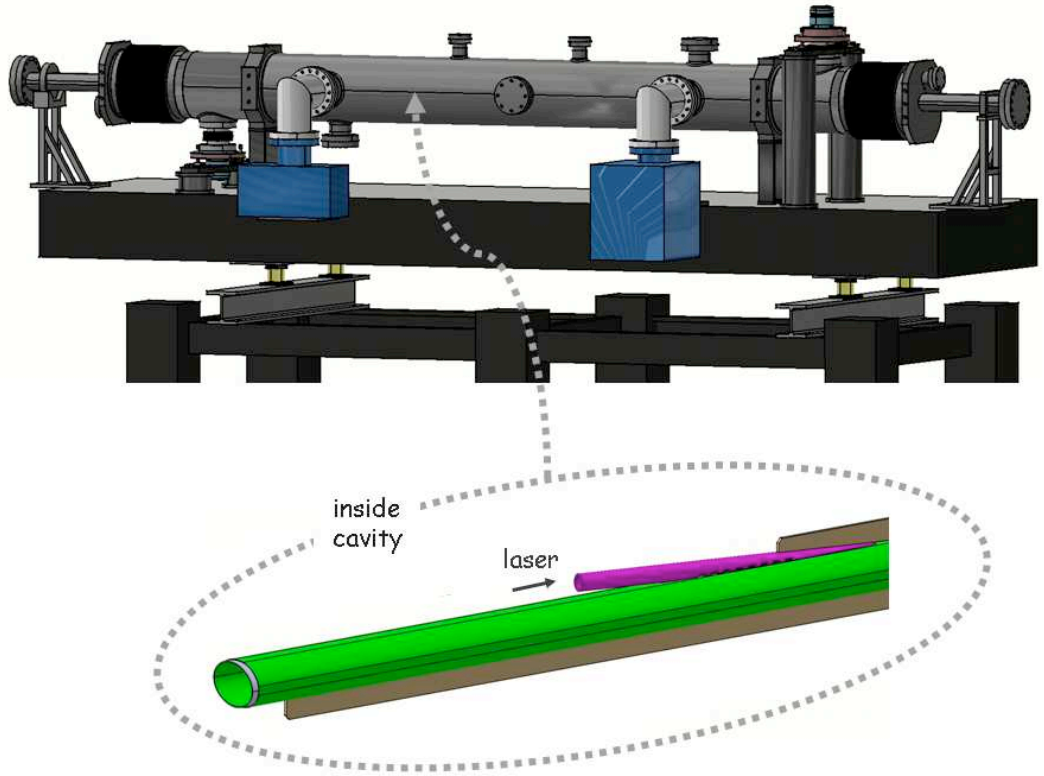

Figure 2.10: Three dimensional technical drawings of the cavity (top sketch) and of the beam pipe inside the cavity (bottom sketch where half is shown). From [67].

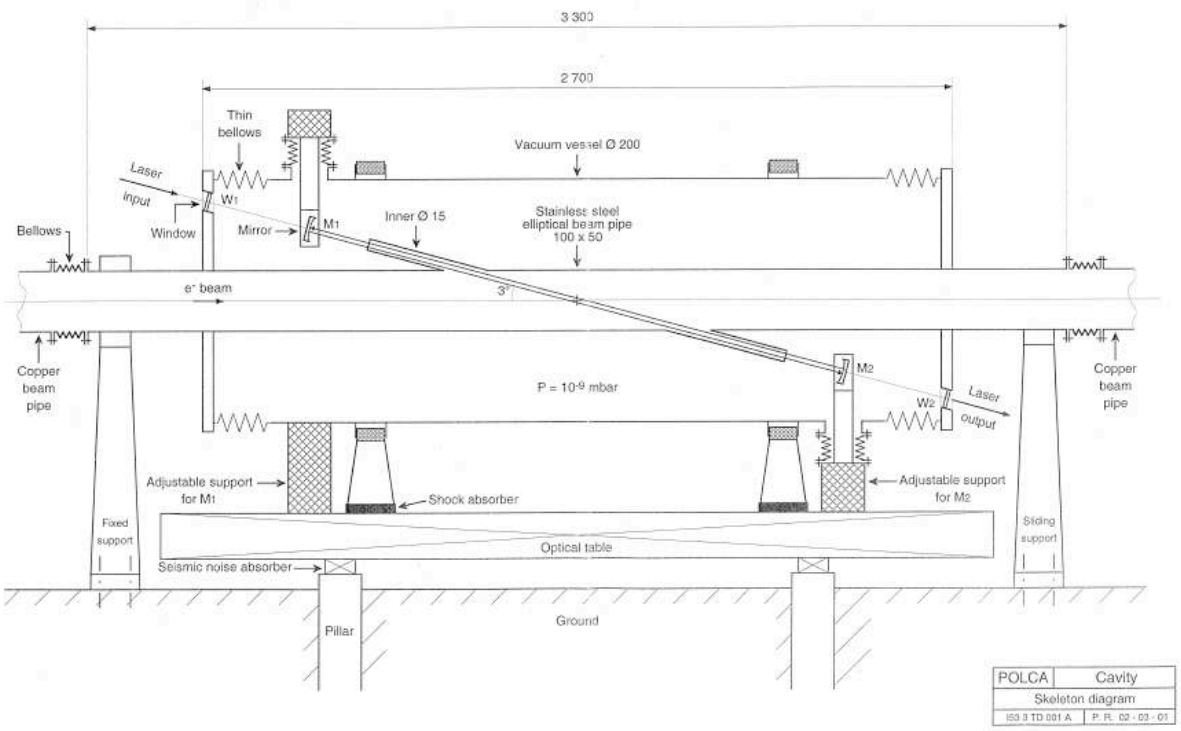

Figure 2.11: Technical design of the cavity system installed in the HERA tunnel with main dimensions. From [67].

Figure 2.12: Picture of the cavity taken during the installation in the tunnel. The laser and the optical components before the cavity entrance are located on a rail parallel to the cavity vessel.

Figure 2.13: Picture of the beam pipe inside the cavity (half is shown). Above the elliptic electron beam pipe, a circular tube is soldered to reduce wake-field excitations. The small holes visible on the picture have been implemented for vacuum conductance purposes between the cavity and the beam pipe.

The mirror mounts

The mirrors also have to be in the vacuum vessel but they cannot be mounted rigidly on the vessel because of heat effects and possible vibrations propagating along the beam pipe during HERA operation. The solution adopted is to mount the mirrors in a post holder fixed to a plate resting on two big cylindrical legs clipped on the optical table, as shown in Figure 2.14. Each mirror is attached to a plate which is moved via three screws by the technique named 'gimbal mount' [70]: with this technique, the axes of rotation of the mirror are othogonal and fixed in space, and the centre of the mirror stays at the same position during alignment operations, as schematized in igure 2.15.

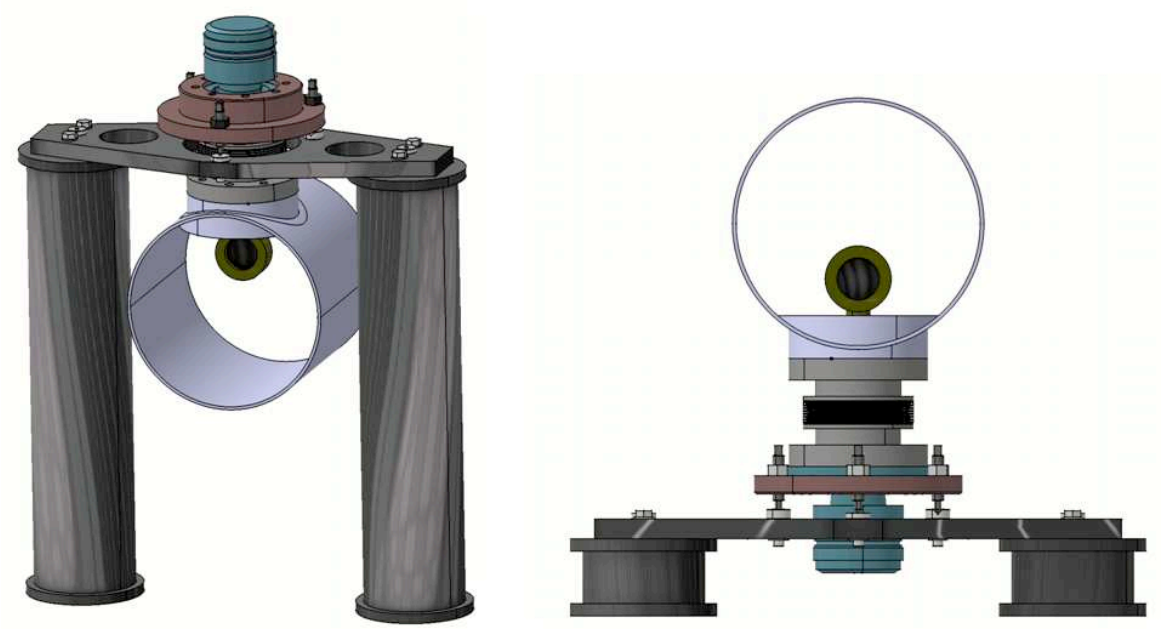

Figure 2.14: Three dimensional technical drawings of the cavity mirror mounts (entrance and exit mirror mounts on the left and right sketches respectively). The cylinder around the mirror is the cavity vessel. The bellows used to isolate the mirror mount from the cavity vessel are visible on the right sketch (below the vessel). From [67].

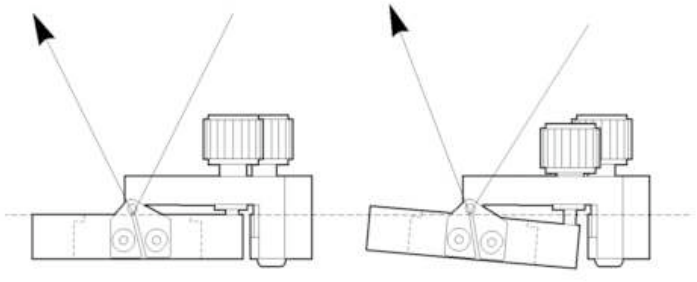

Figure 2.15: Principle of a the gimbal mount technique. The centre of the mirror stays at the same position during alignment operations (only one rotation direction is shown). From [71].

Housing and shielding

Thermal expansions of all mechanical elements must be controlled. Indeed, once turned on, the laser can perform a frequency change over tens of gigahertz with a relatively slow time constant (approximately 1 to 10 seconds). This frequency range induces a constraint on the variation of the distance between the two mirrors once the cavity is locked. This variation must not exceed 100 μm (ΔL $\sim$ 100 μm leads to $\Delta\nu \sim$ 15 GHz) to avoid causing perturbation on the feedback system operation. The whole system is therefore surrounded by an isotherm house. Inside the house the temperature is controlled within 1° via heating lamps and sensors. This is enough with regard to the range of the laser frequency change since all mechanical components are made of stainless-steel of which thermal dilatation is 36 μm per degree.

Another purpose of the cavity housing is the radiation protection. Because the electronic elements located on the optical table are sensitive to radiation, the original design was to put a 3 mm lead shielding all around the cavity house.

The picture in Figure 2.16 shows the isotherm and lead shielding houses installed around the cavity.

Figure 2.16: Picture of the cavity isotherm and lead shielding house installed in the HERA tunnel in summer 2003.

Nevertheless, even with this lead protection, synchrotron radiation coming from the HERMES area has proved to be much larger than anticipated [49, 72]. And, once installed in summer 2003, electronic devices such as laser controler, motorised mirror controler or photodiodes, have begun to suffer serious damage and/or dysfunctionments [72]. Figure 2.17 shows the LPOL beam line configuration and the radiation rate coming from the HERMES experiment. Also the calorimeter area located at 60 m downstream the cavity area has been damaged by radiation synchrotron as shown in pictures of Figure 2.18 taken during the year 2004. Therefore in addition to the 3 mm lead shielding, the most sensitive elements have also been protected as shown in Figure 2.19.

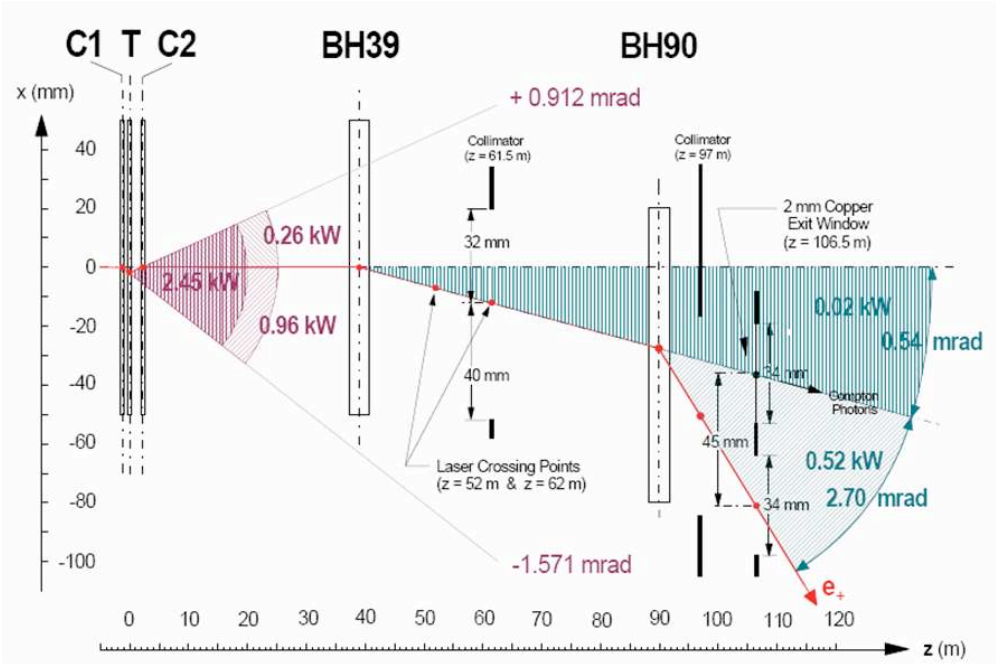

Figure 2.17: LPOL beam line configuration and synchrotron radiation with HERMES transverse target magnet T for an electron beam of 27.5 GeV and 30 mA [73]. Each color corresponds to synchrotron radiation coming from dipoles T, BH39 and BH90.

Figure 2.18: Pictures of radiation damages observed in the year 2004: a hole on lead sheet located in front of the LPOL calorimeter (left picture), calorimeter crystal $NaBi(WO_4)_2$ cracks or breaks (top right picture), damage of scintillation plates (SCSN-38) of the sampling calorimeter (bottom right picture).

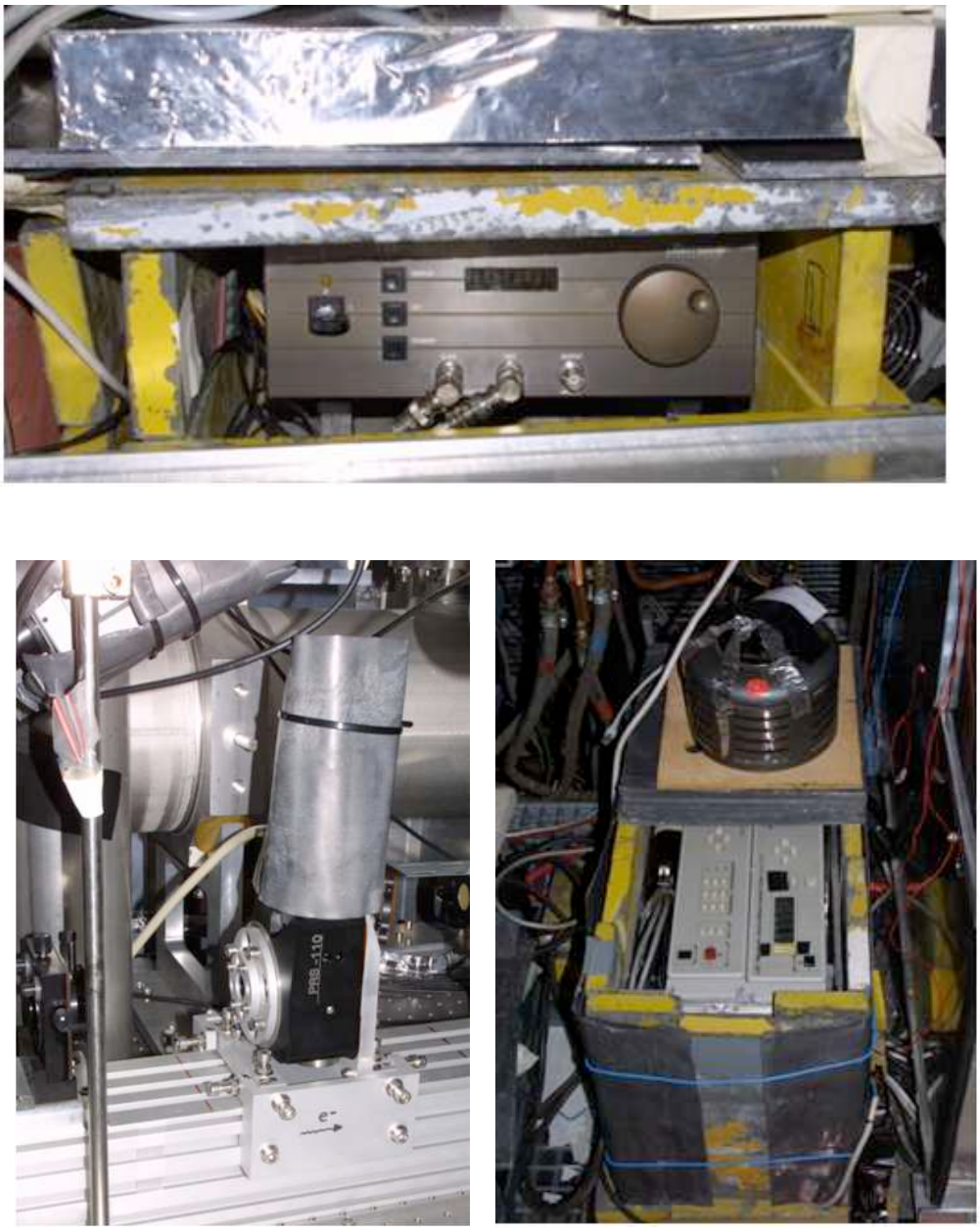

Figure 2.19: Picture of the shielding of the laser controller (top picture), of the controller of the entrance quater wave plate rotating mount (bottom left picture), and of the controllers of the motorised cavity alignment mirrors (bottom right picture).

All these shieldings in addition to the construction and the installation of a beam scraper between HERMES and our cavity area have been essential to preserve our material after damages and repairs that we have conducted in year 2004. These problems have nevertheless generated many months of delay in the startup of the polarimeter and they have cost us nearly two years of data taking.

2.2.2 Optical scheme

A set of optical elements are used to inject adequately the laser beam inside the cavity and to control the light polarisation at the exit of the cavity. A three dimensional overview of the cavity and of the optical scheme is presented in Figure 2.20 where the entrance beam line, the laser beam alignment system and the exit beam line are clearly visible. The main distances separating the optical components are indicated in Figure 2.21.

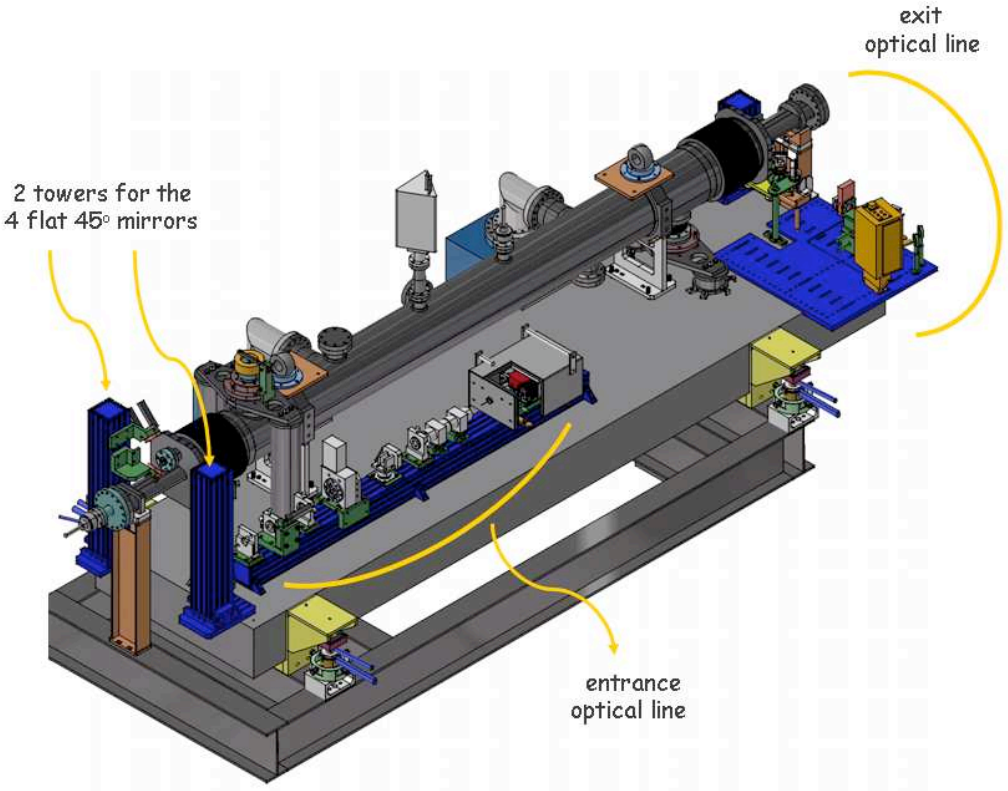

Figure 2.20: Three dimensional technical drawing of the cavity and the optical scheme. From [67].

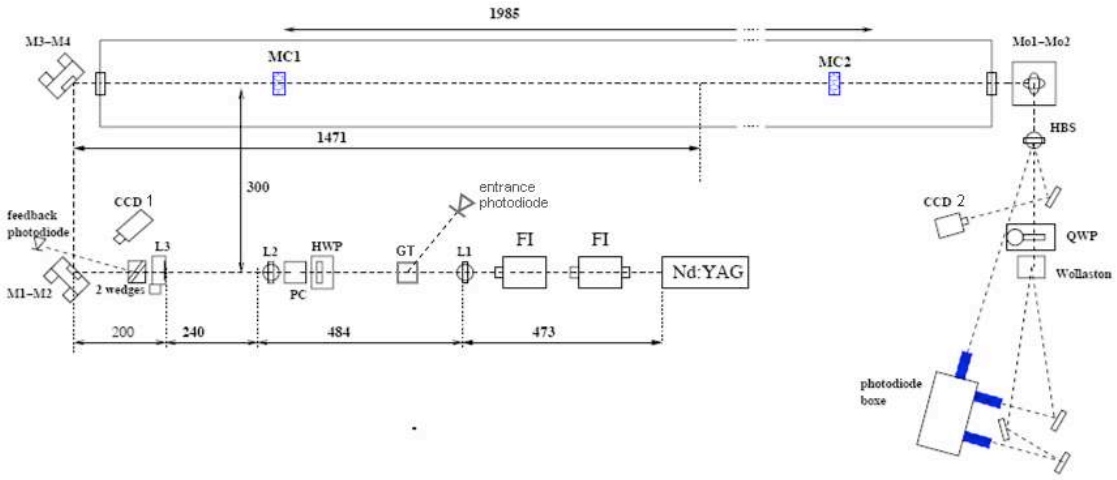

Figure 2.21: Schematic view of the optical scheme with main distances. From [74].

The entrance beam line

Optical elements of the entrance beam line have to create a circular left/right circularly polarised laser beam, match the laser/cavity modes and extract the signal reflected by the cavity for the feedback procedure. A technical drawing of the entrance beam line is shown in Figure 2.22.

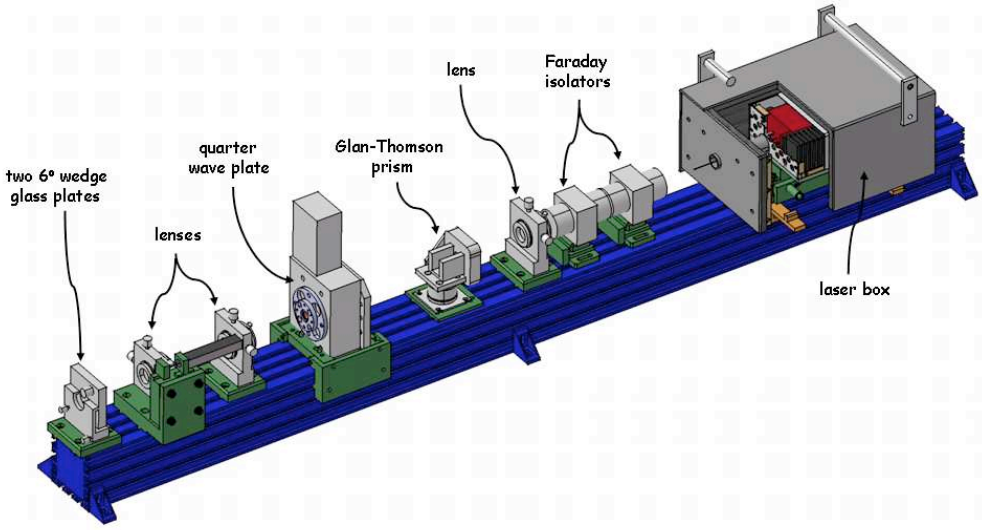

Figure 2.22: Three dimensional technical drawing of the entrance beam line (from [67]). From the right are visible the laser, two Faraday isolators, a lens, a Glan-Thomson prism, a rotating quater wave plate, two other lenses and an assembly of two 6° wedge glass plates.

Starting from the laser box we have the following elements:

- The laser is a finely frequency tunable Nd:YAG laser delivering a $\approx$ 700 mW light beam with a wavelength of 1064 nm (Lightwave 126-1064-700 [66]). There are two ways to modify the laser beam frequency. The first is a fast and fine tuning: the laser beam frequency can change by 3.4 MHz per Volt applied on the actuator of a piezo-electric transducer. The second is a slow frequency variation: the laser beam frequency can change by a temperature variation. The frequency change is by 5 GHz per Volt applied on a Peltier module.

- Two Faraday isolators insure that no reflected beam enters the laser. Indeed this would perturb the laser and then the cavity feedback.

- A first lens ($f_1 = 400$ mm) allows the size of the laser beam to be adjusted.

- A Glan-Thomson prism allows the linear polarisation of the laser beam to be reinforced. It consists of two right-angled calcite prisms glued together. Its principle is the same as a Wollaston prism (see Section 3.3.3) with a different orientation of the optical axes of the prisms.

- An anti-reflected coated quartz quater wave plate is mounted in a motorised rotating stage. It allows the linearly polarised beam to be transformed into a circularly polarised beam (or, depending on the azimuthal angle of the mount, into a elliptically polarised beam). The principle of a quater wave plate is explained in Section 3.3.4.

- Two other lenses ($f_2 = -100$ mm, $f_3 = 250$ mm) provide the spatial mode matching of the laser beam to the cavity. The size and the position of the laser waist are adjusted by putting these lenses at a proper distance from each other. The second lens is mounted on a linear translation stage.

- An assembly of two 6° wedge glass plates allows for the pickup of a part of the beam reflected by the cavity[4]. A silicon photodiode (model S1233 of bandwidth 20 MHz [75]) located in front of the two glass plates reads this reflected cavity signal which is used for the feedback procedure. A picture of these devices is shown in Figure 2.23.

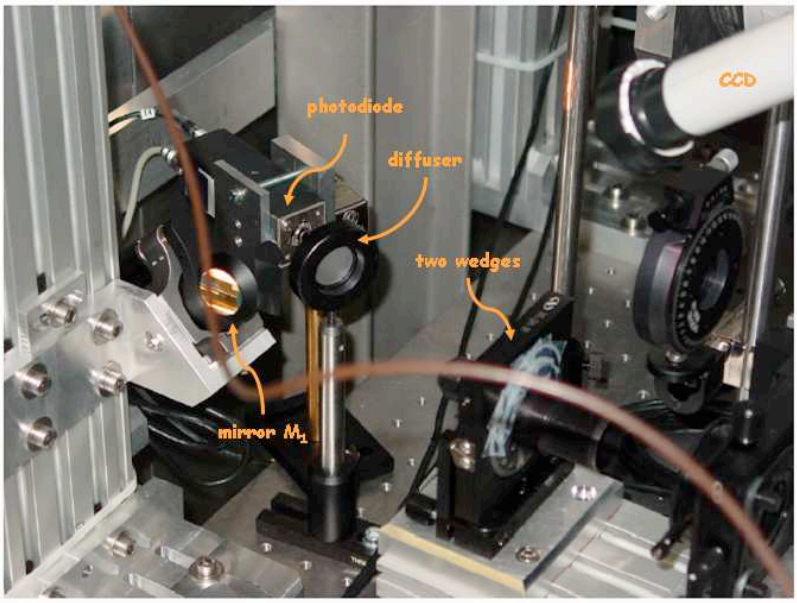

Figure 2.23: Picture of the two 6° wedge plates system (located in a black tube), the silicon feedback photodiode and its readout electronic box (with a diffuser in front), the motorised mirror M_1 and a CCD camera (in white in the right upper corner), the latter two being used for the laser/cavity alignment.

A second silicon photodiode [75], named entrance photodiode in Figure 2.21, measures the reflected cavity signal after passing the Glan-Thomson prism and is used for dedicated characterisation measurements[5] (see Section 6.4).

The alignment system

The alignment of the cavity mirrors MC_1 and MC_2 (see Figure 2.21) onto the geometrical cavity axis is done using a red HeNe laser diode. This laser is visible in Figure 2.12 (between the entrance optical rail and the cavity vessel, mounted on a post holder at a higher height). It is injected inside the cavity through the exit vacuum window by two mirrors rigidly mounted on a movable rail (this two mirrors are visible in Figure 2.25). By moving the cavity mirrors, the reflections of the red laser light on the cavity mirrors are matched to the incident laser beam. We typically achieved an 1 mrad, 1 mm precision after this procedure.

[4]We have used two available wedges but it would have been as simple to use a one face anti-reflection coated parallel plate.

[5]At the origin, the signal of this photodiode should be used for the cavity feedback, but we finally use the two 6° wedges scheme described above to extract the reflected beam independently of its polarisation.

Once the cavity mirrors are geometrically aligned, a system of four SiO_2/Ta_2O_5 dielectric mirrors (named $M_1 - M_4$ in Figure 2.21) is used for the geometrical alignment of the infrared Nd:YAG laser beam on the optical axis of the cavity. The two mirrors M_1 and M_2 are motorised using four Micro-Control stepper motors (CMA-12PP stepper actuator [76]). The travel range is 12.5 mm, the minimum incrementation motion is 0.3 μm and the repeatability is 4 μm.

In principle two mirrors would be sufficient for an alignment of the impact point and of the angle of the laser beam at the entrance cavity window. But we use four mirrors to reduce a birefringence effect due to the small change of the polarisation of the beam after its reflection in a mirror: indeed, the portion of the light reflected from the surface of a dielectric is different for light polarised parralel to the plane of incidence (s-polarised wave) and for light polarised perpendicular to the plane of incidence (p-polarised wave) [77, 78], as schematized in Figure 2.24.

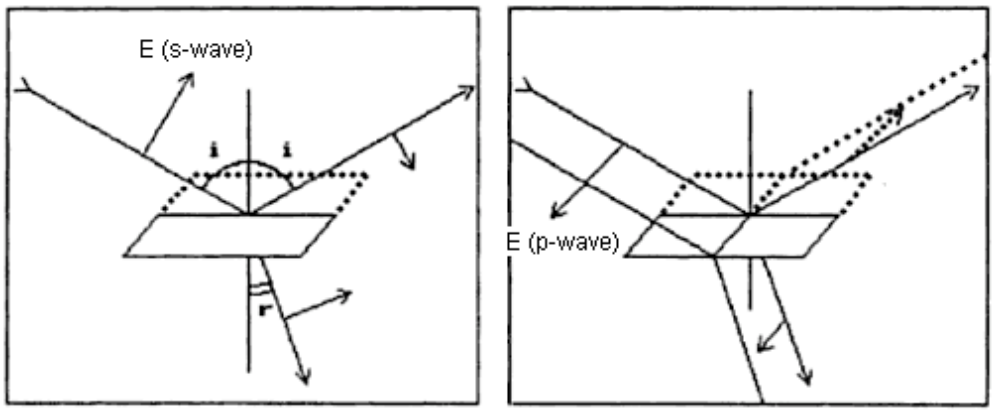

Figure 2.24: Reflection and transmission of the s and p wave components by a dielectric mirror. Left: the electric filed of the wave is inside the incident plane. Right: the electric field is perpendicular to the incident plane. From [79].

Therefore by associating the mirrors by pairs used with the same incident angle but with perpendicaular incident plane, the s-polarised component for the first one becomes the p-polarised component for the second one. This configuration allows the reflectivity difference between the two wave components s and p to be cancelled and the incident polarisation to be conserved.

In order to control the effect of the motorised mirror movements on the beam alignment, an infrared CCD camera (named CCD_1 in Figure 2.21) is located in front of the mirror M_1. It allows the matching of the incident and reflected laser beam spots to be visualised. The mirror M_1 and the camera CCD_1 are visible in Figure 2.23. The principle of the alignment procedure will be described in Section 2.3.1.

The exit beam line

A technical drawing of the optical elements located at the exit of the cavity is shown in Figure 2.25. All elements (excepted the mirrors used for injection of the red HeNe laser diode into the cavity) are also visible in Figure 2.21. We just give here a brief description of these elements and their respective role since they are the object of Chapters 3, 4 and

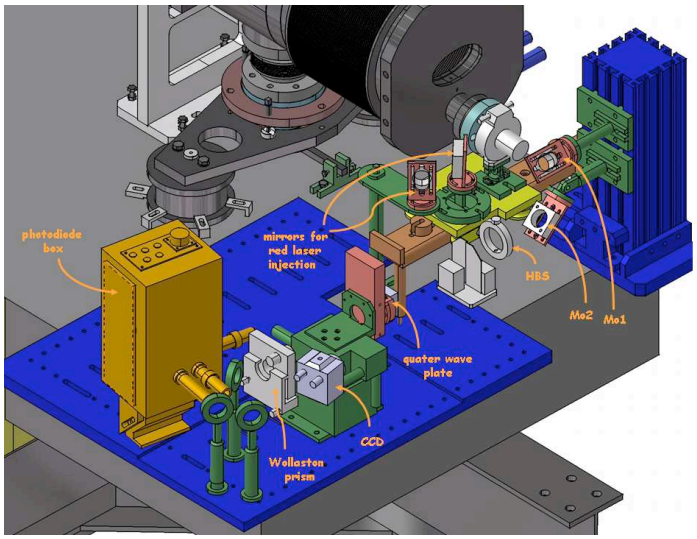

Figure 2.25: Three dimensional technical drawing of the exit beam line. From [67]. The two mirrors used for injection of the red HeNe laser diode into the cavity are also visible.

5. The beam emitted from the cavity is guided with two flat 45° dielectric mirrors (Mo1 and Mo2 in Figure 2.21) to reach an holographic beam sampler (HBS, see Section 3.3.1) which separates spatially the beam into three different beams: a main beam emitted at 0° and two diffracted first order beams emitted at ±10° from the main beam. One of the two first order beams enters an infrared CCD camera (named CCD_2 in Figure 2.21) to visualise the modes of the cavity. The second first order beam and the main beam enter an ellipsometer which consists of a quater wave plate (qwp) (see Section 3.3.4 and Chapter 4), a Wollaston prism (see Section 3.3.3) and three InGaAs photodiodes [80] located in a thermalized box (see Section 3.3.2). The main HBS beam enters the Wollaston prism and two of the photodiodes read the light intensity of the two beams emerging from the Wollaston prism. The third photodiode (named the reference diode in the following) reads the light intensity of the second first order beam diffracted by the HBS. The ellipsometer is devoted to the measurement of the polarisation state of the incident light as described in Chapter 5. A picture of this device is shown in Figure 2.26 [6].

Since the ellipsometer quater wave plate (qwp) will be the subject of Chapter 4, let us give here some details on its mounting system: the qwp is mounted on a mirror mount fixed in the centre of a rotating stage (model PR50 [81]) which is used to rotate azimuthally the ellipsometer quater wave plate. The stage travel range is 360° and the repeatability is 0.05°. Two screws allow the parallelism between the plate and the rotating stage to be adjusted. The rotating stage is then mounted on a two axes horizontal stage, a two angles tilted stage and a vertical translation stage. Linear and tilted stages are controlled manually with micro-metric screws. A picture of the whole qwp mounting system is shown Figure 2.27. We will see in Chapter 4 and 5 that this complete control of the horizontal, vertical and angular qwp positions allows a very precise alignment of the plate (at the level of hundredths of micrometer) to be performed, as required for its characterisation and for accurate measurements of the laser beam polarisation.

[6] After some tests, we have decided that it would be more convenient to have three different photodiode thermal boxes. This explains the different photodiode schemes in Figures 2.25 and 2.26.

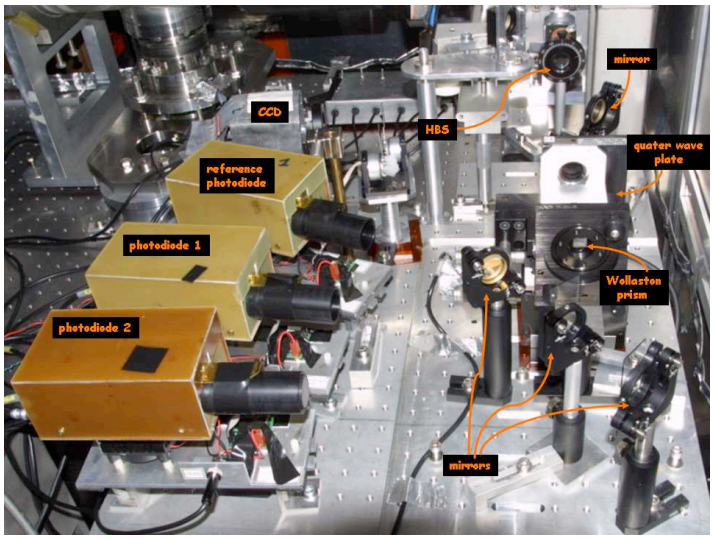

Figure 2.26: Picture of the cavity ellipsometer located at the exit of the cavity.

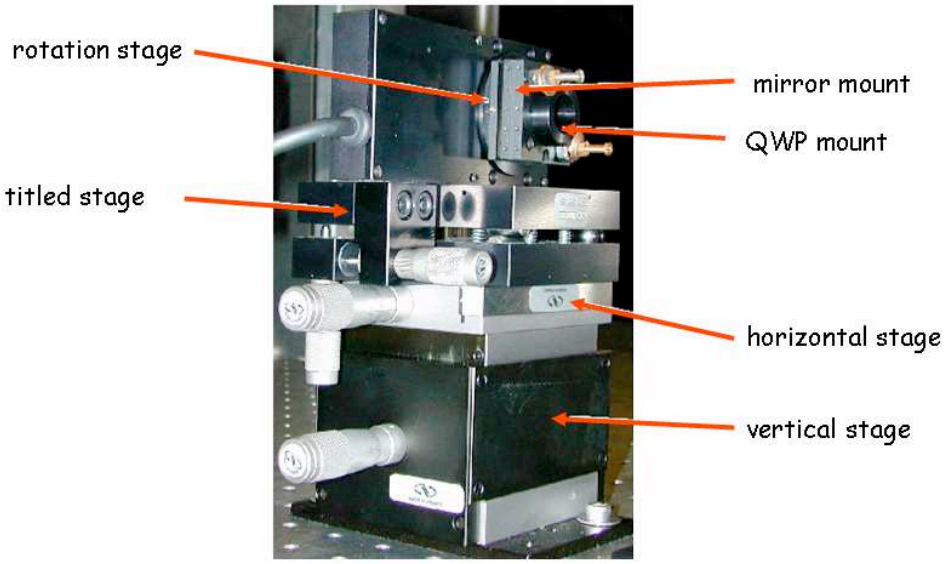

Figure 2.27: Picture of the whole qwp mount system.

2.2.3 Feedback system

Principle

The feedback system between the laser and the cavity is based on the analysis of the phase of the reflected field. The detuning parameter ϵ is defined as the difference between the laser frequency and the nearest resonance cavity frequency in FSR units:

$$\epsilon = \frac{\Delta\nu}{\text{FSR}} \ , \tag{2.20}$$

where $\Delta\nu$ is the difference between the laser frequency and a cavity mode frequency, and FSR is the cavity free spectral range (see Section 2.1.3). One can show [62, 61] that, for a small detuning parameter, the phase of the reflected field is proportional to the detuning parameter and varies very rapidly around a resonance. This is illustrated in Figure 2.28

where the phase of the reflected field is shown as a function of the detuning parameter [7].

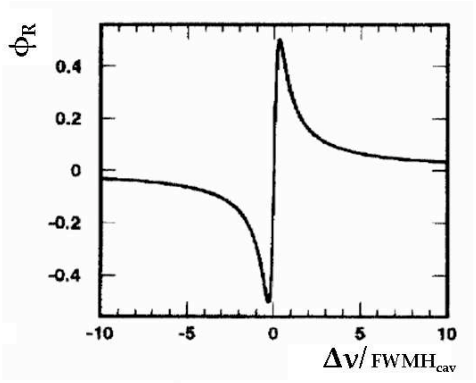

Figure 2.28: Phase of the reflected cavity field as a function of $\epsilon \times$ FSR/FWMH. From [62].

Near a resonance (or more quantitatively when $\Delta\nu <$ FWMH), the expression of the reflected field phase as a function of ϵ can be written as [62]:

$$\tan\phi_{\mathrm{R}}(\epsilon) \simeq 2\pi\epsilon \left[\frac{\mathrm{T}}{\mathrm{P}(1-\mathrm{R})}\right] \ . \tag{2.21}$$

The measurement of this phase may be used to correct for detuning. As there is no detector sensitive to the phase of a laser wave, there is no direct way to measure this phase. Hence, the phase information must be transformed into an intensity information. To do this, the frequency of the laser beam is modulated at a frequency Ω (this wave frequency modulation is equivalent to a phase modulation of the wave [85]). In that way the phase information of the beam reflected by the cavity can be found in the reflected intensity signal measured in a photodiode. This is the idea of the 'Pound-Drever' technique [82, 83, 84] that we use for the cavity feedback.

The feedback procedure

The method is illustrated in Figure 2.29. The frequency of the laser is modulated at a frequency $\Omega = 930$ KHz by applying a sinusoidal voltage of $20 - 40$ mV on the laser piezoelectric actuator (which provides the fast control of the laser frequency). Beside the central laser beam frequency ν_{laser}, two side bands of frequencies $\nu_{\mathrm{laser}} \pm \Omega$ are generated by this modulation. When such a modulated wave arrives in the cavity, and if the frequencies of the system satisfy the following conditions:

$$\Omega \gg \mathrm{FWMH} \ , \tag{2.22}$$

$$\nu_{\mathrm{res}} - \mathrm{FWMH} \lesssim \nu_{\mathrm{laser}} \lesssim \nu_{\mathrm{res}} + \mathrm{FWMH} \ , \tag{2.23}$$

then the reflected field contains the two side bands simply reflected without phase shift (because far from the resonance) and the phase shifted central band. Resulting from the interference between the central and the side bands, the reflected signal measured in a photodiode contains an amplitude modulated component at the frequency Ω depending on the detuning parameter ϵ [61]. It can be written as:

$$\mathrm{V_{diode}} \sim \mathrm{f}(\epsilon) \ \sin(\Omega \mathrm{t} + \psi) \ . \tag{2.24}$$

[7] The curve in Figure 2.28 is computed from a symmetric 80 cm cavity made of two mirrors with reflection and transmission coefficients of 99.99% and 100 ppm respectively [62].

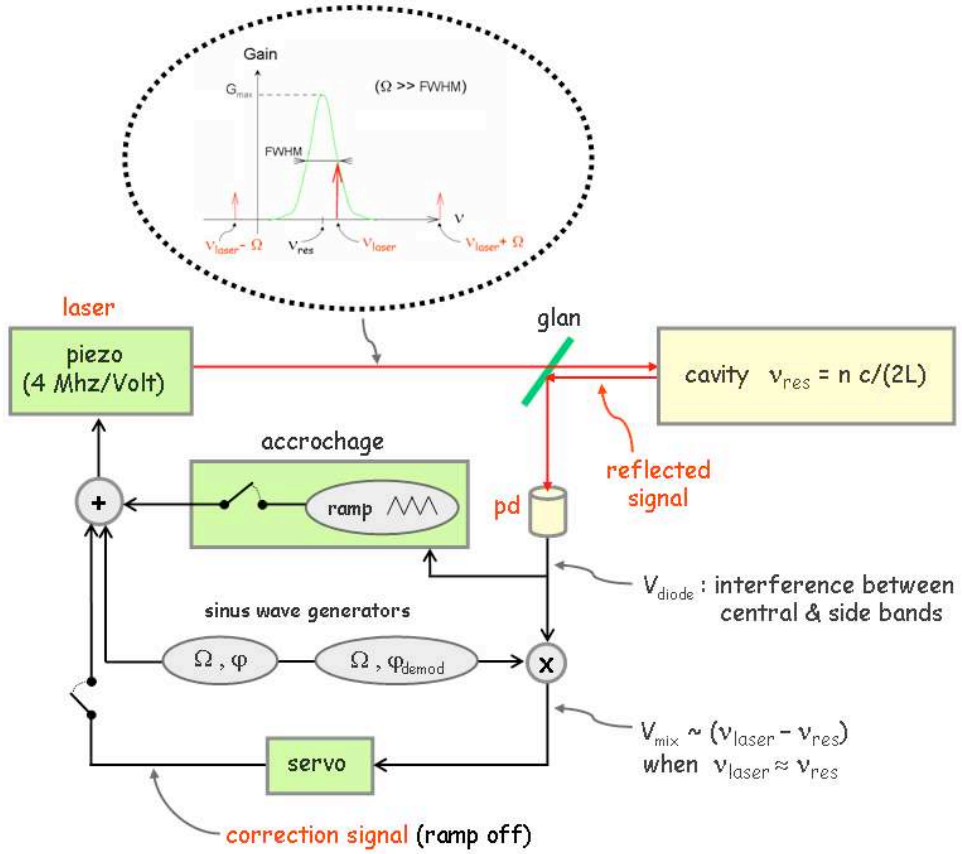

Figure 2.29: Simplified view of the Pound Driver feedback technique.

To extract the term f(ϵ) containing the frequency shift information $\Delta\nu$, the signal V_{diode} is demodulated with a sinusoidal signal $\sin(\Omega t + \psi_{demod})$ with $\psi_{demod} = \psi$. A band pass filter is used to remove the harmonics of the frequency Ω and keeps only a term proportional to f(ϵ) independent on Ω and ψ. The resulting signal V_{mix} is called the error signal. An electronic system (noted 'servo' in Figure 2.29) then determines from the error signal the correction that must be done on the laser frequency. This correction signal is added to the modulation signal and applied on the laser frequency control system.

Of course the correction signals must be applied only when the laser beam frequency is close to a cavity resonance frequency (*i.e.* if the condition (2.23) is fulfilled). To reach this situation, a 20 V peak to peak triangular ramp at a frequency of a few Hertz (noted 'ramp' in Figure 2.29) is supplied to the laser piezo transducer (fast laser control channel) together with the sinusoidal 930 KHz modulation mentioned above. The ramp signal allows a laser frequency scanning of about 90 MHz to be performed and thus a cavity resonance frequency to be crossed regularly. Far from a cavity resonance frequency a wave is completely reflected, whereas near a resonance a wave enters the cavity and the current measured in the photodiode decreases, as schematized in Figure 2.30.

Hence, to decide when the corrections must be applied, the reflected signal is also sent to an electronic module (noted 'accrochage' in Figure 2.29) where, according to its amplitude, the system is switched between the 'closed loop' and the 'open loop' modes. In the 'open loop' mode, the corrections of the laser beam frequency are not applied, whereas

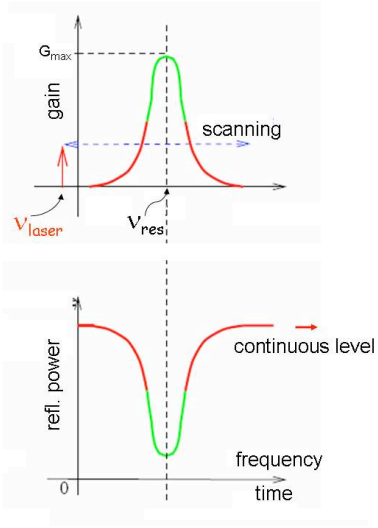

Figure 2.30: Gain (up) and reflected signal (bottom) at the cross of a resonance during a frequency scanning.

in the 'closed loop' mode, the correction signals are sent to the laser. Both the search for resonant frequency and the closing of the feedback loop are automatic procedures. They are schematized in Figure 2.31. The mode locking system is fully self-governing to react in a few seconds to an untimely unlock of the cavity.

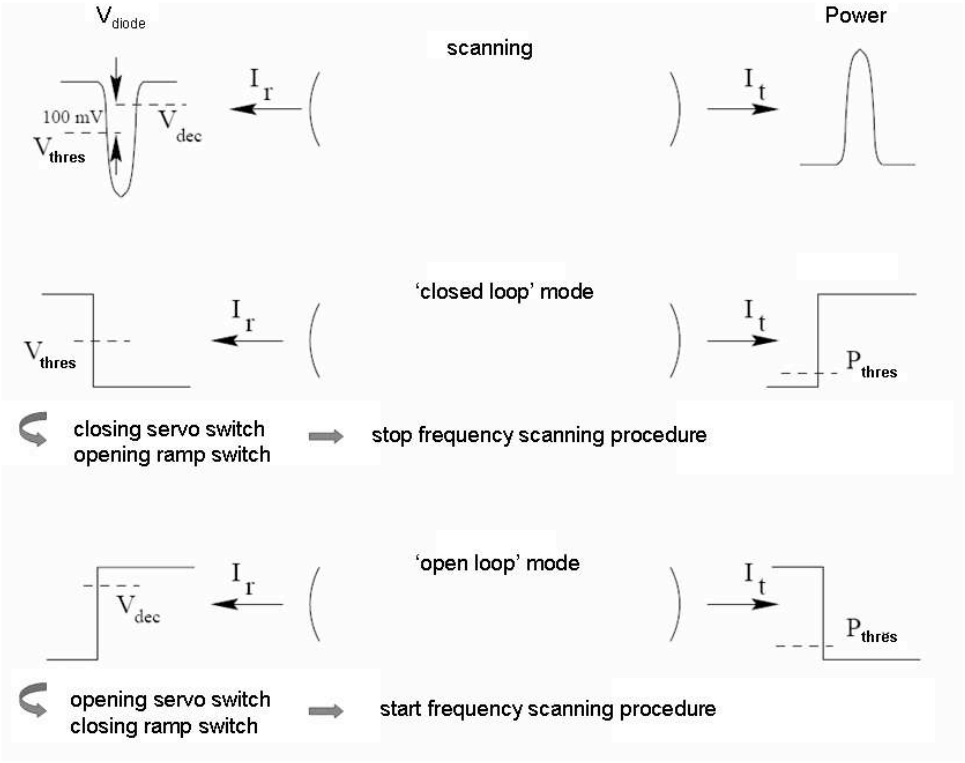

Figure 2.31: Schematic illustration of the automatic locking procedure: during a scanning frequency, when the laser frequency crosses a resonance frequency, V_{diode} sees a voltage drop (top drawing). When $V_{diode} < V_{thres}$ (V_{thres} being a tunable trigger threshold) the 'accrochage' card (see Figure 2.29) sends a 'closed loop' order to the system (middle drawing). During the 'closed loop' mode, if $V_{diode} > V_{dec}$, an 'open loop' mode order is sent to the system (bottom drawing). $V_{dec} - V_{thres}$ is around 100 mV.

2.2.4 The photon detection system

The calorimeter used to measure the energy of the Compton scattered photons is located at sixty meters upstream the cavity area (see Figure 2.9). The photon detector is a sampling calorimeter made of a sandwich of 24 tungsten plates of 3 mm thickness and 24 SCSN38 scintillator plates of thickness 2.6 mm. The SCSN38 is a plastic scintillator doped with butyl-PBD and BDB. The plate dimension is of 40×40 mm^2 and are optically coupled on all sides to wavelength shifter plates that bring light to one photomultiplier placed at the back of the calorimeter after a 27 mm W shielding plate. A technical drawing of the calorimeter is presented in Figure 2.32. The calorimeter is used both by the HERMES-LPOL group and the cavity polarimeter group. It rests on a movable table to put it in or out the scattered photon beam.

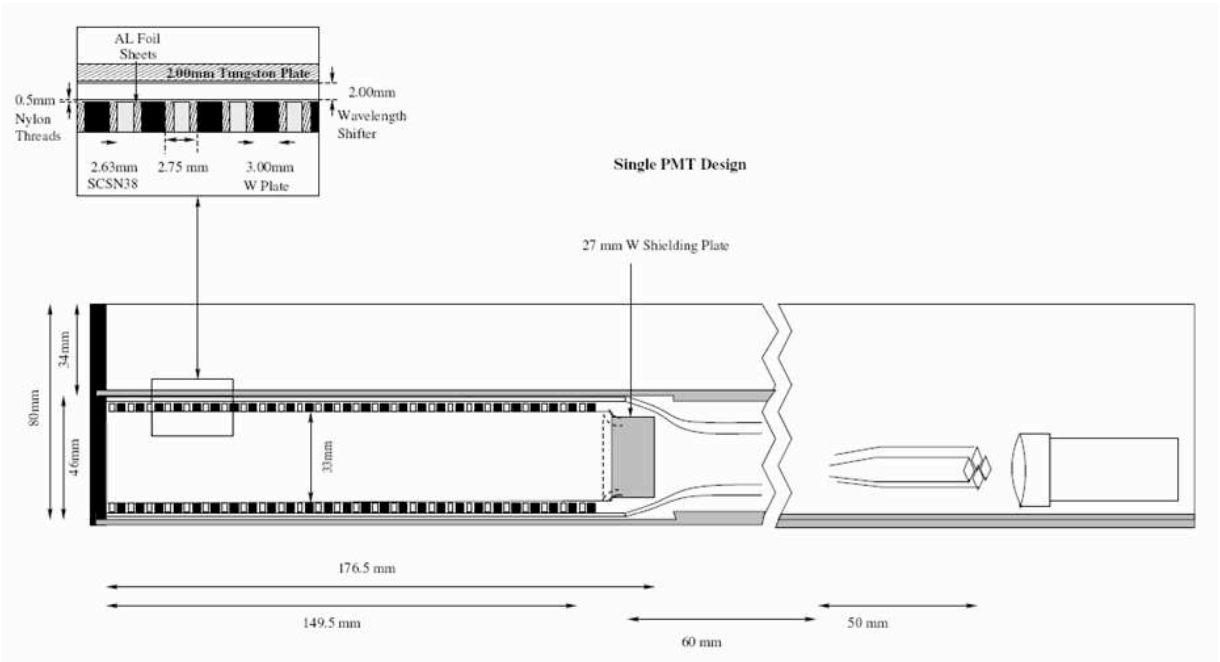

Figure 2.32: Top view of the tungsten/scintillator sampling calorimeter used from the detection of the Compton scattered photons. From [86].

DESY and CERN beam tests has been performed on this calorimeter in the energy range 1-20 GeV [87] to characterise its resolution and its ADC (Analog to Digital Converter) to energy conversion parameter. Results of the calorimeter resolution are shown in Figure 2.33. The resolution is proportional to the inverse of the square root of the energy as:

$$\frac{\sigma(\mathrm{E})}{\mathrm{E}} = \sqrt{\left(\frac{\alpha}{\sqrt{\mathrm{E}}}\right)^2 + \beta^2} \ , \tag{2.25}$$

where the coefficients α and β are equal to 25.9% and 1.28% respectively [87]. ADC to energy conversion results are shown in Figure 2.34 in the energy range 1-20 GeV. Deviations from linearity are smaller than 1%.

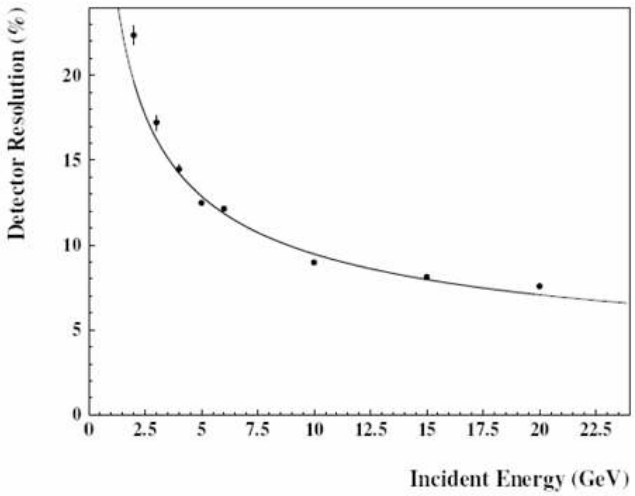

Figure 2.33: Sampling calorimeter energy resolution. From [87].

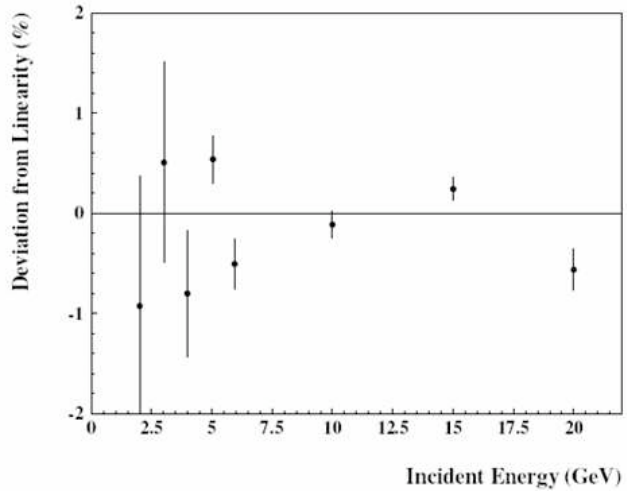

Figure 2.34: Deviation from linearity of ADC to energy conversion of the sampling calorimeter. From [87].

2.2.5 Control and readout

The control and the readout of the system is divided into three parts: a slow control at a frequency of the order of a few Hertz to operate the devices located in the cavity area, the control (at the Hertz level) of the feedback system, and a fast control at 10 MHz to record the calorimeter signals at each bunch crossing (see Figure 2.9). All systems are connected to a personal computer (PC). The slow control system is monitored by a PC connected to a PXI chassis [88] and located in the trailer about 100 m away from the cavity area. It controls all the electronic elements of the cavity area excepted the feedback electronics. Feedback operations are controlled by a second PC located in the tunnel under a concrete slab near the cavity area. These two PC's use LabView software [89] and are accessed from anywhere thanks to Remote-Anything software [90] based on a client-server architecture. The calorimeter DAQ operations are controlled and driven by a third PC located in the trailer and using the PVSS [91] software.

Cavity control in the trailer

On the cavity optical table, several electronic elements are controlled from the PC-PXI located in the trailer: the laser controller (to switch on/off the laser beam, to drive

and control the laser temperature and the laser power), two ESP300 three axes motion controllers [92] (to drive and control the two motorised alignment mirror mounts M_1 and M_2 and the ellipsometer quater wave plate rotating mount), the MoCo controller [93] (to control and drive the azimuthal rotation of the entrance beam line quater wave plate), the heating lamps and eight AD580 temperature sensors [94] (to keep the cavity housing at a constant temperature within 1^o), two CCD cameras (to control visually the alignment and the locking of the cavity), five photodiodes signals (the three of the ellipsometer to measure transmitted cavity signals and the two of the optical entrance beam line to measure reflected cavity signals) which are transported from the tunnel to the trailer by individual 100 m long shielded twisted pair cables to reduce the electromagnetic pickup background. On the PXI rack the following devices are read out:

- A multi-function card (PXI-6025E [95]) containing 16 single analogue inputs digitised by a 12 bits 200 KHz ADC, two 12 bits DAC (Digital to Analog Converter), and 24 I/O (Input/Output) lines. Analogue inputs are used to read out the temperature sensors. I/O lines are used to switch on/off the controller power supplies of the ESP300, the MoCo and the laser, to switch on/off the power supply of the CCD and the PC located in the tunnel and to turn on/off the heating lamps.

- Two multi-channel ADC cards (PXI-2010 [96]), each one containing four independent 14 bit 2 MHz ADC's used for the differential read out of the five photodiode signals.

- A serial RS485 connection device (PXI-8421 [97]) used to drive the controllers of the laser, the two ESP300 stepper motor controllers and the MoCo rotating mount controller.

- A monochrome four channel video board (PXI-1409 [98]) to read out the two CCD cameras.

Examples of control and readout panels using LabView software are shown in Figures 2.35, 2.36, and 2.37.

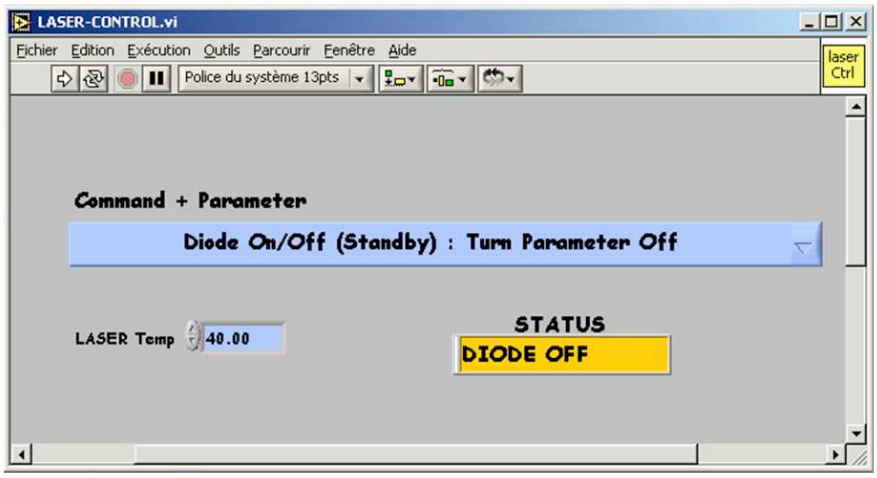

Figure 2.35: LabView panel of the laser control and readout.

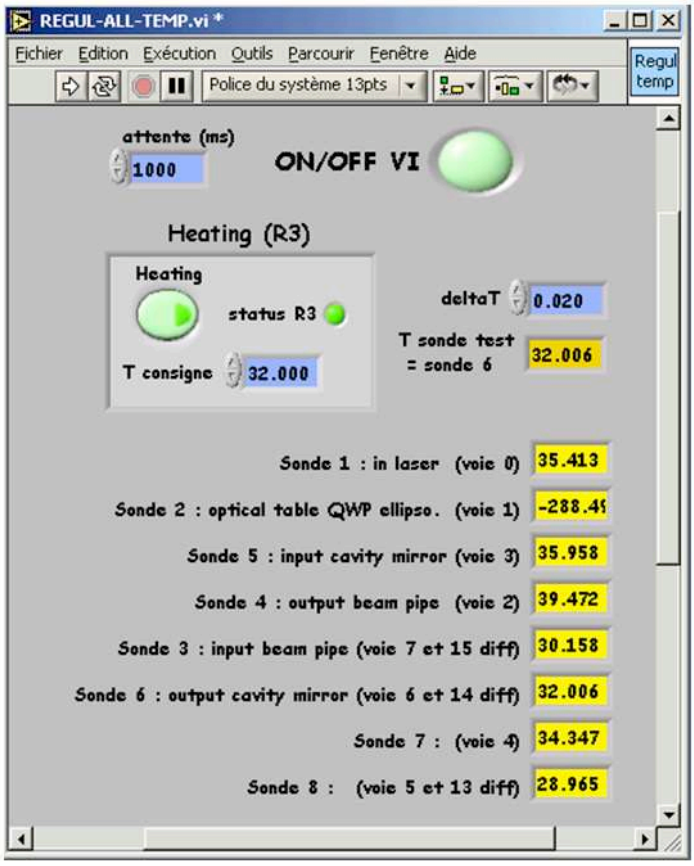

Figure 2.36: LabView panel for the control of the heating regulation system.

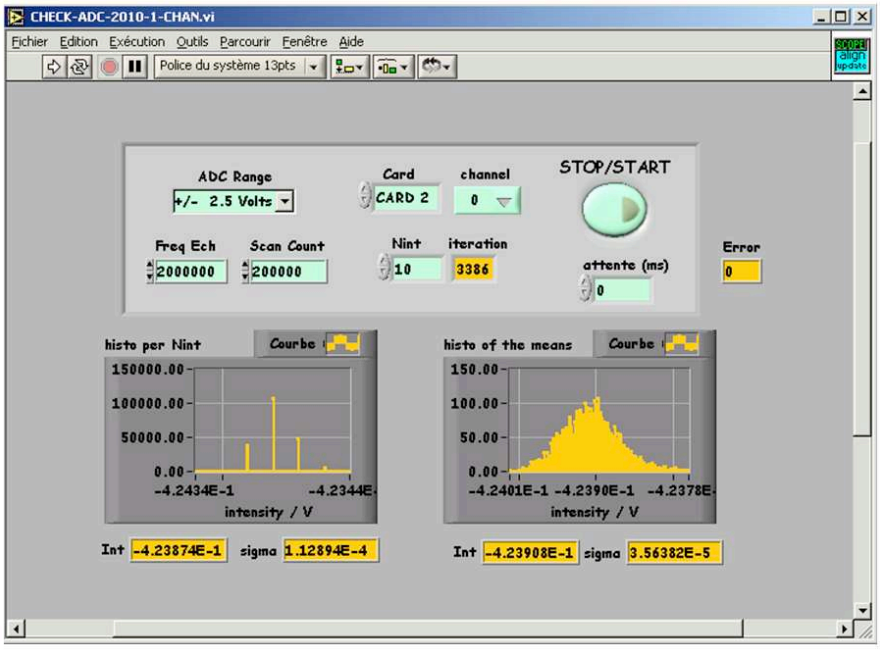

Figure 2.37: LabView panel of one photodiode readout control.

Feedback control in the tunnel

All feedback electronics are located in the tunnel under a concrete slab in front of the cavity housing[8]. The system has been designed and built by the Service d'Instrumentation Génerale (SIG) of Saclay and is a copy of the system used for the CEBAF cavity [63, 61], itself inspired by the PVLAS (Polarizzazione del Vuoto con LASer) experiment system [99]. A functional view of the feedback system whose principle has been described in Section 2.2.3 is presented in Figure 2.38. The operation of the system is as follows:

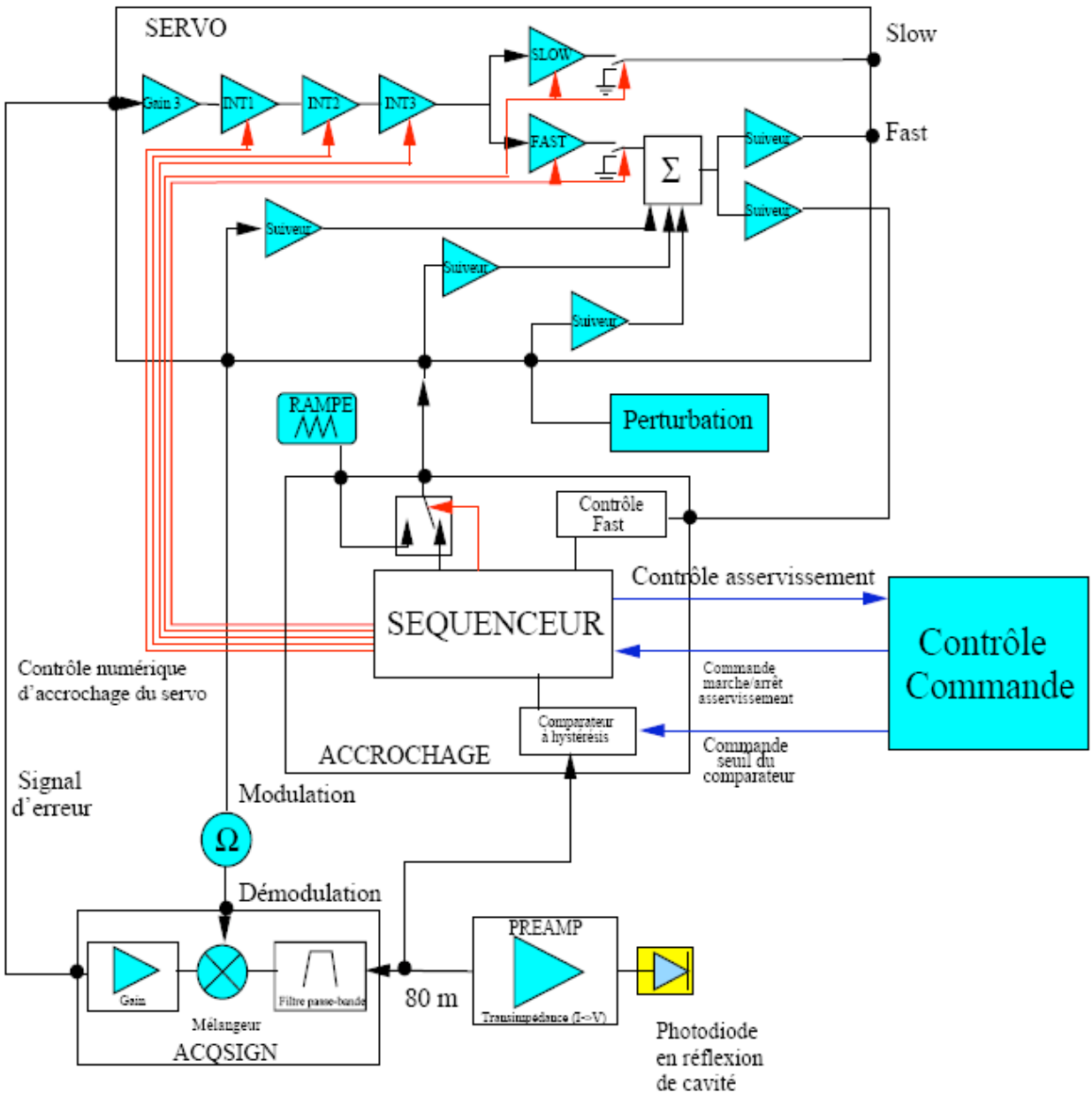

Figure 2.38: View of the feedback electronics. From [61].

[8]Feedback electronics was located in the trailer until the end of the year 2006 where, for unknown reasons, the locking procedure has started to have some instability problems. Hence we have decided to transport all the feedback electronics near the cavity.

Three waveform generators (Agilent 33120A [100]) provide the ramp, the modulation and the demodulation signals. The 'PREAMP' card transforms the current from the photodiode into a voltage signal. The 'ACQSIGN' card constructs the error signal from the photodiode signal mixed with the demodulation signal, filtered and amplified with a gain S_0. The 'SERVO' card then determines from this error signal the correction to be done on the laser frequency. The 'ACCROCHAGE' card, which is connected to the 'SERVO' and the 'ACQSIGN' cards, decides to apply the correction ('closed loop' mode) or not ('open loop' mode). The 'Contrôle Commande' allows all the following feedback parameters to be adjusted automatically: the generator parameters (amplitude, frequency and phase of the ramp, the modulation and the demodulation signals), the mode of the feedback loop ('open loop' or 'closed loop'), the threshold voltage V_{thres} (see Figure 2.31) and the gain S_0 of the 'ACQSIGN' card. The status of the locking can also be visualised. LabView control screens of the feedback procedure is shown in Figure 2.39.

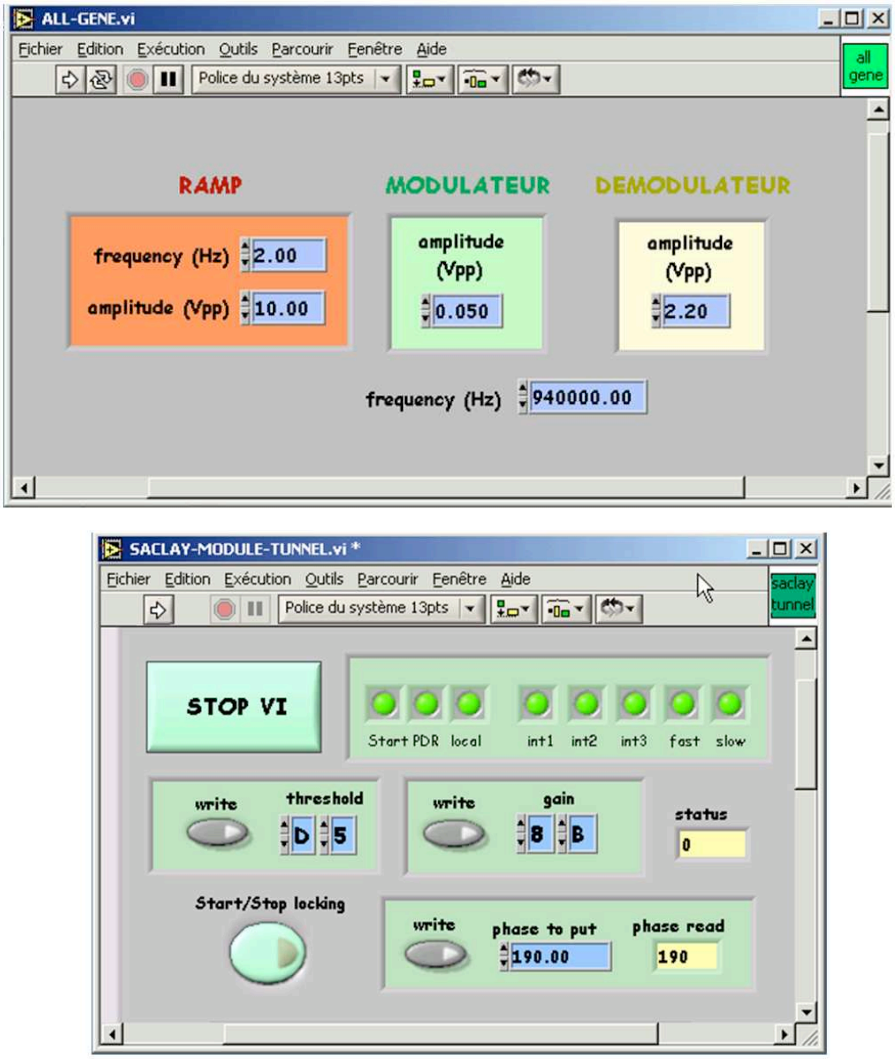

Figure 2.39: LabView panels of the feedback control and driving. Up: three generators command panel. Bottom: driving of the threshold (in hexadecimal unit), the gain (in hexadecimal unit), the locking mode ('Start/Stop locking' button), the demodulation phase ψ_{demod}, and control of the locking status (by the eight green buttons).

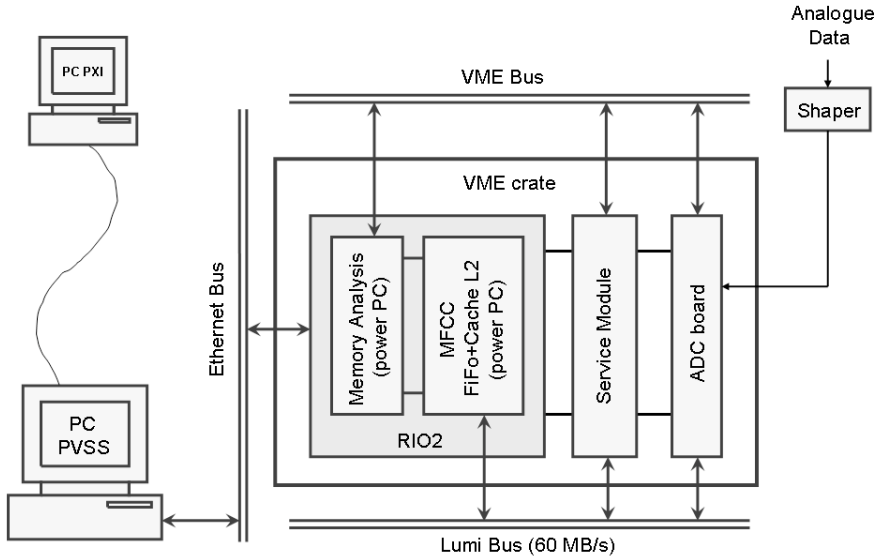

Figure 2.40: Scheme of the calorimeter DAQ front-end hardware electronics.

The principle of the acquisition system is schematized in Figure 2.40 and is as follows: the DAQ system is synchronised to the first HERA electron bunch by the module named 'Service Module' and a dedicated bus (the 'Lumi Bus') is used for the data flow. Starting from the calorimeter, a photo-multiplier (PM) signal is first amplified in a driver board (see Figure 2.9) with a gain of ten. Signals then reach the trailer through two 100 m long 50 Ω coaxial cables (one for the calorimeter signal, one without signal to subtract the base line made of electromagnetic pickup background) and pass in a shaper board which compensates for the skin effect [101] due to cable length and adapts the analogue signal level to the ADC range. A signal pulse is then digitised in a 12 bit ADC card (8 channels, $0-2$ V) at a rate of 40 MHz (*i.e.* four times the HERA clock frequency) providing four samples (every 24 ns) per bunch crossing: the first sample s_1 is a measurement of the baseline. To get a signal proportional to the energy deposit on the calorimeter, the second sample s_2 is performed on the analogue signal at its maximum. For this, a tunable delay between the HERA clock and the ADC is used for the tuning of the sampling position of the ADC with respect to the peak value of the analogue pulse. The third and the fourth samples s_3 and s_4 are performed 24 ns and 48 ns after the second sample. Figure 2.41 shows an example of a calorimeter signal where the ADC sampling is indicated.

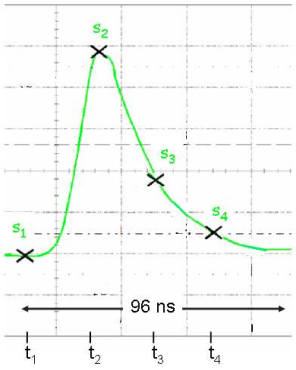

Figure 2.41: Calorimeter PM signal after passing through the Shaper. The ADC samplings (s_1 to s_4) perormed at times t_1 to t_4 are indicated by the crosses.

The digitised data are written in a buffer memory of the ADC board and are continuously added to the FiFo of the MFCC2. The baseline is subtracted from the second sample by the Power-PC. The corrected signal are next transfered to the L2 cache of the Power-PC of the MFCC which fills and stores the energy histograms of the 220 electron bunches. Histograms from the L2 cache are then saved in the Power-PC of the RIO2 board and the memory is refreshed. The transfer of these data is done each 10 sec during the time necessary to change the laser beam polarisation. A detailed description of these DAQ operations can be found in [102]. This DAQ system is similar to the one used for the the H1-luminosity monitor [103, 104]. The essential difference is for us the high acquisition rate of 10 MHz with no trigger which involves a real-time system.

The synchronisation between the laser polarisation switching and the histogram filling and transfer is done thanks the TCP/IP connection [105] between the DAQ-PC and the cavity PC-PXI. TCP/IP transmission functions are built with LabView software. Every 10 seconds, $\approx$ 400000 entries are stored per histogram and per bunch. The time necessary to switch the laser beam polarisation is around 0.5 second (the time to turn the entrance quater wave plate rotating mount, to wait the stabilisation of the cavity power after the change of the laser polarisation, to record the position of the qwp and to send a start signal to the DAQ) and can be considered as our typical 'dead time'.

2.3 Results of the cavity in functionment

In September 2001 and during one year, a test cavity was successfully operated at Orsay. The final cavity was tested and operated at Orsay from December 2002 to February 2003 and was installed in the HERA tunnel during the spring 2003. In this section, the main experimental results concerning the performances of the final cavity operated in the HERA tunnel and the lepton beam polarisation extraction from calorimeter spectra are described.

2.3.1 Laser beam/cavity coupling

Alignment procedure and locking stability

Once the cavity mirrors are geometrically aligned with typical precision of 1 mrad, 1 mm (see Section 2.2.2), the two motorised mirrors M_1 and M_2, the lenses, the photodiode in reflection and the two CCD cameras are used to align the laser beam axis on the optical cavity axis. A scheme showing the principle of the alignment procedure is presented in Figure 2.42.

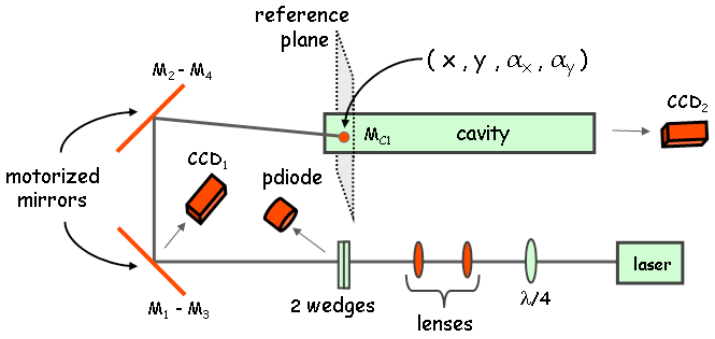

Figure 2.42: Scheme showing all the elements involved in the laser beam/cavity axis alignment.

Using matrix algebra for the calculation of the effects of lens on a gaussian beam [57, 59], the lens positions are first adjusted in order to put the laser waist at the centre of the cavity. Then the alignment procedure is the following:

- A LabView procedure [106] has been written in order to transform the four mirror $M_1 - M_4$ displacements into the four degrees of freedom of the laser beam axis displacements in a given reference plane along the axis z attached to the laser beam propagation. These degrees of freedom are the positions x and y of the laser impact point on the reference plane and the angular inclinations α_x and α_y of the beam with respect to the reference plane. The plane of reference is chosen at the entrance cavity mirror MC_1 (see Figure 2.42).

- For a given laser impact position (x,y), using the entrance CCD_1 camera looking at the light diffusion on the mirror M_1, the angles (α_x, α_y) are varied such that the incident beam and the reflected beam are spatially matched. The accuracy of this matching is given by the laser beam spot outlines on M_1 and by the distance of M_1 from MC_1 (≈ 1 mm and ≈ 1 m respectively) and is about 0.5 mrad.

- The 20 V peak to peak triangular ramp used to cross cavity resonance frequencies (see Section 2.2.3) is supplied on the laser fast channel. The level and the number of excited cavity modes (see Section 2.1.2) are controlled with the reflected signal measured by the feedback photodiode[9] and with the CCD_2 camera at the exit of the cavity. A typical LabView acquisition is presented in Figure 2.43 where both the ramp and the reflected photodiode signals are shown. A camera measurement example is presented in Figure 2.44. In Figure 2.43, odd and even cavity high order modes are present, whereas in Figure 2.44 only a TEM_{01} mode is visible.

- The x and y positions are then changed (and also the angles α_x and α_y to recover the normal incidence) in order to minimise the number of resonant modes, *i.e.* the number of high intensity peaks in Figure 2.43.

- Once the alignment is such that the main resonant modes are the TEM_{00} and TEM_{01} modes, the positions x, y, α_x and α_y are finely adjusted to maximise the reflected peak intensity of the fundamental TEM_{00} mode and minimise the TEM_{01} mode intensity. The cavity is then locked automatically on the fundamental mode using the 'Pound-Drever-Hall' technique described in Section 2.2.3.

When the cavity is strongly missaligned, this alignment procedure takes about one hour. Thanks to the thermalized cavity housing, once the cavity is aligned, the stability of the system is very good. The only times where we had to realign the laser beam were due to hardware problems during which the motorised mirror positions had been lost.

An example of the stability of the locking is shown in Figure 2.45. During twelve hours, only a few delocking periods have happened after which the feedback system has recovered the resonance conditions automatically.

[9]The control of the level and the number of modes should have been done also using the signal transmitted by the cavity measured by one of the ellipsometer photodiode.

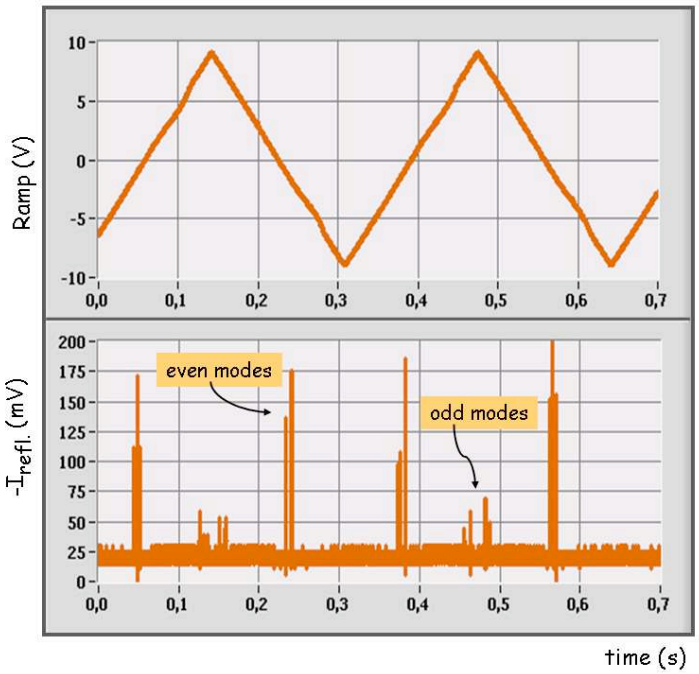

Figure 2.43: 20 V peak to peak triangular ramp signal (up) together with the reflected signal measured by the feedback photodiode (bottom). Odd and even excited cavity modes are indicated.

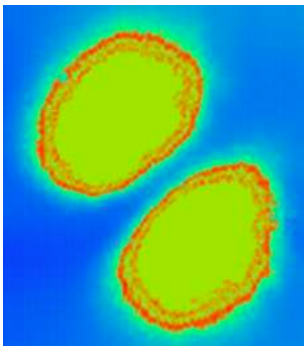

Figure 2.44: Excited TEM_{01} mode visualised after the cavity by the CCD_2 camera.

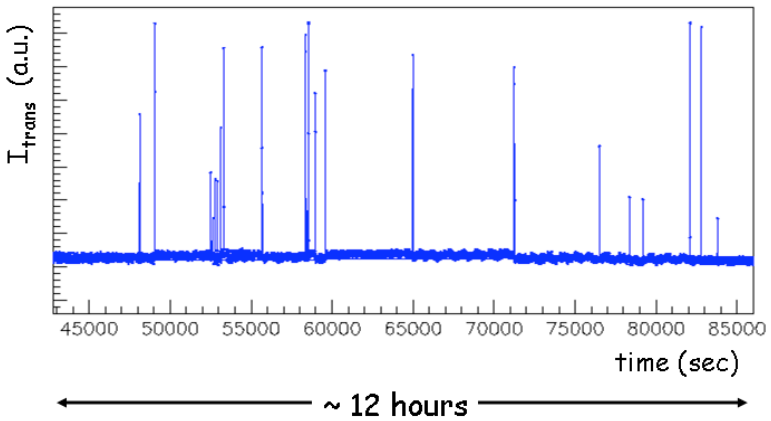

Figure 2.45: Transmitted cavity power measured in the reference ellipsometer photodiode during 12 hours of data taking.

Cavity gain and power

To estimate the gain of the cavity, a simple method is to measure the decay time of the cavity [107, 108]: the power P_{circ} inside a cavity locked in stationary regime is given by equation (2.17). If the laser is suddenly switched off, the circulating power then decreases from the stationary level P_{circ} to the zero level. The measurement of this decreasing time allows the cavity characteristics to be determined.

Indeed, taking the time $t = 0$ when the laser is switched off, after a number n of back and forth trips in the cavity, the decreasing power P_{dec} circulating in the cavity in this transient regime can be written as:

$$P_{dec}\,[t = 2n(L/c)] \;=\; P_{circ}\;\left(R\;e^{2i\Delta\phi}\right)^{n}\;\left[\left(R\;e^{2i\Delta\phi}\right)^{n}\right]^{*}\quad , \tag{2.26}$$

where R is the reflection mirror coefficient, $\Delta\phi$ is the phase shift induced during a light trip from one mirror to another, and "$*$" stands for the complex conjugate operation. After some calculation, equation (2.26) can be written as a function of the decay time T_d of the cavity as:

$$P_{dec}(t) \;=\; P_{circ}\;e^{-t/T_d}\qquad \text{with}\quad T_d \;=\; -\frac{(L/c)}{\ln R}\quad . \tag{2.27}$$

By expending lnR to the first order in R for $R \sim 1$, the finesse $\mathcal{F}$ defined in equation (2.18) and the maximal gain $G_{max} = G_{(\Delta\nu=0)}$ defined in equation (2.17) can be expressed as a function of this decay time as:

$$\mathcal{F} \;\sim\; \frac{\pi\;T_d}{(L/c)}\quad , \tag{2.28}$$

$$G_{max} \;\sim\; \left(1 \;-\; P\;\frac{T_d}{(L/c)}\right)\frac{T_d}{(L/c)}\quad , \tag{2.29}$$

where $P \approx 40$ ppm are the mirror losses. Of course we cannot measure P_{dec} directly since we do not have access to the inside of the cavity, but a measurement of the cavity transmitted power which has obviously the same decay time than P_{dec} allows T_d to be determined.

Figure 2.46 shows a transmitted power measurement performed on our cavity where the laser power has been switched off during a cavity locking period. In the Figure 2.46(a), two curves are shown: the decrease of the cavity transmitted intensity and the decrease of the laser intensity after the laser power switch off. Indeed, once the laser is stopped, its power does not fall to zero instantaneously and the decay time of the laser has to be taken into account in the determination of the cavity decay time. The decrease of the laser intensity is then convoluted with the exponential cavity decay time. Figure 2.46(b) shows the results of this convolution which leads from an exponential fit to:

$$T_d \approx 62\;\mu s \;\Rightarrow\; \begin{cases} \mathcal{F} \approx 29000 \\ G_{max} \approx 5800 \\ \text{FWMH} \approx 2.6\;\text{kHz} \end{cases}$$

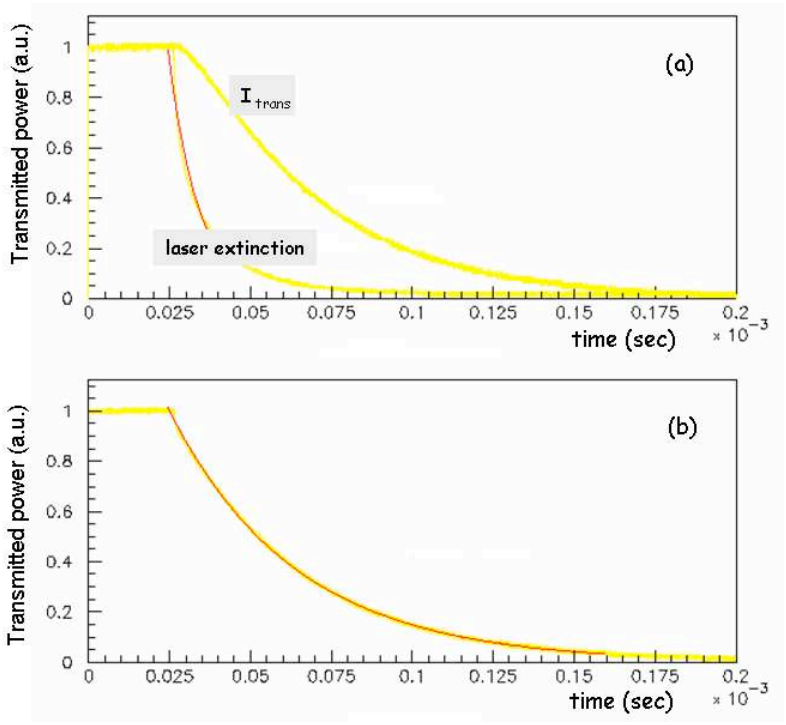

Figure 2.46: (a): transmitted cavity power and laser power extinction measured just after a laser switch off as a function of time. (b): transmitted cavity power convoluted with laser power extinction. The red curves are exponential fit results.

With this estimation of G_{max}, the power P_c inside the cavity at the resonance can now be estimated:

$$P_c = P_{inc} \times G_{max} \quad , \tag{2.30}$$

where P_{inc} is the incident power which is coupled into the cavity. Because of the laser beam linewidth of the order of 5 KHz [66], P_{inc} of formula (2.30) may be smaller than the incident laser power P_{las}. Indeed in this high finesse cavity, FWMH is narrower than the laser linewidth and thus a part of the laser beam cannot be coupled to the cavity if the feedback gain is not high enough [109]. This coupling loss has been estimated by measuring the power reflected by the cavity as described now.

The field of the beam reflected by the locked (respectively unlocked) cavity is called $A_{ref}^{(lk)}$ (respectively $A_{ref}^{(ulk)}$) and the part of the laser beam coupled in the cavity is called A_{cpl} and is defined by:

$$A_{cpl} = c_{cpl} A_{las} \quad ,$$

where c_{cpl} is a coefficient to be determined and A_{las} is the laser incident field. The reflected and circulating fields of equation (2.3) can be rewritten as function of A_{las} and A_{cpl} as:

$$A_{ref}^{(lk)} = r\ A_{las} + i\ t\ A'_{circ} \qquad \text{with :} \quad \begin{cases} A_{circ} &= i\ t\ A_{cpl} + r\ A'_{circ} \\ A'_{circ} &= r\ e^{-2i\Delta\phi}\ A_{circ} \end{cases}$$

Hence, using the expression of the field reflected by the unlocked cavity:

$$A_{ref}^{(ulk)} = r\ A_{las} \quad ,$$

the ratio r_{ref} of the locked cavity reflected power to the unlocked cavity reflected power is written as:

$$r_{ref} = \frac{|A_{ref}^{(lk)}|^2}{|A_{ref}^{(ulk)}|^2} \sim \left[1 - c_{cpl}\left(1 - \frac{\mathcal{F}P}{\pi}\right) \right]^2 .$$

Our different power measurements in the feedback photodiode have provided values of r_{ref} around 0.47 which leads to $c_{cpl}^2 \sim 0.25$. With our laser power functionment $P_{las} = 0.66$ W, the power P_c inside the cavity can then be estimated:

$$P_c \sim P_{las} \times c_{cpl}^2 \times G_{max} \sim 0.96 \text{ KW} . \quad (2.31)$$

As it has been shown in Figure 1.12, this value is enough to reach the statistical uncertainty on the lepton polarisation of order of 1% per bunch and per minute.

2.3.2 Compton photon detection spectra

Bunch structure in the HERA ring

At HERA, 220 bunches circulate in the ring each one spaced by 96 ns. Among these 220 bunches, 40 are empty bunches, 172 are bunches in collision with proton bunches, and 8 are not colliding bunches. A "clean" bunch is defined as a bunch preceeded by at least an empty bunch and therefore leading to a calorimeter signal free of any leakage coming from the previous bunch signal: indeed, after the Shaper, a calorimeter signal remains a little longer than the bunch spacing time[10]. In addition, when the calorimeter data acquisition system starts to operate, a mismatch sometimes occurs between the DAQ time and the HERA clock time. In consequence, the signal baseline is no longer the sample measured at the time t_1 (see Figure 2.41) but the one measured at the time t_4. Signals from two consecutive bunches are schematized in Figure 2.47. If a DAQ time mismatch occurs, the signal of the bunch $n+1$ after baseline substraction is no longer $s2_{n+1} - s1_{n+1}$ but is $s2_{n+1} - s4_n$ and is thus underestimated since bunch signals are a little longer than 96 ns.

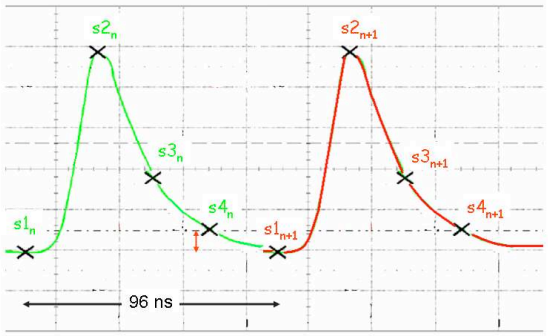

Figure 2.47: Two consecutive bunch signals after passing through the Shaper. The ADC samplings are indicated by the crosses and the little red arrow indicates the magnitude of the leakage.

Polarisation extraction

From the background and Compton differential cross sections, statistical calculations are performed and adjustments using calorimeter energy spectra are done to extract the lepton

[10]This longer time is due to the fact that during a large part of the POLCA data taking, calorimeter signals passed through HERMES electronics [47] before reaching the Shaper leading to signals a little more stretched in time than the one in Figure 2.41.

beam polarisation (see Section 1.3). For each bunch, an adjustment is performed using the data of two consecutive calorimeter spectra, one taken with a right circularly polarised laser beam, the other with a left circularly polarised laser beam. The acquisition time of such a doublet is 2×10 sec (see Section 2.2.5). For a given doublet, the average number of photons per bunch and the lepton polarisation per bunch are determined from the energy distribution probabilities of background and signal processes smeared by the calorimeter response.

One experimental energy spectrum and the corresponding theoretical spectrum resulting from the adjustment are shown in Figure 2.48 for one given bunch. The whole photon energy spectra is presented (a) and also zooms on the synchrotron radiation peak (b), on the Compton photon peak (c) and on the Bremsstrahlung photon edge (d). Figure 2.49 shows the Compton edge spectra for one doublet of histograms. The different amount of Compton photons according to $S_\gamma \pm 1$ is clearly visible.

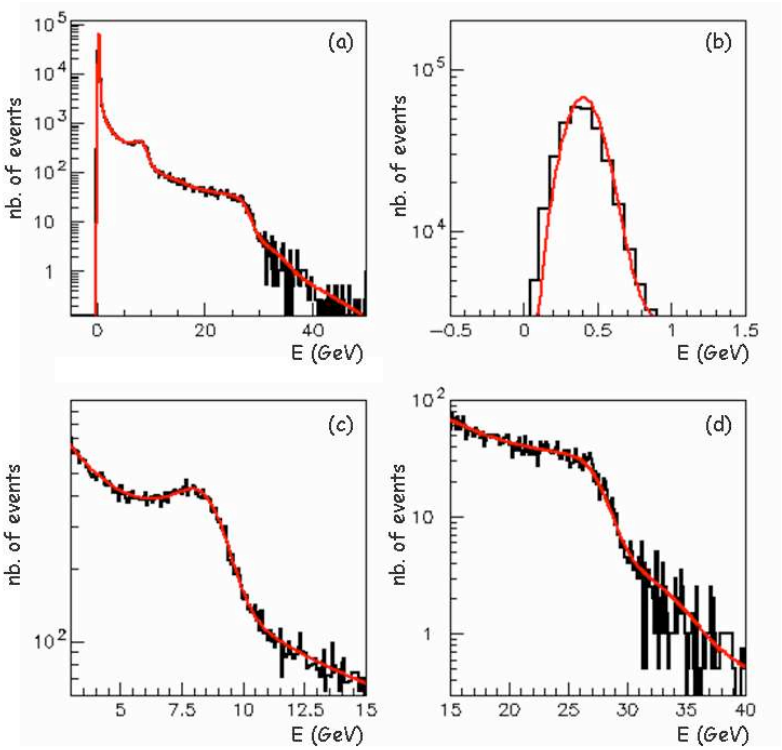

Figure 2.48: Measured (black) and fitted (red) calorimeter energy spectrum of one acquisition histogram: whole distribution (a), synchrotron radiation peak (b), Compton peak (c) and Bremsstrahlung edge (d).

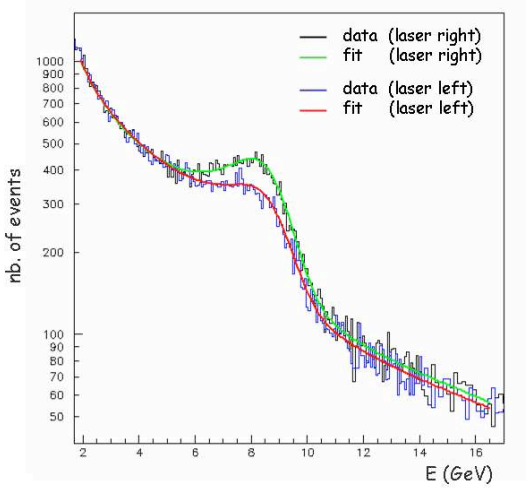

Figure 2.49: Compton edges of two calorimeter energy spectra, each one corresponding to an acquisition of 10 seconds where the laser helicity was left and right respectively. Calorimeter data measurements are in black and blue, the two corresponding fitted distributions are in green and red.

For each spectrum doublet, theoretical distributions shown in Figures 2.48 and 2.49 have been obtained as follows:

- The synchrotron radiation energy (E_{rad}) is extracted firstly at the beginning from a parabolic fit around the position of the radiation synchrotron peak. The synchrotron radiation peak energy is visible in Figure 2.48(b) where E_{rad} is determined with a precision of around 50 MeV. In one histogram, this synchrotron peak contains the largest amount of events and the knowledge of its energy position with a good precision is very important in order not to induce an energy shift which should bias in turn the lepton polarisation determination. Then, once E_{rad} is determined, a grouping of channels around the E_{rad} channel is done to avoid to describe the radiation peak with too much precision. Most of the events of a histogram belongs to the radiation peak channels and including all these channels in the minimisation would give too much weight to these events to the detriment to the Compton events. To perform the grouping of channels, the energy channels closest to the channel E_{rad} are then merged to form a 'big channel'. The number of channels entering in this 'big channel' is chosen as follows: calling N_{rad} the number of events in the channel E_{rad}, all the channels containing more than $c_{mrg} \times N_{rad}$ events are regrouped in the unique 'big channel'. c_{mrg} (< 1) is a parameter to choose before starting the whole adjustment.

- The adjustment of all the following free parameters is then performed, always for each histogram doublet :

  1. The average number n_{black} of black body photons.
  2. The average numbers n_{brem} and $\phi_{brem} \times n_{brem}$ of Bremsstrahlung photons in the histograms recorded respectively with the right and the left circularly polarised laser beam. The flux parameter ϕ_{brem} takes into account the possible changes of the lepton beam condition between the two acqusition times of the doublet.
  3. The average numbers n_0 and $\phi_{comp} \times n_0$ of Compton photons coming from the unpolarised Compton cross section σ_0 (see formula (1.15)) in the histograms recorded respectively with the right and the left circularly polarised laser beam. The flux parameter ϕ_{comp} has been introduced to reflect the small difference observed between the cavity power for the right and the left circularly polarised beams. This effect is due to a small misalignment of the entrance beam line quater wave plate (see Section 2.2.2) leading to laser power change of few percent when the plate is rotated.
  4. The average numbers $P_e \times n_L$ and $-\phi_{comp} \times P_e \times n_L$ of Compton photons coming from the polarised Compton cross section σ_L in the histograms recorded respectively with the right and the left circularly polarised laser beam.

  All the above variables (n_{black}, n_{brem}, ϕ_{brem}, n_0, n_L, ϕ_{comp} and P_e) are determined at the same time by the adjustment. To show the importance of the two flow parameters ϕ_{brem} and ϕ_{comp}, an example of adjustment is presented in Figure 2.50: the blue curve is the result of an adjustment where the two flow parameters have been fixed to the unity and the red one where ϕ_{brem} and ϕ_{comp} were free parameters and have been adjusted. The better agreement between the experimental data and the theory is clearly visible on the red curve.

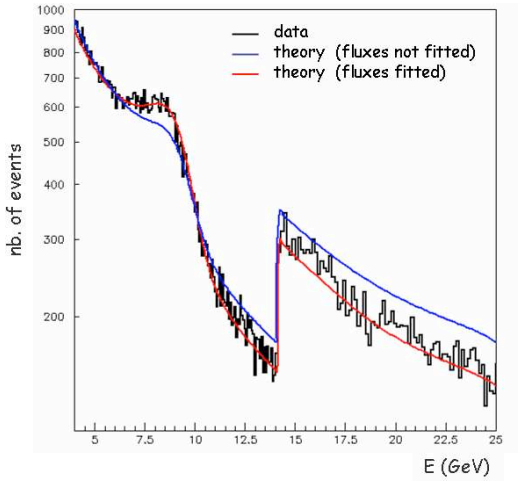

Figure 2.50: Compton edges of one calorimeter energy spectrum: experimental data in black, theory for $\phi_{\rm brem} = \phi_{\rm comp} = 1$ in blue and theory after adjusting $\phi_{\rm brem}$ and $\phi_{\rm comp}$ in red.

From the two spectra on Figure 2.49, the quality of the adjustment has been estimated by calculating the value of the χ^2 in the Compton areas. χ^2 is defined as:

$$\chi^2 = \frac{1}{n_{E_2} - n_{E_1}} \sum_{i=n_{E-1},n_{E_2}} \left(\frac{H_i - T_i}{\sqrt{H_i}} \right)^2 ,$$

where n_{E_1} and n_{E_2} are the first and the last energy bin numbers of the considered region ($E_1 = 2$ GeV and $E_2 = 16.5$ GeV), and H_i (respectively T_i) is the number of data (respectively theoretical) entries in the i^{th} bin. The calculation gives $\chi^2 = 1.06$ and $\chi^2 = 0.99$ for the spectra recorded during a right and a left circularly polarised laser state respectively. These χ^2 values are satisfactory since the lepton polarisation is determined essentially from these Compton edges.

The spectrum of Figure 2.48 comes from a 'clean' bunch. For bunches which are not preceeded by an empty bunch, an additionnal correction is applied to take into account the leakage signal coming from previous bunches (Figure 2.47). The effect of this correction is illustrated in Figure 2.51 where the energy distribution of a bunch preceeded by a non-empty bunch is shown. As shown in Figure 2.51(b), the agreement between the data

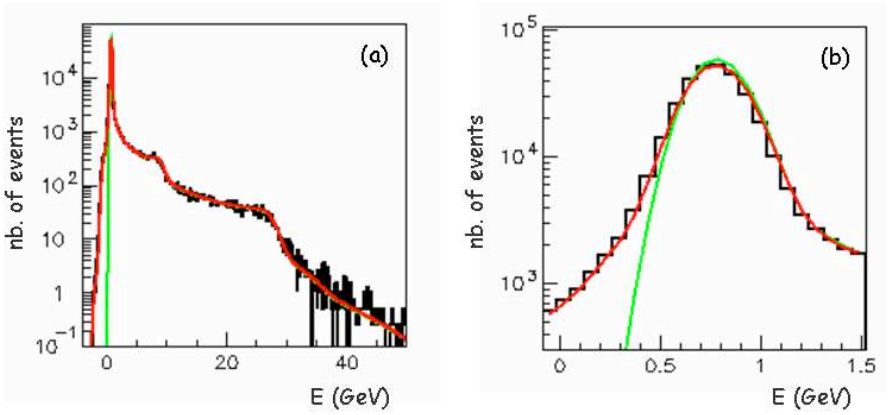

Figure 2.51: Calorimeter energy spectrum of a bunch preceeded by a non-empty bunch: (a) whole distribution, (b) zoom at low energy. Experimental spectra are in black, theoretical ones with and without leakage correction are respectively in red and green.

and the theory at low energy is clearly improved by the leakage correction. The leakage parameter is not a free parameter of the fit but is optimized and fixed at the beginning of the adjustment.

The detector response is also determined, every six or seven minutes, from real data themselves. Indeed, since the acquisition mode is the 'few photon' mode, calorimeter gain and resolution can be extracted from the shape of the photon energy distributions. The calorimeter resolution is parametrised as:

$$\sigma^2(\mathrm{E}) \;=\; \mathrm{c}_0^2 \;+\; \alpha^2\,\mathrm{E} \;+\; \beta^2\,\mathrm{E}^2 \quad , \tag{2.32}$$

where c_0 represents the width of the electronic noise. The ADC-energy conversion is parametrised as:

$$\mathrm{E} = \frac{\mathrm{E}_\ell}{1 + \dfrac{\mathrm{s}_1}{\mathrm{E}_\ell} + \mathrm{s}_2\;\mathrm{E}_\ell} \quad , \quad \text{with} \quad \mathrm{E}_\ell = \mathrm{g}_\ell \times \mathrm{e}_{\mathrm{adc}} \times \mathrm{N}_{\mathrm{adc}} \quad , \tag{2.33}$$

where E_ℓ is the ADC-energy conversion in case there is no non-linearity response effect in the calorimeter, s_1 and s_2 are two coefficients taking into account a possible non-linearity in the calorimeter response respectively at low and high energy, $\mathrm{e}_{\mathrm{adc}}$ is the energy range of one ADC channel ($\mathrm{e}_{\mathrm{adc}} \sim 70$ MeV) and $\mathrm{N}_{\mathrm{adc}}$ is the ADC channel number. The parametrisation (2.33) leads to asymptotic shapes of the ADC-energy curve at low and high energy and a linear behaviour in the middle energy range.

For one doublet of histograms, the parameter c_0 is first determined from the width of the empty bunch energy distributions. An example of the energy spectra of such an empty bunch is shown in Figure 2.52 and leads to $\mathrm{c}_0 \sim 120$ MeV. This value can vary a little in time.

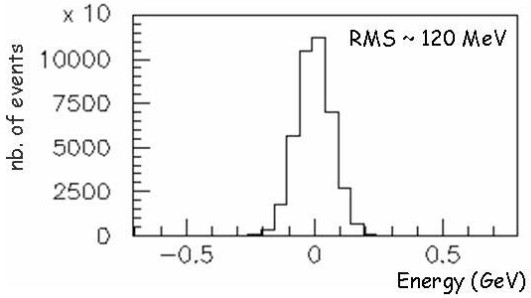

Figure 2.52: Energy spectra of an HERA empty bunch. The RMS of the distribution determines the parameter c_0.

Once c_0 is determined, only 'clean' bunches are selected to determine the calorimeter response. An adjustment is then performed where the free parameters are the calorimeter parameters g_ℓ, s_1, s_2, α and β and the parameters described before (*i.e.* $\mathrm{n}_{\mathrm{black}}$, $\mathrm{n}_{\mathrm{brem}}$, ϕ_{brem}, $\mathrm{E}_{\mathrm{rad}}$, n_0, n_{L}, ϕ_{comp} and P_{e} for each one of the 'clean' bunches). Calorimeter resolution, gain and non-linearity parameters obtained from an adjustment are the following:

$$\begin{cases} \mathrm{c}_0 = 119 \text{ MeV} \\ \alpha = 23.4\% \\ \beta = 0.75\% \end{cases} \qquad \begin{cases} \mathrm{g}_\ell = 1.07 \\ \mathrm{s}_1 = 83 \text{ MeV} \\ \mathrm{s}_2 = 3.4 \text{ MeV}^{-1} \end{cases}$$

Let us make some comments on these detector parameters. Parameters α and β are comparable to those determined by the test beam results (see Section 2.2.4). Concerning the ADC to energy conversion, the order of magnitude of the gain non-linearity coming from the parameters s_1 and s_2 are $\sim 1\%$ and $\sim 4\%$ at 2 GeV and 10 GeV respectively. Depending of the size and the alignment of the calorimeter, electron beam movements could induce a variation of the calorimeter response. Also, the calorimeter can be deteriorated over time because of hard radiation. This is why detector parameters have been determined regularly from the data themselves during the data taking. The polarisation of each doublet as described above is determined using the set of calorimeter parameters closest to this doublet.

Results

An example of polarisation measurements with the cavity polarimeter during ten hours is shown in Figure 2.53. The TPOL polarimeter have been taken data at the same time and the measurements are also visible in the Figure. In Figure 2.53(a) and Figure 2.53(b), each measurement is the average polarisation of the 172 colliding bunches and the 8 non colliding bunches respectively. Each cavity measurement is the average of six doublets (*i.e.* 6×10 sec). The TPOL measurements are performed every minute. For the cavity polarimeter, the statistical precision of the polarisation measurements averaged over all the colliding bunches is of the order of 0.2 percent per minute (error bars are invisible in the figure) and, as expected, is much better than the TPOL uncertainties.

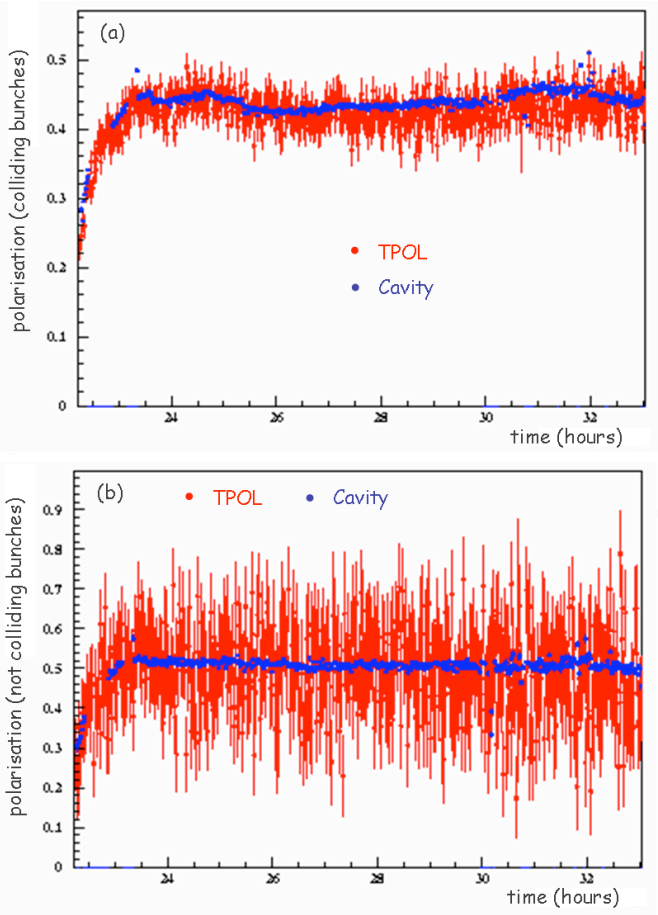

Figure 2.53: HERA-Cavity (blue points) and HERA-TPOL (red points) polarisation measurements of the 172 colliding bunches (a) and of the 8 not colliding bunches (b), as a function of time during about ten hours.

Several data sets have also been recorded with the cavity polarimeter during polarisation build up time. Figure 2.54 shows an example of such polarisation rise time curve. The fit of these data with the polarisation build up formula (1.9) leads to an asymptotic polarisation $P_{ST} = 60.63\%$ and a characteristic time $\tau_P = 24.42$ min. The differences between these values and the ones of formula (1.10) in the case of an ideal machine ($P_{ST} = 92.4\%$ and $\tau_P \approx 40$ min) are due to depolarisation effects described in Section 1.1.4.

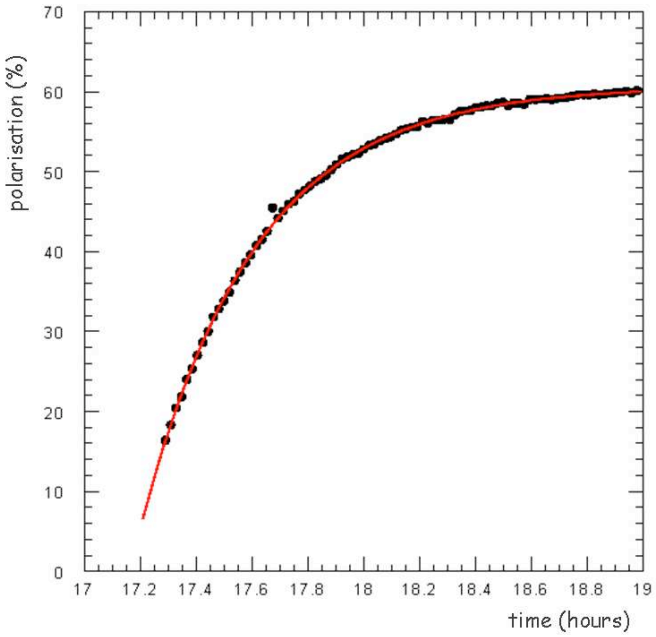

Figure 2.54: Polarisation measurements during a polarisation build up (black points) and rise time curve resulting from a fit with formula (1.9).

These depolarisation effects are visible in Figure 2.55 where the polarisation of the colliding bunches is shown as a function of the proton beam current: as described in Section 1.1.4, more the proton beam current is important, more the leptons are submitted to depolarisation beam-beam effects.

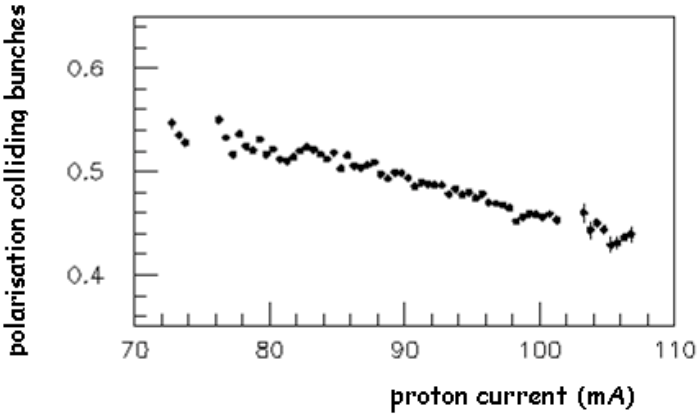

Figure 2.55: Colliding bunches polarisation measurements as a function of the proton beam current.

Average number of Compton photons and uncertainties

Let us now make some comments on experimental average numbers of Compton and backgrounds photons and the comparison with the order of magnitude obtained in the simulations described in Section 1.3.2. Figure 2.56 shows the lepton beam current (a)

and the statistical uncertainty per bunch and per 20 sec (b) as a function of the average number of Compton photons per bunch obtained from the fits. This figure has been done using around 2 hours of data taking where the electron beam current was 32 mA at the beginning and 17 mA after the 2 hours. Histogram (c) in Figure 2.56 shows the average number of Bremsstrahlung photons per bunch during this data taking period. For a typical e-beam current value $I_e \sim 25$ mA, the average number of Compton photons per bunch is $n_\gamma \sim 0.17$ and the statistical uncertainty is 2% per doublet and per bunch. By averaging over a minute (*i.e.* over 3 doublets), the uncertainty is ΔP_e^{stat} / bunch / min $\sim 1.15\%$. Let us remark that the order of magnitude of this uncertainty is in good agreement with the simulated prediction (see Figure 1.12), and that the simulated Bremsstrahlung background level $n_{brem} \sim 0.1$ used to obtain this prediction and the experimental one $n_{brem} \sim 0.3$ are also of the same order of magnitude.

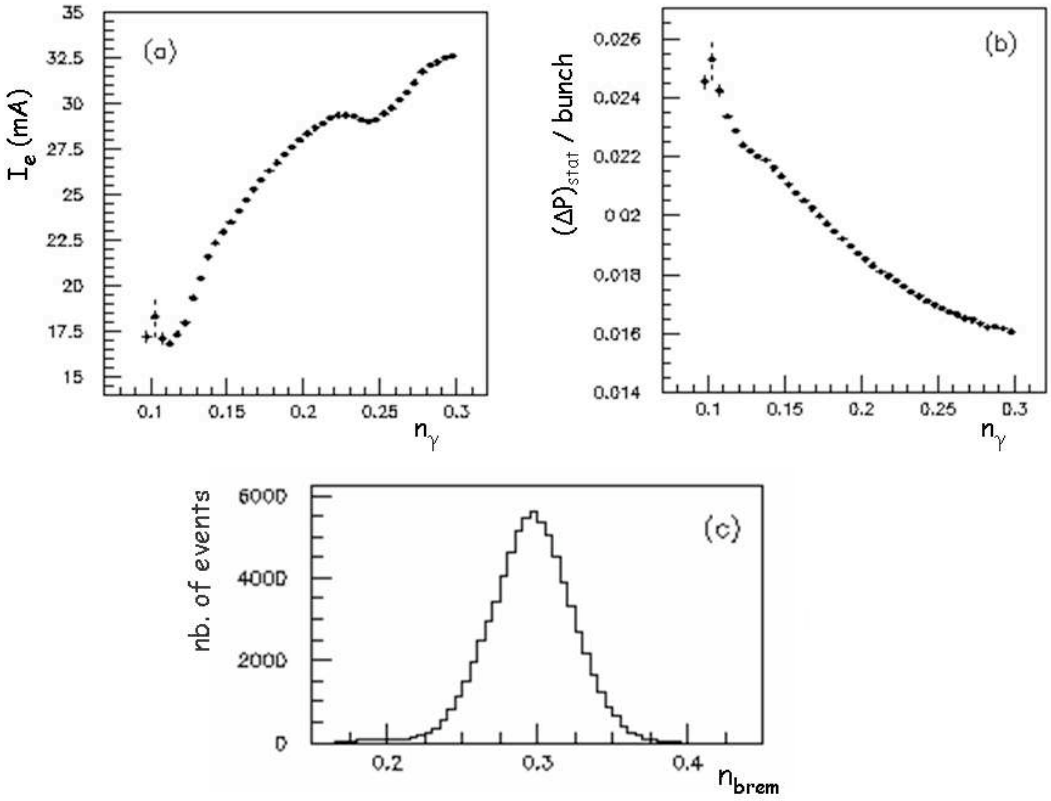

Figure 2.56: Lepton beam current (a) and statistical uncertainty per doublet and per bunch (b) as a function of the average number of scattered Compton photons per bunch resulting from adjustments. (c): histogram of the average number of Bremsstrahlung photons per bunch. All plots correspond to about 2 hours of calorimeter data taking where the electron beam current was 32 mA at the beginning and 17 mA after the 2 hours.

With our estimated cavity power $P_c \sim 0.96$ KW of formula (2.31) and for a lepton beam current $I_e \sim 25$ mA, one expects from Figure 1.12 a number of scattered photons $n_\gamma \sim 0.5$ per bunch. The smaller present rate $n_\gamma \sim 0.17$ could be explained by the fact that the simulation in Figure 1.12 has been done in an ideal case, *i.e.* for an ideal horizontal laser beam / lepton beam alignment. A change in position of the electron beam

has been intentionally generated during a polarimeter data taking. Figure 2.57 shows the average number of Compton photons for several horizontal positions of the lepton beam and illustrates the dependance of the Compton luminosity with respect to the matching of the laser and lepton beams.

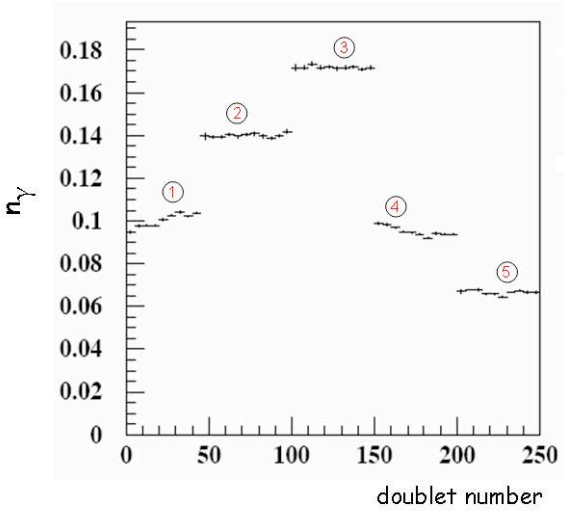

Figure 2.57: Average number of scattered Compton photons as a function of the doublet number, for several lepton beam horizontal positions.
①: arbitrary reference x_0.
②: $x_0 + 0.21$ mm.
③: $x_0 + 0.40$ mm.
④: $x_0 - 0.20$ mm.
⑤: $x_0 - 0.40$ mm.

Anyway, the statistical uncertainty on the lepton beam polarisation measurement per bunch and per minute is of the order of the percent and thus reaches the design requirements.

2.4 Conclusion

In this chapter, after having introduced basic principles of a gaussian beam coupled to a Fabry-Perot resonator, we have described the whole cavity system installed in the HERA tunnel. The main mechanical constraints and the difficulties encountered in such environment have been reported. Then the optical components, the cavity feedback procedure and the photon detection system have been described and the performances and the main results obtained during its operation in the accelerator have been reported. The cavity running was very robust and once aligned, the locking remained very stable. The gain and the power have allowed an average number of scattered Compton photon per bunch of the order of the unity to be reached. The acquisition system at 10 MHz worked very well: one histogram of 400.000 entries was recorded each 10 seconds and a measurement of the polarisation of each of the 180 HERA lepton bunches is performed each 20 secondes. Exploiting the shape of the energy distributions, the sandwich calorimeter has been calibrated on the data themselves and the lepton beam polarisation has been extracted with a statistical uncertainty of order of the percent per bunch and per minute.

Most of the systematic uncertainties can be estimated from the data themselves. These systematics errors come from the choice of certain parameters used in the adjustments or from their uncertainty. These parameters are as follows:

- the gain parametrisation of the photon detector,
- the frequency of the calorimeter calibration,

- the blackbody temperature,
- the merging bin parameter c_{mrg},
- the leakage correction,
- the lepton beam current,
- the lepton beam position,
- the laser power.

All these sources of systematics have been the subject of preliminary studies that will not be described here. The main point is that the addition of all these effects leads to a total systematic of the order of the percent [110].

A last source of systematic error and perhaps the most difficult to control is the knowledge of the Degree Of Circular Polarisation (DOCP) of the light. This quantity, noted S_γ in equation 1.15, is directly involved in the Compton cross section and the level of ignorance of S_γ is transmitted unchanged to the lepton beam polarisation. This quantity S_γ and its uncertainty cannot be determined from the data themselves and dedicated measurements have to be performed in order to decrease the total systematic uncertainty of the lepton polarisation. This is the object of the next chapters which describe the procedure to measure precisely the Degree Of Circular Polarisation of the laser light inside the cavity and to estimate the related uncertainty.

Chapter 3

The ellipsometer

3.1 Introduction

A precise knowledge of the polarisation value of the photon beam inside the cavity is necessary to obtain a good measurement of the HERA lepton polarisation P_e. Indeed the Compton scattering cross section:

$$d\sigma/dE_\gamma \;=\; d\sigma_0/dE_\gamma \;-\; P_e\, S_\gamma\, d\sigma_L/dE_\gamma \tag{3.1}$$

contains a term directly proportional to the light circular polarisation S_γ. To conserve an uncertainty below the percent per bunch per minute level for the measurement of P_e, we intend to measure S_γ with an uncertainty of a few per mill.

To characterise a polarisation state of light, we use a dielectric anisotropic crystal. Indeed, because of their crystalline structure, these materials interact in different way according to the electric field: either they may absorb or reject certain components of the electric field (these materials are called polarisers), or they may delay one field component with respect to the other one, introducing a phase shift between the components (these materials are called delay plates). The anisotropic character of the dielectric leads to the existence in the medium of refraction indices depending on the propagation direction of the wave: two waves, called ordinary and extraordinary, then propagate in the medium with linear orthogonal polarisations. In the general situation, these two waves have two different propagation directions: it is possible in this case to separate the two different orthogonal polarisations. In the particular situation where the two waves propagate in the same direction, a phase velocity leads to a phase shift of a linear polarisation in relation to the other which is orthogonal. The consequence is a change of the incident wave polarisation at the exit of the material. In particular, when this phase shift is equal to $\pi/2$ the dielectric is called a half-wave plate, when it is equal to $\pi/4$ the dielectric is called a quater wave plate.

In order to characterise the polarisation of a light beam, a system called an ellipsometer is used. It allows the transversality of the wave to be characterised. The principle of an ellipsometer is to send a light beam, of any unknown polarisation, through a quater wave plate followed by a Wollaston prism which separates spatially the beam into two orthogonal linear polarised states. By varying the azimuthal angle of the quater wave plate and by analysing the intensities obtained in photodiodes for these different angles, one can infer the polarisation of the incident beam.

This chapter is devoted to describe the ellipsometer located at the exit beam line of our Fabry-Perot cavity. After a brief description of the mathematic description of the light polarisation states, the optical components of the ellipsometer will be described and their precision characterised.

3.2 Jones and Stokes formalism

Before going through the details of the ellipsometer, a mathematic representation of the polarisation states and of the optical components must be defined. From Maxwell's equations and boundary conditions, the expression of an electric field vector associated to an electromagnetic wave can be obtained. In an isotropic medium of optical indice n, a monochromatic plane wave with frequency ω and wave vector $\mathbf{k}$ propagating along the axis oz, is described by its associated field vector:

$$\mathcal{E}(\mathrm{z},\mathrm{t}) \;=\; \mathbf{E}\exp\left[\; i(\omega \mathrm{t} - \mathbf{k}\cdot\mathbf{z})\;\right] \quad ,$$

where $\mathrm{k} = |\mathbf{k}| = \mathrm{n}\omega/\mathrm{c}$ and where $\mathbf{E}$ is a complex vector normal to the vector $\mathbf{k}$ which characterises the polarisation state of the field $\mathcal{E}$. The electric field is given by the real part of the complex expression of $\mathcal{E}$. The polarisation vector $\mathbf{E}$ can be written as:

$$\mathbf{E} \;=\; \mathrm{A_x}\,\mathrm{e}^{i\phi_\mathrm{x}}\mathbf{x} \;+\; \mathrm{A_y}\,\mathrm{e}^{i\phi_\mathrm{y}}\mathbf{y} \quad ,$$

where $\mathrm{A_x}$ and $\mathrm{A_y}$ are real quantities. The projections of $\mathcal{E}$ along the two transverse directions ox and oy are then written as:

$$\mathcal{E}_\mathrm{x} \;=\; \mathrm{A_x}\cos(\omega \mathrm{t} - \mathrm{kz} + \phi_\mathrm{x}) \quad ,$$

$$\mathcal{E}_\mathrm{y} \;=\; \mathrm{A_y}\cos(\omega \mathrm{t} - \mathrm{kz} + \phi_\mathrm{y}) \quad .$$

The time evolution of the extremity of $\mathcal{E}$ describes a trajectory in the transverse plane oxy and is called the wave polarisation state.

The most general polarisation state is an elliptic polarisation: the polarisation vector describes an ellipse in the transverse plane as a function of time. When the two projections $\mathcal{E}_\mathrm{x}$ and $\mathcal{E}_\mathrm{y}$ evolve in phase ($\phi_\mathrm{x} = \phi_\mathrm{y}$), the wave field trajectory oscillates along a straight line. The wave is then linearly polarised in a direction which depends on the quantity ϕ_x and on the two amplitudes $\mathrm{A_x}$ and $\mathrm{A_y}$. When the two projections have the same amplitude ($\mathrm{A_x} = \mathrm{A_y}$) and when their phase shift $\phi_\mathrm{x} - \phi_\mathrm{y}$ is equal to $\pm\pi/2$, the wave is circularly polarised and the vector $\mathcal{E}$ describes a circle in the transverse plane as a function of time.

3.2.1 The Jones representation

The vectorial nature of the polarisation state suggests using a matrix representation to describe it. The Jones representation is a simple way to characterise the polarisation states of a wave [77]. The state is described by a two dimensional complex unitary vector, called the Jones vector $\mathbf{J}$. The electric field can be written as a function of $\mathbf{J}$ as:

$$\mathbf{E} \;=\; \mathrm{E}\,\mathbf{J} \;=\; \begin{pmatrix} \mathrm{A_x}\,\mathrm{e}^{i\phi_\mathrm{x}} \\ \mathrm{A_y}\,\mathrm{e}^{i\phi_\mathrm{y}} \end{pmatrix} . \tag{3.2}$$

- If the polarisation is linear, then $\mathbf{J} = \begin{pmatrix} \cos\chi_P \\ \sin\chi_P \end{pmatrix}$.

- If the polarisation is circular, then $\mathbf{J} = \frac{1}{\sqrt{2}} \begin{pmatrix} 1 \\ \pm\, i \end{pmatrix}$.

  Note that any circularly polarised wave is the superposition of two linearly polarised waves according to two orthogonal directions and dephased by $\pm\pi/2$. In the same way, any linearly polarised wave is the superposition of two circular right and left waves.

- If the polarisation is elliptic and by calling $\phi_P = \phi_y - \phi_x$, then

$$\mathbf{J} = \begin{pmatrix} \cos\chi_P \\ \sin\chi_P \, e^{i\phi_P} \end{pmatrix} . \tag{3.3}$$

The light intensity is written as a function of the Jones vector as: $I = \mathbf{J}^* \cdot \mathbf{J}$, where $\mathbf{J}^*$ is the complex conjugate of $\mathbf{J}$.

The effect of an optical element on the state of polarisation of the light passing through can be described in the Jones representation by a complex two-by-two Jones matrix M_J [111]. The electric field $\mathbf{E}'$ after passing through the optical element can be written as:

$$\mathbf{E}' = M_J \, \mathbf{E} \ ,$$

where $\mathbf{E}$ is the electric fields before the optical element which is described by M_J and can be a delay plates, a polariser or a rotator.

3.2.2 The Stokes representation

The light polarisation can be described in another way, called the Stokes representation [77]. In this representation, a polarisation state is characterised by four parameters: the Stokes parameters. In a light wave, the fraction of the light horizontally, vertically, right and left circularly polarised can be quantified. The parameters allowing for such a description are called S_0, S_1, S_2 and S_γ :

- $S_0 = I_x + I_y$ (the total intensity) is the sum of the intensities of the linear polarisation components along ox (I_x) and oy (I_y),

- $S_1 = I_x - I_y$ is the difference of the intensities of the linear polarisation components along ox and oy,

- $S_2 = I_{+45^o} - I_{-45^o}$ is the difference of the intensities of the linear polarisation components along the ox and oy axes rotated by $\pm 45^o$,

- $S_\gamma = I_G - I_D$ is the difference of the intensities of the left circular polarisation component (I_G) and the right one (I_D).

Mathematically the Stokes parameter expressions are written as:

$$\begin{cases} S_0 = A_x^2 + A_y^2 \\ S_1 = A_x^2 - A_y^2 \\ S_2 = 2\ A_x\ A_y\ \cos\phi_P \\ S_\gamma = 2\ A_x\ A_y\ \sin\phi_P \end{cases} \tag{3.4}$$

where $\phi_P = \phi_y - \phi_x$, and where A_x, A_y, ϕ_x and ϕ_y are the parameters introduced in (3.2). The Stokes parameters are therefore expressed simply and only as function of intensities. For a fully polarised light, these four coefficients are connected by the following relation:

$$S_0^2 = S_1^2 + S_2^2 + S_\gamma^2 \ .$$

S_γ is called the Degree Of Circular Polarisation of the light (noted also DOCP in the following). If $S_\gamma = +1$ ($S_\gamma = -1$), the light is 100% right (left) polarised. This quantity S_γ is the variable of equation (3.1) and has to be determined very precisely. In the same way as the Jones description, the effect of an optical component on the polarisation state can be described by a four-by-four matrix.

The Jones and the Stokes formalisms are equivalent but are more or less appropriate depending to the calculation to be done. For instance in a model where the multiple reflections inside a medium together with the gaussian nature of the wave behaviour are taken into account, the Stokes formalism is more appropriate [50]. For other more simple cases, the Jones formalism can be used as well.

3.3 Experimental setup and precision requirements

A drawing of the ellipsometer device used to characterise the laser light polarisation (as well as some optical components as we shall see in the following) is shown in Figure 3.1. The beam to be analysed passes first through a holographic beam sampler (HBS) in order to extract a small part of the entrance power (about 1%, exact replica of the incident beam). This part of the beam is used as a reference intensity to compensate the effects due to possible laser power variations. Next, the beam passes through a quater wave plate, then through a Wollaston prism which separates spatially the beam in two linear and orthogonal polarisation components. Finally the transmitted beams are detected in two photodiodes. Diffusers are located in front of each photodiode, in order not to be sensitive to the beam pointing instabilities and to be able to decrease or increase the power entering the photodiodes.

The measurement of the Degree Of Circular Polarisation of the light beam with an uncertainty of a few per mill requires a precise control of the characteristics of the ellipsometer optical components (HBS, Wollaston prism and quater wave plate) as well as the response of the photodiodes. In the following, we review these different devices and characterise their degree of precision.

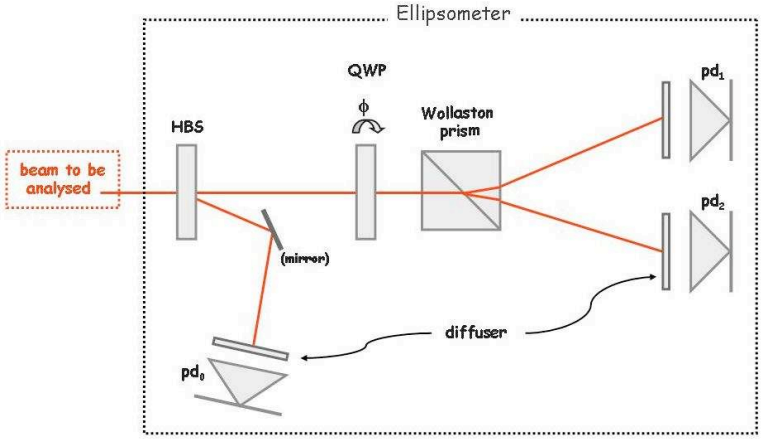

Figure 3.1: Schematic drawing of the ellipsometer used for the photon polarisation measurement: the entrance light to be analysed passes through an holographic beam sampler (HBS), then through a quater wave plate (qwp) and through a Wollaston prism, before being recorded in photodiodes (pd).

3.3.1 The holographic beam sampler (HBS)

The holographic sampler is a hologram in relief engraved on a transparent substrate (silica) inducing forward diffraction. Some precise spatial samplers, from one percent to 10^{-8} percent of the incident power are obtained after passing in a HBS. These samplers have the same polarisation as the incident beam. The schematic of an HBS is shown in Figure 3.2. The first sampler A contains 1% of the incident power and is deviated by ten degrees to the transmitted principal beam.

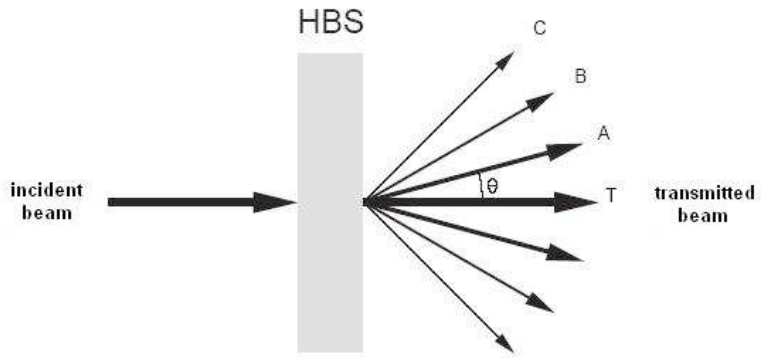

Figure 3.2: Principle of a holographic beam sampler (HBS).

3.3.2 The photodiodes

The detection system consists in three photodiodes called pd_0, pd_1 and pd_2 in Figure 3.1 and a fourth one pd_{sp} for spare. The photodiodes (Hamamatsu, model G8370-02) are constituted by a gallium arseniure and indium alloy (InGaAs). They are low noise photodiodes and are particularly appropriated for the near infrared detection. The associated readout electronics are standard, composed of pre-amplifiers and resistances [112]. These

elements have been chosen to be as stable as possible with respect to temperature variations. In addition, each photodiode and their electronics are thermalized with a Peltier module. Indeed, the temperature variations in the HERA experiment environment might be of a few degrees and could induce a variation of the photodiode readout larger than the required precision. With a Peltier module, a stability level of tenth of a degree is achieved. As shown in Figure 3.3, the photodiodes work in a linear regime if the incident power is below 6 mW [80]. We have to operate them in this regime. The readout of the photodiodes is done with 12 bit analogue digital converters at a maximum sample rate of 2 MHz.

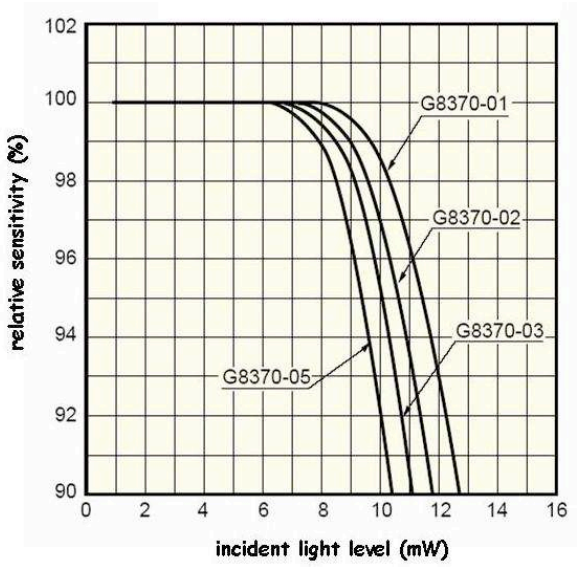

Figure 3.3: Linearity area of the InGaAs photodiodes as a function of the incident power. Our photodiodes are the G8370-02 model (Hamamatsu product) of bandwidth 4 MHz.

The photodiode test device with which the photodiodes has been characterised at the Orsay laboratory is drawn in Figure 3.4. Photodiodes are tested two by two: a 100 mW power infrared beam delivered by a high quality ND:YAG laser ($\lambda = 1064$ nm)[113] is sent through a beam shutter followed by the HBS. In order to stay in the linear working regime, the two tested photodiodes are located so as to receive only one percent of the laser incident power.

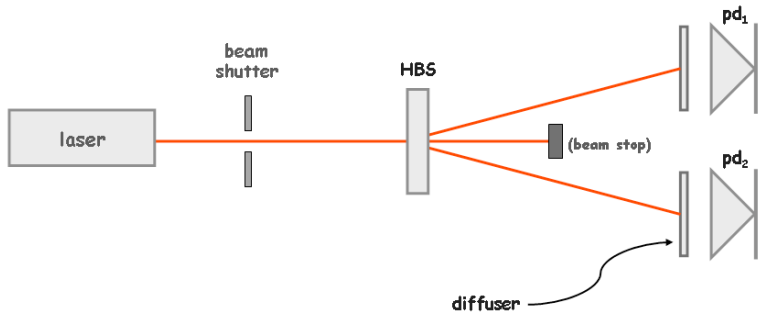

Figure 3.4: Schematic drawing of the optical device used to characterise the photodiodes (laser, beam shutter, beam sampler, two InGaAs photodiodes).

For each measurement, the value of the mean of ten thousand events is recorded. The pedestal of each photodiode is first measured, then the signal with the laser on is measured and the two are subtracted. For this, a beam shutter is located in the beam line, and is opened ("laser on" state) or closed ("laser off" state). An example of pedestal and intensity measurements is shown in Figure 3.5. The total duration of the data taking is a few hours. The plots (a) and (b) show the pedestals of the two photodiodes pd_0 and

pd_1 (called respectively br_0 and br_1). The flat part corresponds to the data taken during the night, the irregular parts reflect the variations of light during the day time. The plots (c) and (d) show the "laser on" signals recorded respectively by the photodiodes 0 (sig_0) and 1 (sig_1). Figures (e) and (f) show the differences ($sig_0 - br_0$) and ($sig_1 - br_1$). The residual dispersion observed on the two plots (e) and (f) is due to laser power variation and is of one to two percents.

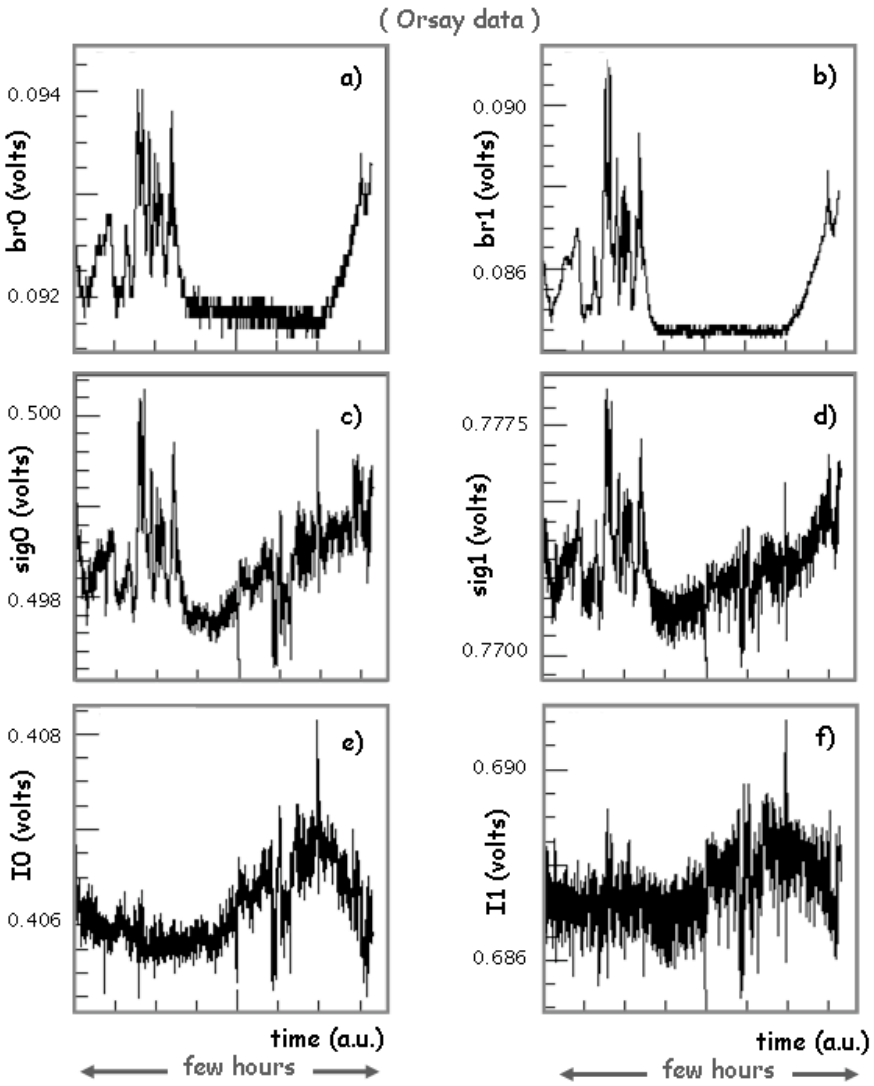

Figure 3.5: Pedestals br_0 (a) and br_1 (b), signals sig_0 (c) and sig_1 (d), and differences ($sig_0 - br_0$) (e) and ($sig_1 - br_1$) (f) for the photodiodes pd_0 and pd_1 as a function of time.

To obtain a measurement of the light polarisation in the cavity with a precision at the per mill level, it is necessary to compensate for these laser power variations. For this, one of the diodes is used as a reference and each diode signal is divided by the reference diode. Figure 3.6(a) shows the ratio $(sig_0 - br_0)/(sig_1 - br_1)$ as a function of time, and Figure 3.6(b) the histogram of this ratio. The histogram in Figure 3.6(b) has a gaussian behaviour and its width at half height leads to $\sigma/M \sim 0.06\%$ where M is its mean value. The use of the reference diode to correct the laser power variation then leads to a good stability of the measurements in time. Signals after pedestal subtractions and

intensity ratio constructions are shown for the other two photodiodes in Figure 3.7 where $\sigma/\mathrm{M} \sim 0.07\%$ for the histogram (d).

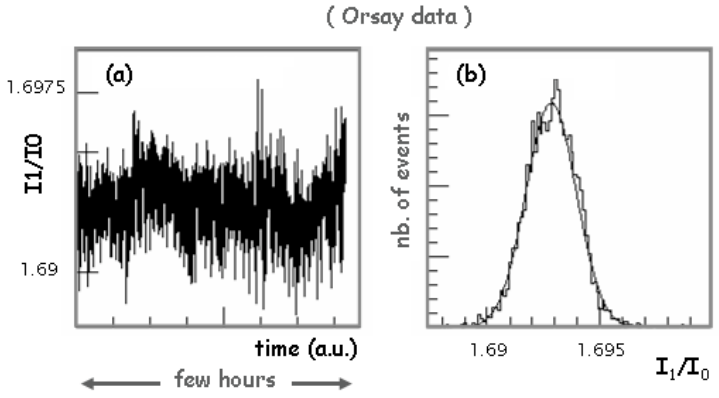

Figure 3.6: Ratio $(\mathrm{sig}_1 - \mathrm{br}_1)/(\mathrm{sig}_0 - \mathrm{br}_0)$ as a function of time (a) and histogram of this ratio (b).

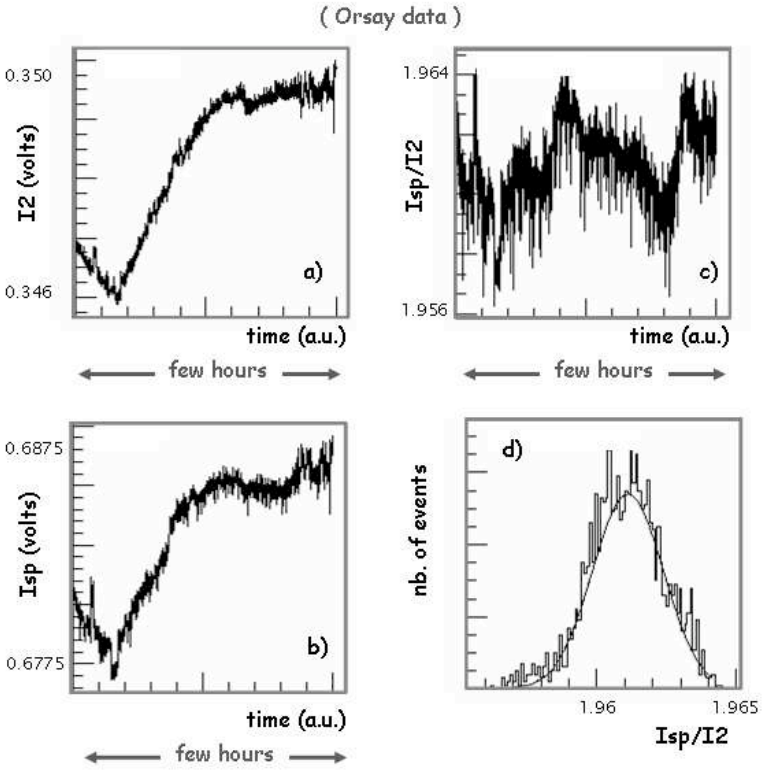

Figure 3.7: Intensities of the two photodiodes pd_2 (a) and $\mathrm{pd}_{\mathrm{sp}}$ (b) and ratio of these two intensities (c), as a function of time. Histogram of the ratio (d).

It is interesting to see the effect of a room temperature variation on a photodiode intensity. Figure 3.8 shows the correlation between the intensity and the temperature variation which has been intentionally generated by varying the room air temperature. The gain in temperature variation obtained by the regulation with the Peltier module is illustrated in Figure 3.9. The temperature inside the photodiode boxes (Figure 3.9(a)) and the corresponding room temperature (Figure 3.9(b)) are shown. The Peltier gain is of the order of 1/10.

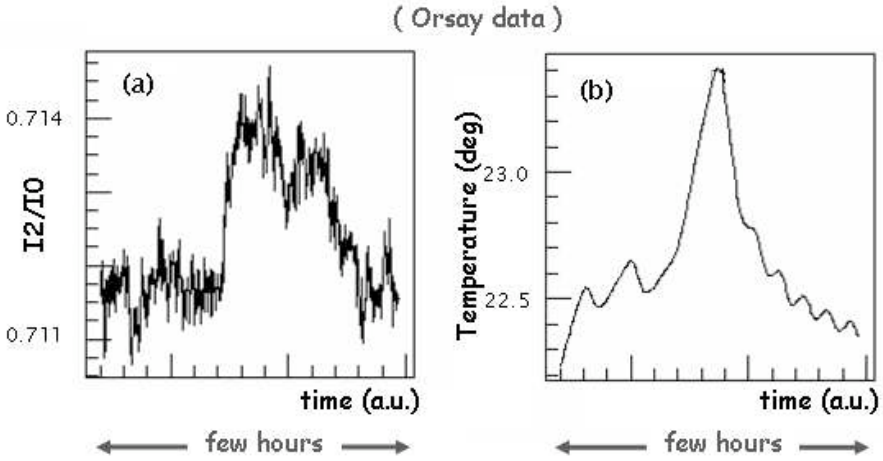

Figure 3.8: Effect of a temperature variation on the photodiode measurements: intensity (a) and room temperature (b), as a function of time.

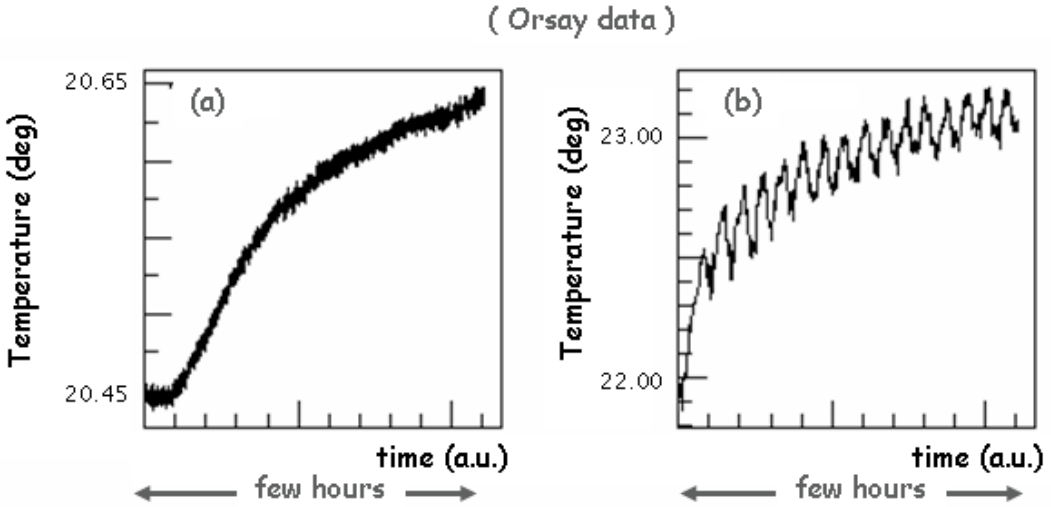

Figure 3.9: Temperature inside a photodiode box cooled by a Peltier module (a) and room temperature (b), as a function of time.

The study of the photodiodes shows that after temperature regulation, pedestal subtractions and intensity ratio constructions, the obtained measurements are controlled at the per mill level.

3.3.3 The Wollaston prism

A Wollaston prism spatially separates the incident laser beam into two orthogonal linear polarised beams. It consists of two prisms cut in the same birefringent calcite crystal. The two prisms are cut and joined so that the optical axes are perpendicular to each other. At the interface between the two prisms, taking into account the orientations of the optical axes, the ordinary and extraordinary rays of a wave are refracted with different angles, making it possible to separate them spatially at the exit interface. The angular separation can reach 30° if the half-prism angles are optimised in order to increase the separation due to the double refraction. A principle schematic of a Wollaston prism is

presented in Figure 3.10 showing the spatial separation of the beam into two orthogonal linear polarised beams.

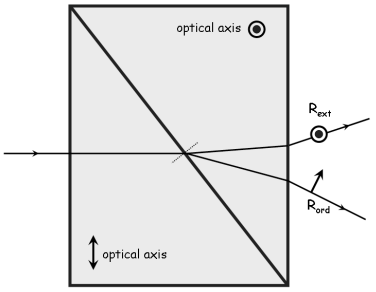

Figure 3.10: Principle schematic of a Wollaston prism.

The main characteristic of the Wollaston is its extinction rate. This rate is given by the manufacturer as less than a few 10^{-5} and has been checked with our photodiodes by rotating a prism in order to cancel one of the two emergent beams for an incident linearly polarised beam. Taking into account a small Wollaston ellipticity (and assuming an extinction rate equal to zero), the Jones matrices associated to the two transmitted states are written in a frame of reference where the cube axes are those of the laboratory [114] as:

$$\mathrm{M^{Wx}} = \begin{pmatrix} 1 & -i\epsilon_x \\ i\epsilon_\mathrm{x} & 0 \end{pmatrix} \quad , \qquad \mathrm{M^{Wy}} = \begin{pmatrix} 0 & -i\epsilon_\mathrm{y} \\ i\epsilon_\mathrm{y} & 1 \end{pmatrix} \quad , \tag{3.5}$$

where ϵ_x and ϵ_y are two Wollaston ellipticity parameters supposed to be very small ($\epsilon_\mathrm{x},\ \epsilon_\mathrm{y} \ll 1$).

3.3.4 The quater wave plate

Quater wave plates most often used are parallel sided quartz plates of thickness e. The quartz is an anisotropic uniaxial medium. When an incident plane wave enters such a medium under normal incidence, two waves then travel inside, linearly polarised and orthogonal to each other. These waves have different phase velocities or in an equivalent way see two different optical indices. These indices are called the ordinary index $\mathrm{n_o}$ and the extraordinary index $\mathrm{n_e}$. The difference $\mathrm{n_o - n_e}$ is the plate birefringence. For uniaxial medium, the eigenvector corresponding to the eigenvalue $\mathrm{n_e^2}$ of the dielectric tensor defines the optical axis of the plate. A more complete formalism of the propagation of a wave through an uniaxial medium is detailed in Appendix A. For a standard quartz quater wave plate, the optical axis is usually located in the plane of the interface.

When a plane wave passes through a quartz plate, a phase shift ϕ_sh is induced between the projection of $\mathbf{E}$ on the optical axis and the projection of $\mathbf{E}$ on the perpendicular to the optical axis. For a plate of thickness e, the plane wave expression $\mathbf{E}\exp[\ i(\omega\mathrm{t} - \mathbf{k}.\mathbf{z})]$ leads to the phase shift:

$$\phi_\mathrm{sh} = \frac{2\,\pi}{\lambda}\,(\mathrm{n_o - n_e})\ \mathrm{e} \quad ,$$

where λ is the wave length of the incident wave. The plate is supposed to be sufficiently thin and the beam sufficiently wide to neglect the spatial transverse shift of the emergent beams. Figure 3.11 shows the passage of a wave through an anisotropic uniaxial medium.

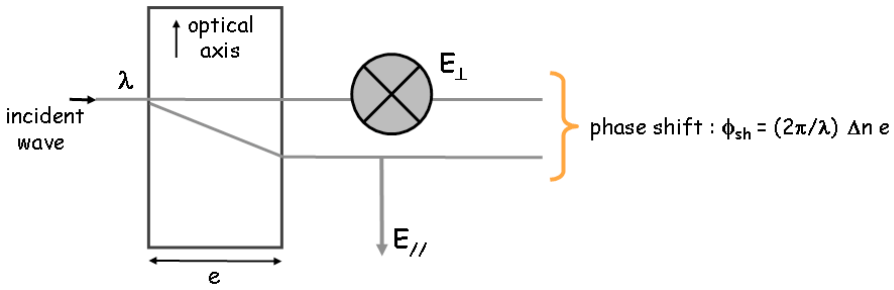

Figure 3.11: Passage of a plane wave through an uniaxial medium: the two components $\mathbf{E}_{||}$ and $\mathbf{E}_{\perp}$ of $\mathbf{E}$ acquire a phase shift the one with respect to the other of an angle ϕ_{sh}.

The two linear and orthogonal polarisation states are simply dephased. Therefore the Jones matrix associated to this dephaser can be written in a frame of reference where one axis coincides with the (ox) axis as:

$$\mathrm{M_J} = \begin{pmatrix} 1 & 0 \\ 0 & \mathrm{e}^{-i\phi_{\mathrm{sh}}} \end{pmatrix} . \tag{3.6}$$

It is easy to verify that when $\phi_{\mathrm{sh}} = \pi/2 + 2\mathrm{k}\pi$ ($\mathrm{k} = 0, 1/2, 1, 3/2...$), an incident wave linearly polarised will emerge from the plate with a circular polarisation. The plate is called in that case a quater wave plate and its thickness is given by:

$$\mathrm{e} = \lambda \frac{4\mathrm{k}+1}{4(\mathrm{n_e} - \mathrm{n_o})} . \tag{3.7}$$

Equation (3.6) represents the Jones matrix of a perfect plate [115] and does not take into account the following effects:

- the gaussian character of the light beam [116],
- the internal multiple reflections inside the plate [116],
- the geometric imperfections of the plate (thickness, misalignments),
- the tilt of the plate in case the incidence is not normal.
- the crystal optical activity [117].

Some of these effects may have non negligible consequences on the polarisation measurements with the ellipsometer. A precise characterisation of the quater wave plate with a more complete model is therefore necessary if we want to keep a good measurement precision of the light polarisation in the cavity. This characterisation will be covered in Section 4.

Chapter 4

The quater wave plate characterisation

To reach the per mill level in the measurement precision of the light polarisation, we have to calculate the transmission of a wave through a quater wave quartz plate. The characteristics of a multi-layers anti-reflective coating is difficult to model and the uncertainty in the accuracy of the modelisation is larger than those obtained with an uncoated plate. We have therefore decided to use an uncoated plate. The aim is to determine the plate characteristics such as the thickness (which is not necessarily equal at a few micrometers close to the thickness given by the manufacturer), the refraction indices (to be compared to the textbook values), as well as some possible plate misalignment parameters. We will see for instance that an error of a few micrometers on the plate thickness leads to an error of a few per mill on the light polarisation measurement.

4.1 The simulation model

The model used for the simulation has to take into account the multiple reflections of the wave inside a plate of a given thickness, as well as some possible plate misalignments relatively to the other optical components. The simulation also has to model the passage of the wave at a non zero incident angle since data will be recorded in such a configuration to characterise our plate. The light beam will be treated as a plane wave since at small incident angle (*i.e.* less than 0.1 rad as it will be the case for us), the comparison between a plane wave treatment and a gaussian wave treatment shows that the gaussian character of the wave can be neglected [116]. Also, the effect of the optical activity of the crystal [117] has been studied and found to be negligible (less than 10^{-6}). Intensities measured by the photodiodes after the Wollaston prism will be simulated in this model and the comparison of the theoretical intensities with the experimental ones will allow effects due to optical misalignments to be separated from effects due to thickness plate defects or effects due to the value of the light polarisation state.

By using the Jones matrices of the different ellipsometer components, the expression of the transmitted field can be determined as a function of one of the initial field. The calculation of the field transmitted by a quartz quater wave plate of a given thickness is detailed in Appendix A, where a non zero incident angle and the presence of multiple reflections inside the anisotropic uniaxial crystal are taken into account.

4.1.1 Ellipsometer transmission matrix

The framework of our calculations is the basis $B_{lab} = (\mathbf{x}_{lab}, \mathbf{y}_{lab}, \mathbf{z}_{lab})$ associated to the Wollaston prism axes: the x and y axes are the optical axes of the Wollaston cube and the basis is orthonormal. In this basis, the two rotating axes of the ellipsometer quater wave plate are the z_{lab} axis (corresponding to an azimuthal rotation of the plate by an angle ϕ) and the x_{lab} axis (corresponding to a non zero incident angle of the light in the quater wave plate, this rotation around x_{lab} rather than around y_{lab} has been arbitrarily chosen). As schematized in Figure 4.1, a wave of wave vector $\mathbf{k_{in}}$ can enter the crystal surface of normal $\mathbf{n}$ with a small incident angle θ_{inc} defined as:

$$\cos\theta_{inc} = (\mathbf{k_{in}} \cdot \mathbf{n})/|\mathbf{k_{in}}| \quad .$$

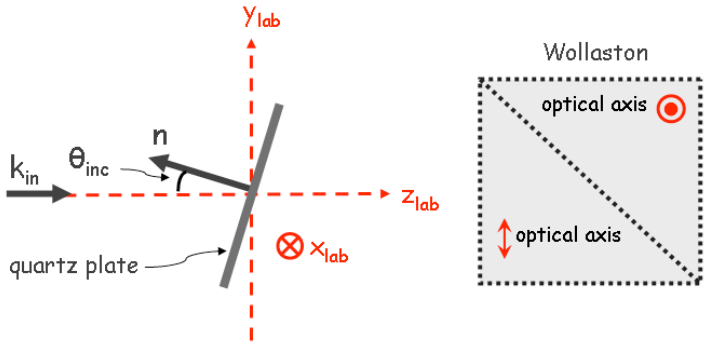

Figure 4.1: Laboratory reference axes $(x_{lab}, y_{lab}, z_{lab})$. $\mathbf{n}$ is the normal to the plate, $\mathbf{k_{in}}$ is the wave vector and θ_{inc} is the angle of incidence of the wave on the plate.

In Appendix A, the calculation of the transmitted wave amplitude passing through a quartz plate is performed. The expression of the transmission matrix of the quater wave plate, called $\mathcal{M}_{qwp}$, is given by the expression (A.33) of Appendix A and is expressed in an orthonormal basis $(\mathbf{s}, \mathbf{p}, \mathbf{k_{in}})$ attached to the crystal plate and to the incident wave such as:

$$\mathbf{s} = \frac{-\mathbf{k_{in}} \times \mathbf{n}}{|-\mathbf{k_{in}} \times \mathbf{n}|} \quad \text{and} \quad \mathbf{p} = \frac{\mathbf{k_{in}} \times \mathbf{s}}{|\mathbf{k_{in}}|} \quad . \tag{4.1}$$

In Figure 4.1, the plate is perfectly aligned and the two bases $(\mathbf{x}_{lab}, \mathbf{y}_{lab}, \mathbf{z}_{lab})$ and $(\mathbf{s}, \mathbf{p}, \mathbf{k_{in}})$ are merged.

A realistic description of the optical system must take into account some experimental misalignments. Two types of misalignment are considered: a misalignment of the quater wave plate plane with respect to the Wollaston prism axes, and a misalignment due to the fact that the laser beam may not enter the quartz exactly at the centre of the rotating mount of the plate.

- **Quater wave plate plane misalignment :**

  When the plate is perfectly aligned, the normal $\mathbf{n}$ to the plate for a small incident angle θ_{inc} is written in the basis B_{lab} as:

$$\mathbf{n} = \frac{1}{\sqrt{1+\theta_{\rm inc}^2}} \begin{pmatrix} 0 \\ \theta_{\rm inc} \\ -1 \end{pmatrix}_{\rm B_{lab}} . \tag{4.2}$$

A small misalignment of the plane plate can be modeled by a small rotation of $\mathbf{n}$ around the y axis of an angle $\delta_{\rm x}$, as schematized in Figure 4.2. The normal to the plate $\mathbf{n_{desal}}$ then acquires a small component along x and is written in the basis $\rm B_{lab}$ as:

$$\mathbf{n_{desal}} = \frac{1}{\sqrt{1+\theta_{\rm inc}^2}} \begin{pmatrix} \dfrac{\delta_{\rm x}}{\sqrt{1+\delta_{\rm x}^2}} \\ \theta_{\rm inc} \\ -\dfrac{1}{\sqrt{1+\delta_{\rm x}^2}} \end{pmatrix}_{\rm B_{lab}} . \tag{4.3}$$

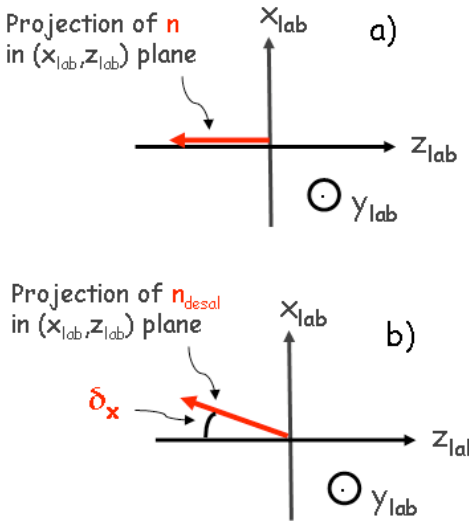

Figure 4.2: Projection of the normal to the quater wave plate in the $(\rm x_{lab}, z_{lab})$ plane: perfect alignment of the plane of the plate with respect to Wollaston axes (a), and misalignment of the plane plate coming from a small tilt $\delta_{\rm x}$ of the plate plane around the $\rm y_{lab}$ axis (b).

The transfer matrix $\rm M_{lab\to desal}$ between the base $\rm B_{lab}$ and the new $(\mathbf{s}, \mathbf{p}, \mathbf{k_{in}})$ basis attached to the misaligned crystal plate can be determined from the relations (4.1) and, assuming $\delta_{\rm x}^2 \ll 1$, is written as:

$$\rm M_{lab\to desal} = \begin{pmatrix} \dfrac{\theta_{\rm inc}}{\sqrt{\theta_{\rm inc}^2+\delta_{\rm x}^2}} & \dfrac{-\delta_{\rm x}}{\sqrt{\theta_{\rm inc}^2+\delta_{\rm x}^2}} & 0 \\ \dfrac{\delta_{\rm x}}{\sqrt{\theta_{\rm inc}^2+\delta_{\rm x}^2}} & \dfrac{\theta_{\rm inc}}{\sqrt{\theta_{\rm inc}^2+\delta_{\rm x}^2}} & 0 \\ 0 & 0 & 1 \end{pmatrix} . \tag{4.4}$$

- **Misalignment of the quater wave plate mechanical centre**

  If the laser beam does not enter at the centre of the plate mount, because the two sides of the plate may not be perfectly parallel, the thickness crossed by the light can vary during the azimuthal rotation of the plate. To take into account this effect, this misalignment is modeled with two parameters d_{cm} and ϕ_{cm} and the plate thickness is written as:

$$e = e_0 \left(1 + \frac{d_{cm}}{e_0} \cos(\phi - \phi_{cm}) \right) \quad . \tag{4.5}$$

  e_0 is the plate thickness at the level of the azimuthal rotation axis and ϕ is the plate azimuthal angle in the laboratory framework. ϕ_{cm} is an arbitrary angle to be determined and translating the fact that the azimuthal position $\phi = 0$ is not a priori the position which maximizes the plate thickness. Such a misalignment is schematized in Figure 4.3.

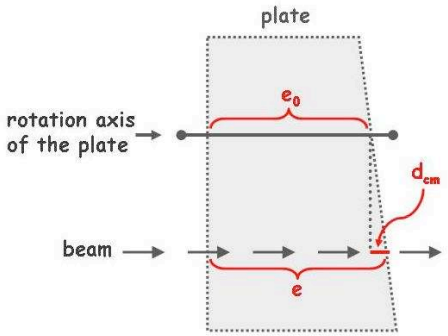

Figure 4.3: Schematic view of a misalignment between the quater wave plate mechanical centre and the impact point of the laser beam.

We now want to find the expression of the field transmitted by the ellipsometer. In the $(\mathbf{x}_{lab}, \mathbf{y}_{lab}, \mathbf{z}_{lab})$ basis of the laboratory, which is our reference, the most general elliptical initial polarisation state $\mathbf{E}^{in}$ is written as function of two angles (see (3.3)) as:

$$\mathbf{E}^{in} = \begin{pmatrix} \cos\chi_P \\ \sin\chi_P \, e^{i\phi_P} \end{pmatrix} . \tag{4.6}$$

By using the transfer matrix $M_{lab\to desal}$ defined in expression (4.4), the thickness plate formula (4.5) and the two transmitted Wollaston matrices M^{Wx} and M^{Wy} defined in (3.5), the two transmitted fields $\mathbf{E}_1$ and $\mathbf{E}_2$ emerging from the Wollaston prism can be written as:

$$\begin{aligned} \mathbf{E}_1 &= M_{lab\to desal} \, M^{Wx} \, M^{-1}_{lab\to desal} \, \mathcal{M}_{qwp} \, M_{lab\to desal} \, \mathbf{E}^{in} \quad , \\ \mathbf{E}_2 &= M_{lab\to desal} \, M^{Wy} \, M^{-1}_{lab\to desal} \, \mathcal{M}_{qwp} \, M_{lab\to desal} \, \mathbf{E}^{in} \quad , \end{aligned} \tag{4.7}$$

and the intensities I_1 and I_2 received in the photodiodes pd_1 and pd_2 are written as a function of the fields as[1]. :

$$I_1 = |\mathbf{E}_1|^2 \quad , \quad I_2 = |\mathbf{E}_2|^2 \quad . \tag{4.8}$$

Formula (4.8) will be used in the following to simulate signals emerging from the Wollaston prism and detected in the photodiodes.

[1] I_1 and I_2 refer in fact to ratios I_1/I_0 and I_2/I_0 (see Section 3.3.2 and Figure 3.1) but for more clarity, the writting of reference signal I_0 will be omitted.

4.1.2 Some comparisons between the complete and the simple models

To estimate quantitatively the effects of the model described above, some examples have been chosen and the intensities have been simulated and compared using the complete model and a model which does not include internal multiple reflections or possible misalignments of the plate.

Internal multiple reflections inside the plate

To illustrate the effect of the multiple reflections calculated in Appendix A, Figures 4.4, 4.5 and 4.6 show some simulated intensities I_1 and I_2 of a wave transmitted by the ellipsometer as a function of the azimuthal angle of the quater wave plate. In Figure 4.4, the incident wave has been simulated with a linear polarisation, in Figures 4.5 and 4.6 with a circular and elliptical polarisation respectively. For each plot, two simulations have been used: one using a simple model without taking into account internal multiple reflections and one using the complete model of Appendix A. In these simulations, the Wollaston prism is considered as perfect, the quater wave plate is perfectly aligned and the incidence is normal. These simulations show that there are differences of more than 15% in the transmitted intensities according to the model used for the simulation and that it is therefore very important to use a realistic model.

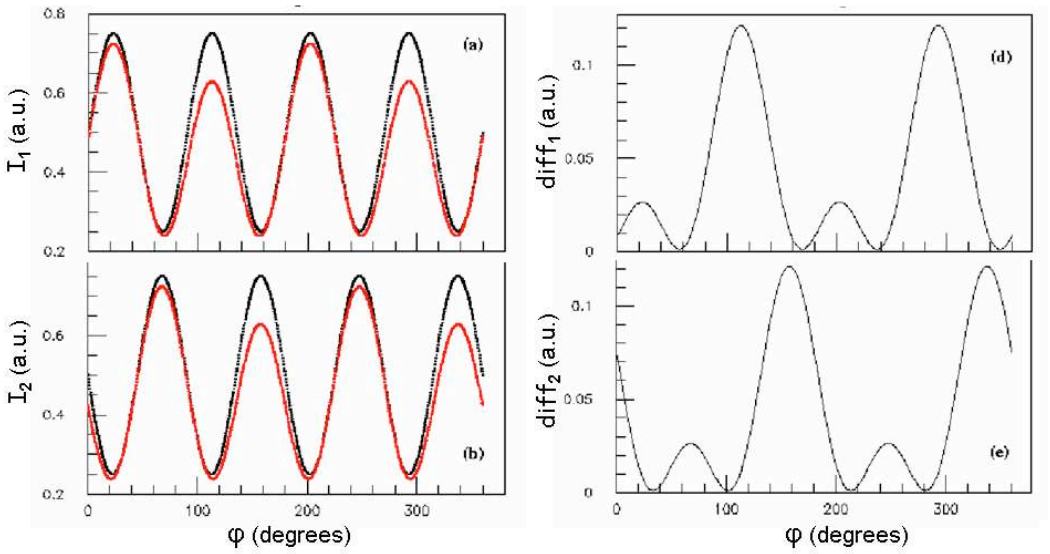

Figure 4.4: (a) and (b): signals I_1 and I_2 normalised to the unity and generated with a linear incident polarisation, versus the azimuthal quater wave plate angle. Black (respectively red) curves: simulation without (respectively with) taking into account internal multiple reflections. (d) and (e): differences of the two models for I_1 and I_2 versus ϕ.

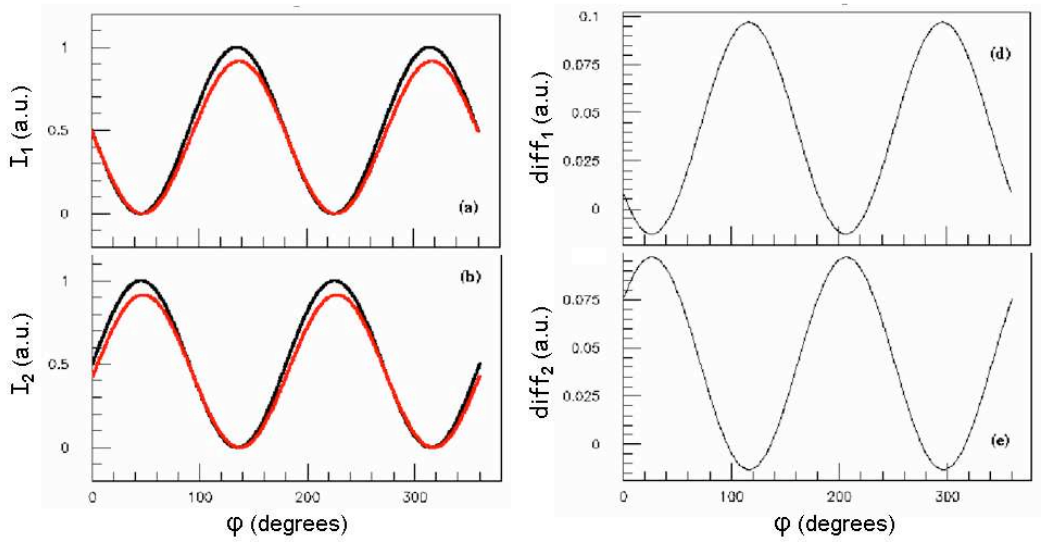

Figure 4.5: (a) and (b): signals I_1 and I_2 normalised to the unity and generated with a circular incident polarisation, versus the azimuthal quater wave plate angle. Black (respectively red) curves: simulation without (respectively with) taking into account internal multiple reflections. (d) and (e): differences of the two models for I_1 and I_2 versus ϕ.

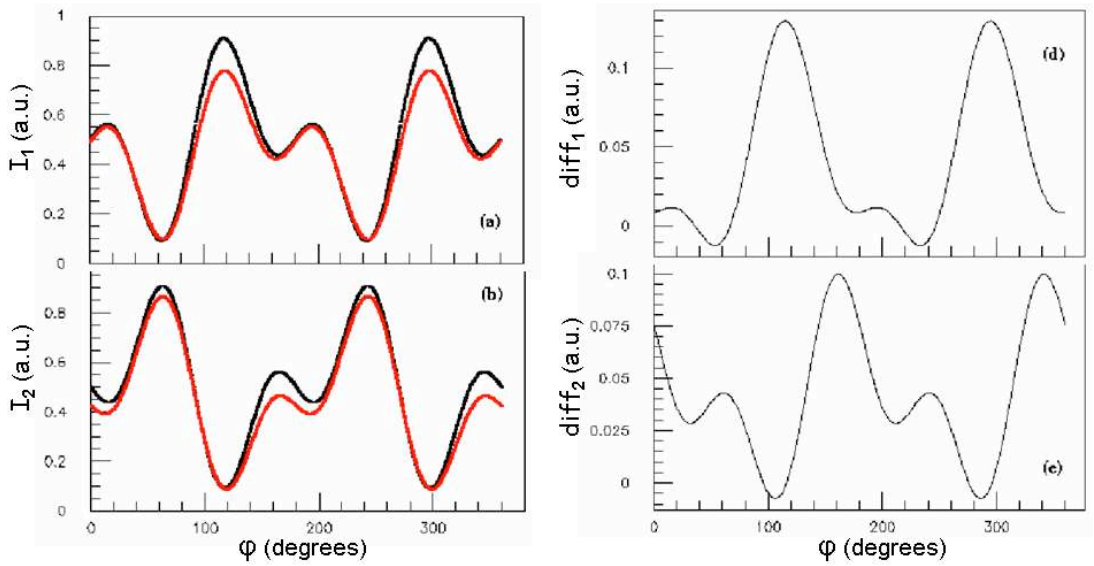

Figure 4.6: (a) and (b): signals I_1 and I_2 normalised to the unity and generated with a elliptical incident polarisation (with $\chi_P = 45^o$ and $\phi_P = 30^o$, see formula (4.6)), versus the azimuthal quater wave plate angle. Black (respectively red) curves: simulation without (respectively with) taking into account internal multiple reflections. (d) and (e): differences of the two models for I_1 and I_2 versus ϕ.

Misalignment of the quater wave plate plane

To estimate the effect of a misalignment of the quater wave plate with respect to the Wollaston axis, some intensities have been simulated with the complete model and at the four following different alignment parameters:

θ_{inc}	2.246°	2.246°	4.211°	4.211°
δ_x	0	$5{\cdot}10^{-4}$	0	$5{\cdot}10^{-4}$

where θ_{inc} is the angle of incidence of the plate and δ_x is the misalignment parameter schematized in Figure 4.2 and defined in equation (4.3). Figure 4.7 shows the quantity $\Delta I_2 = [\, I_{2(\delta_x=0)} - I_{2(\delta_x=5{\cdot}10^{-4})} \,] \,/\, I_{2(\delta_x=0)}$ for the two different angles of incidence. A plane tilt δ_x of 0.5 mrad leads to a bias ΔI_2 of 1% to 2%[2].

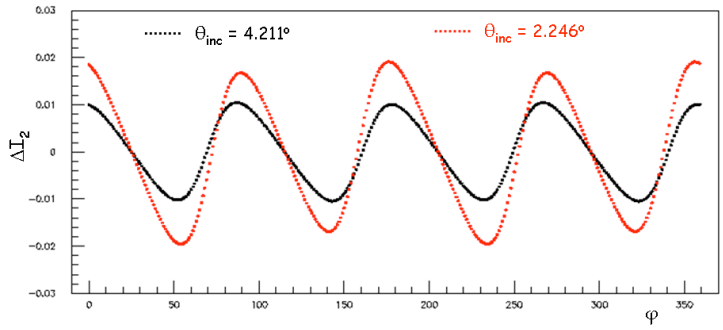

Figure 4.7: $\Delta I_2 = [\, I_{2(\delta_x=0)} - I_{2(\delta_x=5{\cdot}10^{-4})} \,] \,/\, I_{2(\delta_x=0)}$ as a function of the quater wave plate azimuthal angle ϕ (in degrees), for $\theta_{inc} = 4.211°$ in black and $\theta_{inc} = 2.245°$ in red.

Misalignment of the quater wave plate mechanical centre

The effect of such a misalignment is illustrated in Figure 4.8. This figure shows the difference between the generated intensity I_2 in the case of a perfect alignment of the plate mechanical centre with respect to the laser beam impact, and the intensity I_2 in the case of a small misalignment as defined in equation (4.5). A misalignment parameter d_{cm} =0.05 μm has been chosen for these simulations, which for instance corresponds to a non parallelism of the plate sides of 1 mrad and a misalignment of the centre of the plate of 0.5 mm. The angle ϕ_{cm} has been simulated at 20° for the black curve and at 340° for the red curve. Figure 4.8 shows that the effect of such a misalignment may be of several per mill on the intensities received by the photodiodes.

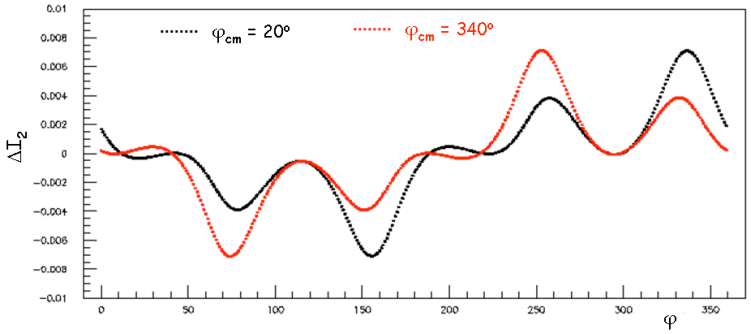

Figure 4.8: $\Delta I_2 = [\, I_{2(d_{cm}=0)} - I_{2(d_{cm}=0.05\ \mu m\ ,\ \phi_{cm})} \,] \,/\, I_{2(d_{cm}=0)}$ for $\phi_{cm} = 20°$ in black and $\phi_{cm} = 340°$ in red, as a function of the quater wave plate azimuthal angle ϕ (in degrees).

[2]The quantity ΔI_2 is a function of $\delta_x^2/\theta_{inc}^2$ that explains its larger value for smaller θ_{inc} as shown in Figure 4.7.

These examples of simulation show that taking into account all the characteristics of the system such as the quater wave plate characteristics or the optical component misalignments is necessary to model the intensities transmitted by the ellipsometer with a precision of a few per mill. With this model it is now possible to determine precisely the experimental parameters involved in the light polarisation measurement.

4.2 Principle of parameter determination

4.2.1 Experimental setup and data taking procedure

The ellipsometer used for the determination of the quater wave plate parameters is the one in Figure 3.1. For this purpose, what is called "beam to be analysed" is a 100 mW power infrared beam delivered by a high quality ND:YAG laser [113] passing first through a beam shutter and then through a high quality Glan-Thomson prism to provide a purely linear polarisation (the extinction ratio of the Glan-Thomson prism given by the manufacturer is around 10^{-5} [118]). The beam then passes into the ellipsometer to be analysed. Before mounting the HBS and the quater wave plate in the ellipsometer, the Glan-Thomson prism and the Wollaston prism have been azimuthally aligned by minimising one of the intensities measured after the Wollaston and maximising the other. In that way, one of the Wollaston axes is along the beam polarisation direction. This pre-alignment is useful to know that the value of the polarisation angle χ_P of the incident wave (defined in (4.6)) is near 0^o or 90^o.

As shown in Figure 4.9, data are then taken in the following way: for various azimuth orientations of the quater wave plate optical axis (*i.e.* for various rotations around its normal axis of an angle ϕ) and for various angles of incidence (*i.e.* for various rotations of the plate around the x axis of an angle θ_{inc}), signals sig_0, sig_1 and sig_2 are measured in the photodiodes pd_0, pd_1 and pd_2 and the ratios $\text{sig}_1/\text{sig}_0$ and $\text{sig}_2/\text{sig}_0$ (called I_1 and I_2 respectively) are computed as described in Section 3.3.2. In order to adjust the various angles of incidence θ_{inc} and azimuthal angles ϕ, the quater wave plate is mounted on a mirror mount fixed at the centre of a motorised rotating stage. The rotating stage is itself mounted on two linear stages (vertical and horizontal) and on a two angle tilting stage. The linear and tilting stages are manually controlled with micro-metric screws (see Figure 2.27).

We will see in the following that to avoid degeneracy in the determination of the quater wave plate parameters, we must use two different quartz plates of different thicknesses. These plates, manufactured by FICHOU Company, have the following characteristics:

- pl_1 is a plate of order 1/2 (k=1/2 in expression (3.7)), of thickness $\text{e}_1^{\text{nom}} = 91.2\ \mu\text{m}$ with a delay tolerance of 1/300. According to the manufacturer, the parallelism between the two faces of the plate is of the order of 10 seconds of arc. Once calibrated, this plate is the one which is used for the measurement of the light polarisation during the lepton-laser interactions at HERA.

- pl_2 is a plate of order 5 and of thickness $\text{e}_2^{\text{nom}} = 639.9\ \mu\text{m}$, which is used only for the calibration procedure of the plate pl_1.

Each plate is mounted one after the other in the ellipsometer and, for each one, the number of θ_{inc} tilts per plate is called N_k (N_1 tilts for the plate pl_1 and N_2 tilts for the plate pl_2). For one given θ_{inc}, each plate is azimuthally rotated through one full turn (360^o) in steps of 1^o.

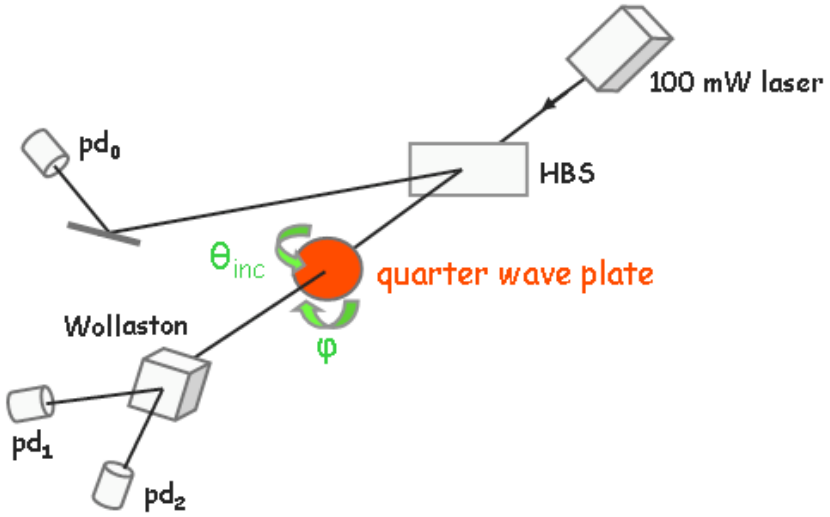

Figure 4.9: Schematic drawing of the ellipsometer used to calibrate the quater wave plate. The plate is rotated azumuthally of an angle ϕ, and the laser beam enters the plate with an angle of incidence θ_{inc}.

4.2.2 The χ^2

Using all sets of data, the minimisation of a χ^2 is performed to determine the characteristic parameters of the quater wave plate as well as the initial state polarisation. Explicitly, the expression of the χ^2 is:

$$\chi^2 = \chi^2_{pl_1} + \chi^2_{pl_2} \quad , \tag{4.9}$$

where χ_{pl_1} and χ_{pl_2} are the χ^2 of each plate, *i.e.*:

$$\chi^2_{pl_k} = \sum_{j=1,N_k} \sum_{i=1,360} \left[\left(\frac{R^j_{1,k}\, T^{ij}_{1,k} - I^{ij}_{1,k}}{\sigma^{ij}_{1,k}} \right)^2 + \left(\frac{R^j_{2,k}\, T^{ij}_{2,k} - I^{ij}_{2,k}}{\sigma^{ij}_{2,k}} \right)^2 \right] \quad . \tag{4.10}$$

- $T^{ij}_{1,k}$ and $T^{ij}_{2,k}$ are the theoretical intensities I_1 and I_2 calculated at the i^{th} value of ϕ and the j^{th} value of θ_{inc} for the plate pl_k.
- $I^{ij}_{1,k}$ and $I^{ij}_{1,k}$ are the intensities I_1 and I_2 measured in the photodiodes at the i^{th} value of ϕ and the j^{th} value of θ_{inc} for the plate pl_k.

- $\sigma^{ij}_{1,k}$ and $\sigma^{ij}_{2,k}$ are the uncertainties associated to the measured intensities I_1 and I_2 respectively.

- $R^j_{1,k}$ and $R^j_{2,k}$ are two normalisation factors which are easily determined since the solve of $\partial\chi^2/\partial R = 0$ leads to analytic expressions for R.

The two theoretical intensities $T^{ij}_{1,k}$ and $T^{ij}_{2,k}$ are some functions of parameters to be determined with the minimisation, and are written as:

$$T^{ij}_{(1,2)1}(\Delta n_o, \theta_{turn}, \chi_P, \phi_P, \epsilon_x, \Delta e_1, \phi_{0_1}, \delta_{x_1}, \phi_{cm_1}, d_{cm_j}) \quad ,$$

$$T^{il}_{(1,2)2}(\Delta n_o, \theta_{turn}, \chi_P, \phi_P, \epsilon_x, \Delta e_2, \phi_{0_2}, \delta_{x_2}, \phi_{cm_2}, d_{cm_l}) \quad ,$$

where $j = 1, N_1$ and $l = N_1 + 1, N_1 + N_2$. The meaning of these parameters is as follows:

- Δn_o measures the difference between the fitted ordinary index n_o and the textbook one N_o and is defined by:

  $$n_o = N_o(1 + \Delta n_o) \ .$$

  Because the constraints are not sufficient to fit the two quartz indices n_o and n_e at the same time, the extraordinary index n_e stays fixed (the quantity which is in fact determined by the fit is the birefringence $n_e - n_o$). The quartz indices being already determined at a few 10^{-5} level by previous studies [119, 120, 121], the fit of n_o will provide a good test of the validity of our model. The values of N_o and N_e which will be used in the fit are extrapolated from the measurements of [119] and [120] at room temperature (18°). Figure 4.10 shows these measurements in the infra-red region and the straight line fit which leads to $N_e = 1.542866$ and $N_o = 1.534129$ at our wavelength $\lambda = 1064$ nm.

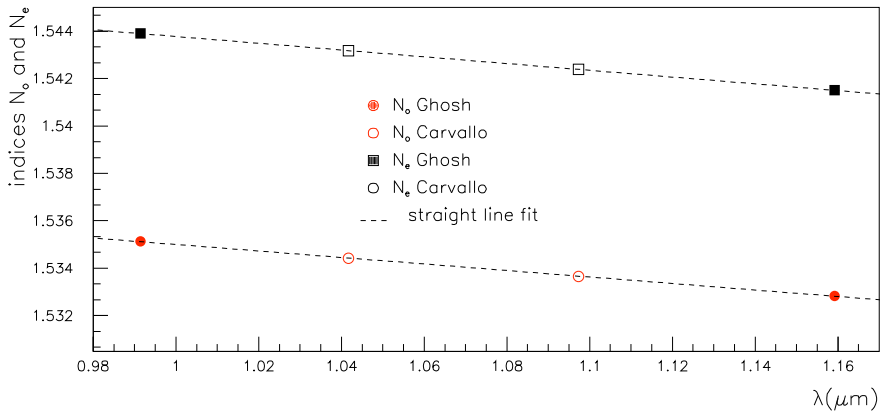

Figure 4.10: Quartz ordinary and extraordinary indices at room temperature as a function of the wavelength from the references [119] and [120]. The dashed line is a simple fit with a straight line. The index values extrapolated at $\lambda = 1.064$ μm are $N_e = 1.54286$ and $N_o = 1.53412$.

- θ_{turn} is the angle corresponding to one turn of the rotating stage screw around the x axis (this rotation allows the plate to be rotated to have a non zero incident angle). One turn contains 50 divisions and the corresponding angle value given by the manufacturer [122] is around 20 arcsec per division with an unknown uncertainty. This parameter has therefore to be fitted. θ_{inc} being the angle of incidence when the plane of the plate is well aligned with respect to the Wollaston prism axes, we have:

$$\theta_{\text{inc}} = \theta_{\text{turn}} \times \text{N}_{\text{turn}} \quad , \tag{4.11}$$

  where N_{turn} is the number of screw turns done to generate the incidence angle θ_{inc}. Taking into account some misalignement of the plate plane, the expression of the real incident angle θ, defined as function of the normal to the plate $\mathbf{n_{desal}}$ and the initial wave vector $\mathbf{k_{in}}$, is determined from equations (4.3) and (4.11) and is written as:

$$\cos\theta = -\frac{\mathbf{k_{in}} \cdot \mathbf{n_{desal}}}{|\mathbf{k_{in}}|} = \frac{1}{\sqrt{1 + (\theta_{\text{turn}} \times \text{N}_{\text{turn}})^2}\sqrt{1 + \delta_{\text{x}}^2}} \quad .$$

- χ_{P} and ϕ_{P} are the two angles defined in equation (4.6) characterising the initial polarisation state of the wave.

- ϵ_{x} is the Wollaston prism ellipticity parameter defined in equation (3.5). Because we have chosen to rotate the plate around the x axis to generate a non zero incident angle, the χ^2 is only sensitive to the parameter ϵ_{x} and not to the parameter ϵ_{y}.

- Δe_1 and Δe_2 are the thickness variations of the quater wave plates with respect to the manufacturer values $\text{e}_1^{\text{nom}} = 91.2$ μm and $\text{e}_2^{\text{nom}} = 639.9$ μm.

- ϕ_{0_1} and ϕ_{0_2} are two azimuthal reference angles translating the fact that the azymuthal orientations of the optical axes in the planes of the plates are not a priori at the position $\phi = 0$.

- δ_{x_1} and δ_{x_2} are the misalignment parameters of the first and second quater wave plate respectively which have been defined in equation (4.3).

- ϕ_{cm_1} and ϕ_{cm_2} are the angles defined in equation (4.5) for the first and the second quater wave plate respectively.

- $\text{d}_{\text{cm}_\text{j}}$ and $\text{d}_{\text{cm}_\text{l}}$ (where $\text{j} = 1, \text{N}_1$ and $\text{l} = \text{N}_1 + 1, \text{N}_1 + \text{N}_2$ are the misalignment parameters defined in equation (4.5). Each $\text{d}_{\text{cm}_\text{j}}$ (respectively $\text{d}_{\text{cm}_\text{l}}$) corresponds to a misalignment in a given incident angle configuration of the plate pl_1 (respectively pl_2).

4.2.3 Data samples

To characterise our optical system and particulary the quater wave plate used to measure the polarisation of the light, the following sets of data have been recorded:

- four data sets called D_1, D_2, D_3, D_4 where the thiner plate was used and the incident angle θ_{inc} was equal to 0.55°, 2.20°, 3.30° and 4.125° respectively. These angles of incidence corresponded to $\text{N}_{\text{turn}} = 2$, 8, 12, 15 respectively.

- two data sets called D_5, D_6 where the thicker plate was used and $\theta_{inc} = 0.55^o,\ 3.30^o$ respectively (corresponding to $N_{turn} = 2,\ 12$ respectively).

A 360^o azimuthal turn is done for each one of the six D_i files. Twenty measurements are recorded at each of these 360 azimuthal positions in order to have higher precision on each measurement and a better estimation of experimental errors. Figure 4.11 shows the experimental measured intensities I_1 and I_2 as a function of the azimuthal angle ϕ, for the six data samples D_i.

To be able to check the minimisation procedure, a set of six Monte Carlo samples have been simulated with formula (4.8) and with parameter values of Table 4.1.

Δe_1 (μm)	0.6700	θ_{turn} (rad)	4.90×10^{-3}
Δe_2 (μm)	0.5700	d_{cm_1} (nm)	30.00
ϕ_{0_1} (deg)	115.00	d_{cm_2} (nm)	15.00
ϕ_{0_2} (deg)	158.00	d_{cm_3} (nm)	-15.00
δ_{x_1}	5.0×10^{-4}	d_{cm_4} (nm)	65.00
δ_{x_2}	-3.0×10^{-4}	d_{cm_5} (nm)	20.00
Δn_o	-3.0×10^{-6}	d_{cm_6} (nm)	-40.00
χ_P (deg)	89.50	ϕ_{cm_1} (deg)	-98.00
ϕ_P (deg)	10.00	ϕ_{cm_2} (deg)	-4.00
ϵ_x	-6.0×10^{-4}		

Table 4.1: Parameters used in the simulation of the six D_i data sets.

Generated uncertainties have to be simulated as near as possible to experimental ones and for this, we have first to estimate the uncertainties of the data measurements and, once determined, use them to generate our Monte Carlo samples. Let us estimate the experimental errors of our measurements: to take into account some long term effect (of about one minute) due to possible temperature drift or any other unknown cause, the error associated to the j^{th} measurement has been taken as the dispersion of the set of the twenty measurements. These dispersions, called $\sigma_{I^j_{1,2}}$ have then been parametrised by a straight line fit as:

$$\sigma_{I^j_{1,2}} = A_{1,2}\ I^j_{1,2} + B_{1,2}\ \ , \tag{4.12}$$

where subscripts 1 and 2 refer to intensities I_1 and I_2 respectively, and the superscript j to the j^{th} measurement. The straight line fits of the six data samples lead to the parameters $A_{1,2}$ and $B_{1,2}$ of Table 4.2.

	D_1	D_2	D_3	D_4	D_5	D_6
A_1	0.00965	0.00769	0.00793	0.00719	0.0268	0.0291
B_1	0.00037	0.00208	0.00195	0.0010	-0.0218	0.0184
A_2	0.00662	0.00666	0.00701	0.00633	0.0198	0.0252
B_2	0.00197	-0.00267	-0.01131	0.00083	0.0670	-0.0226

Table 4.2: Parameters $A_{1,2}$ and $B_{1,2}$ coming from the adjustments (4.12).

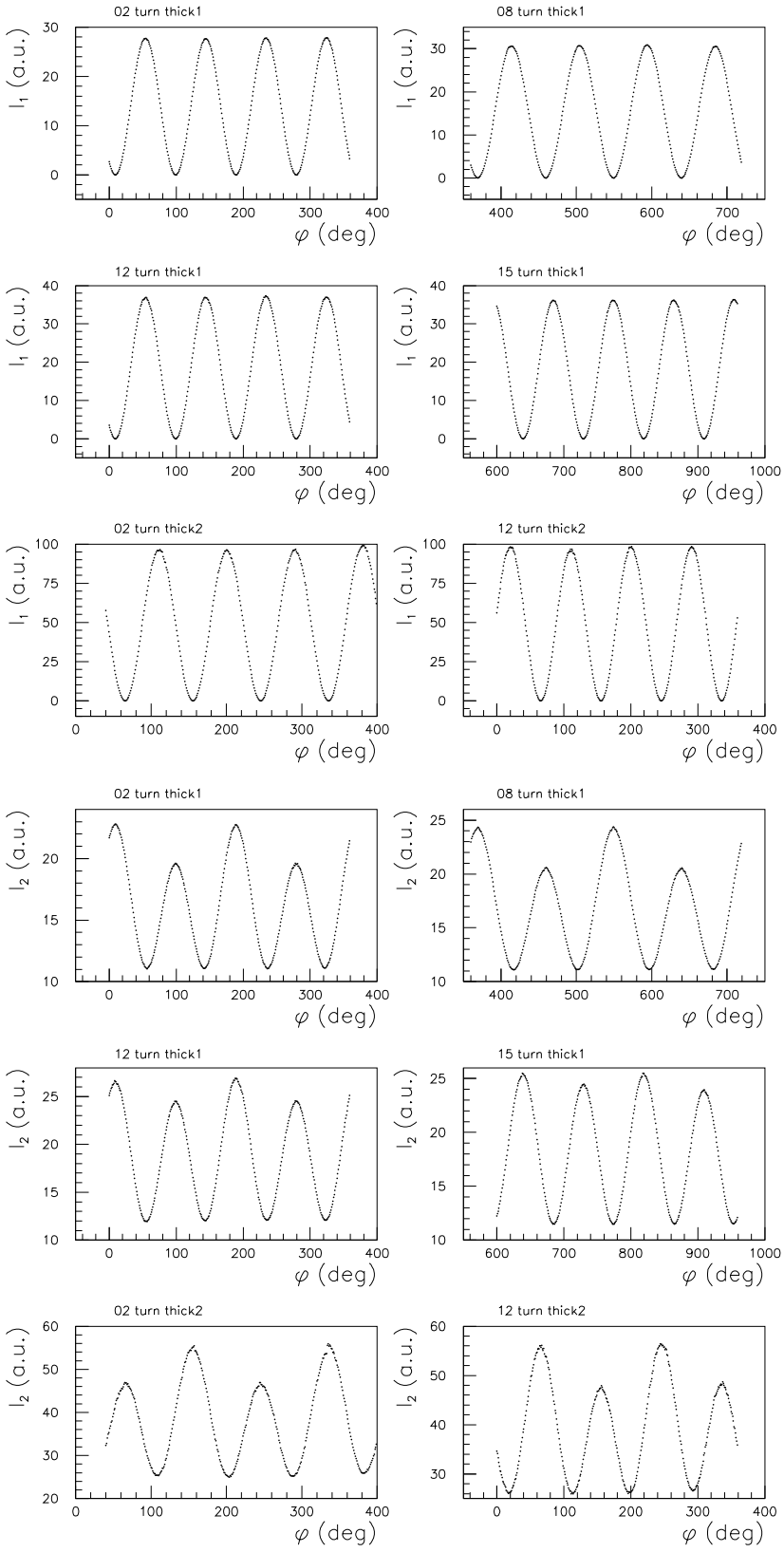

Figure 4.11: Experimental intensities I_1 and I_2 measured in the photodiodes pd_1 and pd_2 as a function of the plate azimuthal angle ϕ and at different angles of incidence and with the two plates pl_1 and pl_2 (called here thick1 and thick2).

Then, for the six Monte Carlo files simulated with the parameters of Table 4.1, the errors of measurement are simulated using these simple parametrisations with the same $(A_{1,2}, B_{1,2})$ values as for the real data. Experimental and simulated errors on I_1 and I_2 intensities as function of intensities I_1 and I_2 are shown in Figures 4.12, 4.13, 4.14, 4.15, 4.16 and 4.17 for the six data samples D_1 to D_6. Experimental measurements are shown in plots (a) and (b) of these figures, simulated data in plots (c) and (d). Straight line fits coming from the parametrisation (4.12) are also visible on the six experimental data plots.

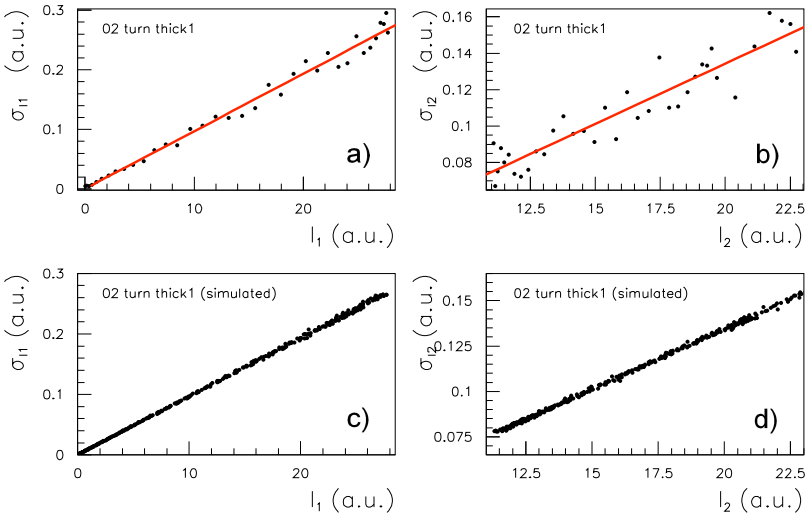

Figure 4.12: Errors σ_{I_1} (a) (respectively (c)) and σ_{I_2} (b) (respectively (d)) as a function of I_1 and I_2 for the data (respectively MC) sample D_1. The red straight line in the data plots is the result of the adjustment (4.12).

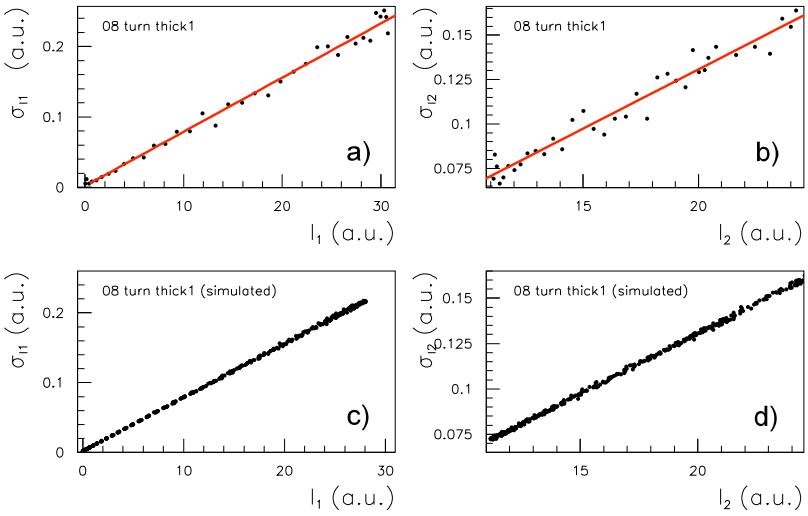

Figure 4.13: Errors σ_{I_1} (a) (respectively (c)) and σ_{I_2} (b) (respectively (d)) as a function of I_1 and I_2 for the data (respectively MC) sample D_2. The red straight line in the data plots is the result of the adjustment (4.12).

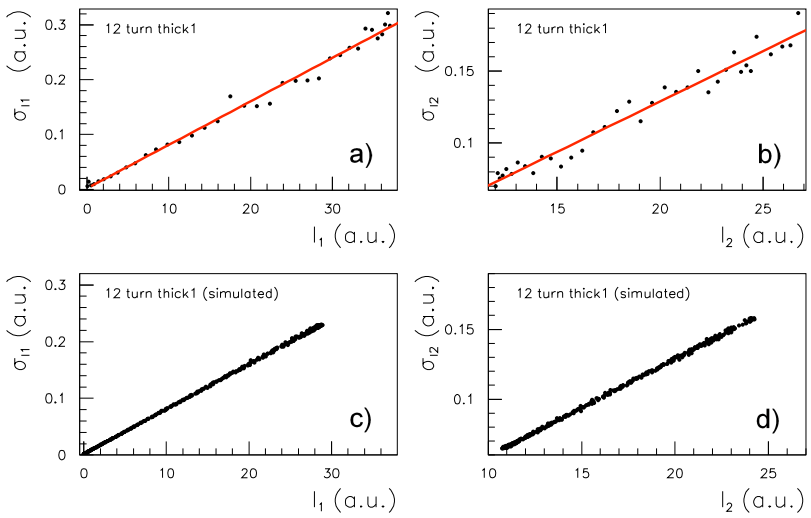

Figure 4.14: Errors σ_{I_1} (a) (respectively (c)) and σ_{I_2} (b) (respectively (d)) as a function of I_1 and I_2 for the data (respectively MC) sample D_3. The red straight line in the data plots is the result of the adjustment (4.12).

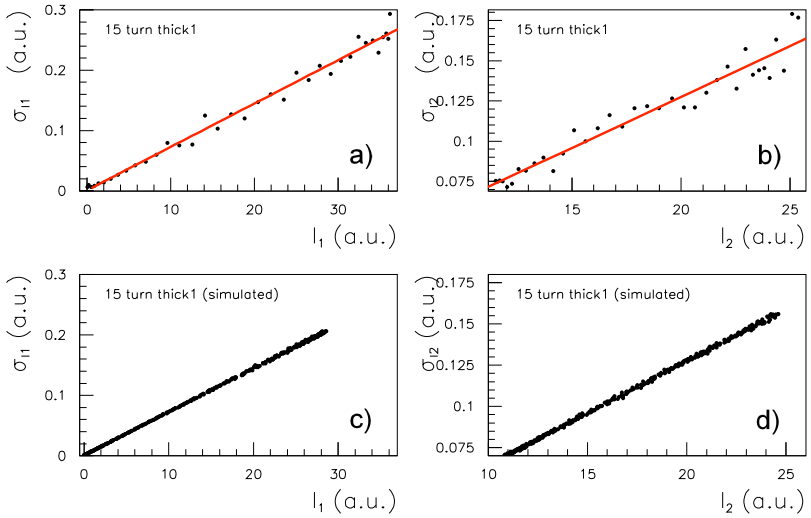

Figure 4.15: Errors σ_{I_1} (a) (respectively (c)) and σ_{I_2} (b) (respectively (d)) as a function of I_1 and I_2 for the data (respectively MC) sample D_4. The red straight line in the data plots is the result of the adjustment (4.12).

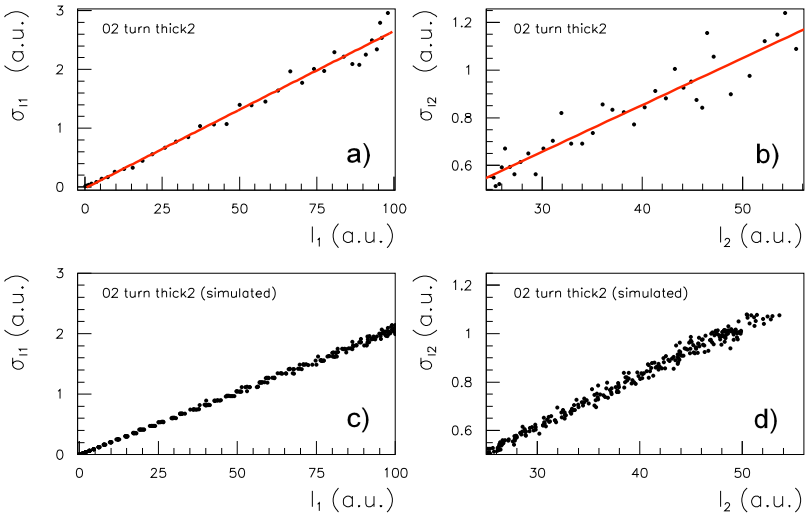

Figure 4.16: Errors σ_{I_1} (a) (respectively (c)) and σ_{I_2} (b) (respectively (d)) as a function of I_1 and I_2 for the data (respectively MC) sample D_5. The red straight line in the data plots is the result of the adjustment (4.12).

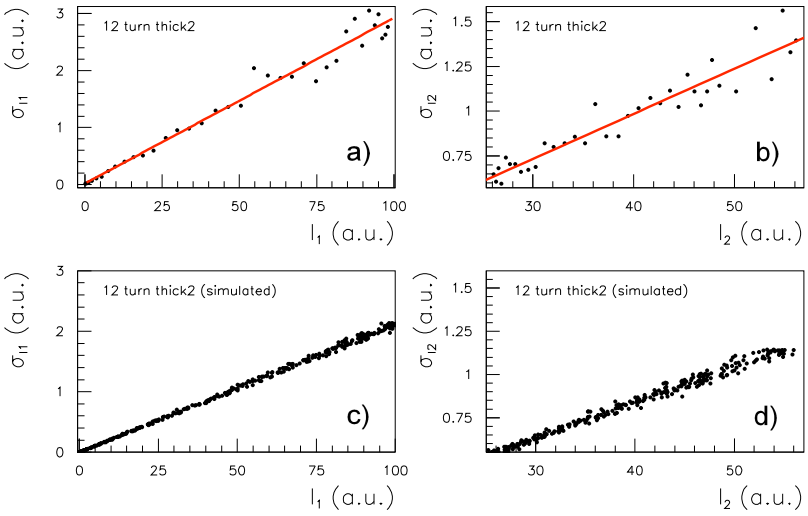

Figure 4.17: Errors σ_{I_1} (a) (respectively (c)) and σ_{I_2} (b) (respectively (d)) as a function of I_1 and I_2 for the data (respectively MC) sample D_6. The red straight line in the data plots is the result of the adjustment (4.12).

It is visible in these figures that measurements and errors of the six experimental data samples are similar to measurements and errors of the six Monte Carlo samples.

4.3 Preliminary Monte Carlo studies

4.3.1 Necessity of a second quater wave plate

As it is mentioned in Section 4.2 an additional quater wave plate is necessary to resolve the degeneracy in the determination of some parameters. To illustrate this point, Figure 4.18 shows the value of the χ^2 as function of the thickness variation Δe_1 and the index variation Δn_0, in two situations: plot a) shows the χ^2 calculated using the six simulated data samples D_1 to D_6 of Table 4.1[3] and plot b) shows the χ^2 calculated using only the four simulated data samples D_1 to D_4 of the plate pl_1. For this study, the simulated uncertainties were such that $\sigma/I = 0.5\%$ and were generated with a gaussian shape. To draw the $\chi^2(\Delta e_1, \Delta n_0)$ function, all other parameters (θ_{turn}, ϵ_x, Δe_2, ϕ_{0_1}, ϕ_{0_2}, δ_{x_1}, δ_{x_2}, ϕ_{cm_1}, ϕ_{cm_2} and d_{cm_i}) have been fixed to their generated value. Figure 4.18(b) shows that the determination of the true values of Δe_1 and Δn_0 is not possible when only the data of one plate are used. Indeed, several different pairs (Δe_1,Δn_0) minimise the χ^2 (on the plot, only 2 pairs are shown for clarity). In plot a) the degeneracy is resolved by the addition of the data samples of the second quater wave plate. We have checked that even by simulating more data sets (at other angles of incidence for instance) with typical uncertainties of 0.5%, the degeneracy cannot be resolved by using data set coming from only one plate.

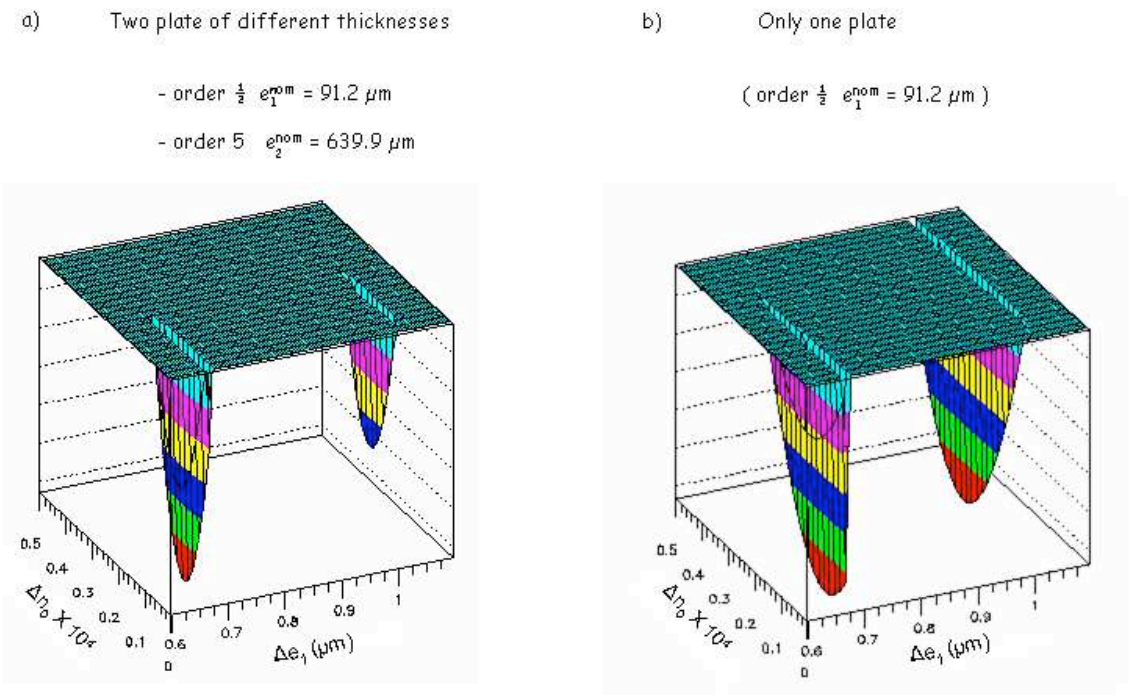

Figure 4.18: χ^2 as a function of the thickness variation Δe_1 of the plate pl_1 and as a function of the ordinary index variation $\Delta n_0 \times 10^4$. a): the χ^2 contains the generated data samples of the two plates pl_1 and pl_2. b): the χ^2 contains only the generated data samples of the plate pl_1.

[3]The generated value of the parameter Δn_o is 0.1×10^{-4} in this study, and not the value of Table 4.1.

This degeneracy is illustrated more quantitatively in Figure 4.19 where the χ^2 is plotted as a function of Δe_1 (a) and as a function of $\Delta n_0 \times 10^4$ (b) separately (all other parameters remaining fixed at their generated value). Here, only points corresponding to local minima have been drawn (between these minima, the χ^2 values are very large). Even by staying in physical ranges for Δe_1 (a few μm) and for $\Delta n_0 \times 10^4$ (a few 10^{-1}), the degeneracies are clearly visible.

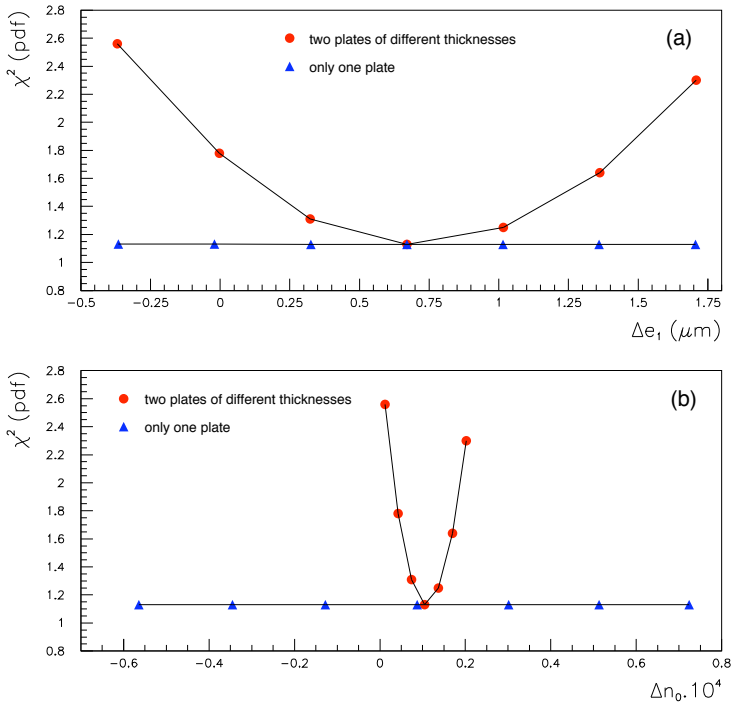

Figure 4.19: χ^2 per degree of freedom (pdf) as a function of the thickness variation Δe_1 of the plate pl_1 (a) and as a function of the ordinary index variation $\Delta n_0 \times 10^4$ (b). Red circle: the χ^2 contains the generated data samples of the two plates. Blue triangle: the χ^2 contains only the generated data samples of the plate pl_1.

4.3.2 Correlation between the thickness plate and the DOCP determination

Let us come back to the only important quantity involved in the lepton polarisation measurement: the Degree Of Circular Polarisation of the light (DOCP or S_γ) which appears directly in the Compton cross section formula (3.1). To estimate the effect of the quater wave plate thickness value on the determination of the DOCP, a data sample has been simulated with only one quater wave plate and using the complete model taking into account multiple reflections inside the quartz. The sample contains 360 points corresponding to one turn of the quater wave plate and has been generated with an arbitrary initial polarisation, an incident angle of 4^o and a plate thickness e_{gen}. By using this sample and the χ^2 previously defined, the DOCP has been adjusted by several fits by fixing for each fit the plate thickness to a value e slightly different from the simulated one and by fixing all the others parameters of the χ^2 to their generated value. The curve in Figure 4.20 shows the relative error on the DOCP determination as a function of the quantity $e - e_{gen}$. In

this figure, we can see that an ignorance of one micometer on the plate thickness leads to a systematic error of about 0.5% on the DOCP determination.

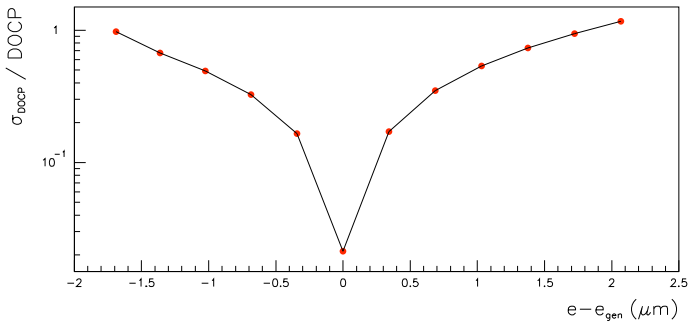

Figure 4.20: Relative error on the DOCP determination as a function of $e - e_{gen}$, e_{gen} being the generated plate thickness value.

Therefore it is necessary to determine the plate thickness very precisely to keep a systematic error at the per mill level on the measurement of the photon circular degree of polarisation. It is only possible to reach this per mill level by using the model described previously, including a correct treatment of the quartz medium properties and taking into account small misalignments in our optical system.

4.3.3 χ^2 sensitivity to the the different parameters

Before going into details of the whole fit using the data samples, let see how the χ^2 is sensitive to the parameters to be determined. For this, the six simulated data samples D_1 to D_6 described in Section 4.2.3 are used[4] and the χ^2 defined in (4.9) and (4.10) is constructed. Figures 4.21, 4.22 and 4.23 show the value of the χ^2 as a function of each one of the simulated parameters. All these minimisations are done with only one free parameter, all the others being fixed to their generated value.

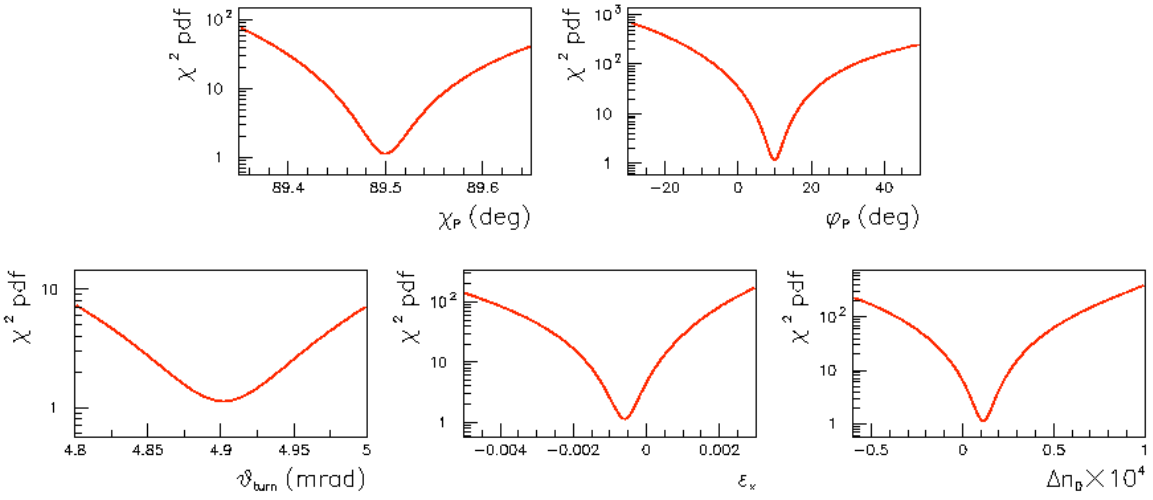

Figure 4.21: Value of the χ^2 per degree of freedom (pdf) as a function of χ_P, ϕ_P, θ_{turn}, ϵ_x and Δn_o (see Section 4.2.2 for the meaning of these parameters).

[4]With two differences: the generated value of the parameter Δn_o is 10^{-5} instead of -3×10^{-6} and the simulated data have been generated with an error of 0.5% on each signal.

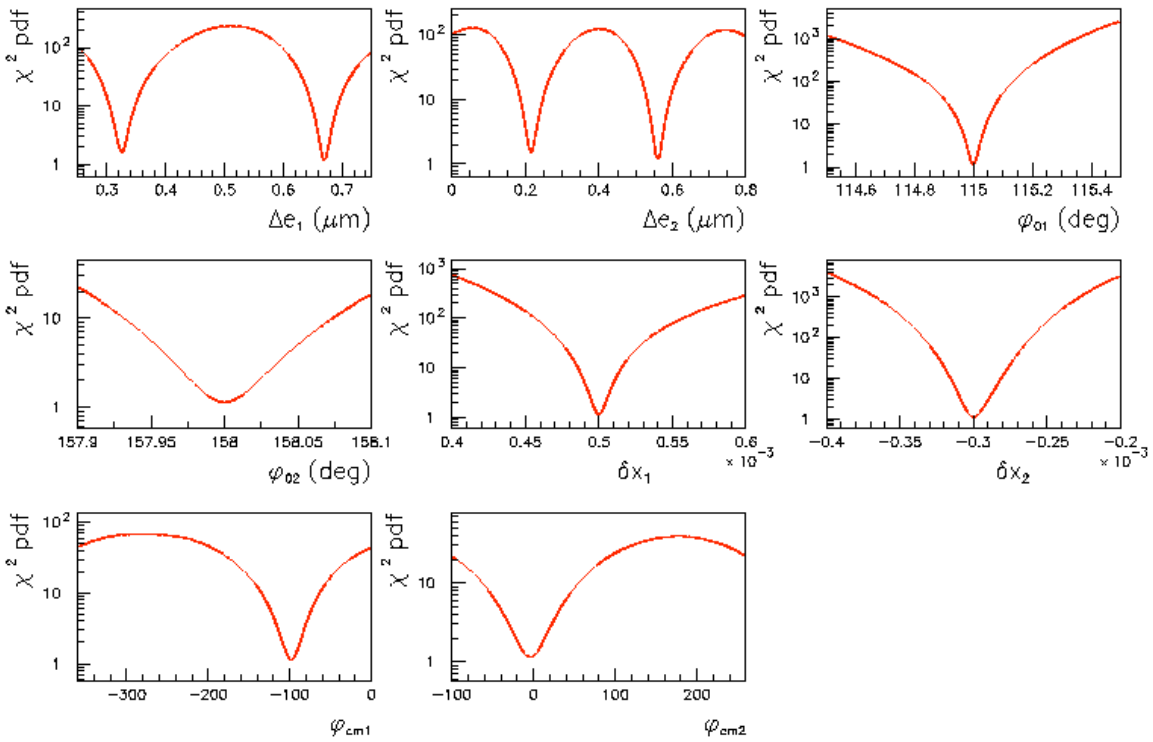

Figure 4.22: Value of the χ^2 per degree of freedom (pdf) as a function of Δ_{e_1}, Δ_{e_2}, ϕ_{0_1}, ϕ_{0_2}, δ_{x_1}, δ_{x_2}, ϕ_{cm_1}, ϕ_{cm_2} (see Section 4.2.2 for the meaning of these parameters).

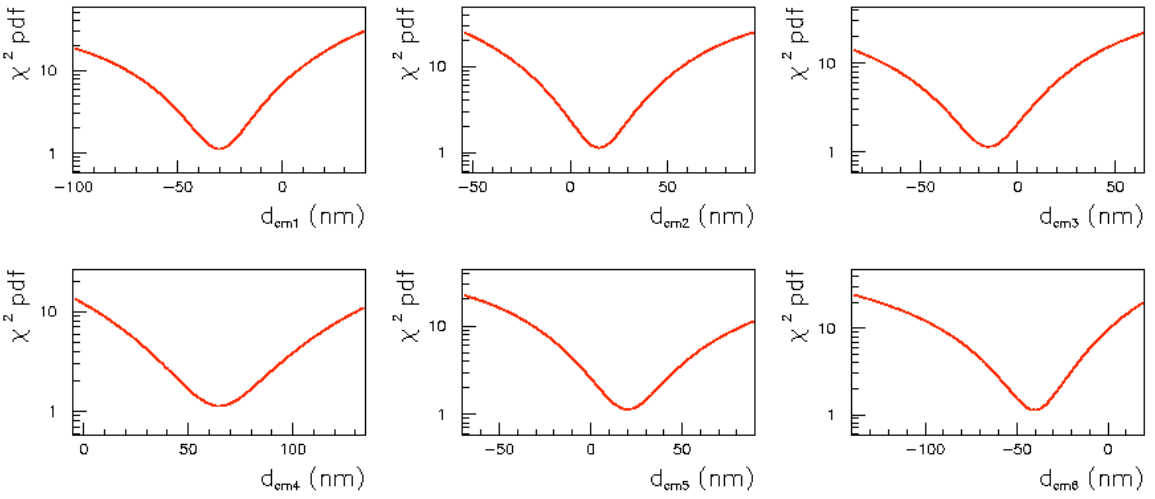

Figure 4.23: Value of the χ^2 per degree of freedom (pdf) as a function of d_{cm_i} (i = 1, 6) (see Section 4.2.2 for the meaning of these parameters).

These functions show that the χ^2 is sensitive to each one of the parameters which has to be determined in the whole fit. Because these minimisations are performed with only one free parameter, these plots are just a way to have an idea of the shapes of the χ^2 functions.

4.4 Results

4.4.1 Minimisation of the χ^2

Using first the six simulated data sample files, the minimisation procedure is tested in order to be sure that the minimum of the χ^2 leads to the generated parameter values and this, when all the parameters are now fitted at the same time. As shown by the shapes of the $\chi^2(\Delta e_1)$ and $\chi^2(\Delta e_2)$ functions of Figure 4.22, several fits have to be made to find the minimum of the χ^2 with different starting values for Δe_1 and Δe_2 spaced by about 0.3 μm.

The result of the best fit is summarised in Table 4.3 where the fitted parameters leading to the smaller χ^2 are compared to the generated ones. Table 4.3 gives also the errors on the fitted parameters coming from the minimisation.

	generated	fitted	error
Δe_1 (μm)	0.67	0.67100	0.00023
Δe_2 (μm)	0.57	0.56913	0.00073
$\Delta n_o \times 10^6$	-3.0	-1.810	0.304
ϕ_{0_1} (deg)	115.0	114.990	0.004
ϕ_{0_2} (deg)	158.0	157.990	0.004
χ_P (deg)	89.50	89.514	0.00676
ϕ_P (deg)	10.0	10.892	0.49893
$\theta_{turn} \times 10^3$ (rad)	4.90	4.9017	0.0062
$\epsilon_x \times 10^4$	-6.0	-6.936	0.585
$\delta_{x_1} \times 10^4$	5.0	4.9988	0.0084
$\delta_{x_2} \times 10^4$	-3.0	-3.0029	0.0057
d_{cm_1} (nm)	-30.0	-30.325	0.34620
d_{cm_2} (nm)	15.0	14.916	0.30257
d_{cm_3} (nm)	-15.0	-14.954	0.31568
d_{cm_4} (nm)	65.0	65.093	0.45259
d_{cm_5} (nm)	20.0	20.593	1.0827
d_{cm_6} (nm)	-40.0	-41.142	0.95668
ϕ_{cm_1} (deg)	-98.0	-98.33	0.24269
ϕ_{cm_2} (deg)	-4.0	-3.972	1.1663

Table 4.3: Parameters resulting from the fit using the generated data files D_i (i=1,6) defined in Section 4.2.3 and errors on these fitted parameters.

Figure 4.24 (respectively 4.25) shows the good agreement between the simulated intensities I_1 (respectively I_2) and the theoretical ones resulting from the fit, as a function of the azimuthal quater wave plate angle ϕ, for the six independent Monte Carlo samples.

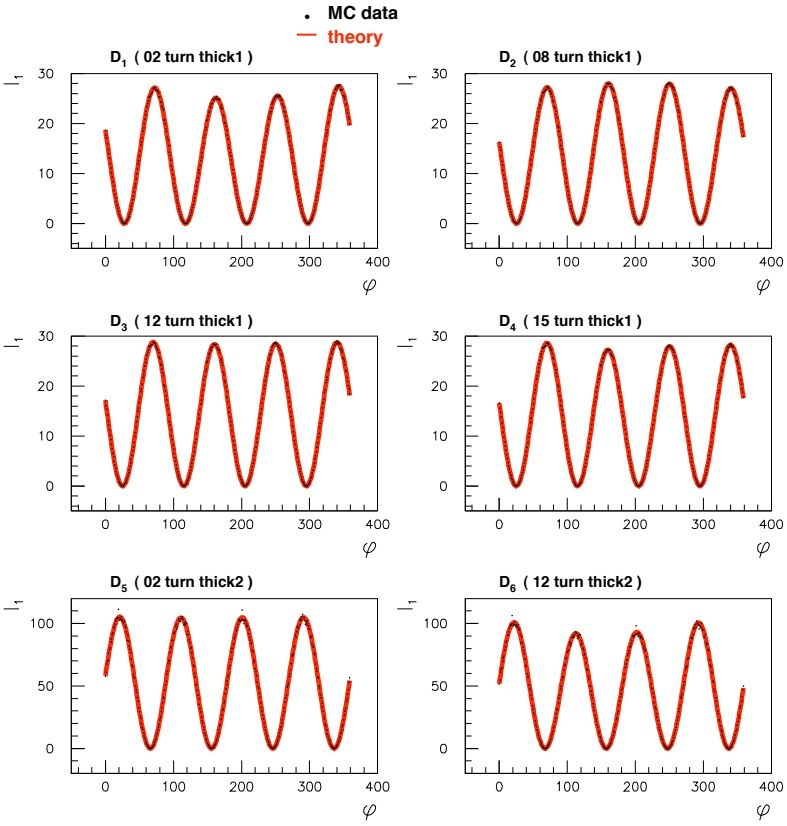

Figure 4.24: Simulated and theoretical intensities I_1 as a function of the quater wave plate angle ϕ for the six Monte Carlo samples.

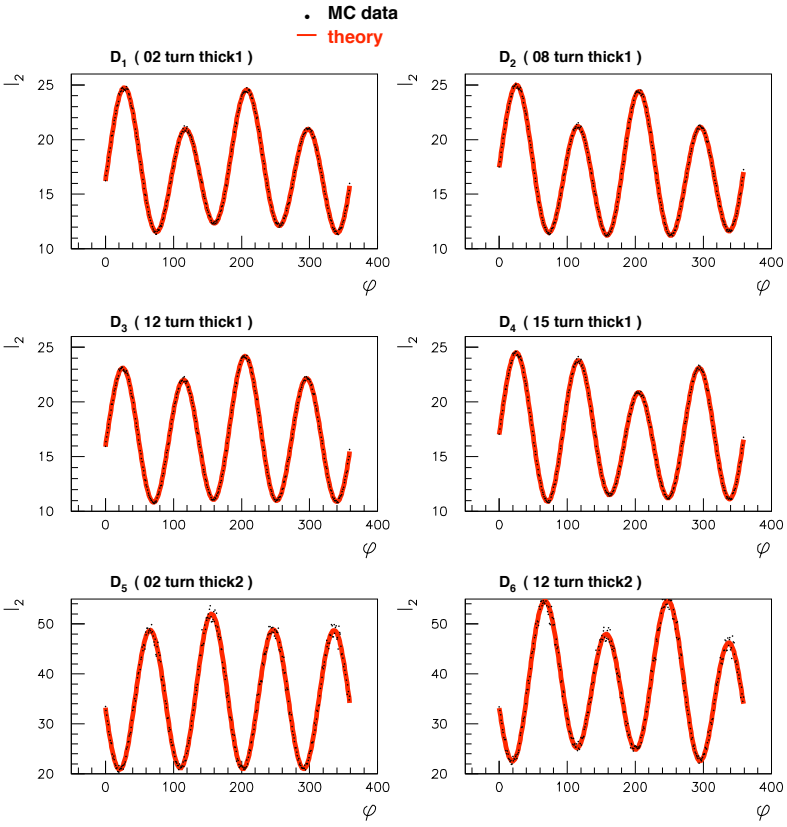

Figure 4.25: Simulated and theoretical intensities I_2 as a function of the quater wave plate angle ϕ for the six Monte Carlo samples.

The pull distribution: pull $= \sum \frac{(\mathrm{I}-\mathrm{R\ T})}{\sigma}$ is presented for the whole simulated sample in Figures 4.26 and for the six simulated samples D_1 to D_6 independently in Figure 4.27. The sum in the pull definition is over each datum entering the χ^2 fit, and the quantities I, R and T are the ones defined in (4.10) where subscipts and superscripts have been omitted. With these tests using simulated files generated with errors comparable to the experimental data ones, we have checked that all the parameters can be determined at the same time and at a few per mill level. Note that the choice to use four different angles of incidence for the plates pl_1 and two for the plate pl_2 results from a simulation study in which it has been shown that this number of files is sufficient to determine all the parameters of the problem.

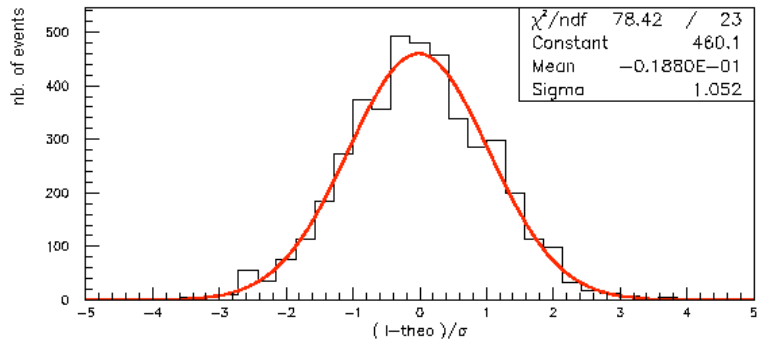

Figure 4.26: Distribution of the pull (I−R T)/σ for the whole simulated sample.

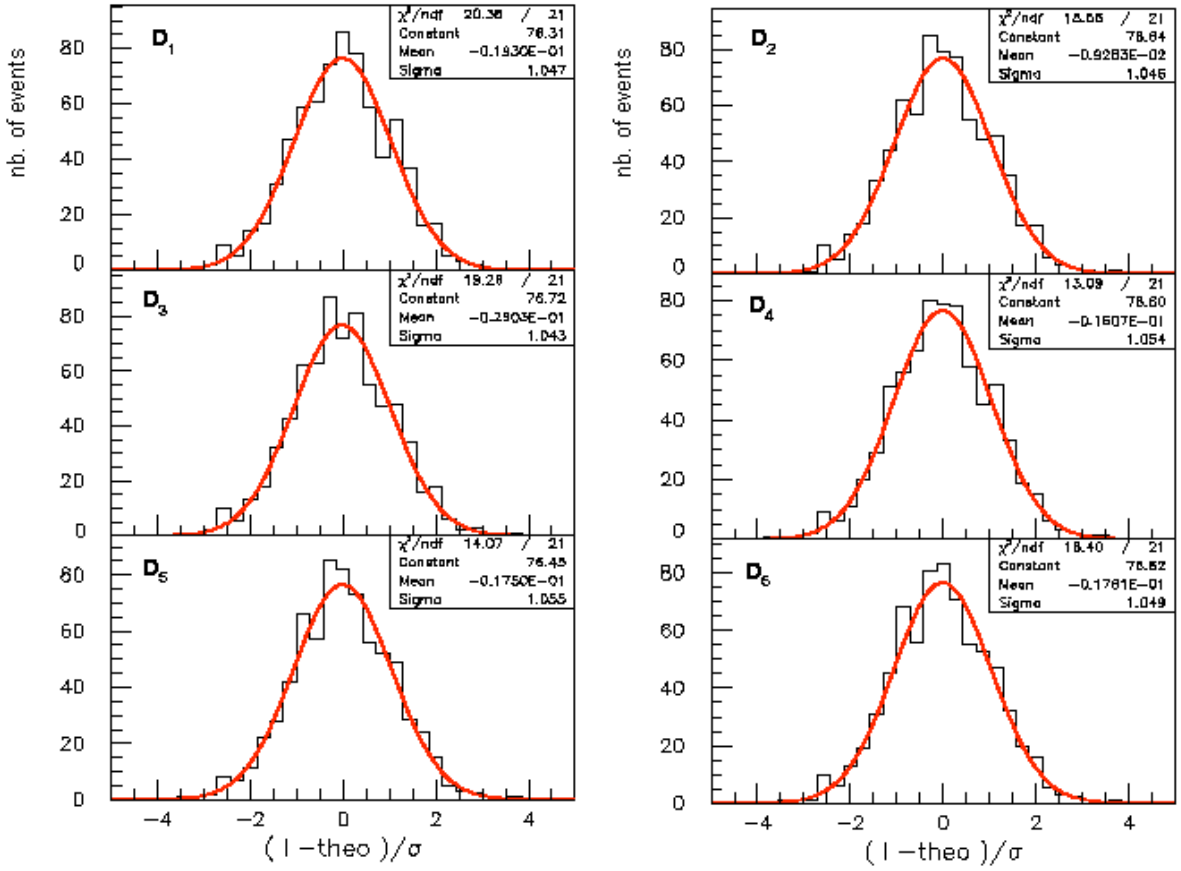

Figure 4.27: Distribution of the pull (I−R T)/σ for the six independent simulated samples D_1 to D_6.

Experimental data have been treated in the same way as generated ones, *i.e.* with exactly the same fit procedure. Numerical results coming from the minimisation are presented in Table 4.4.

	fitted	error
Δe_1 (μm)	0.35084	0.00029
Δe_2 (μm)	0.67159	0.00134
$\Delta n_o \times 10^6$	5.1299	0.3491
ϕ_{0_1} (deg)	99.004	0.0085
ϕ_{0_2} (deg)	155.32	0.0141
χ_P (deg)	90.365	0.0167
ϕ_P (deg)	-6.4002	1.0921
$\theta_{turn} \times 10^3$ (rad)	5.4764	0.0073
$\epsilon_x \times 10^4$	-7.903	1.019
$\delta_{x_1} \times 10^4$	0.03325	0.00588
$\delta_{x_2} \times 10^4$	0.00379	0.02165
d_{cm_1} (nm)	-0.652	0.351
d_{cm_2} (nm)	1.381	0.304
d_{cm_3} (nm)	-1.677	0.303
d_{cm_4} (nm)	6.980	0.363
d_{cm_5} (nm)	6.489	0.521
d_{cm_6} (nm)	-0.412	1.085
ϕ_{cm_1} (deg)	-83.402	2.615
ϕ_{cm_2} (deg)	-22.598	4.785

Table 4.4: Parameters resulting from the fit using the real data files D_i (i=1,6) defined in Section 4.2.3.

In Figure 4.28 (respectively 4.29) are presented experimental intensities I_1 (respectively I_2) compared with theoretical ones coming from the fit, as a function of the angle ϕ, for the six independent data samples D_i (i=1,6). These figures show a very good agreement between measurements and theoretical intensities.

The fit quality is better visualised in Figures 4.30 and 4.31 which show the pull distributions for the whole data sample and for the six data files independently. A gaussian fit on the whole data pull histogram leads to a standard deviation of the order of 0.7. This is no doubt due to the fact that we have slightly overestimated our measurement errors by using in the fit the dispersion of the twenty points of measurements (see Section 4.2.3) instead of taking their standard deviation in order to be more conservative for the long term photodiode measurement variations. Compared to Monte Carlo pull distributions in Figure 4.27, some slightly non-gaussian components are present on experimental data distributions (see for instance the pull of files D_1, D_3 and D_4 in Figure 4.31), but these effects are very "light".

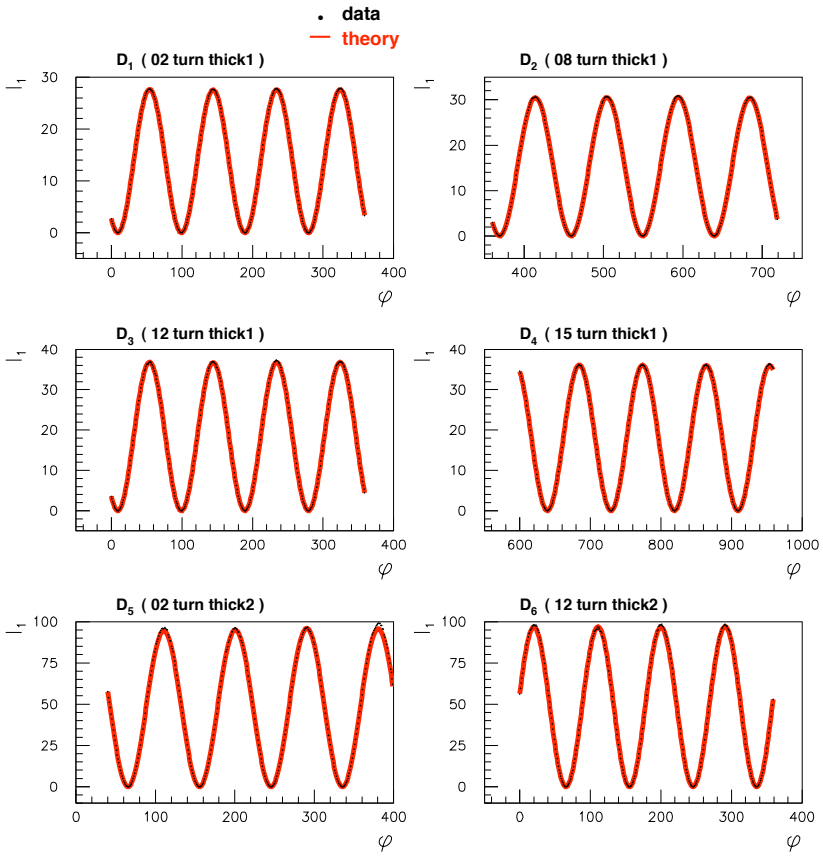

Figure 4.28: Experimental data and theoretical intensities I_1 as a function of ϕ for the six data samples.

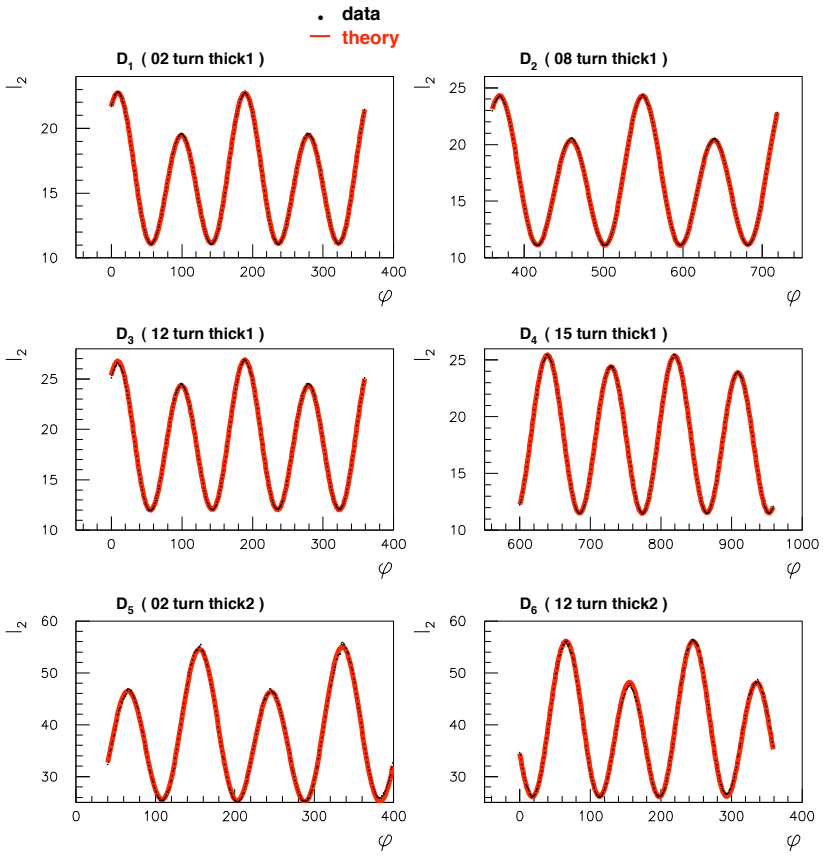

Figure 4.29: Experimental data and theoretical intensities I_2 as a function of ϕ for the six data samples.

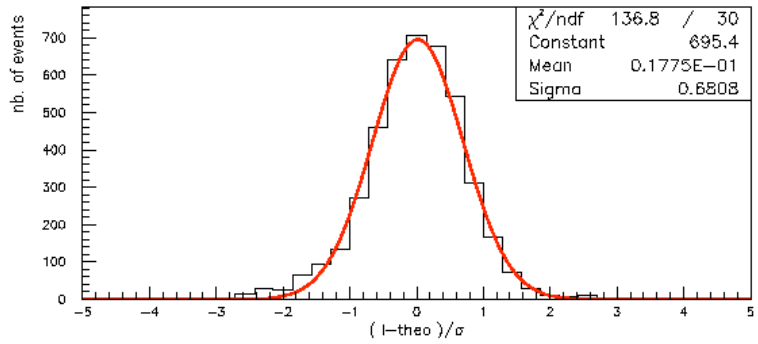

Figure 4.30: Distribution of the pull (I− R T)/σ for the whole data sample.

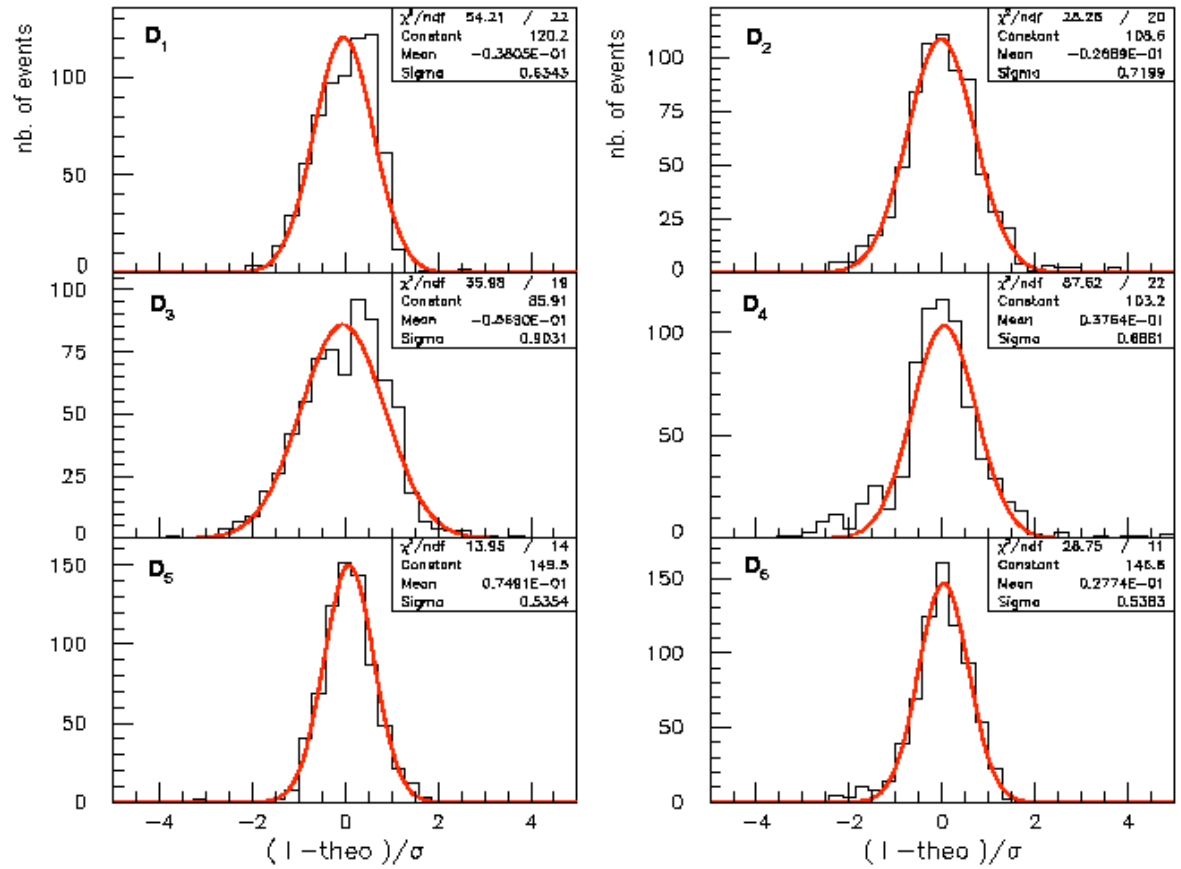

Figure 4.31: Distribution of the pull (I − R T)/σ for the six independent data samples D_1 to D_6.

4.4.2 Coherence of fitted parameters

In this section, some comments are made on the parameters of Table 4.4 coming from the fit of the experimental data samples.

Birefringence

The value of Δn_o of Table 4.4 obtained from the data fit corresponds to a quartz birefringence of 8.729×10^{-3}. This value can be compared to birefringence measurements

previously determined in [120] and [121]. In [121], the measurements have been done at a temperature of 22°, in [120] at a temperature of 18°. For our measurements, the temperature of the room was 25°. The variations of optical indices with temperature have been measured as a function of the wavelength in [123] and the values extracted from this reference at λ =1064 nm are:

$$\begin{aligned} dn_o/dT &= -7.7 \times 10^{-6}\ K^{-1}\ , \\ dn_e/dT &= -9.3 \times 10^{-6}\ K^{-1}\ . \end{aligned} \tag{4.13}$$

Taking these formula, birefringences $n_e - n_o$ of [120] and [121] rescaled at T = 25°, together with the value of the birefringence coming from our quater wave plate calibration, are shown in Figure 4.32. Our value is thoroughly consistent with the ones tabulated in references.

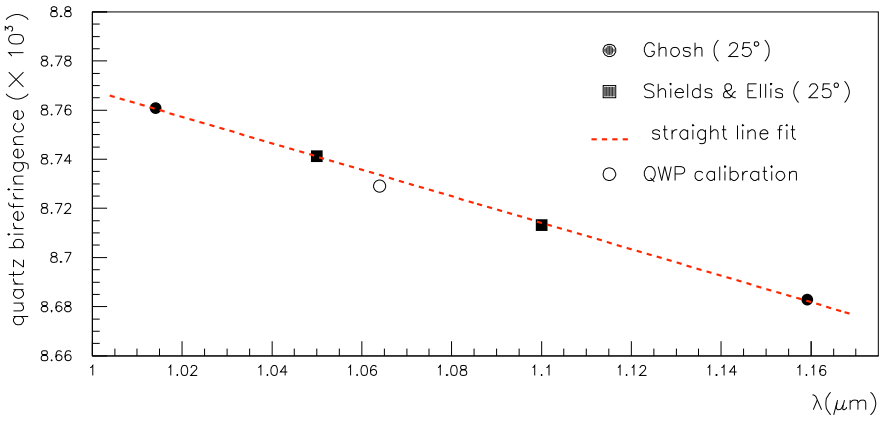

Figure 4.32: Quartz birefringence values at T = 25° as a function of the wavelength. The two black circles come from [120] rescaled from T = 18° to T = 25° with formula (4.13), the two black squares come from [121] rescaled from T = 22° to T = 25°. The dashed line is a straight line fit using these four points. Our birefringence value coming from the plate calibration is indicated by the open circle.

Thicknesses

In Table 4.4, thickness differences Δe_1 and Δe_2 are small with respect to values and tolerances given by the manufacturer (*i.e.* 91.4 μm thickness for plate pl_1, 639.9 μm for plate pl_2, with a tolerance for a non-parallelism of the sides of 10 arcsec and a tolerance of delay of 1/300). They are well determined and compatible with the specifications of the plates.

Misalignment of the centres of the plates

With a non-parallelism of the plate sides of the order of 10 arcsec given by the manufacturer, misalignment parameters d_{cm_i} of Table 4.4 correspond to misalignments of the centre of the plate mounts (related to the impact laser point) of the order of few tens micrometers. These values are realistic since the plate has been very precisely aligned before taking the data. To do this alignment, each plate had been displaced transversally

in all directions with the micro-metric screws, and for each position, one azimuthal plate turn had been done and corresponding data recorded in ellipsometer photodiodes. Then, the best alignment was the one which best equalised the height of all maxima separated by 180°. This is illustrated in Figure 4.33 which shows the intensity I_2 of two sets of data simulated with $d_{cm} = 65$ nm (in black) and with $d_{cm} = 0$ nm (in red).

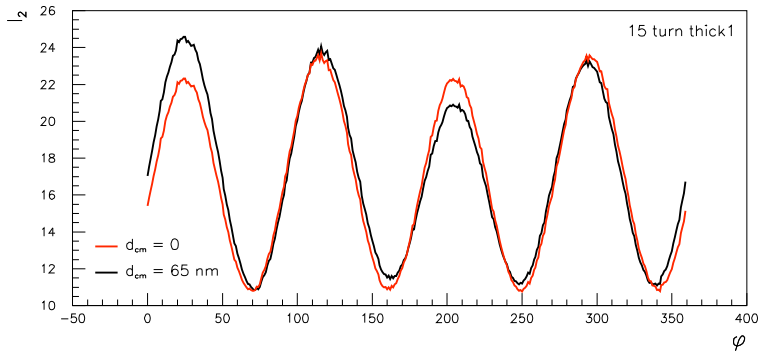

Figure 4.33: Simulated I_2 intensities as a function of the azimuthal plate angle ϕ (in degrees), for misalignment parameters $d_{cm} = 65$ nm (black line) and $d_{cm} = 0$ nm (red line).

The height of two peaks separated by 180° are equal for the perfect aligned data sample, while for $d_{cm} = 65$ nm it is not the case. In this latter case, taking a mis-parallelism plate sides of 10 arcsec, the difference between the centre of the plate mount and the impact point of the laser is around one millimeter.

Wollaston ellipticity

The Wollaston prism ellipticity ϵ_x is found to be less than one per mill.

Degree Of Circular Polarisation

Concerning the DOCP, its expression and its standard deviation are derived from the two angles χ_P and ϕ_P describing the light polarisation state. According to (3.2), (3.3) and (3.4), they are written as:

$$\begin{aligned} \mathrm{DOCP} &= 2\,\cos\chi_P\,\sin\chi_P\,\sin\phi_P \quad , \\ \sigma_{\mathrm{DOCP}} &= 2\,\sqrt{(\sin\phi_P\,\sigma_{\chi_P})^2 \;+\; (\cos\chi_P\,\sin\chi_P\,\cos\phi_P\,\sigma_{\phi_P})^2}\;. \end{aligned} \tag{4.14}$$

Fit results for χ_P, ϕ_P, σ_{χ_P} and σ_{ϕ_P} in the simulated sample (which we recall have been generated as near as possible to the data, and in particular with simulated uncertainties similar to the experimental ones) and in the data sample lead to:

$$\begin{aligned} \mathrm{DOCP}^{\mathrm{MC}}_{\mathrm{fit}} &= 3.031 \times 10^{-3} \pm 1.6 \times 10^{-4}\;, \\ \mathrm{DOCP}^{\mathrm{DATA}}_{\mathrm{fit}} &= 1.420 \times 10^{-3} \pm 2.50 \times 10^{-4}\;. \end{aligned}$$

For the simulated sample, the difference between the generated DOCP and the fitted DOCP is equal to 1.75×10^{-4}. Note that for the data sample, the DOCP value of 1.420×10^{-3} is a reasonable value as the incidence wave is supposed to be linearly polarised. This is of course also the case of the simulated sample since the initial state polarisation has been generated in an almost completely linearly polarised state.

4.5 Conclusion

As a conclusion, we can say that with a 100 mW stable infra-red laser, we were able to determine at the per mill level all the parameters of our ellipsometer system in the environment of a laboratory. This can only be performed by using a model as complete as possible for the description of the propagation of the light inside our quartz quater wave plate, and by taking into account the possible experimental misalignments of the ellipsometer optical components. By simulating data samples as close as possible to experimental ones, we have checked that we can really rely on our simulation model and our fitting procedure.

Chapter 5

Degree Of Circular Polarisation measurement in the HERA tunnel

The calibration of the ellipsometer in a laboratory environment has provided the main characteristics of the quater wave plates pl_1 and pl_2: their real thickness, in addition to some non negligible misalignment parameters of the plates with respect to the other optical devices of the system, and has also provided the characteristics of the Wollaston prism. This calibration has made it possible to prove the validity of the fitting model. The ellipsometer, where from now only the plate pl_1 is used, is now located in the accelerator to measure the degree of polarisation of the light.

5.1 Experimental setup

The ellipsometer located in the HERA tunnel is the one shown in Figure 3.1 where so-called "beam to be analysed" is now the light coming from the cavity (and no longer the light coming directly from a laser as it was the case in the calibration procedure described in Section 4.2). A simple overview of the optical schematic is presented in Figure 5.1.

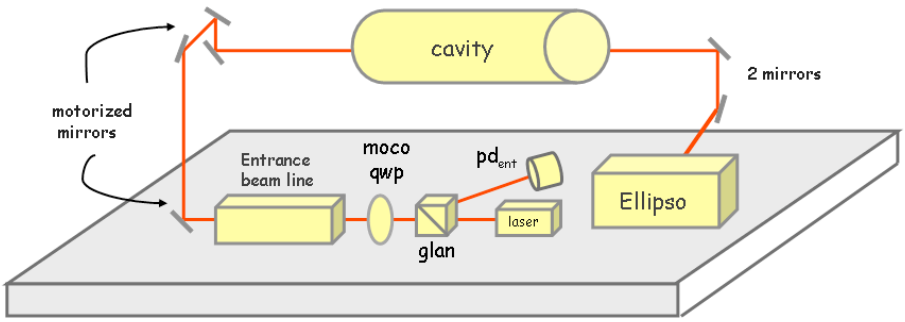

Figure 5.1: Basic optical schematic of the cavity system installed in the HERA tunnel. The box called "ellipso" is the ellipsometer in Figure 3.1.

The laser beam passes first through a Glan-Thomson prism (aligned along the direction of the laser beam polarisation) to provide a purely linear polarisation and also to let pass the beam which goes back after its reflection by the cavity entrance mirror when the cavity is unlocked. This return beam is analysed in the photodiode pd_{ent} behind the Glan to determine the azimuthal angles of the entrance quater wave plate for which the

light is circularly polarised (Section 5.5). This entrance plate is called "moco qwp"[1]in the following and in Figure 5.1. The return beam is also used to determine the transfer matrix of the entrance optics (Section 6.4). After the Glan, the beam passes through the "moco qwp" where it acquires an elliptical polarisation depending on the azimuthal angle of the plate, and then enters the optical entrance beam line. The entrance beam line is composed of lenses (to put the waist of the beam at the centre of the cavity) and of a glass plate to pick up a part of the beam used for the locking procedure. After that, the beam is precisely aligned with four motorised mirrors before entering the cavity. At the exit of the cavity, the beam is aligned with two mirrors to enter the ellipsometer. Of course if the cavity is not locked, almost no light enters the cavity. Therefore all the following studies using ellipsometer data are done when the cavity is locked and stable.

5.2 Photodiode behaviour on the accelerator environment

Because the environment has changed between the Orsay Hall and the HERA accelerator (different temperatures, presence of quadrupole and dipole fields, of synchrotron radiation, of accelerating cavities, of long cables and pickup), some additional noise could affect the precision level of the photodiode measurements obtained in the Orsay laboratory environment (see Section 3.3.2). Therefore, a new study of the errors of measurements was performed when the ellipsometer system is put in the HERA tunnel.

Figure 5.2 shows the signal from one photodiode divided by the reference photodiode signal. 200.000 points enter the histogram and the measurement lasted 0.1 sec. This short time measurement distribution looks gaussian and the statistical uncertainty of the signal $\sigma = 1.24 \times 10^{-3}/\sqrt{200.000}$ is largely sufficient for the required per mill level.

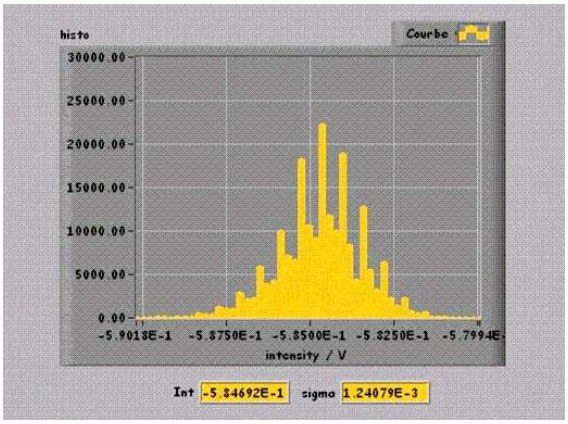

Figure 5.2: Histogram of a ratio of ellipsometer intensities, containing 200.000 entries. The data has been taken in the HERA tunnel (when cavity was locked) and has lasted 0.1 sec. Artificial peaks are due to the ADC resolution.

It is important to estimate some long term uncertainties, *i.e.* some systematic effects or random drift of photodiode signals during the time needed to take an ellipsometer data set. This time corresponds to one turn of the ellipsometer quater wave plate during which 200.000 data are recorded at various azimuthal angles of the plate. To give an order of magnitude, this time is about twenty minutes if data are recorded every one degree and ten minutes if data are recorded every two degrees.

[1]The name "moco" refers to the MoCo controller [93] which controls and drives the azymuthal rotations of this plate (Section 2.2.5).

Therefore, to estimate these long term measurement errors, a set of data has been recorded in the ellipsometer for approximately fifteen minutes each. Each data set corresponds to one particular azimuthal angle of the ellipsometer quater wave plate. The choice of these angles was made in order to sweep all the intensity range of the two photodiodes pd_1 and pd_2. A characteristic example of such measurements is shown in Figure 5.3 where two data samples (each one lasting fifteen minutes) are presented: left histograms (a), (b) and (c) show a "good" situation measurement, while right histograms (d), (e) and (f) show a "bad" one. In the figure, (a) and (d) are the distributions of the reference intensity I_0, (b) and (e) the distributions of the intensity I_2 and (c) and (f) are the ratios $r_2 = I_2/I_0$. On the left side, one sees that the variations of I_0 and I_2 are well compensated by the ratio during the fifteen minutes of the data taking. The right side plots show measurements recorded with the same quater wave plate azimuthal position but at a different moment. One can see two populations in the ratio histogram (f).

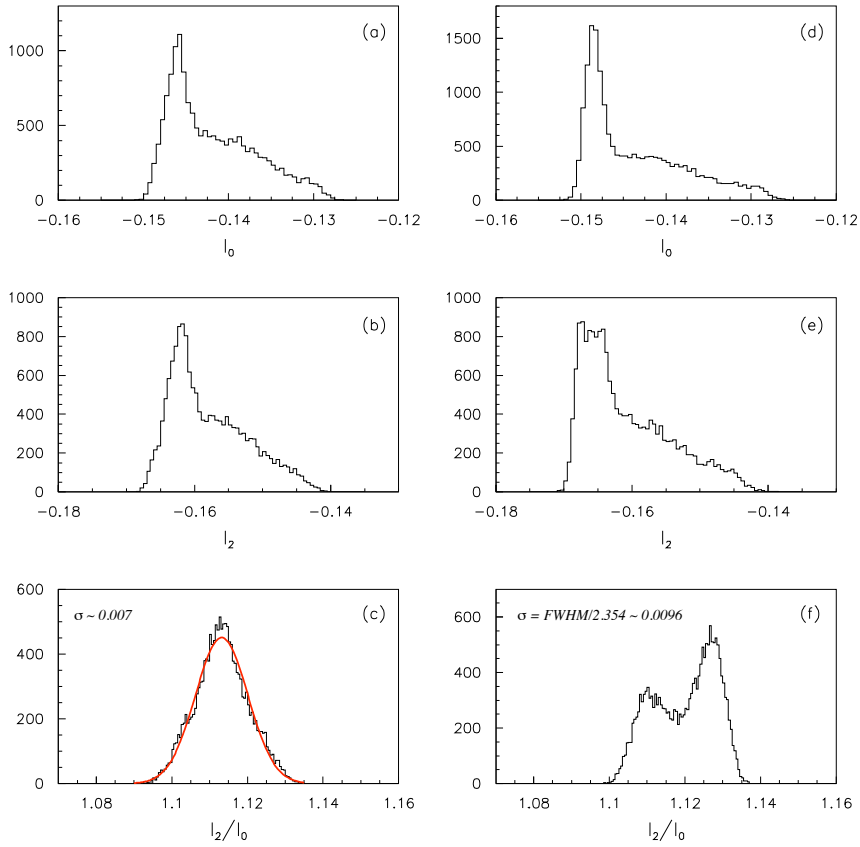

Figure 5.3: Histograms of I_0 (a) and (d), I_2 (b) and (e), $r_2 = I_2/I_0$ (c) and (f) for two sets of data taking during fifteen minutes each. Left histograms correspond to the first data set, right ones correspond to the second data set. The red curve on (c) is the result of a gaussian fit.

To take into account this kind of drift, the error $\sigma_{r_{1,2}}$ associated to a given intensity ratio $r_{1,2}$, will be equal to the standard deviation of the histogram whether it has a gaussian shape or not. In that way, the unknown long term effects such as those illustrated in Figure 5.3(f) are included as measurement errors. From now, as in Chapter 4, the writting of the reference signal I_0 is omitted and the notations r_1 and r_2 are replaced by I_1 and I_2.

As in the case of the data taken in the Orsay laboratory (see Section (4.12)), the standard deviations σ have been parametrised as $\sigma_{I_{1,2}} = A_{1,2}\, I_{1,2} + B_{1,2}$. Figure 5.4 shows the errors σ_{I_1} and σ_{I_2} as a function of I_1 and I_2 respectively and the corresponding fitted straight line.

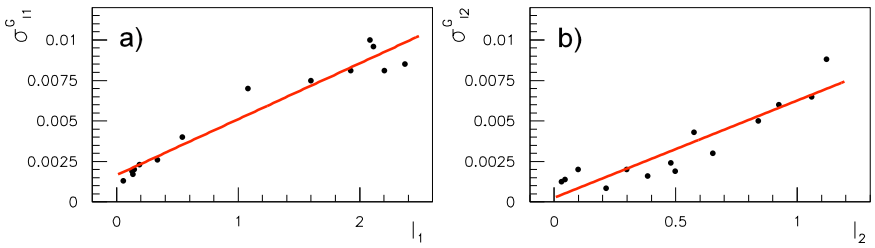

Figure 5.4: (a): Errors σ_{I_1} of the measurements I_1 as a function of I_1 for data sets recorded at various azimuthal angles of the ellipsometer quater wave plate. (b): same for I_2. The fits $\sigma_{1,2} = A_{1,2}\, I_{1,2} + B_{1,2}$ are indicated by a red line.

Let us make a few remarks: firstly, Figure 5.4 is rather similar to Figures 4.12 to 4.15 concerning data errors estimated in the Orsay environment. Secondly, concerning the time of measurement, *i.e.* the choice of the values of the plate azimuthal angle used in one ellipsometer data acquisition, we could wonder whether this time could not be decreased (by taking data not all the degrees or all the two degrees, but with larger intervals) in order to reduce the systematic effects illustrated in Figure 5.3(f). This has been investigated and this effect of data time measurement variations will be dealt with in Section 5.5.

5.3 Optical system parameters in the HERA tunnel

Having now some realistic error functions, we are able to measure regularly the degree of polarisation of the laser beam with the ellipsometer. But before this, as it has been done in Section 4, the system should first be characterised again since all the optical components have been dismounted to be installed in the tunnel. The compatibility of the parameters we will obtain in the tunnel with those determined in Section 4 should also be checked. In a similar way to what has been done in Section 4, each procedure, before being applied on real data, will be tested on a simulated sample first.

5.3.1 Data and Monte Carlo files

In order to have enough constraints, three sets of data have been recorded, each one with a different position of the azimuthal angle of the quater wave plate located in the entrance beam line (called "moco qwp" on Figure 5.1). In that way, the light entering in the ellipsometer has various polarisation states. For each one of these three polarisation states, the ellipsometer quater wave plate has been turned azimuthally by steps of 1^o from 0^o to 360^o. For these data taking the incidence was normal, which means that the parameter N_{turn} of equation (4.11) is null.

To be able to check the procedure and its results, three files (D_1, D_2, D_3) have been simulated with the parameters of Table 5.1 where the polarisation states defined by χ_P

and ϕ_P are denoted by the superscripts (1), (2) and (3) for D_1, D_2 and D_3 respectively. As for the real data taking, each D_i file contains 360 different values of the azimuthal angle ϕ separated by step of 1°. In addition, in order to have generated samples as close as possible to the real data samples, the Monte Carlo data have been simulated with the same errors functions as the ones coming from the data study described in Section 5.2. Experimental photodiode signals I_1 and I_2 recorded with the three different initial polarisation states and simulated signals I_1 and I_2 generated at the three polarisation states of Table 5.1 are presented in Figure 5.5 as a function of the ellipsometer plate azimuthal angle.

Δe	0.67 μm	$\chi_P^{(1)}$	-25^o
Δn_o	7.4 10^{-6}	$\chi_P^{(2)}$	-30^o
ϕ_0	-13.0^o	$\chi_P^{(3)}$	9^o
ϵ_x	-6.0 10^{-4}	$\phi_P^{(1)}$	102^o
δ_x	-3.0 10^{-5}	$\phi_P^{(2)}$	-42^o
d_{cm}	12.0 nm	$\phi_P^{(3)}$	165^o
ϕ_{cm}	-21.0^o		

Table 5.1: Parameters used for the simulation of the samples D_1, D_2 and D_3.

The meaning of the parameters[2] of Table 5.1 has already been explained in Section 4.2.2. According to the generated values of Table 4.1, the Wollaston ellipticity parameter ϵ_x must have the same value, the thickness plate Δe may only be slightly different because of the positioning of the plate in its mount, while all the other parameters may change because of their dependence on the alignment of the system, or because of a different environment, or because of light polarisation states. Indeed:

- Δn_o depends on the temperature,
- Δe, ϕ_0, δ_x, d_{cm} and ϕ_{cm} depend on the way the ellipsometer quater wave plate has been positioned according to the optical system,
- $\chi_P^{(i)}$ and $\phi_P^{(i)}$ (i=1,3) describe the different light polarisation states.

5.3.2 Fits

In the same way as in Section 4.2.2, a χ^2 is constructed and minimised to determine all the ellipsometer parameters. The explicit expression of the χ^2 is:

$$\chi^2 = \sum_{j=1,N_d} \sum_{i=1,360} \left[\left(\frac{R_1^j \; T_1^{ij} - I_1^{ij}}{\sigma_1^{ij}} \right)^2 + \left(\frac{R_2^j \; T_2^{ij} - I_2^{ij}}{\sigma_2^{ij}} \right)^2 \right] \quad , \tag{5.1}$$

where the subscript N_d corresponds to the number of data files ($N_d = 3$), subscripts 1 and 2 refer to intensities I_1 and I_2, the superscript j refers to the j^{th} data file and the subscript i to the i^{th} value of the azimuthal qwp angle ϕ. The theoretical intensities T_1^{ij} and T_2^{ij} are functions of all the parameters of Table 5.1 which are the free parameters of the χ^2. I_1^{ij}

[2]Subscripts 1 to 6 which refered to the different plates and the several incident angles in Table 4.1 are removed from now since only the plate pl_1 at normal incidence is used in the ellipsometer.

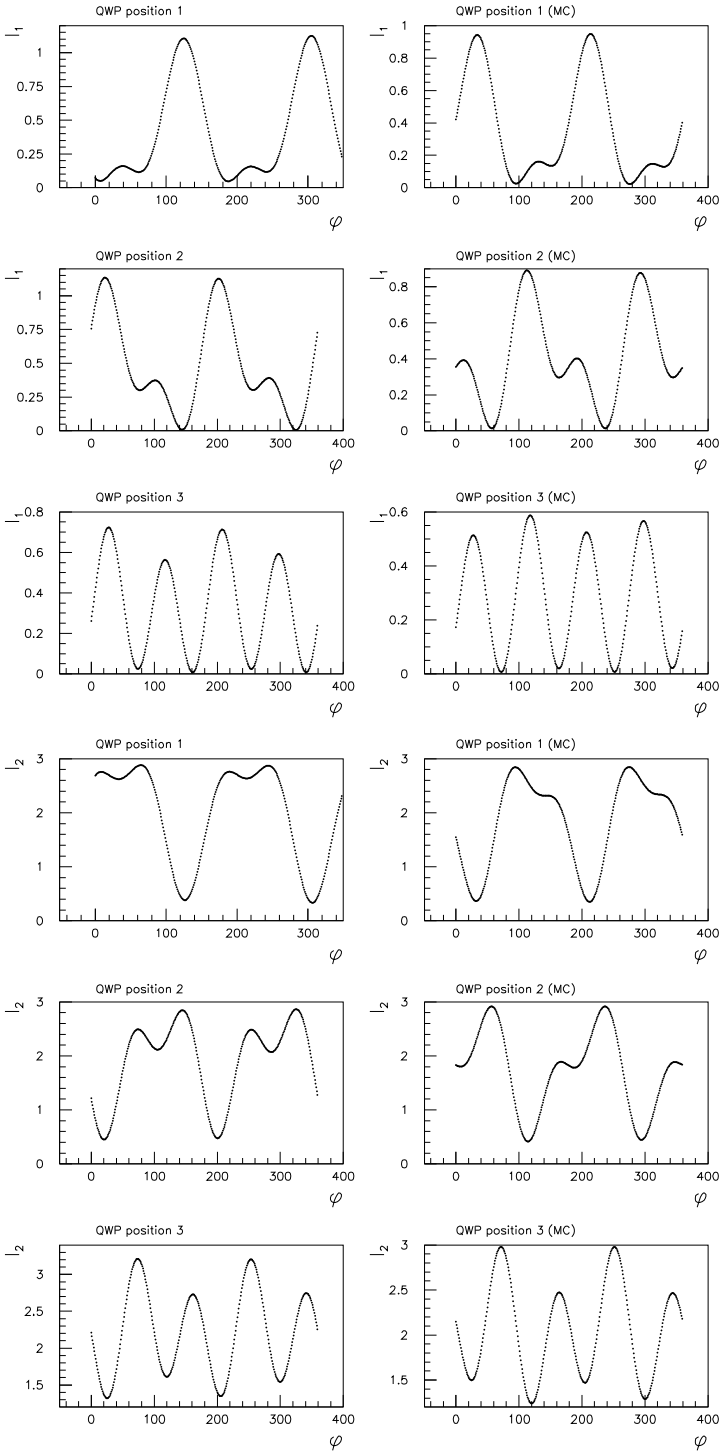

Figure 5.5: Intensities I_1 and I_2 measured (left plots) and simulated (right plots) in the ellipsometer as a function of the azimuthal angle ϕ of the ellipsometer quater wave plate. " QWP position 1, 2, 3 " denote three different azimuthal angles of the entrance quater wave plate ("moco qwp" in Figure 5.1), *i.e.* three different light polarisation states.

and I_2^{ij} are the measured intensities, σ_1^{ij} and σ_2^{ij} are the associated uncertainties described in Section 5.2. The quantities R_1^j and R_2^j are determined analytically.

Let us remark that the problem of the degeneracy of the doublet $(\Delta e, \Delta n_o)$ encountered in Section 4 does not arise here since the thickness of the ellipsometer quater wave plate has already been determined. Compared to the Orsay calibration of Section 4, the thickness plate may be slightly different only because of the quater wave plate positioning which could be slightly different at Orsay and in the tunnel. But because of our very carefully alignment, the impact point of the laser on the plate could have moved at most of a few millimeters between the Orsay alignment and the HERA tunnel one. Therefore, according to the plate side tolerance (a non-parallelism of the two sides smaller than 10 arcsec), the thickness range can be restricted here to the Δe_1 value of Table 4.4 (of Table 4.3 for the simulated plate) plus or minus some tenth of micrometers.

Parameters resulting from the minimisation of the χ^2 are listed in Table 5.2 for the Monte Carlo files, where they are compared to the generated ones. All parameters are well recovered by the minimisation.

	generated	fitted	error
Δe (μm)	0.67	0.6656	0.0004
$\Delta n_o \times 10^6$	7.4	7.237	0.984
ϕ_0 (deg)	-13.0	-13.033	0.043
$\chi_P^{(1)}$ (deg)	-25.00	-24.991	0.007
$\phi_P^{(1)}$ (deg)	102.0	102.03	0.022
$\chi_P^{(2)}$ (deg)	-30.00	-29.982	0.012
$\phi_P^{(2)}$ (deg)	-42.0	-42.030	0.019
$\chi_P^{(3)}$ (deg)	9.00	8.9794	0.011
$\phi_P^{(3)}$ (deg)	165.0	164.919	0.043
$\epsilon_x \times 10^4$	-6.0	-5.875	1.340
$\delta_x \times 10^5$	-3.0	-2.166	3.509
d_{cm} (nm)	12.0	11.449	0.150
ϕ_{cm} (deg)	-21.0	-20.195	0.713

Table 5.2: Parameters resulting from the fit using the three generated data samples defined in Section 5.3.1, and errors on these fitted parameters.

Again here, the Monte Carlo study allows first to be sure that the minimum found by the minimisation is the right one, and secondly, because the Monte Carlo data have been generated as near as possible to the real data, we have also checked that the misalignment parameters, the quater wave plate thickness and the polarisation states of the laser beam can be determined at the per mill level in the tunnel environment with these three data sets simulated with different polarisation states.

The fit using the experimental data has been performed in the same way as the Monte Carlo fit and the results are summarised in Table 5.3. These results will be discussed in Section 5.4.

	fitted	error
Δe (μm)	0.31335	0.0002
$\Delta n_o \times 10^4$	0.12136	0.0031
ϕ_0 (deg)	−12.911	0.005
$\chi_P^{(1)}$ (deg)	25.286	0.007
$\phi_P^{(1)}$ (deg)	77.601	0.020
$\chi_P^{(2)}$ (deg)	−30.604	0.011
$\phi_P^{(2)}$ (deg)	42.334	0.019
$\chi_P^{(3)}$ (deg)	−9.515	0.010
$\phi_P^{(3)}$ (deg)	15.033	0.043
$\epsilon_x \times 10^3$	−1.180	0.128
$\delta_x \times 10^5$	−1.518	1.675
d_{cm} (nm)	−15.294	0.149
ϕ_{cm} (deg)	−29.184	0.511

Table 5.3: Parameters resulting from the fit using the three experimental DESY data samples described in Section 5.3.1, and errors on these fitted parameters.

Figure 5.6 (respectively 5.7) shows the good agreement between simulated (respectively experimental) data samples and theoretical intensities, for the three D_i files.

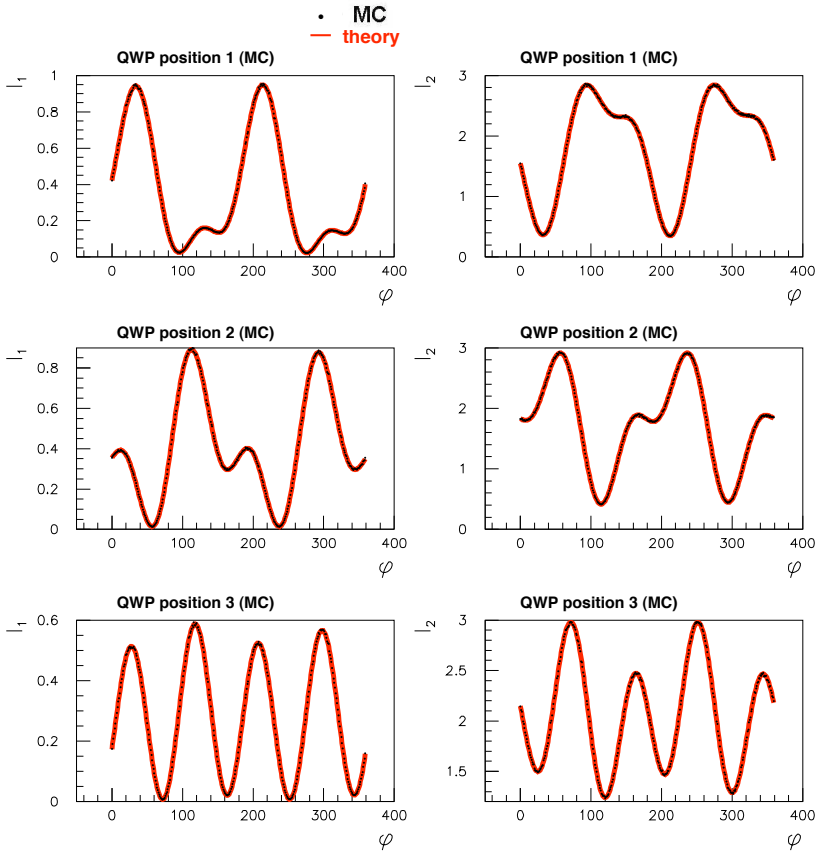

Figure 5.6: Simulated and theoretical intensities I_1 and I_2 as a function of ϕ for the three Monte Carlo samples.

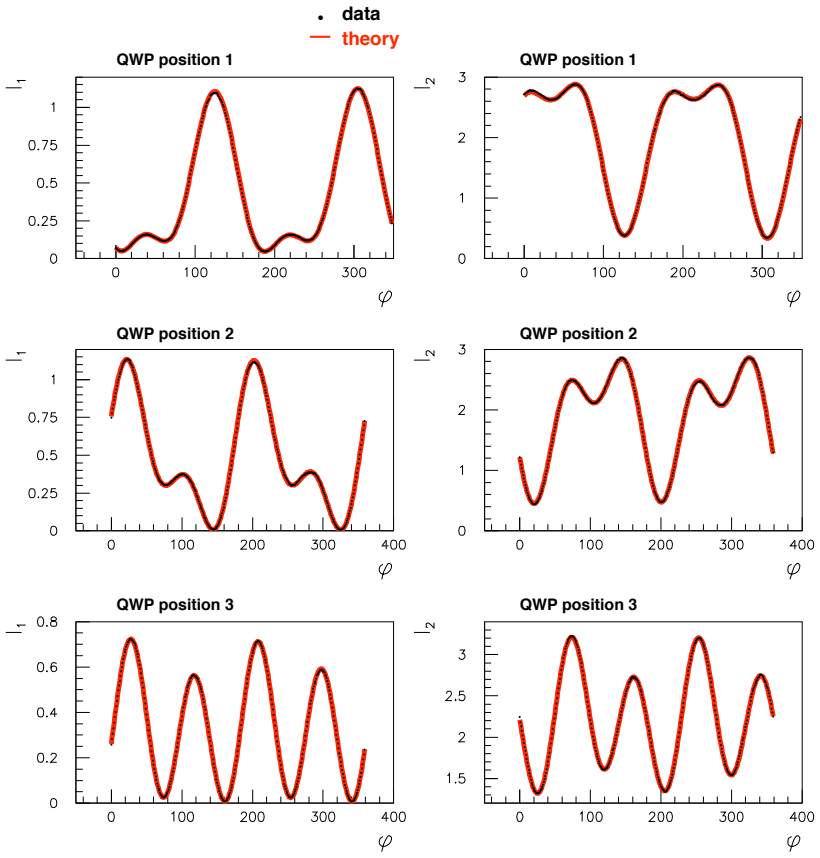

Figure 5.7: Experimental and theoretical intensities I_1 and I_2 as a function of ϕ for the three experimental DESY data samples.

In Figure 5.8 the inclusive pull distributions defined by pull $= \sum \frac{(\mathrm{I-R\ T})}{\sigma}$ are presented for the data (a) and the Monte Carlo (b) samples. The sum in the pull definition is over each datum entering the χ^2 fit, and the quantities R, T, I are defined in (5.1). Pull distributions are shown for the three data and Monte Carlo samples independently in Figure 5.9.

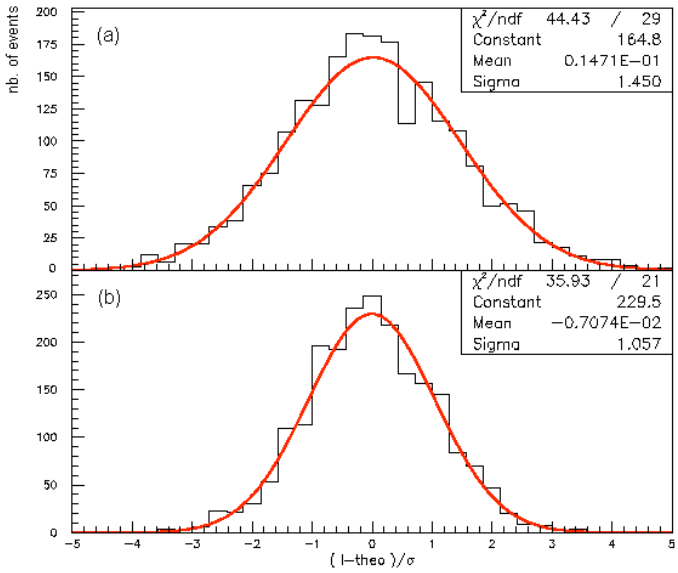

Figure 5.8: Inclusive distribution of the pull $\sum[(\mathrm{I-R\ T})/\sigma]$ for the whole DESY data sample (a) and for the whole simulated sample (b).

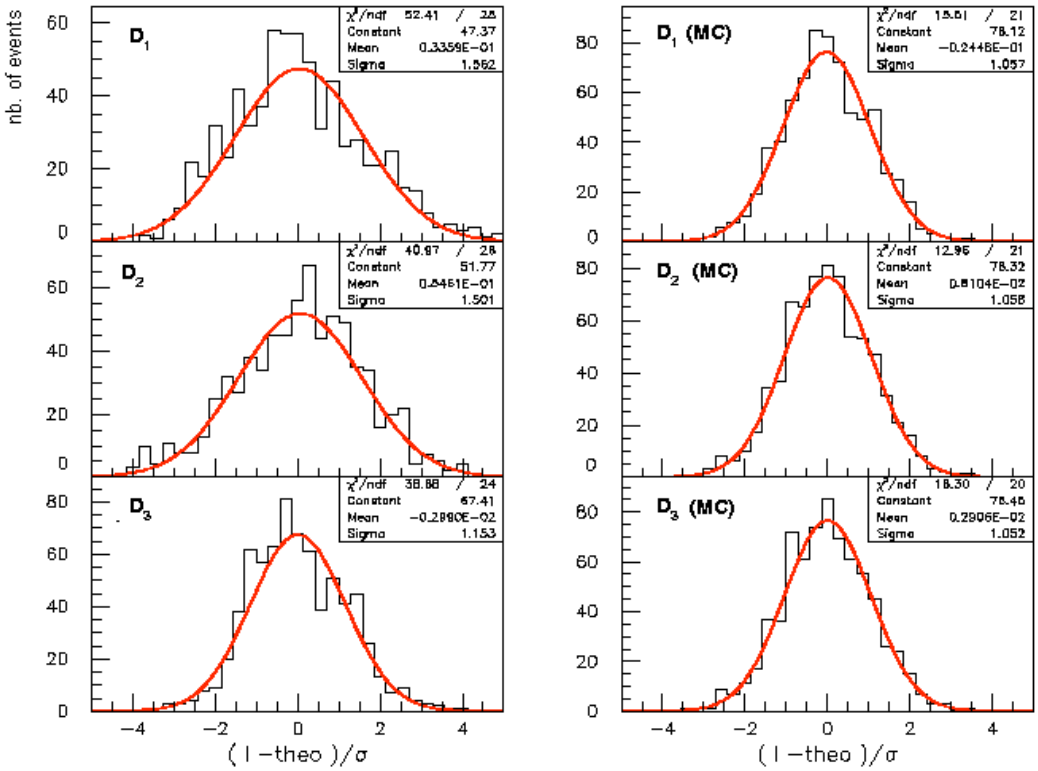

Figure 5.9: Distribution of the pull $\sum[(\mathrm{I}-\mathrm{R\ T})/\sigma]$ for the three independent DESY experimental data (left side plots) and simulated (right side plots) samples D_1, D_2 and D_3.

The main points of these results are firstly that the agreement between the experimental data and the theoretical intensities of Figure 5.7 is extremely good, and secondly that the shapes of the experimental data pull distributions shown in left plots of Figure 5.9 and in Figure 5.8(a) look gaussian enough (the standard deviations coming from gaussian fits are between 1.05 and 1.56). This shows that our data are well understood and that the fit providing the optical parameters of the ellipsometer in the HERA tunnel stays of good quality.

5.4 Coherence and compatibility of the parameters

In this section, fit results of Table 5.3 are commented and comparisons are made with the parameters of Table 4.4 resulting from the fit using experimental data taken at Orsay and described in Section 4.

5.4.1 Thickness

The thickness values of Table 4.4 ($\Delta e_1 = 0.35084\ \mu m$) and Table 5.3 ($\Delta e = 0.31335\ \mu m$) are in good agreement according to the fact that the plate can have a small non-parallelism of less than 10 seconds of arc and that the plate could be positioned slightly differently at Orsay and in the tunnel: when the plate is inserted in the optical system, the impact

points of the laser on the plate at Orsay and in the tunnel may be different of about a millimeter. As an indication, these two thickness values and the 10 seconds of arc tolerance value lead to a plate position shift between the Orsay and the tunnel alignment of 0.7 mm with respect to the laser beam.

Let us make two remarks about the temperature and the stress of the plate: the possible quartz thermal dilatation [124, 118] because of the change of temperature between the Orsay and the tunnel environments is negligible (< 0.5 nm). Also, the manufacturer provided us with a plate mounting which does not include stress. We have therefore neglected these two effects in the interpretation of our results.

5.4.2 Wollaston ellipticity

Whereas we have used the same Wollaston prism, the Wollaston ellipticity parameter of Table 5.3 is noticeably different from the one of Table 4.4. Figure 5.10 shows the value of the χ^2 as a function of ϵ_x, using our three D_i Monte Carlo samples (a) or our three D_i experimental samples (b). The small sensitivity of the χ^2 to the parameter ϵ_x is clearly visible and is due to the fact that the incidence angles are null in the data taking of the three D_i in the HERA tunnel. This function $\chi^2(\epsilon_x)$ can be compared to the one of Figure 4.21 in which the minimum is much more pronounced because of the non-null laser-plate incidences. Nevertheless, the value of ϵ_x coming from the fit using the Orsay data samples and the one coming from the present fit remain compatible. They are indicated in Figure 5.10(b).

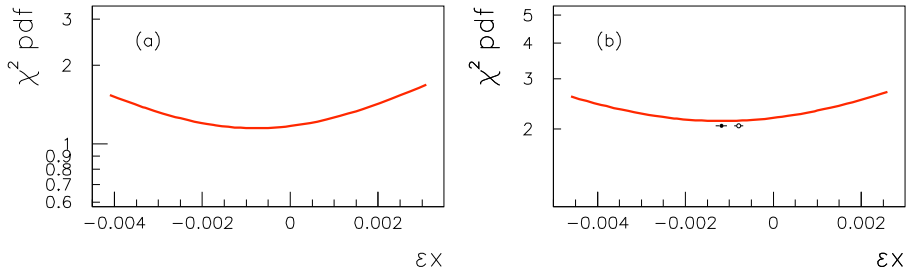

Figure 5.10: χ^2 values per degree of freedom as a function of the parameter ϵ_x using the three Monte Carlo (a) and the three experimental (b) samples described in Section 5.3.1. In the right plot are also indicated the value of ϵ_x of Table 4.4 (open circle) and the value of ϵ_x of Table 5.3 (black circle) coming from the present fit.

5.4.3 Birefringence

As was done in Section 4.4, the value of the birefringence obtained from the fitted value Δn_o of Table 5.3 can be compared with the textbook values. Figure 5.11 shows our birefringence value and the quartz birefringence textbook values coming from [120] and [121] as a function of the wavelength. In this figure, textbook points have been rescaled at the tunnel temperature of 35° by using equations (4.13). The good agreement of our birefringence value with the textbook ones gives again a good confidence of the model used.

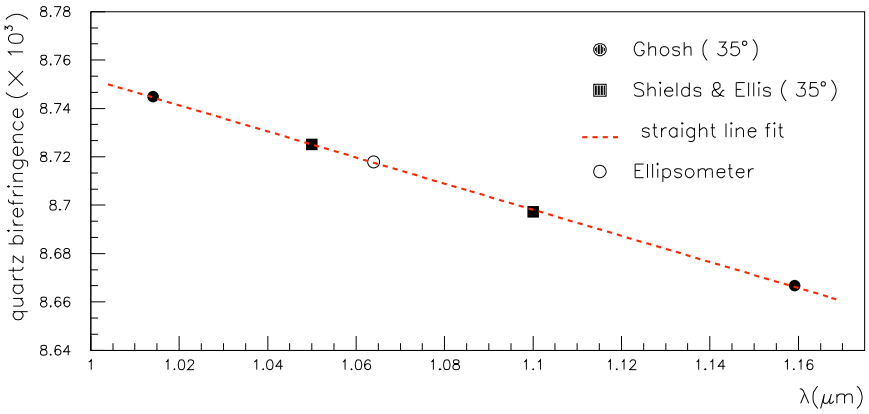

Figure 5.11: Quartz birefringence values at 35° as a function of the wavelength. The two black circles come from [120] rescaled from 18° to 35° with formula (4.13), the two black squares come from [121] rescaled from 22° to 35°. The dashed line is a simple straight line fit using these four points. Our birefringence value coming from the fit using the three data samples D_i is indicated by the open circle.

5.4.4 Misalignment of the plane of the plate

The shape of the function $\chi^2(\delta_x)$ is drawn in Figure 5.12 for the Monte Carlo sample (a) and for the data sample (b). This latter can be compared to the function $\chi^2(\delta_x)$ of Figure 4.22: as for the Wollaston ellipticity, the χ^2 here is not very sensitive to the misalignment parameter δ_x. This is still due to the null incidence of the laser on the plate and therefore to the cancellation of certain terms in the χ^2. This parameter is therefore compatible with zero.

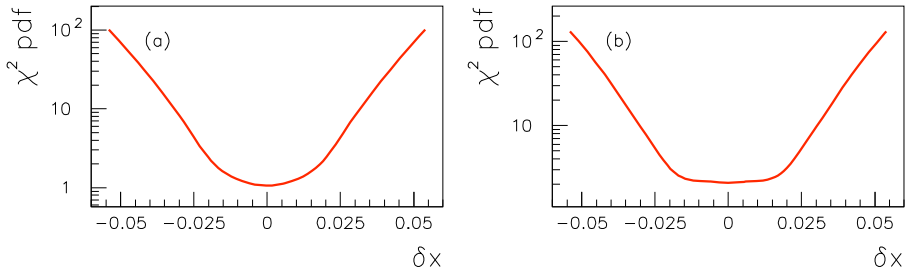

Figure 5.12: χ^2 values per degree of freedom as a function of the parameter δ_x using the three Monte Carlo samples (a) or the three experimental data samples (b) described in Section 5.3.1.

We have then checked that the ellipsometer parameters obtained in Chapter 4 in the Orsay Laboratory are consistent with those determined later in the more noisy HERA tunnel environment. These latter will be used in the measurements of the Degree Of Circular Polarisation of the light performed regularly during the data taking at HERA.

5.5 Regular DOCP measurements and systematics

During the polarisation data taking, measurements of the light Degree Of Circular Polarisation have been performed, either as a simple check, or when the azimuthal position of the entrance quater wave plate ("moco qwp" in Figure 5.1) has been optimised, or when

a hardware problem has occurred. Such hardware problems can be a blocking of the controller driving the rotating mount in which is placed the "moco qwp" which circularly polarises the laser light. In that case, the reference "moco qwp" azimuthal position is lost and the left and right circular azimuthal positions have to be determined again.

The Degree Of Circular Polarisation are measured by recording data with the ellipsometer when the cavity system is in its running condition, *i.e.* when the cavity is locked and when the azimuthal angle of the entrance quater wave plate is such as the light is right or left circularly polarised.

5.5.1 Azimuthal circular positions of the "moco qwp"

A right (respectively a left) circularly polarised light corresponds to an azimuthal angle of the "moco qwp" entrance quater wave plate which maximises the intensity recorded after a round trip (cavity unlocked) in the photodiode $\mathrm{pd_{ent}}$ located behind the Glan (see Figure 5.1). Indeed, as schematized in Figure 5.13, the Glan prism located just behind the laser is aligned in order to let pass the component of the incident laser wave parallel to the optical table. Passing through the quater wave plate, the wave becomes right (left) circularly polarised if the quater wave plate axes are orientated at 45° (−45°) with respect to the Glan axes. After the cavity mirror reflection, the phase of the wave is shifted of π and the beam becomes then left (right) circularly polarised. After passing through the quater wave plate in the return direction, the wave becomes vertically polarised and is reflected by the Glan at 90° and detected in the photodiode $\mathrm{pd_{ent}}$.

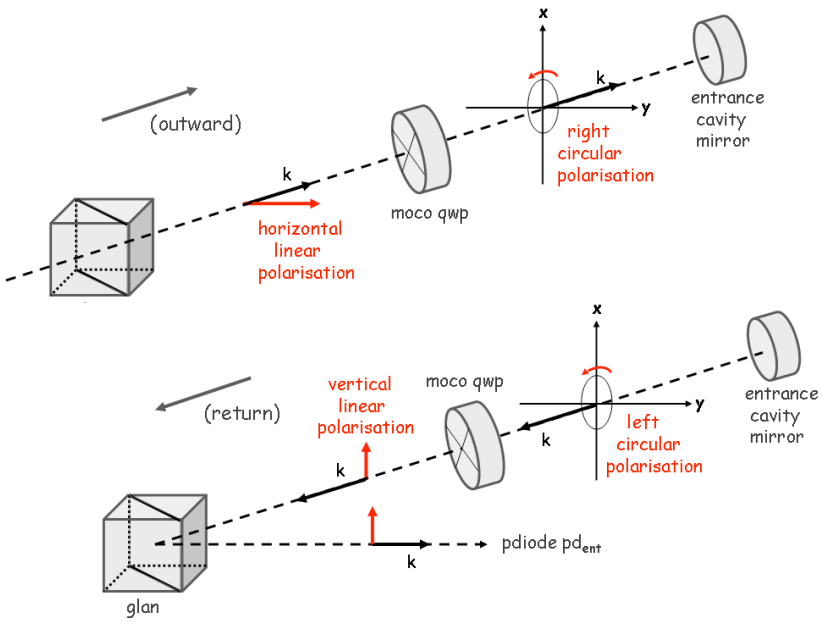

Figure 5.13: Principle of extraction of the wave reflected by the entrance cavity mirror when the cavity is unlocked. Red vectors represent the polarisation vector of the beam.

A typical example of experimental intensities recorded in the photodiode $\mathrm{pd_{ent}}$ as a function of the azimuthal angle ϕ_{moco} of the plate "moco qwp" is shown in Figure 5.14. In this figure the four maxima of intensity around −1.7 a.u. give the four "moco qwp"

azimuthal positions for which the laser beam is circularly polarised ($\phi_{\text{moco}} \sim -160^{\text{o}}, \sim -70^{\text{o}}, \sim 20^{\text{o}}, \sim 110^{\text{o}}$ in the figure).

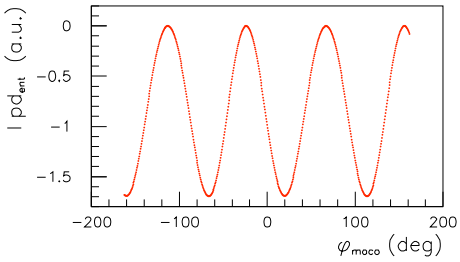

Figure 5.14: Experimental intensities recorded in the photodiode pd_{ent} when the cavity is unlocked, as a function of the azimuthal angle of the entrance quater wave plate "moco qwp".

5.5.2 DOCP measurements

Some examples of pull distributions (pull $= \sum[(\text{I} - \text{R T})/\,\sigma]$) are presented in Figure 5.15. The fourteen distributions are the results of fourteen independant fit using four-

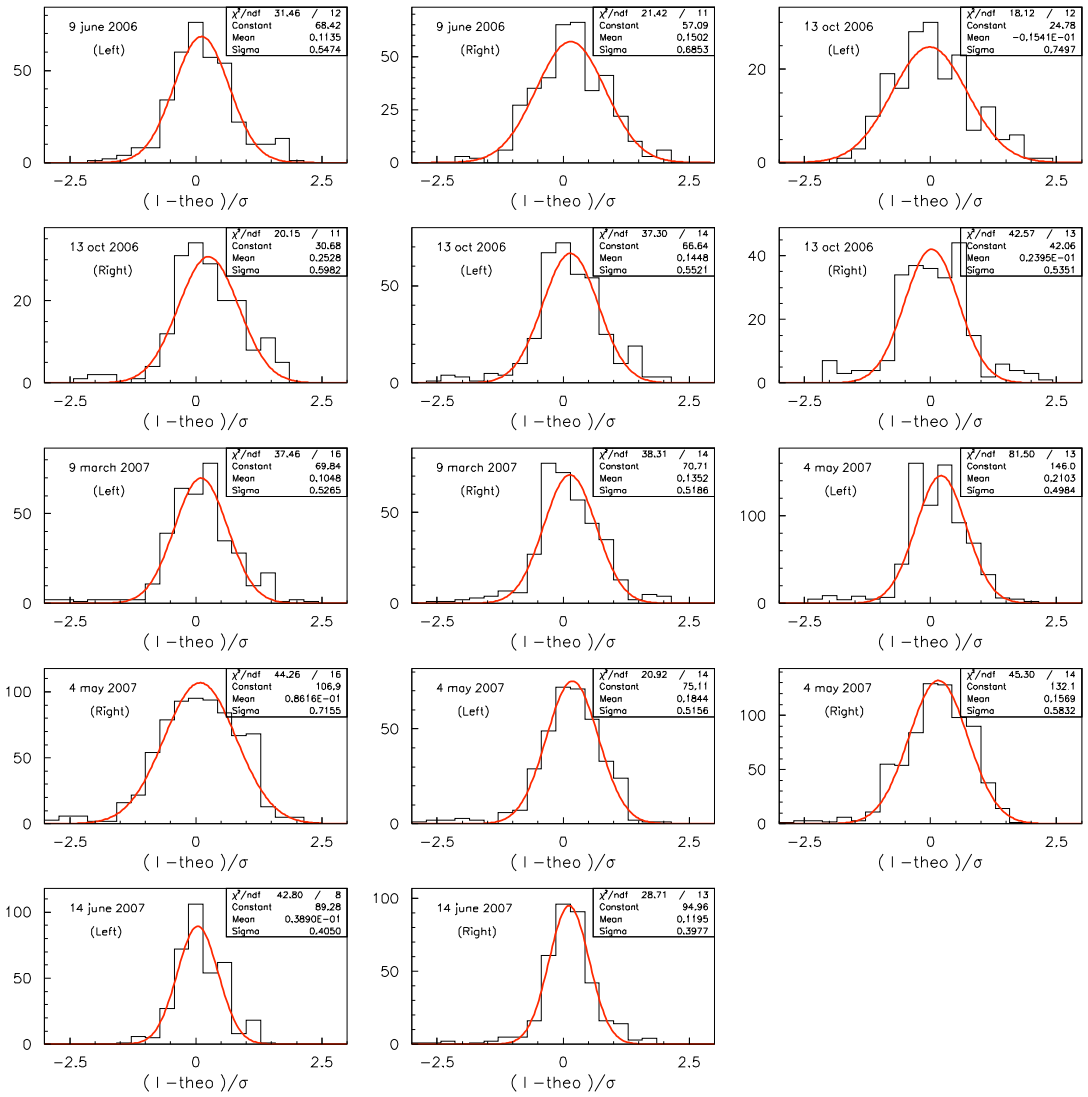

Figure 5.15: 14 pull distributions $\sum[(\text{I} - \text{R T})/\,\sigma]$ coming from the χ^2 minimisation of 14 independant data samples recorded in the ellipsometer from June 2006 to June 2007.

teen independent data samples. These data have been taken when the "moco qwp" is azimuthally positionned at a right or a left circular position, these positions being determined from curves as the one in Figure 5.14. Each of these samples contains 180 measurements of the photodiode signals corresponding to one azimuthal turn of the ellipsometer quater wave plate where one measurement is done every two degrees. The total time of data taking is about eleven minutes for each sample. Each pull distribution of Figure 5.15 come from the minimisation of the χ^2 of expression (5.1) in which the free parameters are the initial polarisation state parameters χ_{P} and ϕ_{P}.

From formula (4.14) and from the values of χ_{P} and ϕ_{P} returned by the minimisation, the DOCP values and their errors have been determined. They are listed in Table 5.4.

moco position #	date	DOCP value
1_{L}	6 June 2006	-0.98159 ± 0.00026
1_{R}		0.99713 ± 0.00011
1_{L}	13 October 2006	-0.98098 ± 0.00037
1_{R}		0.99771 ± 0.00014
2_{L}	13 October 2006	-0.99621 ± 0.00012
2_{R}		0.99480 ± 0.00028
3_{L}	9 March 2007	-0.97731 ± 0.00033
3_{R}		0.99276 ± 0.00019
3_{L}	4 May 2007	-0.97433 ± 0.00038
3_{R}		0.99242 ± 0.00021
4_{L}	4 May 2007	-0.99474 ± 0.00016
4_{R}		0.99765 ± 0.00008
4_{L}	14 June 2007	-0.99388 ± 0.00018
4_{R}		0.99690 ± 0.00013

Table 5.4: Values of Degree Of Circular Polarisation (DOCP) coming from 14 independant fits using 14 data samples taken from June 2006 to June 2007.

Let us make a few comments on the results of Table 5.4. Firstly, during one year (from June 2006 to June 2007), the "moco qwp" left and right circular positions have been changed only three times. Each time, a new curve of $\mathrm{pd}_{\mathrm{ent}}$ signal as a function of ϕ_{moco} was done to re-determine these circular positions. This was done after an hardware problem on the "moco qwp" rotating mount controller or after a dedicated check work involving the "moco qwp" or the photodiode $\mathrm{pd}_{\mathrm{ent}}$. Secondly, as shown in Table 5.4, DOCP measurements are very stable in the course of time: indeed ellipsometer measurements performed at a given "moco qwp" position and at several months of interval are stable at a few per mill level (see measurements # 1, 3, and 4 in Table 5.4). Over a one year period, the value of the DOCP showed an uncertainty of around two percent for two days only, due to a hardware problem detected too late.

5.5.3 Ellipsometer systematics

We have shown at the end of Section 5.2 that the data taking time of one set of ellipsometer measurements can have an effect on the photodiode intensity distributions, because of

long term random effects. This data taking time depends on the chosen interval between two consecutive azimuthal angles of the ellipsometer quater wave plate. We recall that for all the results of Table 5.4, data have been taken every two degrees which corresponds to an acquisition time of about eleven minutes.

To study the effect of this time of measurement on the DOCP values, we have fixed the "moco qwp" to a given position and several sets of measurements have been performed by the ellipsometer with different times of measurement (*i.e.* with different intervals between two consecutive azimuthal positions of the ellipsometer quater wave plate). Pull distributions resulting from the fits using these sets of measurements are shown in Figures 5.16 and 5.17 for a left and a right "moco qwp" position respectively.

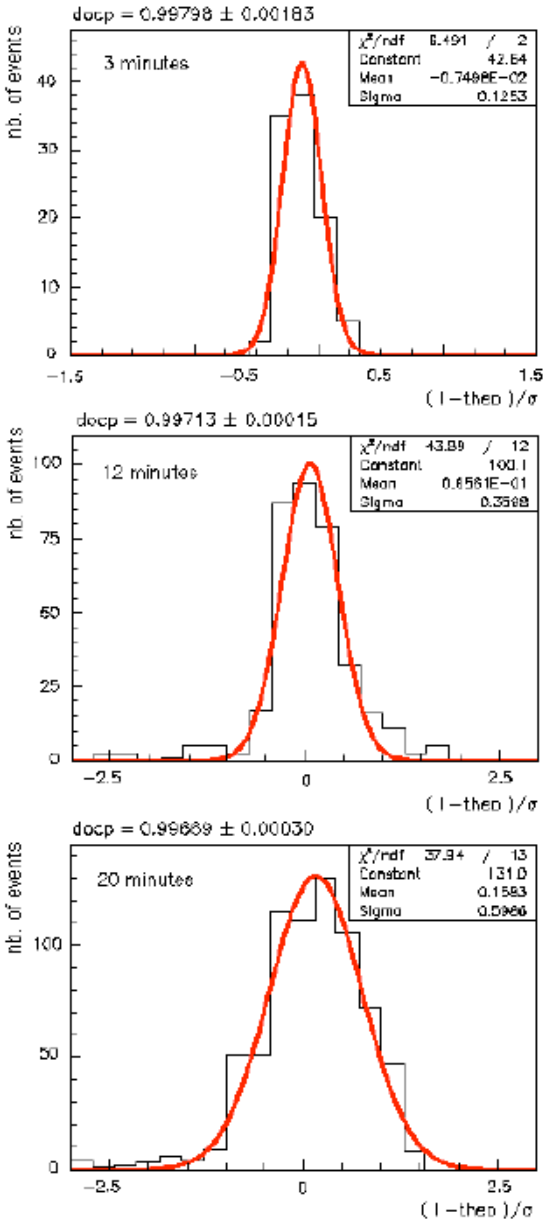

Figure 5.16: Pull distributions coming from three sets of ellipsometer measurements recorded with a different data taking time (3, 12 and 20 minutes) for a given right circular position of the "moco qwp". The corresponding values of the DOCP are also indicated.

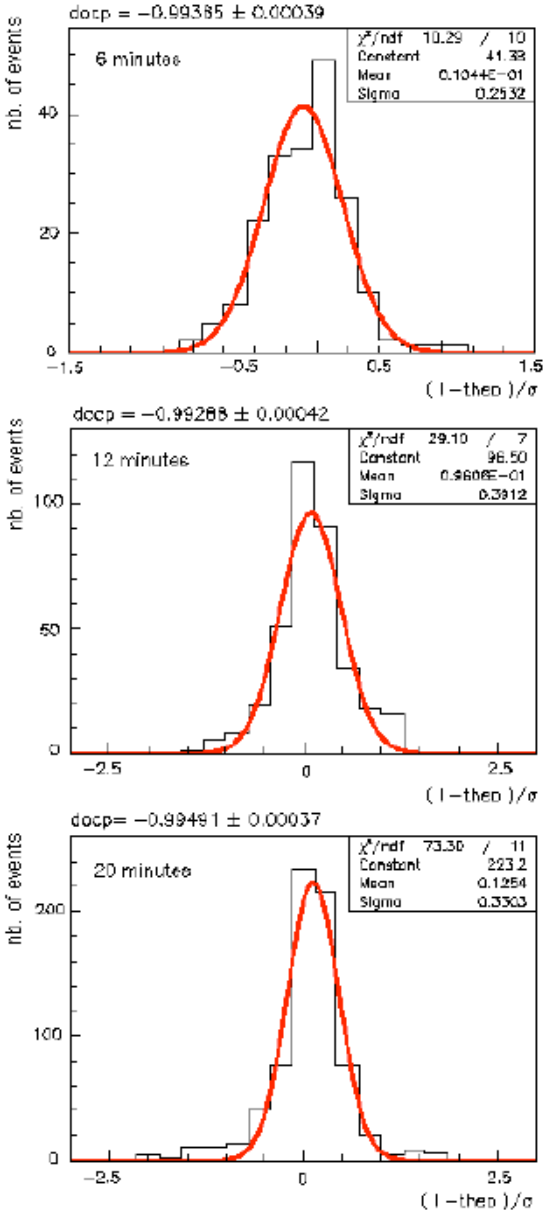

Figure 5.17: Pull distributions coming from three sets of ellipsometer measurements recorded with a different data taking time (6, 12 and 20 minutes) for a given left circular position of the "moco qwp". The corresponding values of the DOCP are also indicated.

In Figures 5.16, the pull distributions come from χ^2 minimisations using three data sets of which the time of acquisition was respectively three, twelve and twenty minutes. The "moco qwp" was in a right circular position. The three pull distributions look correct and the three values of the DOCP are compatible inside one and half per mill. In Figure 5.17, this systematic study is shown for a left circular "moco qwp" position and three data samples. The acquisitions of the three data sets lasted respectively six, twelve and twenty minutes. One sees that the differences of the three DOCP values are smaller than two per mill.

This study shows that the choice of the time of measurement may change of a few per mill the value of the DOCP. Having a large number of measurements and thus a larger probability of being disturbed by some long term effects, or on the contrary having less

measurements and less systematic effects, leads to a maximal shift of the DOCP values around two per mill. To remain conservative, an error of three per mill associated to the ellipsometer time of measurement will be considered as a systematic error for the final uncertainty on the DOCP.

Chapter 6

DOCP coherence and its total error

6.1 Introduction

The previous studies have provided precise values of the DOCP measured in the ellipsometer. These Degrees Of Circular Polarisation are measured at the entrance of the ellipsometer whereas the quantity involved for the determination of the HERA lepton beam polarisation is the laser DOCP at the interaction point, *i.e.* at the centre of the cavity. Therefore the main question is to deduce the DOCP at the centre of the cavity from the DOCP measured at the entrance of the ellipsometer. A priori these two values are the same, but because of the presence of optical components between the two points, it is possible that a small shift light be induced. The transport of the DOCP between the centre of the cavity and the entrance of the ellipsometer as well as the determination of the systematic errors associated to this transport are the objects of Sections 6.2 and 6.3. This chapter is also devoted to check the coherence of the values of the Degree Of Circular Polarisation at different points of our optical system. As this idea to measure the DOCP at various points was not envisaged at the beginning when the system was conceived, we will use all the information available in our setup to try to determine the transport of S_γ along the optical line and to check the coherence between several measurements at different points of the system. This will be studied in Section 6.5.

A global view of the whole cavity system composed of the entrance optical line, the cavity itself, the exit optical line and the ellipsometer is recalled in Figure 6.1.

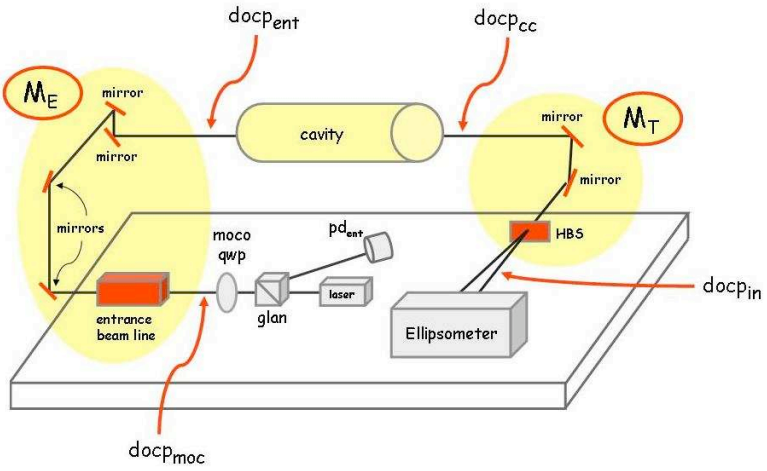

Figure 6.1: Basic optical schematic of the whole cavity system.

The four different points used in the following to check the DOCP coherence are indicated in Figure 6.1, as well as the entrance and the exit beam lines characterised by the transfer matrices M_E and M_T to be determined.

6.2 Parasitic ellipticity in the optical system

The set of DOCP of Table 5.4 characterises the light which enters the ellipsometer. The polarisation state of this light is not necessarily the same as the polarisation state of the light inside the cavity. Indeed between the centre of the cavity and the entrance of the ellipsometer, several optical elements can be a source of birefringence and may induce parasitic ellipticity modifying the laser beam polarisation. This small birefringence could introduce a systematic bias such that the DOCP measured by the ellipsometer would not be the DOCP at the cavity centre. Between the centre of the cavity and the ellipsometer itself, the following optical elements could induce some birefringence:

- the Fabry-Perot cavity mirror (substrate and its multi-layer coating) where possible birefringence effects can occur through thermoelastic deformation or during the manufacture of the multi-layers, and the mirror mounting system which could generate birefringence inside the substrate because of mechanical stress,

- the Fabry-Perot cavity exit vacuum window constituted of fused silica, where birefringence could be induced because of mechanical strains (during the manufacture of the window or because of air/vacuum pressure),

- the system constituted of the two 45° mirrors used to guide the light into the ellipsometer, and of the holographic beam sampler located at the entrance of the ellipsometer.

A simplified schematic view of the exit cavity mirror and vacuum window is presented in Figure 6.2.

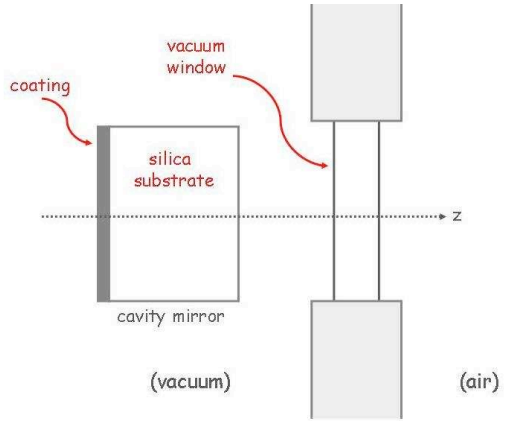

Figure 6.2: Basic drawing of the Fabry-Perot vacuum window and the exit mirror.

6.2.1 Birefringence in isotropic materials

Before estimating the possible parasitic birefringence caused by these optical elements, let us give some basic principles of the behavior of isotropic materials. In isotropic materials, birefringence occurs when the medium is deformed such that the isotropy is lost in one direction. At normal incidence, the small birefringence of such a non-absorbing element can simply be described by the Jones matrix of a delay plate:

$$\mathrm{M}_{\phi_{\mathrm{bir}}} = \begin{pmatrix} 1 & 0 \\ 0 & \mathrm{e}^{i\phi_{\mathrm{bir}}} \end{pmatrix} ,$$

where ϕ_{bir} is the birefringence. Assuming a light perfectly circular, the associated electric field is then written as:

$$\mathbf{E}_{\mathrm{circ}} = \frac{\sqrt{2}}{2} \begin{pmatrix} 1 \\ i \end{pmatrix} ,$$

and the DOCP is equal to 1. The electric field $\mathbf{E}$ of the beam after passing though the birefringent deformed element can then be written as a function of the birefringence ϕ_{bir} and as a function of an angle θ defining the orientation of the neutral axes of the matrix $\mathrm{M}_{\phi_{\mathrm{bir}}}$ with respect to the laboratory frame:

$$\mathbf{E} = \mathrm{R}_{\theta}^{-1}\, \mathrm{M}_{\phi_{\mathrm{bir}}}\, \mathrm{R}_{\theta}\, \mathbf{E}_{\mathrm{circ}} ,$$

where R_{θ} is a 2×2 rotation matrix. From this expression of $\mathbf{E}$, a small calculation allows the expression of the DOCP after passing through an optical element of birefringence $\phi_{\mathrm{bir}} \ll 1$ to be obtained:

$$\mathrm{DOCP} = 1 - \phi_{\mathrm{bir}}^2/2 . \tag{6.1}$$

In the following, the order of magnitude of the birefringences of the optical elements located between the cavity centre and the ellipsometer is estimated in order to evaluate the biases induced on the DOCP values.

6.2.2 Fabry-Perot exit mirror, its coating and its mount

A birefringence can occur in the cavity mirror silica substrate through thermoelastic deformation due to the high circulating power [125] in the cavity. This effect is numerically estimated in [50] (page 152) by considering a confocal cavity of 2 meter length, a laser wavelength $\lambda = 1064$ μm, a beam spot diameter of ≈ 1.5 mm on the cavity mirrors, a circulating power of 10 kW and a coating transmission coefficient of $\approx 10^{-6}$. The result is a birefringence below 1 mrad that leads according to (6.1) to a negligible DOCP bias of the order of 10^{-6}.

A birefringence can also occur in the multi-layers coating of the cavity mirror and then leads to parasitic ellipticity during the transmission of the beam through the exit mirror. This birefringence has been measured for instance in [126], [127] and [128] for cavity finesses of 6600, 86500 and 100000 respectively. In all these measurements the order of magnitude of the mirror birefringence is $\phi_{\mathrm{bir}} \approx 10^{-6}$ rad. Our multi-layer coating mirrors leading to a finess of about 30000, we can use this birefringence order of magnitude and we conservatively take $\phi_{\mathrm{bir}} = 2.2 \times 10^{-6}$ rad [127]. Of course, with such a birefringence value, the difference $\phi_{\mathrm{bir}}^2/2$ of the Degree Of Circular Polarisation values in the cavity and at the exit of the cavity is totally negligible.

The last source of birefringence for the cavity mirror is the mounting system schematized in Figure 6.3. It consists of a spring pushing a ring in contact with the cavity mirror.

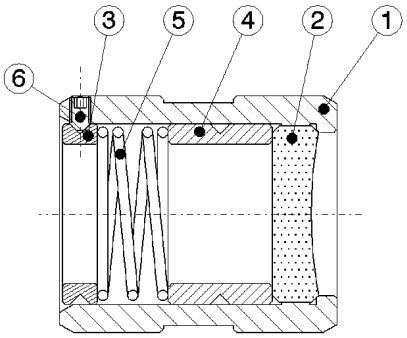

Figure 6.3: Technical drawing of the cavity mirror mount system. From [129].
① : mirror holder,
② : mirror,
③ : spacer,
④ : spacer,
⑤ : spring,
⑥ : stop screw.

The force supplied by the spring on the mirror has been measured [130] and estimated to be at most 2 N that leads to a birefringence of the order of 10^{-11} rad for our 6 mm thickness mirror (see [50] page 122). This effect is negligible.

6.2.3 Fabry-Perot exit vacuum window

The two vacuum windows of the Fabry-Perot cavity are constituted of glass-metal soldering ring from VERMETAL. The birefringence induced by the mechanical constraints due to the air/vacuum pressure have been estimated in [50] (page 150) and found to be less than 1 mrad which leads to a negligible DOCP bias.

Although the glass is fused silica, mechanical constraints could appear during the manufacturing process [131]. A special dedicated study was performed to measure the induced birefringence. A robust method to determine the birefringence of an optical element consists in turning it between two crossed polarisers and measuring the variations of the transmitted intensities coming from a laser. These variations as a function of the azimuthal rotation angle lead to the parameter ϕ_{bir} of the element. This study on the vacuum window has been done by M. Linz at the ENS laboratory in Paris [132]. The birefringence has been measured for the main part of the window by making a two dimension spatial scan. Results are presented in Figure 6.4: the three curves correspond

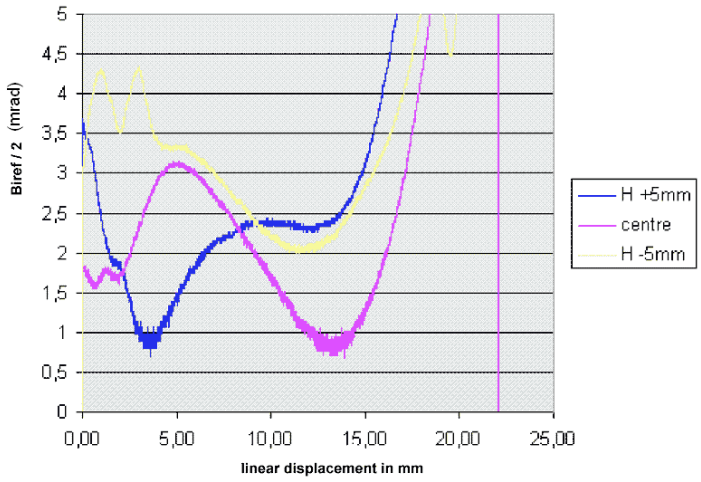

Figure 6.4: Results of the vacuum window birefringence measurements $\phi_{\text{bir}}/2$ as a function of the window position.

to three different positions of the window (centre and ±5 mm apart) with respect to the laser beam, along an arbitrary direction. For each one of these positions, a scan has been done in the other direction from 0 to 22 mm (the centre of the window corresponds to 11 mm). Within a few millimeters from the window centre, the birefringence remains inferior to 5 mrad. This means that the parasitic ellipticity due to the small birefringence of the window is, at the utmost, of the order of 25×10^{-6} which is negligible compared to our required precision.

6.2.4 The system of the two mirrors and the HBS

The dominant source of parasitic ellipticity is the 45° dielectric mirrors since the mirrors have different reflection coefficients for the electric field component in the plane of incidence and for the electric field component perpendicular to the plane of incidence (see Figure 2.24). To determine this parasitic ellipticity, several dedicated sets of data have been taken with the ellipsometer in order to determine the transfer matrix of this exit optical system. The procedure allowing the determination of the characteristic parameters of this exit transfer matrix is the object of the next section.

6.3 Exit transfer matrix

6.3.1 Experimental setup and data taking

Before dismounting the whole setup at the end of the HERA experiment in July 2007, we have performed a dedicated experiment to characterise the optical system composed of the two mirrors and the HBS, located at the exit of the cavity. The matrix of this system is called M_T. To determine M_T elements, the configuration of the cavity system is the one schematized in Figure 6.5: a linear Glan polariser has been added between the exit window of the cavity and the first mirror used to guide the light in the ellipsometer. This allows us to make sure that the beam, before going through the optical elements we want to study, is completely linearly polarised. The DOCP at the entrance of the ellipsometer is called $\mathrm{DOCP_e}$.

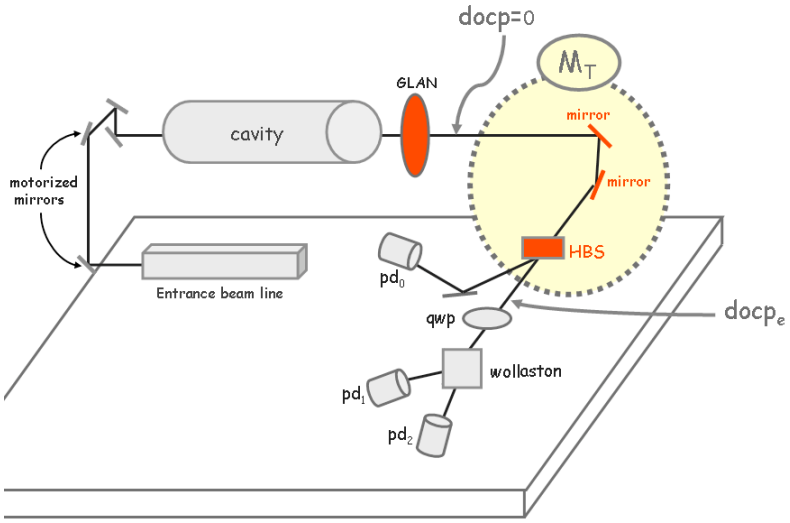

Figure 6.5: Basic optical schematic of the cavity system used to determine the transfer matrix M_T between the exit of the cavity and the ellipsometer.

The data taking procedure is the following: for one given azimuthal position ϕ_G of the Glan, the ellipsometer quater wave plate has been rotated every 6^o from 0^o to 360^o. This was done for the several azimuthal Glan positions $\phi_G = 0^o$, -20^o, -40^o, -60^o, -80^o, 80^o, 60^o, 40^o. All these data have been used together in a fit to determine the polarisation states of the beam after the HBS, *i.e.* the (ξ^e, ϕ^e) doublets at each ϕ_G position. The χ^2 used for this minimisation procedure is the one of formula (5.1).

Figure 6.6 (respectively Figure 6.7) shows the good agreement between the experimental data and the theoretical intensities I_1 (respectively I_2) for the eight data samples. The inclusive pull distribution $(I-R\ T)/\sigma$ including all the data samples is presented in Figure 6.8 and shows a good fit quality. Results of the Degrees Of Circular Polarisation $DOCP_e$ and their associated errors σ_{DOCP_e} coming from the fitted (ξ^e, ϕ^e) doublets are listed in Table 6.1 for the eight ϕ_G positions. One sees from Table 6.1 that the $DOCP_e$ values are not compatible with zero. This means that the polarisation states are not completely linear as it would be the case if the system of the two mirrors and the HBS did not have any parasitic birefringence. To be able to correct for the bias between the values of the DOCP at the exit of the cavity and at the entrance of the ellipsometer, the system has to be modeled with a transfer matrix M_T.

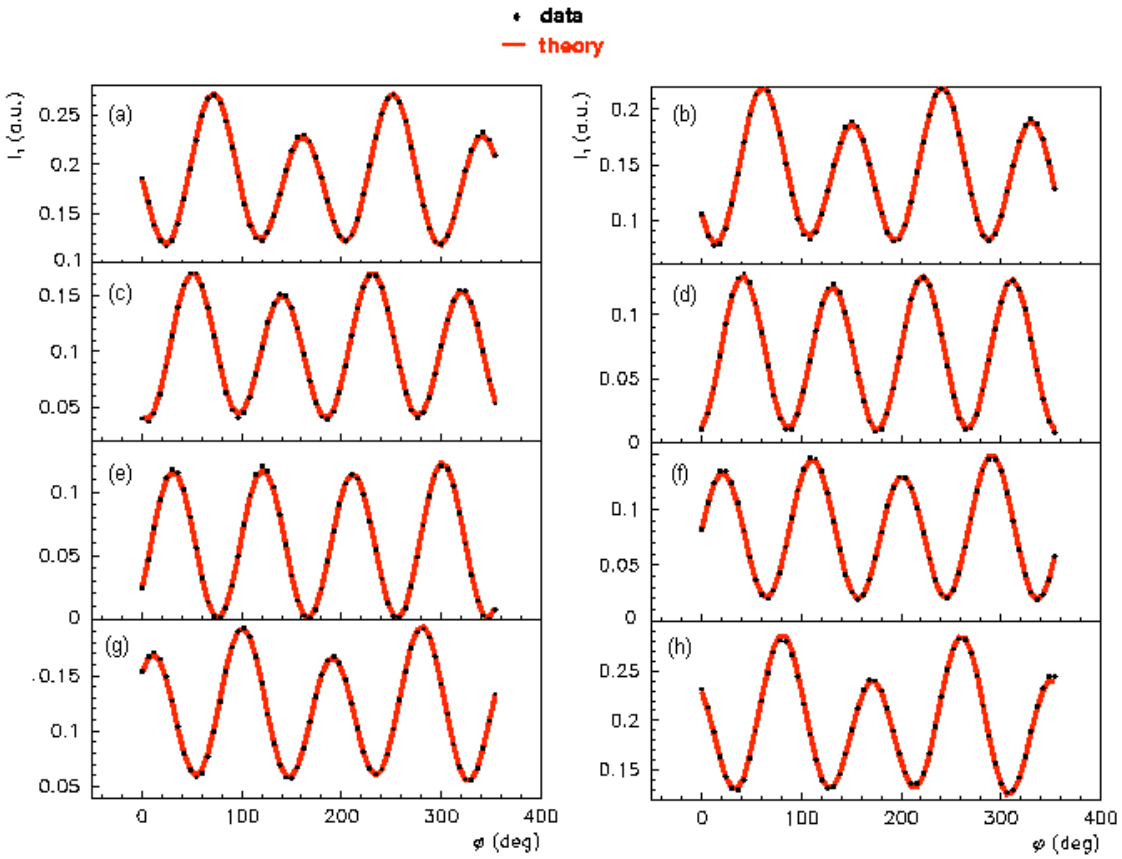

Figure 6.6: Experimental and theoretical intensities I_1 as a function of the azimuthal angle ϕ of the ellipsometer quater wave plate, for the eight different azimuthal Glan positions ϕ_G: $\phi_G = -20^o$ (a), $\phi_G = -40^o$ (b), $\phi_G = -60^o$ (c), $\phi_G = -80^o$ (d), $\phi_G = 80^o$ (e), $\phi_G = 60^o$ (f), $\phi_G = 40^o$ (g), $\phi_G = 0^o$ (h).

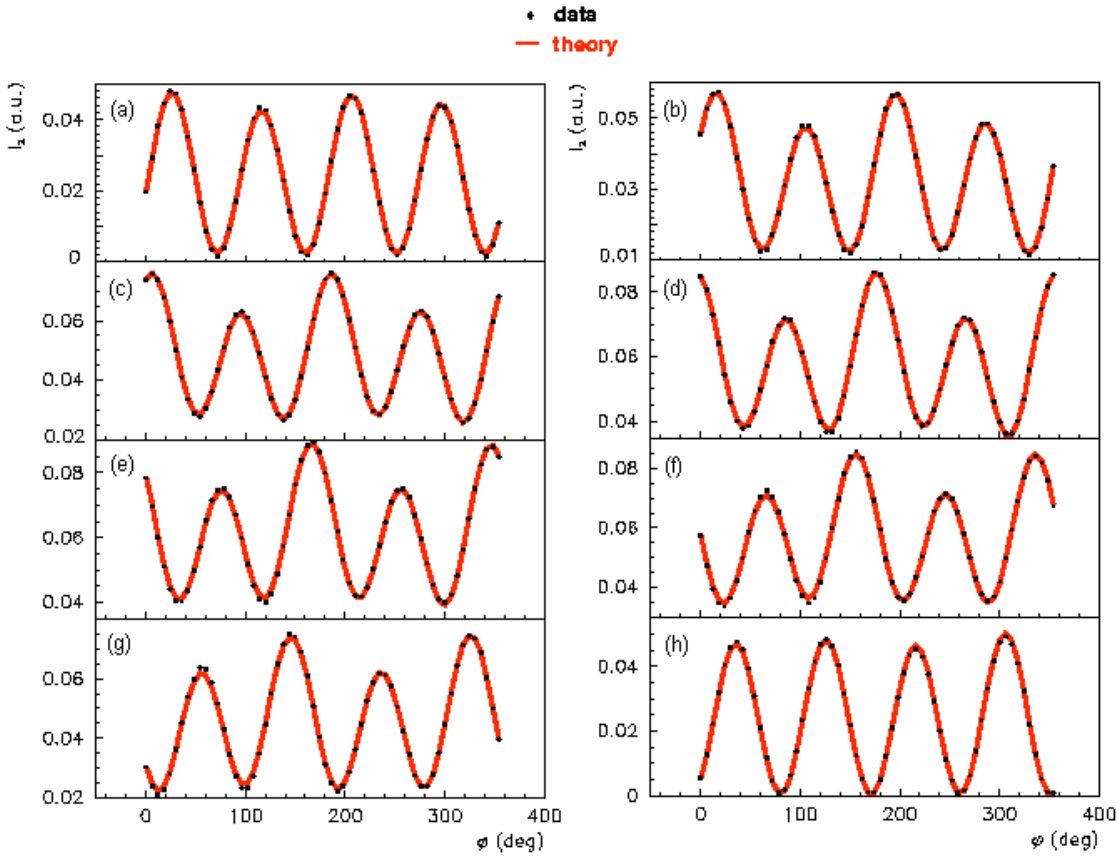

Figure 6.7: Experimental and theoretical intensities I_2 as a function of the azimuthal angle ϕ of the ellipsometer quater wave plate, for the eight different azimuthal Glan positions ϕ_G: $\phi_G = -20^o$ (a), $\phi_G = -40^o$ (b), $\phi_G = -60^o$ (c), $\phi_G = -80^o$ (d), $\phi_G = 80^o$ (e), $\phi_G = 60^o$ (f), $\phi_G = 40^o$ (g), $\phi_G = 0^o$ (h).

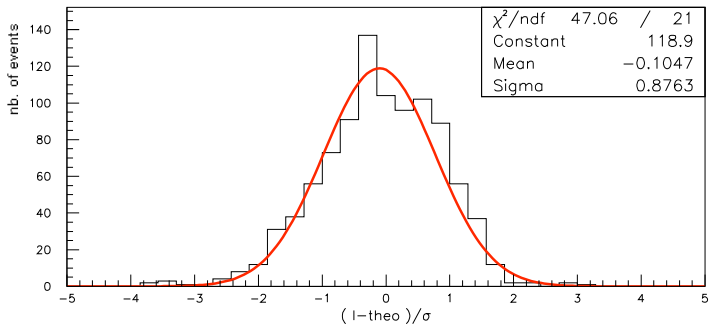

Figure 6.8: Inclusive pull distribution $(I - R\ T)/\sigma$ of the eight data samples recorded in the ellipsometer at the eight azimuthal Glan positions.

ϕ_G (in ^{o})	0	−20	−40	−60	−80	80	60	40
$DOCP_e \times 10^2$	1.032	−0.362	−1.987	−2.880	−2.447	−0.962	0.894	2.109
$\sigma_{DOCP_e} \times 10^2$	0.153	0.153	0.165	0.172	0.182	0.192	0.176	0.162

Table 6.1: $DOCP_e$ values and their errors coming from fits using the experimental data recorded at eight azimuthal angles ϕ_G of the Glan polariser.

6.3.2 The matrix M_T

An optical theorem demonstrated by R. Clark Jones [133] states that any optical system composed of any non-absorbing components may always be replaced by an optical system composed of four elements: the four element system consists of a partial polariser placed between two delay plates, with the addition of a rotator inserted at any position in the system. The Jones matrix of a partial polariser is called P_p, that of a delay plate G_γ and that of a rotator R_θ. Under the assumption that no power is absorbed in optical materials, they are written as [134]:

$$P_p = \begin{pmatrix} p_1 & 0 \\ 0 & p_2 \end{pmatrix} \ , \ G_\gamma = \begin{pmatrix} e^{i\gamma} & 0 \\ 0 & e^{-i\gamma} \end{pmatrix} \ , \ R_\theta = \begin{pmatrix} \cos\theta & -\sin\theta \\ \sin\theta & \cos\theta \end{pmatrix} . \tag{6.2}$$

Following the Jones theorem [133] and starting with a completely linear polarisation state $\mathbf{E_c}$ at the exit of the cavity, the theoretical final state $\mathbf{E_{th}}$ at the entrance of the ellipsometer can be modeled as follows:

$$\mathbf{E_{th}} = M_T \ \mathbf{E_c} \ , \quad \text{with} \quad M_T = R_{\theta_1} \ G_{\gamma_1} \ R_{\theta_2} \ P_p \ R_{\theta_3} \ G_{\gamma_2} \ , \tag{6.3}$$

where the two polarisation states $\mathbf{E_{th}}$ and $\mathbf{E_c}$ are written as:

$$\mathbf{E_{th}} \ = \ \begin{pmatrix} \cos\xi^{th} \ e^{i\phi_x^{th}} \\ \sin\xi^{th} \ e^{i\phi_y^{th}} \end{pmatrix} \quad , \quad \mathbf{E_c} \ = \begin{pmatrix} \cos\phi_G \\ \sin\phi_G \end{pmatrix} \ . \tag{6.4}$$

Expressions (6.2), (6.3) and (6.4) allow the expressions of ξ^{th}, ϕ_x^{th} and ϕ_y^{th} to be obtained as function of the parameters θ_1, θ_2, θ_3, γ_1, γ_2, p_1 and p_2 of the matrix M_T and as a function of the angle ϕ_G of the polarisation initial state. Then the minimisation of the χ^2 defined by:

$$\chi^2 \ = \ \sum_{j=1,N_d} \left[\left(\frac{\xi_j^{th} - \xi_j^e}{\sigma_{\xi_j^e}} \right)^2 \ + \ \left(\frac{\phi_j^{th} - \phi_j^e}{\sigma_{\phi_j^e}} \right)^2 \right] \tag{6.5}$$

leads to the parameters of the transfer matrix M_T. In expression (6.5), $\phi^{th} = \phi_y^{th} - \phi_x^{th}$, N_d refers to the number of data files ($N_d = 8$ corresponding to our eight sets of measurement described in the previous section), and ξ_j^e and ϕ_j^e are the polarisation state parameters corresponding to the $DOCP_e$ values of Table 6.1.

A Monte Carlo study of this system has shown that some parameters of the matrix M_T are completely correlated and that the system can be described only with one delay plate and one partial polariser at one parameter p. Therefore we restrict the matrix M_T at the following expression:

$$M_T = \begin{pmatrix} \cos\theta_1 & -\sin\theta_1 \\ \sin\theta_1 & \cos\theta_1 \end{pmatrix} \begin{pmatrix} e^{i\gamma} & 0 \\ 0 & e^{-i\gamma} \end{pmatrix} \begin{pmatrix} \cos\theta_2 & -\sin\theta_2 \\ \sin\theta_2 & \cos\theta_2 \end{pmatrix} \begin{pmatrix} p & 0 \\ 0 & 1 \end{pmatrix} . \tag{6.6}$$

Using our eight (ξ^e, ϕ^e) doublets determined in Section 6.3.1, the minimisation of the χ^2 leads to the following results for the angle of the delay plate and the partial polariser parameter:

$$\begin{cases} 2\gamma &= 26.25 \pm 2.83 \text{ mrad} \\ p &= 1.0010 \pm 0.0009 \ . \end{cases} \tag{6.7}$$

6.3.3 $\mathrm{DOCP_{cc}}$ at the exit of the cavity

Having determined the transfer matrix $\mathrm{M_T}$ with the addition of a Glan polariser in the system, the DOCP at the exit of the cavity have now to be determined as a function of the DOCP at the entrance of the ellipsometer, and this for any measurement we have made with the ellipsometer. The polarisation state at the exit of the cavity is called $\mathbf{E_{cc}}$ and is determined by the relations:

$$\mathbf{E_{cc}} = \mathrm{M_T^{-1}}\ \mathbf{E_{in}}\ \ , \quad \text{with} \quad \mathbf{E_{cc}} = \begin{pmatrix} \cos\chi_{\mathrm{cc}}\ \mathrm{e}^{i\phi_{\mathrm{x}}} \\ \sin\chi_{\mathrm{cc}}\ \mathrm{e}^{i\phi_{\mathrm{y}}} \end{pmatrix}\ \ ,$$

where the matrix $\mathrm{M_T^{-1}}$ is the inverse of the transfer matrix $\mathrm{M_T}$ and where the field $\mathbf{E_{in}}$ is the polarisation state at the entrance of the ellipsometer defined in (4.6). The development of this expression and the definition of the DOCP (3.4) lead to the relation:

$$\mathrm{DOCP_{cc}} = \mathrm{DOCP_{in}} \times \mathrm{F}(\theta_1, \theta_2, \gamma, \mathrm{p}, \chi_{\mathrm{P}}, \phi_{\mathrm{P}})\ \ , \tag{6.8}$$

where χ_{P}, ϕ_{P} and $\mathrm{DOCP_{in}}$ are the polarisation state angles and the Degree Of Circular Polarisation determined at the entrance of the ellipsometer (*i.e.* for instance the DOCP values of Table 5.4). Values of F and $\mathrm{DOCP_{cc}}$ are presented in Table 6.2 where we can see that the parasitic birefringence due to the optical components between the exit of the cavity and the entrance of the ellipsometer induces biases of at maximum five per mill and sometimes less. Errors on $\mathrm{DOCP_{cc}}$ in Table 6.2 have been calculated from the elements of $\mathrm{M_T}$ and their uncertainties: for all possible combinations of $\mathrm{M_T}$ elements ($\gamma + \sigma_\gamma$ and $\mathrm{p} + \sigma_{\mathrm{p}}$, or $\gamma - \sigma_\gamma$ and $\mathrm{p} + \sigma_{\mathrm{p}}$, or $\gamma + \sigma_\gamma$ and $\mathrm{p} - \sigma_{\mathrm{p}}$, or $\gamma - \sigma_\gamma$ and $\mathrm{p} - \sigma_{\mathrm{p}}$), calculations of

$\mathrm{DOCP_{in}}$	F	$\mathrm{COR_{DOCP}}$	$\mathrm{DOCP_{cc}}$
−0.98159	1.0049	4.792×10^{-3}	−0.97680±0.00036
0.99713	1.0017	-1.675×10^{-3}	0.99546±0.00019
−0.98098	1.0050	4.891×10^{-3}	−0.97609±0.00037
0.99771	1.0015	-1.522×10^{-3}	0.99618±0.00017
−0.99621	1.0019	1.884×10^{-3}	−0.99433±0.00017
0.99480	1.0027	-2.634×10^{-3}	0.99217±0.00030
−0.97731	1.0054	5.250×10^{-3}	−0.97206±0.00040
0.99276	0.9981	1.910×10^{-3}	0.99467±0.00032
−0.97433	1.0058	5.638×10^{-3}	−0.96869±0.00042
0.99242	0.9980	1.988×10^{-3}	0.99441±0.00033
−0.99474	1.0025	2.440×10^{-3}	−0.99230±0.00020
0.99765	1.0016	-1.628×10^{-3}	0.99602±0.00018
−0.99388	1.0027	2.723×10^{-3}	−0.99116±0.00022
0.99690	1.0019	-1.891×10^{-3}	0.99501±0.00021

Table 6.2: Set of $\mathrm{DOCP_{in}}$ values measured at the ellipsometer entrance (*i.e.* values of Table 5.4), corresponding values of the bias F defined in (6.8), differences $\mathrm{COR_{DOCP}} = \mathrm{DOCP_{cc}} - \mathrm{DOCP_{in}}$ (where $\mathrm{DOCP_{cc}}$ is the DOCP values just after the exit of the cavity), and $\mathrm{DOCP_{cc}}$ values. The errors on $\mathrm{DOCP_{cc}}$ come from the $\mathrm{M_T}$ parameters uncertainties (see text).

$\mathrm{DOCP_{cc}}$ have been performed and the error on one $\mathrm{DOCP_{cc}}$ value is the maximum change with respect to the central value (the central value being calculated with the values γ and p of formula (6.7)).

Each bias is calculable for each ellipsometer measurement and does not enter as a systematic error but is explicitly determined to correct each DOCP measurement.

6.3.4 Cross-check

Let us finish with a cross-check of this study. For this, a set of data have been recorded with the additional linear Glan polariser located this time after the HBS (*i.e.* between the HBS and the quater wave plate, see Figure 6.5). As previously, ellipsometer data sets have been taken at several azimuthal angles of the Glan. Applying the same fit procedure (described in Section 6.3.2) we expect the matrix $\mathrm{M_T}$ to be compatible with the identity since there is no optical component between the Glan and the entrance of the ellipsometer. And indeed, the result of the fit leads to an angle γ_{check} for the delay plate compatible with zero and a partial polariser parameter $\mathrm{p_{check}}$ compatible with the unity:

$$\begin{cases} 2\gamma_{\mathrm{check}} &= 1.47 \pm 4.01 \text{ mrad} \\ \mathrm{p_{check}} &= 1.0040 \pm 0.0050 \, . \end{cases}$$

Using these parameters, biases $\mathrm{DOCP_{check}}$-$\mathrm{DOCP_{in}}$ for the twelve measurements of Table 5.4 are of the order of 7×10^{-5} (more precisely all of them are between 3.0×10^{-5} and 1.0×10^{-4}) which is compatible with zero taking into account the measurement uncertainties of Table 5.4.

6.3.5 Summary

The birefringence of the HBS alone had been measured before its utilisation in our cavity system and the result had given a birefringence compatible with zero [132]. During these measurements, the holographic beam sampler was not screwed in its mount. In order to preserve this null birefringence, a "stress free" stick has been used to mount the HBS in the optical line in the tunnel at HERA.

Therefore, the HBS being not the cause of parasitic ellipticity, the biases of a few per mill coming from the exit cavity transfer matrix is due to the two mirrors system. That confirms a measurement done at Saclay in 1999 for the TJNAF Polarimeter [135], in which the effect of the two mirrors on the DOCP had been measured and found to be of the order of a few per mill.

6.4 The entrance transfer matrix $\mathrm{M_E}$

Although the previous studies have provided a precise value of the DOCP and of its systematics, here, we aim at characterising the entrance optical elements by a matrix $\mathrm{M_E}$ (see Figure 6.1) to understand the DOCP transport between the entrance quater wave plate (the "moco qwp" of Figure 6.1) and the ellipsometer and to verify that it is compatible with our expectations. The entrance beam line, composed of lens and mirrors, will be described using the R. Clark Jones optical theorem [133] already cited in the previous section.

6.4.1 M_E determination principle

To determine the parameters of the matrix M_E, one dedicated set of data have been recorded with the photodiode pd_{ent} located just behind the Glan of the entrance beam line (see Figure 6.1), when the cavity is not locked. In that way the beam linearly polarised by the Glan passes through the "moco qwp" and through the entrance optical elements M_E, then is reflected by the cavity entrance mirror, and then passes again through the system M_E-moco-Glan in the other direction. The "moco qwp' used to polarise the beam is rotated azimuthally and data are taken every half degree. Data recorded at the various "moco qwp" azimuthal angles in the photodiode pd_{ent} are called I_{diode} and will allow the elements of the matrix M_E to be determined.

When the system was conceived, the photodiode pd_{ent} was only devoted to determine the azimuthal "moco qwp" positions leading to a right or a left circular polarisation of the laser beam (by simply recording a curve as the one of Figure 5.14). Thus, there was no particular study of the response and of the measurement uncertainties of this photodiode. In order to have a better control on pd_{ent} (and since the ellipsometer is not used for this special dedicated study), before taking data, we have replaced the photodiode pd_{ent} by a photodiode belonging to the ellipsometer (in the following nevertheless we keep the same name pd_{ent}).

6.4.2 The model

To calculate the light path through the optical system and its return, it is not necessary to make calculation for its passage in the back direction. Indeed a reversibility theorem [133] states that for a given matrix M describing the light path through a given system, the matrix corresponding to the light path in the opposite direction is the transposed of the matrix M.

In this study, although the photodiode pd_{ent} is an ellipsometer photodiode (and then precisely controlled), the measurement precision is not as good as the ellipsometer one because of the absence of a reference photodiode to compensate the laser power variations. Consequently, we will not develop a complete model to determine the entrance transfer matrix: the Glan polariser, the "moco qwp" quater wave plate (which is a plate treated with an anti-reflection coating) and the cavity mirror will be considered as perfect, and the error associated to each pd_{ent} measurement will be the width of each pd_{ent} measurement distribution without taking into account possible systematic effects and without seeking to parametrise these errors. The order of magnitude of the pd_{ent} errors is of one to two percent.

In a frame attached to the horizontal and vertical axes of the Glan, and starting with an assumed perfect horizontal linear polarisation state E_{start} just after the Glan:

$$E_{start} = \begin{pmatrix} 1 \\ 0 \end{pmatrix} \quad ,$$

the theoretical field E_{pd} associated to the intensity detected in the photodiode can be written as:

$$\mathbf{E_{pd}} = G_{lan}\ M_{entr}^{(T)}\ M_{mir}\ M_{entr}\ E_{start} \quad , \tag{6.9}$$

where:

- G_{lan} is the matrix of the Glan polariser letting pass only the vertical component of the field when the beam returns:

$$G_{lan} = \begin{pmatrix} 0 & 0 \\ 0 & 1 \end{pmatrix} \quad ,$$

- M_{mir} is the Jones matrix of the cavity mirror:

$$M_{mir} = \begin{pmatrix} 1 & 0 \\ 0 & 0 \end{pmatrix} \quad ,$$

- M_{entr} is the transfer matrix of the system composed of the elements to be characterised and of the rotating "moco qwp":

$$M_{entr} = M_E \; R_{\theta_a} \; M_{moco} \; R_{\theta_b} \quad .$$

  Expression of M_E is the same as M_T (see expression (6.3)). The "moco qwp" being considered as perfect, *i.e.* without any defect and in which no multiple reflection occur, the expression of the Jones matrix M_{moco} is given by (3.6) where $\phi_{sh} = \pi/2$. R_{θ_a} and R_{θ_b} are two 2×2 rotation matrices introduced to reflect the azimuthal orientation of the "moco qwp" with respect to the Glan polariser axes.

- $M^{(T)}_{entr}$ is the transposed of M_{entr}.

Theoretical intensities received by the photodiode are called I_{theo} and are written as $I_{theo} = |\mathbf{E_{pd}}|^2$. As before, a Monte Carlo sample has been simulated, as closely as possible to the real data. Figure 6.9 shows the simulated and experimental intensities recorded in the photodiode pd_{ent} as a function of the "moco qwp" azimuthal angle ϕ_{moco}.

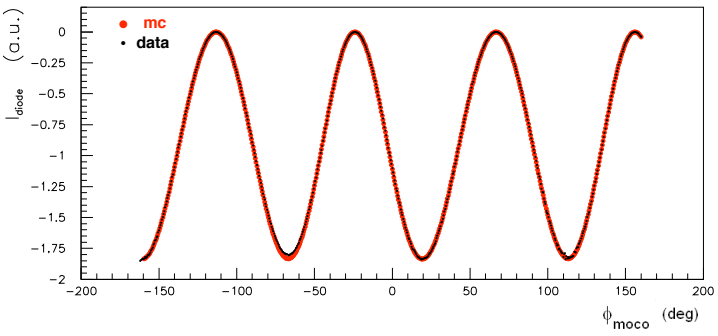

Figure 6.9: Simulated intensities I_{theo} (big red points) and experimental data intensities I_{diode} (small black points) recorded in the photodiode pd_{ent} located behind the Glan when the cavity is unlocked, as a function of the azimuthal angle of the "moco qwp".

In order to determine the elements of the matrix M_E, the following χ^2 is then constructed:

$$\chi^2 = \sum_{i=1,N} \left(\frac{R\, I^i_{theo} - I^i_{diode}}{\sigma^i} \right)^2 \quad , \tag{6.10}$$

where N is the number of measurements (around 500), I^i_{theo} are the theoretical intensities calculated at the i^{th} value of the azimuthal "moco qwp" angle ϕ_{moco}, I^i_{diode} are the intensities measured in the photodiode pd_{ent} at the i^{th} value of ϕ_{moco}, σ^i are the errors associated to the measured intensities I_{diode} and are of the order of one to two percent, and R is a normalisation factor which is easily determined since the resolution of $\partial\chi^2/\partial R = 0$ leads to analytic expressions for R.

6.4.3 Fit and results

A short study of the simulated data has shown that the data are well described by using only one delay plate and one polariser in the expression of M_E. The transfer matrix M_E is therefore written as (6.6), and thus depends only on two parameters called γ_E and p_E, and on two rotation angles called θ_{E_1} and θ_{E_2}. The χ^2 has firstly been minimised by using the simulated sample to check that the elements of M_E are well determined by the minimisation procedure. Values of these elements are presented in Table 6.3.

parameter	simulated	fitted
γ_E (mrad)	−32.81	−33.04±0.14
p_E	1.17	1.179±0.004
θ_{E_1} (deg)	6.50	6.466±0.028
θ_{E_2} (deg)	−12.50	−11.805±0.064

Table 6.3: Simulated elements of M_E and results of the fit using the simulated sample of Figure 6.9.

On the real data, the minimisation leads to the following γ_E and p_E parameters:

$$\begin{cases} \gamma_E = -32.83 \pm 0.51 \text{ mrad} \\ p_E = 1.167 \pm 0.013 \ , \end{cases} \tag{6.11}$$

The good agreement between the experimental intensities and the theoretical ones is presented in Figure 6.10 and the distributions of the pull $\sum(I_{diode} - R\ I_{theo})/\sigma$ for the experimental and simulated data samples are presented in Figure 6.11.

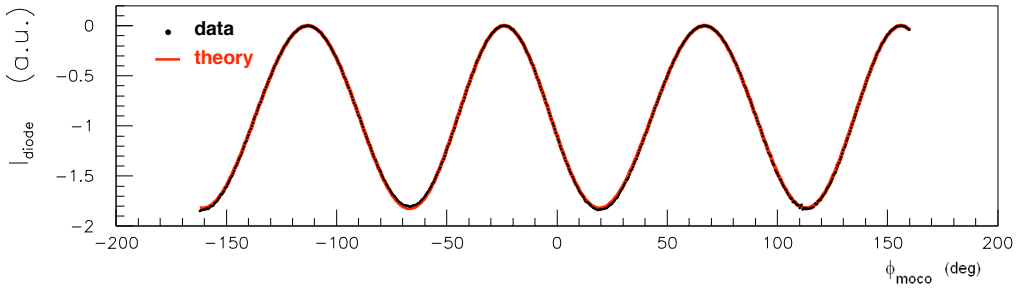

Figure 6.10: Data measurements (black points) and theoretical intensities (red line), as a function of the azimuthal angle of the "moco qwp".

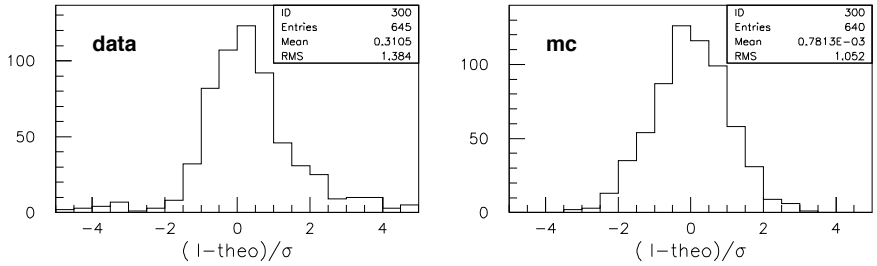

Figure 6.11: Pull distributions $\sum(I_{diode} - R\ I_{theo})/\sigma$ for the experimental (left) and simulated (right) data samples.

Effects of the matrix M_E are illustrated in Figures 6.12 and 6.13. Figure 6.12 shows the ratio of the experimental intensities over the theoretical ones (I_{diode}/I_{theo}) when the minimisation has been done (black dotted line) and when the matrix M_E has been fixed to the identity (red full line). In Figure 6.13, intensities recorded in pd_{ent} and normalised to the unity have been simulated using two sets of parameters of the matrix M_E: the one determined in the data fit (formula (6.11)) and a matrix M_E equal to the identity. Whereas the intensity maxima are spaced of exactly 90° when M_E is the identity (red full line), they are spaced two by two by 93.6° and 86.4° when M_E is the real entrance optical matrix (black dotted line). It is interesting to remark that these two spacing values are also observed on the experimental intensities as shown in Figure 6.10.

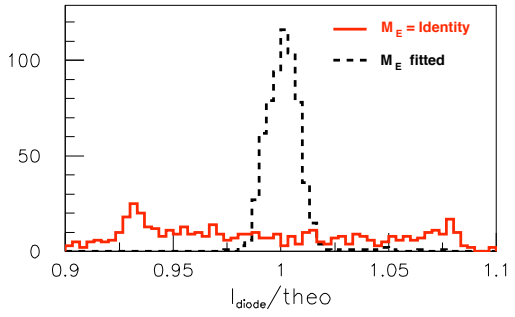

Figure 6.12: Ratio I_{diode}/I_{theo} of the measured intensities over the theoretical ones when the minimisation is done (black dotted line) and when the matrix M_E is fixed to the identity (red full line).

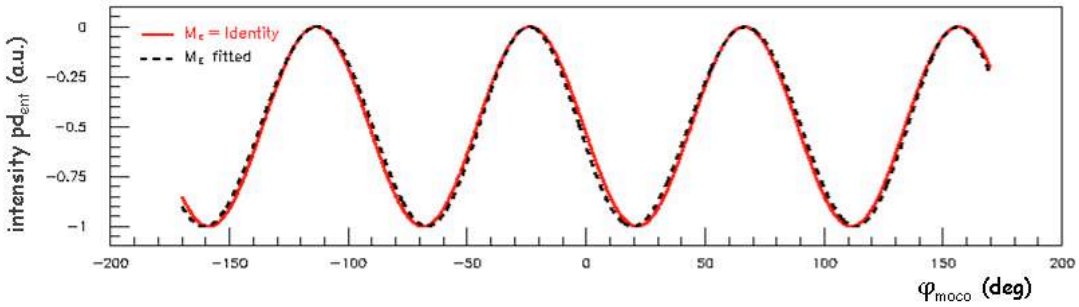

Figure 6.13: Simulated intensities normalised to the unity recorded in the photodiode pd_{ent} after a round trip through the entrance beam line. The red full line has been simulated with M_E equal to the identity, the black dotted line with the M_E elements coming from the experimental data fit (formula (6.11)).

For this study, because no reference photodiode has been used during the data taking, the results can be affected by a systematic drift of the laser power variation, which can be of the order of the percent. This could explain the non gaussian behaviour of the data pull distribution in Figure 6.11. Nevertheless, even if this data pull is not really gaussian, its good behaviour as well as the effect of the correction presented in Figure 6.12 give a good confidence of our simple model.

6.5 Coherence and total error of the DOCP

6.5.1 Coherence of the DOCP values

Having now obtained the transfer matrices M_E and M_T of the entrance and exit beam lines, we can compare the values of the DOCP measured or estimated at different places

of the cavity system, and check the coherence of these values in order to make sure that there is no additional unknown large effect which could induce a bias on the DOCP at the centre of the cavity. We recall that the different locations where the DOCP values are determined (see Figure 6.1) are as follows:

- $\mathrm{DOCP_{moc}}$ is the value of the DOCP just after the entrance quater wave plate which is considered as perfect. It is calculated from a perfect linear polarised beam passing through a perfect quater wave plate of matrix $\mathrm{M_J}$ (expression (3.6) with $\phi_{\mathrm{sh}} = \pi/2$) turned at an azimuthal angle ϕ_{moco}. The associated field $\mathbf{E_{moc}}$ is written as:

$$\mathbf{E_{moc}} = \mathrm{M_J} \begin{pmatrix} \cos\phi_{\mathrm{moco}} \\ \sin\phi_{\mathrm{moco}} \end{pmatrix} . \tag{6.12}$$

- $\mathrm{DOCP_{ent}}$ is the value of the DOCP before the cavity entrance mirror, *i.e.* the DOCP of the beam after its passage through the entrance beam line characterised by the matrix $\mathrm{M_E}$ determined in Section 6.4. The associated field $\mathbf{E_{ent}}$ is written as:

$$\mathbf{E_{ent}} = \mathrm{M_E}\ \mathbf{E_{moc}} . \tag{6.13}$$

- $\mathrm{DOCP_{cc}}$ is the DOCP of the light at the exit of the cavity and is calculated from the polarisation measured by the ellipsometer and from the exit optical line transfer matrix $\mathrm{M_T}$ determined in Section 6.2.4. The associated field $\mathbf{E_{cc}}$ is written as:

$$\mathbf{E_{cc}} = \mathrm{M_T^{-1}}\ \mathbf{E_{in}} , \tag{6.14}$$

  where $\mathbf{E_{in}}$ is the field associated to the light entering the ellipsometer.

- $\mathrm{DOCP_{in}}$ is the DOCP value at the entrance of the ellipsometer and is determined from ellipsometer data samples with the fitting procedure described in Section 5.3.

To check the coherence of the DOCP values, the "moco qwp" has been positioned at eleven different azimuthal angles near a right or a left circular position and for each one of these positions a set of data have been recorded in the ellipsometer to measure the corresponding $\mathrm{DOCP_{in}}$ value. We recall that a right or a left "moco qwp" position corresponds to an azimuthal angle which maximises the intensity recorded after a round trip (cavity unlocked) in the photodiode $\mathrm{pd_{ent}}$ located behind the Glan. From the ellipsometer measurements, the eleven $\mathrm{DOCP_{in}}$ values have been derived, and from (6.12), (6.13) and (6.14), the values of $\mathrm{DOCP_{moc}}$, $\mathrm{DOCP_{ent}}$ and $\mathrm{DOCP_{cc}}$ have been deduced. Figure 6.14 (a) (respectively (b)) shows these four DOCP values for five (respectively six) "moco qwp" azimuthal angles around a right (respectively a left) circular position. This figure allows the evolution of the laser beam DOCP to be followed along the optical path through the different optical elements of the setup.

For the measurement of the HERA lepton beam polarisation, the only relevant quantity is the Degree Of Circular Polarisation inside the cavity, to which of course we do not have access. But all the above studies allow us to know the DOCP before the entrance of the cavity ($\mathrm{DOCP_{ent}}$) and just at the exit of the cavity ($\mathrm{DOCP_{cc}}$), this for several points around a right and a left circular "moco qwp" position. Figure 6.15 is similar to Figure

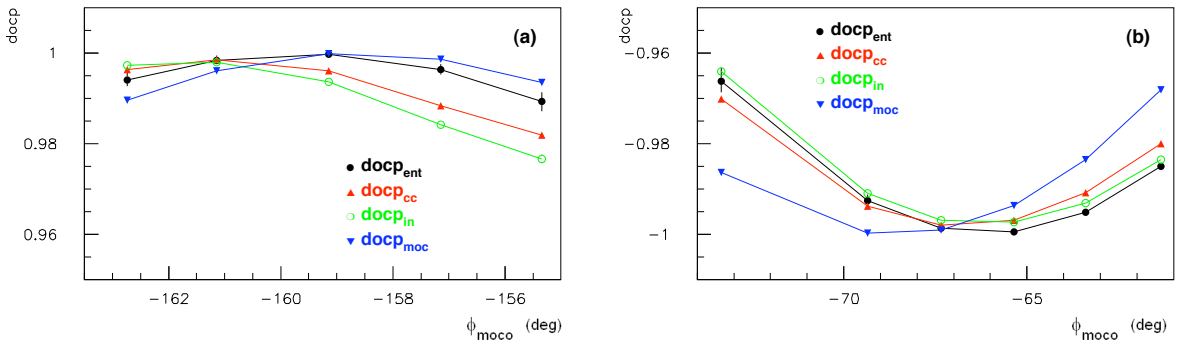

Figure 6.14: Values of DOCP for five "moco qwp" azimuthal angle ϕ_{moco} around a right circular position (a) and for six angles ϕ_{moco} around a left circular position (b). The meaning of the measurement is indicated in the figure.

6.14 but shows only the relevant values $\mathrm{DOCP_{ent}}$ and $\mathrm{DOCP_{cc}}$ around the right (Figure 6.15(a)) and the left (Figure 6.15(b)) circular "moco qwp" positions with, in addition, the associated errors coming from the determination of the transfer matrices $\mathrm{M_E}$ and $\mathrm{M_T}$. In this figure is also presented the difference between $\mathrm{DOCP_{ent}}$ and $\mathrm{DOCP_{cc}}$ around the right position (c) and around the left one (d). The dotted lines indicate the positions of the maxima of the theoretical curve $\mathrm{I_{pd_{ent}}}(\phi_{\mathrm{moco}})$ (see Figure 6.13) simulated with the fitted $\mathrm{M_E}$ parameters of formula (6.11).

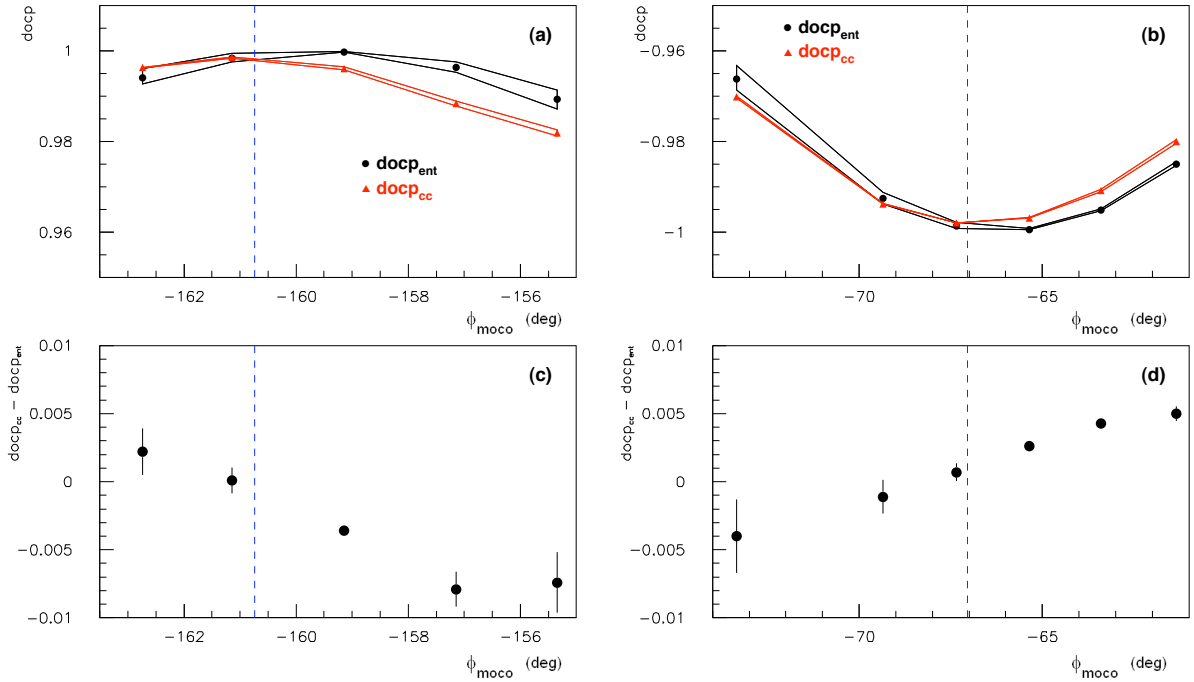

Figure 6.15: $\mathrm{DOCP_{ent}}$ (black point) and $\mathrm{DOCP_{cc}}$ (red triangles) around a right (a) and the left (b) circular "moco qwp" position, and difference $\mathrm{DOCP_{ent}} - \mathrm{DOCP_{cc}}$ around the right (c) and the left (d) position, as a function of the "moco qwp" azimuthal angle. Dotted lines indicate the position of the "moco qwp" used during the HERA data taking.

For each ϕ_{moco}, the value of the Degree Of Circular Polarisation at the centre of the cavity is located between the two corresponding DOCP_{ent} and DOCP_{cc} values. And as shown in Figure 6.15, around the two circular positions indicated by dotted lines, the differences $\text{DOCP}_{\text{ent}} - \text{DOCP}_{\text{cc}}$ are less than five per mill. A part of this few per mill shift could be explained by the presence of the small birefringence due to multi-layers coating cavity mirrors that we have mentioned in Section 6.2.2. We recall that the order of magnitude of this mirror birefringence is $\phi_{\text{bir}} = 2.2 \times 10^{-6}$ rad [127]. Because of the resonant optical cavity, this phase shift due to a single passage of the light in the reflected coating is amplified by a factor $\text{A} = (1 + \text{R})/(1 - \text{R})$ [128]. If $\text{R} \approx 1$, the factor A can be written as $2\mathcal{F}/\pi$ where $\mathcal{F}$ is the finesse of the cavity. With our cavity finesse $\mathcal{F} \approx 30000$, the amplified phase shift is ≈ 0.042 rad and according to (6.1) the effect on the Degree Of Circular Polarisation is $\approx 10^{-3}$. Since we don't know the exact value of our mirror coating birefringence, the difference between DOCP_{ent} and DOCP_{cc} could thus be explained. However, there could also be another source of systematic uncertainty because of the light power variation not compensated by a reference diode measurement in the determination of DOCP_{ent}.

Anyway, the above study of the entrance beam line does not claim to give a precise measurement of DOCP_{ent} but is devoted to check the coherence of the system and particularly the coherence of measurements just before and just after the centre of the cavity.

6.5.2 The total error on the DOCP

According to all the studies described in this document, we are now able to give a value for the systematic uncertainty associated to each value of the DOCP at the laser beam/lepton beam interaction point. The total systematic error σ_{syst} which are common to all measurements of DOCP at the centre of the cavity is written as:

$$\sigma_{\text{syst}} \;=\; \sigma_{\text{trans}} + \sigma_{\text{time}} \quad , \tag{6.15}$$

where $\sigma_{\text{trans}} < 3 \times 10^{-6}$ is the uncertainty related to the transfer between the inner of the cavity and the exit of the cavity (Sections 6.2.2 and 6.2.3), and $\sigma_{\text{time}} \approx 3 \times 10^{-3}$ is the uncertainty attached to the ellipsometer data taking time (Section 5.5.3). As shown in the previous sections, either these errors have been estimated from previous works on the subject, or they come from our own dedicated studies.

The value of the Degree Of Circular Polarisation of the laser beam inside the cavity is therefore written as:

$$\text{DOCP} \;=\; \text{DOCP}_{\text{in}} \;-\; \text{COR}_{\text{DOCP}} \;\pm\; \sigma_{\text{exit}} \;\pm\; \sigma_{\text{syst}} \quad , \tag{6.16}$$

where:

- DOCP_{in} is the Degree Of Circular Polarisation measured by the ellipsometer (Section 5.5.2),
- COR_{DOCP} is a correction factor determined for each ellipsometer measurement from the expression (6.6) of the transfer matrix, from the parameters γ and p of formula

(6.7) and from a doublet (χ_P, ϕ_P) resulting from an adjustment using an ellipsometer data sample as described in Section 5.5.2,

- σ_{syst} is the systematic error (6.15) and is $\approx 3 \times 10^{-3}$,
- σ_{exit} is the error related to the optics located at the exit of the cavity: it contains an error such as those in Table 5.4 coming from the fits using ellipsometer data samples, and a error such as those in Table 6.2 coming from the determination of the exit transfer matrix M_T. This error σ_{exit} is different for each measurement and is of the order of a few 10^{-4}.

6.6 summary

The precise and fast Fabry-Perot cavity polarimeter which was installed in the tunnel of the HERA collider in 2003 has taken data until the end of HERA in summer 2007. Our cavity system was very similar to the cavity installed in the CEBAF accelerator, and this has proved to be a great benefit for us. The cavity has shown a very stable behavior during all the data taking in term of locking and gain. The calorimeter acquisition system at 10 MHz and the intra-cavity power allowed a measurement of the lepton polarisation every twenty seconds to be obtained with a statistical uncertainty of about 1% per lepton bunch and per minute. Several dedicated studies, precise and often long, have been performed to characterise optical components of the system, first at Orsay in the environment of a laboratory, and then in the HERA tunnel. The effect on the light polarisation state of each one of these components has been studied and taken into account in the determination of the Degree Of Circular Polarisation S_γ of the laser beam. These measurements made it possible to determine the value of S_γ at the laser beam-lepton beam interaction point, *i.e.* at the center of the Fabry-Perot cavity, with a total uncertainty of a few per mill. This precision has never been reached in the hostile and noisy environment of a particle collider, in which, in addition, we had only one short access per month. The quantity S_γ being directly involved in the Compton process cross section, the passage from the percent level to the per mill level in the precision of its measurement has proved difficult but necessary to conserve a systematic error on the lepton polarisation below the percent. By showing that it is possible to measure S_γ with this high precision in the environment of a particle collider, these results also provide an evidence of feasibility for the current studies of precise and fast Compton polarimeters to be installed in futur linear colliders [44, 136, 137].

I would like to thank all the persons who have participated in this project and have helped to carry out the design, the building and the installation of the system, and also the polarimeter data taking, the data analyses and all the optical studies described in this document.

Outlook

The polarimeter which has been described in this document is based on the Compton scattering process where the Compton photon gains energy after the scattering. This process which converts electron kinetic energy into high energy photons is often called Inverse Compton Scattering (ICS) process. ICS is involved in many scientific domains and to conclude this document, let us give an overwiew of various ICS applications.

ICS in Astrophysics

In atrophysics, the detection of scattered Compton photons can provide informations on the density perturbations of the universe. For instance, using the Sunyaev-Zel'dovich effect (SZ effect) [138, 139] in which cosmic microwave backround (CMB) photons are scattered by electrons in the hot gas surronding galaxies, clusters of galaxies can be observed. The magnitude of the SZ effect is independent of redshift and depends only on the characteristics of the cluster itself allowing very distant clusters to be detected. One of the task of the PLANCK satellite [140] is to measure the distortion of the black body spectrum of the CMB [141] in order to constitute a catalog of galaxie clusters and then provide some informations about the matter and energy content of the universe. Several others phenomena in the universe might be explained by the Compton effect, as γ-ray burst emissions [142, 143, 144], pulsar emissions [145, 146], or luminosity spectrum of accreting black holes which is believed to come from the inverse Compton process [147, 148].

Polarimetry

In the particle accelerator domain, we have seen in this document that the inverse Compton process can be used to measure precisely the polarisation of electron and positron beams, and that a Compton polarimeter has the advantage of a non destructive measurement which can be performed continually while beams are in collision. Compton polarimeter has been used for instance in the SLD experiment at SLAC [149], at the electron stretcher ring ELSA of Bonn University [150], at the CEBAF accelerator [63] and at the HERA collider. As shown in this document, the uncertainties on the lepton polarisation measurements using a Compton polarimeter can be very well controlled and remain below the per mill level. At futur linear TeV scale machines, polarised e^- and e^+ beams are forseen. The polarisation has an important impact in the physic program [137] and high precision physics requires the knowledge of the polarisation with a relative uncertainty around 0.1% [151]. Compton polarimetry would have the ability to reach such a precision and the current design at futur linear colliders is to use Compton polarimeters [152, 153].

Polarised electron source

Another challenge at futur linear machines is the generation of polarised positron beams with a high degree of polarisation. A method to generate polarised positrons consists on Compton scattering of circularly polarised laser light off a relativistic electron beam, followed by e^+e^- pair creation in a thin target. Using a few GeV energy electron beam, Compton photon energy is of order of few tens of MeV. During the pair creation process, the Compton photon polarisation is transmitted and positrons are longitudinally polarised. This concept has been already tested at KEK [154] and the polarisation of the positron beam produced by this method has been measured to be larger than 70% with a conversion rate inside the target around 10^{-3} [155]. Thus, to obtain a polarised photon beam at the MeV energy scale for the generation of polarised positron sources, the inverse Compton scattering method would be an alternative to the undulator schemes in futur linear collider design projects [156, 157].

Photon Colliders

In addition to the e^+e^- physics program, futur linear colliders give also the opportunities to study $\gamma\gamma$ and γe interactions at the TeV scale. By using the ICS method (Compton scattering of laser light off a TeV energy scale electron beam) for creating of high energy γ beams, $\gamma\gamma$ and γe colliders can be obtained with luminosity and energy comparable to the ones of the basic e^+e^- colliders [158, 159]. Some phenomena can be studied better at photon colliders than at e^+e^- colliders due to much larger cross sections or to higher accessible masses [160]. In addition, in photon colliders, photons can be produced with a high degree of circular polarisation as well as in a linearly polarised state by simply changing the polarisation of the laser light [161, 162]. This allows in the Higgs sector for instance to determine easily whether or not a neutral Higgs boson is CP eigenstate by using the different types of Compton photon polarisations [163]. A photon collider may provide a powerful means to understand electroweak symmetry breaking and physics beyond the standard Model and, in some scenarios, is the best machine for the discovery of new physics [164, 165, 167].

Nonlinear QED effect studies

An other application of high energy photons produced by the ICS process is the possibility to observe nonlinear quantum electrodynamic (QED) effects. In QED, the interaction between photons (or in an equivalently way between photons and an external field) introduces nonlinear corrections in the theory. By observing a photon in a strong magnetic field, one can measure some of these nonlinear effects. For this purpose, an experiment was proposed in 1991 (but not realised) to measure the vacuum birefringence by measuring the phase shift acquired by photons propagating in a strong magnetic field (10 Tesla over a 10 meter length) [168]. Because the birefringence induced by the magnetic field is inversely proportional to the photon wavelenght, the use of high energy ICS photons at the GeV energy scale allowed several orders of magnitude to be gained in the sensibility of the measurement compared to the use of laser light photons. In this experiment, the source of high energy photon was the scattered photons from ICS of a circularly polarised

laser beam off the HERA electron beam. The measurement of the degree of polarisation of ICS photons before and after the strong field allowed the induced vacuum birefringence to be infered. Other nonlinear QED studies have been performed using the benefit of the ICS process in high energy accelerator (see for instance [169]). Of course, one can imagine to make this type of experiment at the next linear collider to increase the sensitivity of measurements thanks to higher produced ICS photons.

Compact X-ray sources

Another domain of ICS application concerns the Compton based X-ray sources. X-ray produced with conventional X-ray tubes are simple and robust but most of the power generated by these tubes is converted into heat. In addition, tubes are not tunable across a broad energy range. Hence, they cannot provide enough intense focusing quasi-monochromatic beams required for specific studies in biology, chemistry or cultural heritage sciences. Synchrotron sources which deliver high intensity beams are today the best machines to perform ambitious searches using diffraction, absorption, diffusion, imaging or spectroscopy and they are used with good results [170, 171, 172]. But synchrotron machines are large, cannot be inserted in laboratory, and offer limit access time. Hence, since the exceptional development of high power femtosecond lasers, the interest in compact X-ray sources has became very important. These sources are in full development over recent years. The principle of a compact X-ray source based on the inverse Compton effect is to produce an intense X-ray beam by scattering a high power focused laser beam off a high intensity focused electron beam of few tens MeV energy. Such a source has to be designed and built in a small pratical form to be located in a laboratory, a museum or a hospital. In addition to the compactness, the source should have the possibility to adjust the ICS photon frequency by varying the electron beam energy and/or the laser frequency. This makes possible a wide range of studies requiring intense monochromatic beams at various X-ray energies.

Currently, most ambitious projects aim to produce 10^{12}-10^{13} ph/sec of a few tens of KeV energy in an energy bandwidth $\Delta E/E$ of order of 1-10%. Table 6.4 presents an overview of Compton compact source projects and their main characteristics. Experiments currently in operation (PLEIADES [173, 174], Vanderbilt [175, 176], SLAC [177], Waseda [178, 179], AIST [180], Tsinghua [181], LUCX [182] and TERAS [189]) have already demonstrated the feasibility of X-ray production by inverse Compton scattering, but the delivered X-ray beam intensity is not sufficient to carry out a large domain of studies requiring more brightness. To enhance both the electron/laser interaction repetition frequency and the laser power at the Compton interaction point, a high power and high repetition frequency laser can be coupled with a high-finesse optical cavity and this device integrated in a low energy storage ring. This scheme based on multiple passages of electrons is the one adopted in the Lycean Technology machine [190, 191], and in the Kharkov [192], TTX [193, 194] and ThomX [195] projects. Although the MIT project is not a storage ring scheme, the design brightness value is very large and the source size exceptionally small with moderate divergence [185]. In this project, a short superconducting linac produces a very low emittence (< 1 mm.mrad) electron beam with a 100 MHz repetition rate. Always in the linear scheme, the Japanese project "Quantum Beam" is already approved and funded. In this machine, a multi-bunch electron linac

and a pulsed amplified laser stacking in a cavity generate a high quality and high flux X-ray beam [187, 188]. Currently, the only machine in operation delivering a photon flux comparable to the flux from the first generation synchrotron facilities is the Lycean Technology project whose installation directed by R. Ruth began in 2002. Today the machine provides a tunable energy X-ray beam of 10^{12} ph/sec in 2% energy bandwidth [196] and the first phase contrast imaging have been obtained recently [197].

Experiment	Type	Energy	Flux (10% bw)	Source size
*PLEIADES (LLNL) [173, 174]	linear	10−100 KeV	10^6/pulse@10Hz	18 μm
*Vanderbilt [175, 176]	linear	15−50 KeV	10^{10}/pulse@0.01Hz	30 μm
*SLAC [177]	linear	20−85 KeV		
*Waseda Univ. [178, 179]	linear	0.25−0.5 KeV	5.10^3/pulse@5Hz	
*AIST, Japan [180]	linear	10−40 KeV	10^6/sec	30 μm
*Tsinghua Univ. [181]	linear	4.6 KeV	1.7 10^4/sec	
*LUCX (KEK) [182]	linear	33 KeV	4.10^3/pulse@12.5Hz	80 μm
+Japan (UTNL) [183, 184]	linear	10−40 KeV	10^9/sec	
MIT project [185]	linear	3−30 KeV	3.10^5/pulse@100MHz	2 μm
MXI System [186]	linear	8−100 KeV	10^8/pulse@10Hz	
Quantum Beam (KEK) [187, 188]	linear	$\sim$ 35 KeV	10^{13}/sec	3 μm
*TERAS (AIST) [189]	circular	1−40 MeV	5.10^4/sec	2 mm
*Lycean Tech. [190, 191]	circular	7−35 KeV	5.10^{12}/sec	30 μm
Kharkov (NSC KIPT) [192]	circular	10−500 KeV	2.6 10^{13}/sec (25MHz)	35 μm
TTX (THU, China) [193, 194]	circular	20−80 KeV	2.10^{12}/sec	35 μm
ThomX (LAL) [195]	circular	50 KeV	$\sim 10^{12}$ (20MHz)	70 μm

Table 6.4: Compact X-ray source projects. Star symbol (*) refers to machine in operation and symbol (+) to machine in construction.

Let us finish with a brief description of the ThomX project since the machine should be constructed at the LAL laboratory. The project is going to be developed by LAL, SOLEIL, CELIA, ILE, L.M.A. and Thalès laboratories. The ThomX machine design is presented in Figure 6.16 and the main parameters are described as follows. At nominal operating point, a 1 nC electron bunch is accelerated in a 50 MeV linac and is injected in a 15 meter circumerence storage ring with normalised emittance around 5 πmm.mrad. A 100 W average power picosecond pulsed laser of wavelength 1 μm and repetition rate 40 MHz (few μJ per pulse) is injected into a very high finesse optical cavity leading to an increase of the pulse energy up to few mJ per pulse. Laser/electron interactions occur at 20 MHz, *i.e.* at each electron revolution. In order to maintain the electron beam quality, electron bunches are re-injected periodically at a frequency of 50 Hz. About 10^{12} ph/sec in 10% energy bandwidth and with a maximum energy of 50 KeV in the forward direction are expected from the ThomX source. As shown in Figure 6.16, the electron beam/laser beam interaction point is located between dipoles. This design has the advantage to locate the optical cavity mirrors outside of the ring and to place X-ray optics closer to the interaction point.

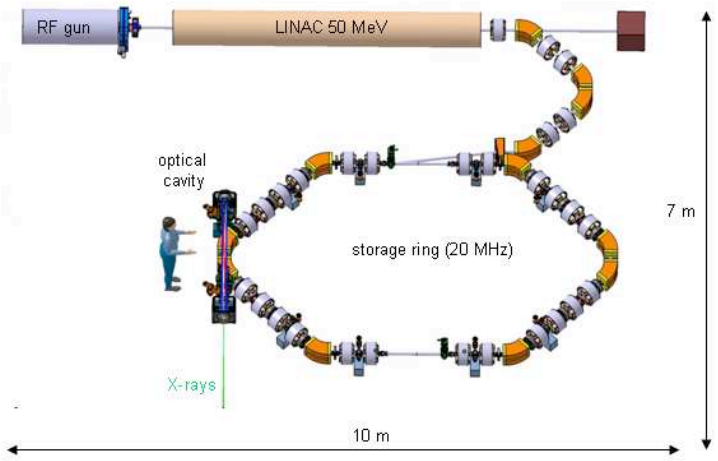

Figure 6.16: Technical drawing of ThomX. From [198].

This overview of Compact ICS source ambitious projects has shown that they are much more powerful (flux, monochromaticity, directivity and tunability) than the existing laboratory X-ray sources such as X-tubes or rotating anodes. In Figure 6.17 the performances of synchrotron machines, rotating anode tubes and the ThomX Compton machine are presented by plotting their brightness as a function of the emitted X-ray energy. The most efficient rotating anode (FR-E+SuperBright model [199]), providing a brightness comparable to the first generation synchrotron machine, a 8.10^9 ph/sec maximum flux and a 200 μm beam size, does not allow nevertheless to develop ambitious analysis techniques mentionned above. ICS sources cannot compete the third generation of synchrotron in term of integrated emitted flux and brightness but can be placed near the first generation radiation facilities with in addition the avantage of producing a much harder X-ray beam and of course of being located in museum, laboratories or hospitals.

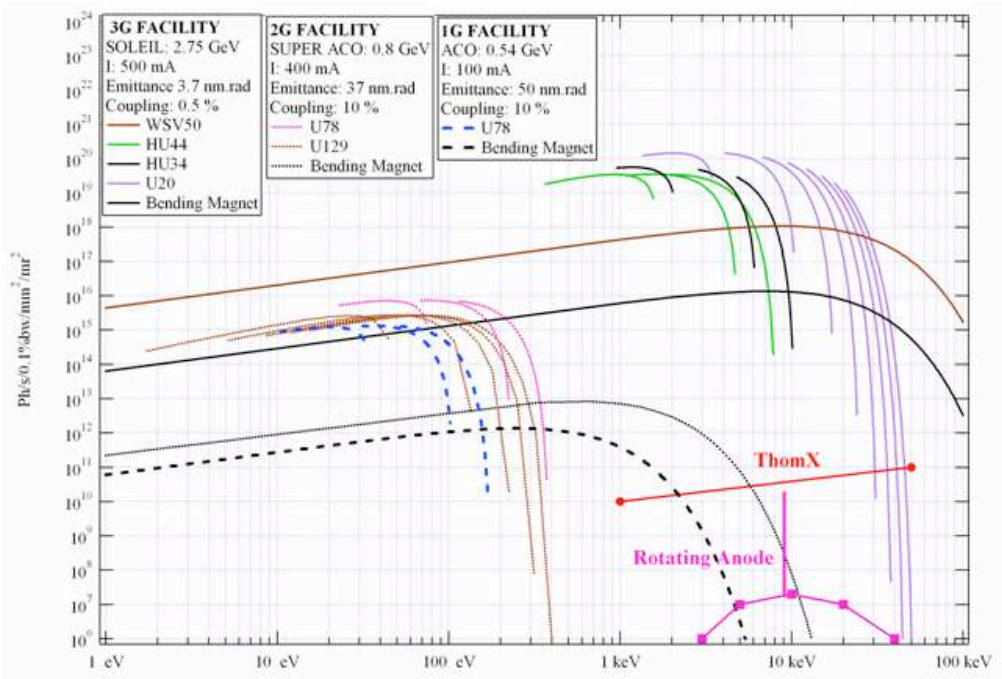

Figure 6.17: Performances of different radiation sources. The ThomX Compton source project is also visible. From [200].

Appendix A

Propagation of a plane wave in an uniaxial medium

This annex is devoted to describe the formalism of a wave propagating in an isotropic medium and crossing an anisotropic medium of thickness ℓ. We will show how to obtain the expression of the field transmitted by this uniaxial anisotropic medium, homogeneous, non-magnetic and transparent. The incident wave is supposed to be plane and the uniaxial medium without anti-reflected coating. Firstly, general solutions of a wave propagating in such an uniaxial anisotropic medium are derived from Maxwell and medium equations (Section A.1.1). Then, using boundary continuity conditions at the interface between the two media, the amplitudes of the fields at the two interfaces will be calculated (Section A.2). Finally, the expression of the total transmitted field taking into account the multiple reflections inside the medium will be given (Section A.3).

A.1 Plane wave in an anisotropic homogeneous medium

References [201, 202, 203, 204] are constantly used in the formalism described in the following.

A.1.1 Maxwell equations

Fundamental equations in electrodynamics are Maxwell's equations:

$$\begin{cases} \nabla \times \mathcal{E} + \dfrac{\partial \mathcal{B}}{\partial \mathrm{t}} = \mathbf{0} \ , \\ \nabla \times \mathcal{H} - \dfrac{\partial \mathcal{D}}{\partial \mathrm{t}} = \mathcal{J} \ , \\ \nabla \cdot \mathcal{D} = \rho \ , \\ \nabla \cdot \mathcal{B} = 0 \ . \end{cases} \tag{A.1}$$

$\mathcal{E}$ and $\mathcal{H}$ are respectively the electric field and the magnetic field, $\mathcal{D}$, $\mathcal{B}$, ρ and $\mathcal{J}$ are respectively the electric displacement, the magnetic induction, the charge density and the

current density. To obtain a unique solution of the field vectors, Maxwell's equations have to be completed with the following medium equations:

$$\mathcal{D} \;=\; \epsilon\,\mathcal{E} \;=\; \epsilon_0\,\mathcal{E} \;+\; \mathbf{P} \;\;, \tag{A.2}$$

$$\mathcal{B} \;=\; \mu\,\mathcal{H} \;=\; \mu_0\,\mathcal{H} \;+\; \mathbf{M} \;\;, \tag{A.3}$$

where ϵ is the dielectric tensor, μ the permeability tensor, $\mathbf{P}$ the electric polarisation vector and $\mathbf{M}$ the magnetic polarisation vector. If the medium is isotropic, ϵ and μ are scalar quantities.

A.1.2 Calculation in the principal system

In an optically anisotropic medium, the propagation of a plane wave is determined by the dielectric tensor ϵ which connects the displacement vector and the electric field vector through equation (A.2). In a non-magnetic and transparent medium, this tensor ϵ is real and symmetric. Therefore it is possible to find three orthogonal axes $(\mathrm{a},\mathrm{b},\mathrm{c})$ such as the non diagonal terms of the tensor ϵ are null. In such a frame, called the principal frame of reference, ϵ is written as:

$$\epsilon \;=\; \begin{pmatrix} \epsilon_\mathrm{a} & 0 & 0 \\ 0 & \epsilon_\mathrm{b} & 0 \\ 0 & 0 & \epsilon_\mathrm{c} \end{pmatrix} \;=\; \epsilon_0 \begin{pmatrix} \mathrm{n}_\mathrm{a}^2 & 0 & 0 \\ 0 & \mathrm{n}_\mathrm{b}^2 & 0 \\ 0 & 0 & \mathrm{n}_\mathrm{c}^2 \end{pmatrix} \;\;,$$

$$\epsilon_\mathrm{a} = \epsilon_0\;\mathrm{n}_\mathrm{a}^2 \qquad , \qquad \epsilon_\mathrm{b} = \epsilon_0\;\mathrm{n}_\mathrm{b}^2 \qquad , \qquad \epsilon_\mathrm{c} = \epsilon_0\;\mathrm{n}_\mathrm{c}^2 \;\;.$$

ϵ_a, ϵ_b and ϵ_c are the principal dielectric constants and n_a, n_b and n_c are the principal refracting indices. Typically, the directions of the axes of the principal frame of reference correspond to the crystal axes of symmetry. We want to study the propagation of a plane wave in such a non-magnetic transparent anisotropic medium.

The most general expression of an electric field $\mathcal{E}$ and a magnetic field $\mathcal{H}$ associated to a plane wave is written as:

$$\mathcal{E} \;\;=\;\; \mathbf{E}\,\exp\left[\; i\;(\omega \mathrm{t} - \mathbf{k}\cdot\mathbf{r})\;\right] \;\;,$$

$$\mathcal{H} \;\;=\;\; \mathbf{H}\,\exp\left[\; i\;(\omega \mathrm{t} - \mathbf{k}\cdot\mathbf{r})\;\right] \;\;,$$

where $\mathbf{k}$ is the wave vector. By substituting $\mathcal{E}$ and $\mathcal{H}$ in (A.1), (A.2) and (A.3), and by eliminating the field $\mathcal{H}$ and the time, one obtains:

$$\mathbf{k}\times(\mathbf{k}\times\mathbf{E}) \;+\; \omega^2\mu\epsilon\mathbf{E} \;=\; 0 \;\;. \tag{A.4}$$

Equation (A.4) can also be written as:

$$\mathrm{M}\begin{pmatrix} \mathrm{E}_\mathrm{a} \\ \mathrm{E}_\mathrm{b} \\ \mathrm{E}_\mathrm{c} \end{pmatrix} \;=\; 0 \;\;, \tag{A.5}$$

where the matrix M in the system of principal coordinates is written as:

$$\mathrm{M} \equiv \begin{pmatrix} \omega^2\mu\epsilon_\mathrm{a} - \mathrm{k_b^2} - \mathrm{k_c^2} & \mathrm{k_a k_b} & \mathrm{k_a k_c} \\ \mathrm{k_a k_b} & \omega^2\mu\epsilon_\mathrm{b} - \mathrm{k_a^2} - \mathrm{k_c^2} & \mathrm{k_b k_c} \\ \mathrm{k_c k_a} & \mathrm{k_c k_b} & \omega^2\mu\epsilon_\mathrm{c} - \mathrm{k_a^2} - \mathrm{k_b^2} \end{pmatrix} \quad . \tag{A.6}$$

The determinant of M must be null so that a non-trivial solution exists. This condition $\det(\mathrm{M}) = 0$ gives the following relation between ω and $\mathbf{k}$:

$$\frac{\mathrm{k_a^2}}{\mathrm{k^2} - \omega^2\mu\epsilon_\mathrm{a}} + \frac{\mathrm{k_b^2}}{\mathrm{k^2} - \omega^2\mu\epsilon_\mathrm{b}} + \frac{\mathrm{k_c^2}}{\mathrm{k^2} - \omega^2\mu\epsilon_\mathrm{c}} = 1 \quad , \tag{A.7}$$

provided that the denominators are not null. Equation (A.7) being quadratic in $\mathbf{k}^2$, two solutions $\mathbf{k^{(1)}}$ and $\mathbf{k^{(2)}}$ exist for the wave vector $\mathbf{k}$, corresponding to two waves having different phase velocities. The resolution of the propagation equation (A.5) gives the directions $\mathbf{e^{(1)}}$ and $\mathbf{e^{(2)}}$ of the electric fields $\mathbf{E}$ associated to these two waves: in the most general case, the directions of the field vectors associated to each of the two wave vectors solution of (A.7) are:

$$\mathbf{e^{(1,2)}} \sim \left(\frac{\mathrm{k_a^{(1,2)}}}{(\mathrm{k^2})^{(1,2)} - \omega^2\mu\epsilon_\mathrm{a}} \, , \, \frac{\mathrm{k_b^{(1,2)}}}{(\mathrm{k^2})^{(1,2)} - \omega^2\mu\epsilon_\mathrm{b}} \, , \, \frac{\mathrm{k_c^{(1,2)}}}{(\mathrm{k^2})^{(1,2)} - \omega^2\mu\epsilon_\mathrm{c}} \right) \quad ,$$

provided that the denominators are not null. In a non absorbing medium, ϵ is real and all the components of these fields are real.

A.1.3 Case of an uniaxial medium

In the general case, the three principal indices are different. But lots of optical materials exist for which two of the principal refraction indices are equal and can be written as:

$$\epsilon_\mathrm{a} = \epsilon_\mathrm{b} = \epsilon_0 \, \mathrm{n_0^2} \qquad , \qquad \epsilon_\mathrm{c} = \epsilon_0 \, \mathrm{n_e^2} \quad . \tag{A.8}$$

This type of crystal is known as uniaxial (as the quartz or the calcite). The c axis of the principal coordinate system in that case is called the optical axis. $\mathrm{n_o}$ is called the ordinary index, $\mathrm{n_e}$ the extraordinary index. In such a uniaxial medium, equation (A.7) can be simplified as:

$$\left(\frac{\mathrm{k_a^2} + \mathrm{k_b^2}}{\mathrm{n_e^2}} + \frac{\mathrm{k_c^2}}{\mathrm{n_o^2}} - \frac{\omega^2}{\mathrm{c^2}} \right) \left(\frac{\mathrm{k^2}}{\mathrm{n_o^2}} - \frac{\omega^2}{\mathrm{c^2}} \right) = 0 \quad . \tag{A.9}$$

The two terms of equation (A.9) give the relation between ω and $\mathbf{k}$ for the two waves solution of (A.5). These two waves are known respectively as the ordinary wave (O) and the extraordinary wave (E).

The module of the wave vector $\mathbf{k_o}$ of the ordinary wave is independent of the direction of propagation; it is given by the relation:

$$\frac{\mathrm{k_o^2}}{\mathrm{n_o^2}} - \frac{\omega^2}{\mathrm{c^2}} = 0 \quad , \tag{A.10}$$

while the relation connecting the wave vector $\mathbf{k_e}$ and ω for the extraordinary wave is written as:

$$\frac{k_{ea}^2 + k_{eb}^2}{n_e^2} + \frac{k_{ec}^2}{n_o^2} - \frac{\omega^2}{c^2} = 0 \quad . \tag{A.11}$$

Direction of the ordinary field o

By using the relation (A.10), the matrix M of (A.6) for an ordinary wave of wave vector $\mathbf{k_o} = (k_{oa}, k_{ob}, k_{oc})$ is written as:

$$M_{ord} = \begin{pmatrix} k_{oa}^2 & k_{oa}k_{ob} & k_{oa}k_{oc} \\ k_{oa}k_{ob} & k_{ob}^2 & k_{ob}k_{oc} \\ k_{oc}k_{oa} & k_{oc}k_{ob} & \frac{\omega^2}{c^2}(n_e^2 - n_o^2) + k_{oc}^2 \end{pmatrix} ,$$

and the resolution of (A.5) gives the direction of the field associated to the ordinary wave in the system of principal axes:

$$\mathbf{o} = N_o \ (k_{ob} \ , \ -k_{oa} \ , \ 0) \quad , \tag{A.12}$$

where N_o is a factor of normalisation such as $\mathbf{o} \cdot \mathbf{o} = 1$.

Direction of the extraordinary field e

In the same way, by using the relation (A.11), the matrix M associated to the extraordinary wave of wave vector $\mathbf{k_e} = (k_{ea}, k_{eb}, k_{ec})$ is written as:

$$M_{ext} = \begin{pmatrix} \frac{\omega^2}{c^2}n_o^2 - k_e^2 + k_{ea}^2 & k_{ea}k_{eb} & k_{ea}k_{ec} \\ k_{ea}k_{eb} & \frac{\omega^2}{c^2}n_o^2 - k_e^2 + k_{eb}^2 & k_{eb}k_{ec} \\ k_{ec}k_{ea} & k_{ec}k_{eb} & \frac{\omega^2}{c^2}n_e^2 - k_e^2 + k_{ec}^2 \end{pmatrix} ,$$

and the direction of the associated extraordinary electric field in the system of the principal axes is:

$$\begin{aligned} &\text{if} \ \ k_{ec} \neq 0 \ : \qquad \mathbf{e} = N_e \left(\frac{k_{ea}}{k_e^2 - \frac{\omega^2}{c^2}n_o^2} \ , \ \frac{k_{eb}}{k_e^2 - \frac{\omega^2}{c^2}n_o^2} \ , \ \frac{k_{ec}}{k_e^2 - \frac{\omega^2}{c^2}n_e^2} \right) \\ &\text{if} \ \ k_{ec} = 0 \ : \qquad \mathbf{e} = (\ 0 \ , \ 0 \ , \ 1 \ ) \quad , \end{aligned} \tag{A.13}$$

where N_e is a normalisation factor such as $\mathbf{e} \cdot \mathbf{e} = 1$.

A.2 Passage of a plane wave through an anisotropic uniaxial medium

The question is now to calculate, in a given reference frame, the transmission and reflection coefficients of a wave passing through an anisotropic uniaxial crystal. For this, it is necessary to calculate the amplitudes of the reflected and refracted electric fields at the interface between the isotropic medium and the crystal, and at the interface between the crystal and the isotropic medium. The uniaxial anisotropic crystal can for instance be the quartz and the isotropic medium the air.

A.2.1 Double refraction at the interface air-quartz

We consider an uniaxial crystal whose principal axes are called a, b and c and the associated unit vectors **a**, **b** and **c**. The optical axis is the c axis. We recall that for this crystal the principal dielectric constants satisfy equation (A.8). The surface of the crystal is supposed to be in the (xy) plane of an orthonomal (**x**,**y**,**z**) reference frame. The orientation of the crystal c axis in this reference frame is characterised by two angles θ_c and ϕ_c: θ_c is the angle between **c** and **z**, ϕ_c the angle between the projection of **c** on the (xy) plane and the vector **x**. **b** is chosen perpendicular to **z** and (**a**,**b**,**c**) is an orthonormal reference frame. The crystal orientation and the frame vectors are schematised in figure A.1.

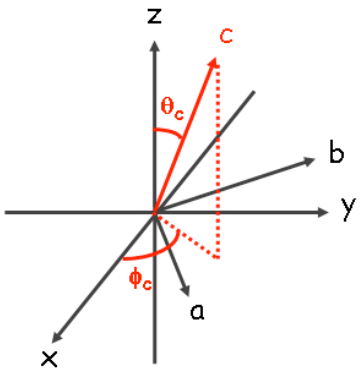

Figure A.1: Laboratory coordinate system (x, y, z) and principal coordinate system (a, b, c). The crystal optical axis is represented by the vector **c**.

In this framework, expressions of vectors **x**, **y**, **z** can be written as function of the principal reference frame vectors **a**, **b**, **c** as:

$$\begin{cases} \mathbf{x} = (\ \cos\theta_c\ \mathbf{a} + \sin\theta_c\ \mathbf{c}\ )\ \cos\phi_c - \sin\phi_c\ \mathbf{b} \\ \mathbf{y} = (\ \cos\theta_c\ \mathbf{a} + \sin\theta_c\ \mathbf{c}\ )\ \sin\phi_c + \cos\phi_c\ \mathbf{b} \\ \mathbf{z} = -\ \sin\theta_c\ \mathbf{a} + \cos\theta_c\ \mathbf{c}\ \ . \end{cases} \tag{A.14}$$

We consider now an incident plane wave of wave vector $\mathbf{k_{in}}$ arriving on the crystal surface or emerging from the crystal, as shematised in figure A.2. $\mathbf{k_{in}}$ is such that the incident plane (*i.e.* the plane formed by the normal to the crystal surface and $\mathbf{k_{in}}$) is the (yz) plane. Therefore, the tangential component of $\mathbf{k_{in}}$ along the x axis is null. We call β the tangential component of the incident wave along y and k_z its longitudinal component along z. The incident wave can be in the air or in the crystal. k_{oz} and k_{ez} are the longitudinal components of the ordinary and extraordinary wave vectors $\mathbf{k_o}$ and $\mathbf{k_e}$ of the field refracted or reflected by the crystal. The reflected or refracted wave vector in the air is called $\mathbf{k'}$. Passages of a wave through the air-quartz and quartz-air interfaces are schematised by the drawings (a) and (b) in figure A.2 respectively. Using the Snell low and the following boundary conditions at the interface:

$$(\mathbf{k_{in}}\cdot\mathbf{x})_{z=0} = (\mathbf{k'}\cdot\mathbf{x})_{z=0} = (\mathbf{k_o}\cdot\mathbf{x})_{z=0} = (\mathbf{k_e}\cdot\mathbf{x})_{z=0} = 0\ ,$$

$$(\mathbf{k_{in}}\cdot\mathbf{y})_{z=0} = (\mathbf{k'}\cdot\mathbf{y})_{z=0} = (\mathbf{k_o}\cdot\mathbf{y})_{z=0} = (\mathbf{k_e}\cdot\mathbf{y})_{z=0} = \beta\ ,$$

allows the wave vectors to be written in the laboratory reference frame as:

$$\mathbf{k_{in}} = \begin{pmatrix} 0 \\ \beta \\ k_z \end{pmatrix}_{xyz} \quad , \quad \mathbf{k'} = \begin{pmatrix} 0 \\ \beta \\ k'_z \end{pmatrix}_{xyz} \quad ,$$
$$\mathbf{k_o} = \begin{pmatrix} 0 \\ \beta \\ k_{oz} \end{pmatrix}_{xyz} \quad , \quad \mathbf{k_e} = \begin{pmatrix} 0 \\ \beta \\ k_{ez} \end{pmatrix}_{xyz} \quad . \tag{A.15}$$

From here, we have now to determine the wave vectors $\mathbf{k_o}$ and $\mathbf{k_e}$ as well as the ordinary and extraordinary field directions $\mathbf{o}$ and $\mathbf{e}$.

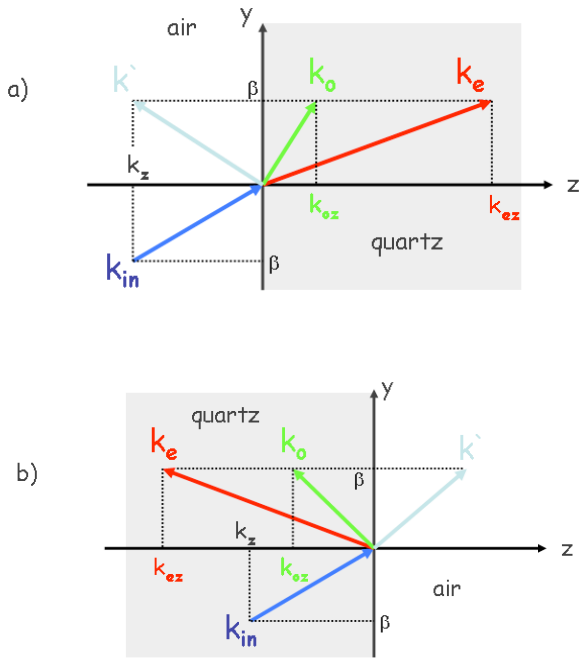

Figure A.2: Projection in the (yz) plane of the reflection and refraction of a plane wave at the interface between an isotropic medium and an anisotropic uniaxial medium (a) and at the interface between an anisotropic uniaxial medium and an isotropic medium (b).

General case

Considering the ordinary and the extraordinary wave vectors $\mathbf{k_o}$ and $\mathbf{k_e}$ of (A.15) and a given initial state defined by the values of β, k_z, θ_c and ϕ_c, from (A.14) $\mathbf{k_o}$ and $\mathbf{k_e}$ are written as:

$$\mathbf{k_{o(e)}} = \begin{pmatrix} \beta\cos\theta_c\sin\phi_c & -k_{oz(ez)}\sin\theta_c \\ \beta\cos\phi_c & \\ \beta\sin\theta_c\sin\phi_c & +k_{oz(ez)}\cos\theta_c \end{pmatrix}_{abc} \quad , \tag{A.16}$$

where the only unknown quantities are k_{oz} and k_{ez}. By using equations (A.10), (A.11) and (A.16), expressions of k_{oz} and k_{ez} are written as:

$$
\begin{aligned}
k_{oz}^2 &= \left(\frac{n_o\,\omega}{c}\right)^2 - \beta^2 \ , \\
k_{ez} &= \frac{v \pm \sqrt{v^2 - 4uw}}{2u} \ ,
\end{aligned}
\tag{A.17}
$$

where:

$$
\left\{
\begin{array}{l}
u = \dfrac{\sin^2\theta_c}{n_e^2} + \dfrac{\cos^2\theta_c}{n_o^2} \\[2ex]
v = \beta\,\sin\phi_c\,\sin(2\theta_c)\left(\dfrac{1}{n_e^2} - \dfrac{1}{n_o^2}\right) \\[2ex]
w = \dfrac{\beta^2\,\sin\phi_c^2\,\cos^2\theta_c \;+\; \beta^2\;\cos^2\phi_c}{n_e^2} \;+\; \dfrac{\beta^2\,\sin\phi_c^2\,\sin^2\theta_c}{n_o^2} \;-\; \dfrac{\omega^2}{c^2}
\end{array}
\right.
$$

The directions **o** and **e** of the electric fields associated to $\mathbf{k_o}$ and $\mathbf{k_e}$ are obtained in the principal reference frame (a, b, c) from equations (A.12), (A.13), (A.16) and (A.17).

We have thus determined the wave vectors and the directions of fields associated to the refracted and reflected waves at a quartz-air interface in the most general case, *i.e.* when the optical axis is tilted in any way with respect to the interface. But in most of crystals this is not the case and the crystal is cut parallel to its optical axis.

Case where the optical axis belongs to the interface plane

If the optical axis **c** is in the interface plane (xy), one has $\theta_c = -\pi/2$, the opposite sign being arbitrarily chosen in order to have $\mathbf{a} = \mathbf{z}$. In this condition, calling N_o and N_e two normalisation factors such as $\mathbf{o}\cdot\mathbf{o} = 1$ and $\mathbf{e}\cdot\mathbf{e} = 1$, expressions of $\mathbf{k_o}$, $\mathbf{k_e}$, **o** and **e** in the laboratory reference frame (x, y, z) and in the principal reference frame (a, b, c) can be simplified as follows:

$$
\mathbf{k_o} = \begin{pmatrix} k_{oz} \\ \beta\,\cos\phi_c \\ -\beta\,\sin\phi_c \end{pmatrix}_{abc} \ , \qquad \mathbf{k_e} = \begin{pmatrix} k_{ez} \\ \beta\,\cos\phi_c \\ -\beta\,\sin\phi_c \end{pmatrix}_{abc} \ ,
$$

$$
\mathbf{o} \;=\; N_o \begin{pmatrix} \beta\,\cos\phi_c \\ -\,k_{oz} \\ 0 \end{pmatrix}_{abc} \;=\; N_o \begin{pmatrix} k_{oz}\,\sin\phi_c \\ -\,k_{oz}\,\cos\phi_c \\ \beta\,\cos\phi_c \end{pmatrix}_{xyz} \ ,
$$

$$\begin{cases} \mathbf{e} \;=\; \mathrm{N_e} \begin{pmatrix} \dfrac{\mathrm{k_{ez}}}{\mathrm{k_e^2} - \frac{\omega^2}{\mathrm{c}^2}\,\mathrm{n_o^2}} \\ \dfrac{\beta\,\cos\phi_\mathrm{c}}{\mathrm{k_e^2} - \frac{\omega^2}{\mathrm{c}^2}\,\mathrm{n_o^2}} \\ \dfrac{\beta\,\sin\phi_\mathrm{c}}{\mathrm{k_e^2} - \frac{\omega^2}{\mathrm{c}^2}\,\mathrm{n_e^2}} \end{pmatrix}_{\mathrm{abc}} \;=\; \mathrm{N_e} \begin{pmatrix} \mathrm{k_o^2}\,\cos\phi_\mathrm{c} \\ \mathrm{k_{oz}^2}\,\sin\phi_\mathrm{c} \\ -\,\beta\,\mathrm{k_{ez}}\,\sin\phi_\mathrm{c} \end{pmatrix}_{\mathrm{xyz}} \\ \\ \mathbf{e} \;=\; \begin{pmatrix} 0 \\ 0 \\ 1 \end{pmatrix}_{\mathrm{abc}} \;=\; \begin{pmatrix} -\,\cos\phi_\mathrm{c} \\ -\,\sin\phi_\mathrm{c} \\ 0 \end{pmatrix}_{\mathrm{xyz}} \qquad \text{if} \;\; (\beta\,\sin\phi_\mathrm{c}) = 0 \;\;, \end{cases}$$

with:

$$\begin{cases} \mathrm{k_{oz}^2} \;=\; \left(\dfrac{\mathrm{n_o}\,\omega}{\mathrm{c}}\right)^2 \;-\; \beta^2 \\ \mathrm{k_{ez}^2} \;=\; \left(\dfrac{\mathrm{n_e}\,\omega}{\mathrm{c}}\right)^2 \;-\; \beta^2 \;\left(\cos^2\phi_\mathrm{c} + \dfrac{\mathrm{n_e^2}}{\mathrm{n_o^2}}\,\sin^2\phi_\mathrm{c}\right) \;\;, \end{cases}$$

$$\begin{cases} \mathrm{k_o^2} \;\;=\;\; \dfrac{\mathrm{n_o^2}\,\omega^2}{\mathrm{c}^2} \\ \mathrm{k_e^2} \;\;=\;\; \dfrac{\mathrm{n_e^2}\,\omega^2}{\mathrm{c}^2} \;+\beta^2\,\sin^2\phi_\mathrm{c}\;\left(1 - \dfrac{\mathrm{n_e^2}}{\mathrm{n_o^2}}\right) \;\;, \end{cases}$$

and:

$$\beta = \mathrm{k_{in}}\,\sin\theta \qquad , \qquad \mathrm{k_{in}} = \frac{\omega}{\mathrm{c}}\,\mathrm{n} \;\;.$$

In the latter expressions, θ is the incidence angle and n the optical index of the incident isotropic medium.

Case where the incidence is normal and c is in the interface plane

When in addition the incidence is normal, by putting $\beta = 0$ in the previous equations, expressions of the wave vectors of the ordinary and extraordinary fields can be again

simplified as follows:

$$\begin{cases} \mathbf{k_o} = \begin{pmatrix} k_{oz} \\ 0 \\ 0 \end{pmatrix}_{abc} = \begin{pmatrix} 0 \\ 0 \\ k_{oz} \end{pmatrix}_{xyz} , \\ \\ \mathbf{k_e} = \begin{pmatrix} k_{ez} \\ 0 \\ 0 \end{pmatrix}_{abc} = \begin{pmatrix} 0 \\ 0 \\ k_{ez} \end{pmatrix}_{xyz} , \\ \\ \text{with : } \quad k_{oz(ez)} = \pm \dfrac{\omega}{c} n_{o(e)} , \end{cases} \tag{A.18}$$

and the directions of the ordinary and extraordinary fields are simply written as:

$$\begin{aligned} \mathbf{o} &= \frac{k_{oz}}{|\, k_{oz}\,|} \begin{pmatrix} \sin\phi_c \\ -\cos\phi_c \\ 0 \end{pmatrix}_{xyz} = \frac{k_{oz}}{|\, k_{oz}\,|} \begin{pmatrix} 0 \\ -1 \\ 0 \end{pmatrix}_{abc} , \\ \mathbf{e} &= \begin{pmatrix} -\cos\phi_c \\ -\sin\phi_c \\ 0 \end{pmatrix}_{xyz} = \begin{pmatrix} 0 \\ 0 \\ 1 \end{pmatrix}_{abc} . \end{aligned} \tag{A.19}$$

After having determined the direction of the electric field associated to the ordinary and extraordinary waves at the interface, we now want to determine the amplitudes of these fields. For this, it is necessary to involve the field continuity conditions at the interface between the two mediums.

A.2.2 Electromagnetic propagation : air $\rightarrow$ quartz

As illustrated in figure A.3, the electric field and the wave vector associated to an incident plane wave coming from the air are called respectively $\mathbf{E_i}$ and $\mathbf{k}$. The fields reflected and refracted at the interface between the air and the quartz are called $\mathbf{E_r}$ and $\mathbf{E_t}$. The reference basis (x, y, z) is such as the normal to the crystal surface $\mathbf{n_s}$ is the opposite of the $\mathbf{z}$ axis, the $\mathbf{x}$ axis is orthogonal to the $(\mathbf{k}, \mathbf{n_s})$ incident plane and (**x**,**y**,**z**) is orthonormal. We have chosen z = 0 at the interface, z < 0 in the air and z > 0 inside the quartz. In that framework the electric fields can be written as:

$$\begin{aligned} \mathbf{E_i} &= (A_s\mathbf{s} + A_p\mathbf{p})\, e^{-i\mathbf{k}\cdot\mathbf{r}}\, e^{i\omega t} , \\ \mathbf{E_r} &= (B_s\mathbf{s} + B_p\mathbf{p'})\, e^{-i\mathbf{k'}\cdot\mathbf{r}}\, e^{i\omega t} , \\ \mathbf{E_t} &= (C_o\mathbf{o}\, e^{-i\mathbf{k_o}\cdot\mathbf{r}} + C_e\mathbf{e}\, e^{-i\mathbf{k_e}\cdot\mathbf{r}})\, e^{i\omega t} , \end{aligned} \tag{A.20}$$

where $\mathbf{s}$, $\mathbf{p}$ and $\mathbf{p'}$ are three unit vectors defined by:

$$\mathbf{s} = \frac{-\mathbf{k}\times\mathbf{n_s}}{|-\mathbf{k}\times\mathbf{n_s}|} \quad , \quad \mathbf{p} = \frac{\mathbf{k}\times\mathbf{s}}{|\mathbf{k}|} \quad , \quad \mathbf{p'} = \frac{-\mathbf{k'}\times\mathbf{s}}{|\mathbf{k}|} , \tag{A.21}$$

with:

$$\mathbf{k} \;=\; \beta\mathbf{y} + \mathrm{k_z}\mathbf{z} \qquad , \qquad \mathbf{k'} \;=\; \beta\mathbf{y} - \mathrm{k_z}\mathbf{z} \qquad , \qquad \mathbf{n_s} = -\mathbf{z} \;\; . \tag{A.22}$$

$\mathbf{s}$ is equal to $\mathbf{x}$ and is perpendicular to the (kz) incident plane. $\mathbf{p}$ and $\mathbf{p'}$ belong to the incident plane. $\mathbf{o}$ and $\mathbf{e}$ are two unit vectors parallel to the electric field vectors of the ordinary and extraordinary refracted waves. $\mathbf{k_o}$ and $\mathbf{k_e}$ are the two corresponding wave vectors. $\mathbf{k_o}$, $\mathbf{k_e}$, $\mathbf{o}$ and $\mathbf{e}$ are given by equations (A.15), (A.16), (A.17), (A.12) and (A.13). In that case of the propagation air-quartz, $\mathrm{k_{oz}}$ and $\mathrm{k_{ez}}$ are positive.

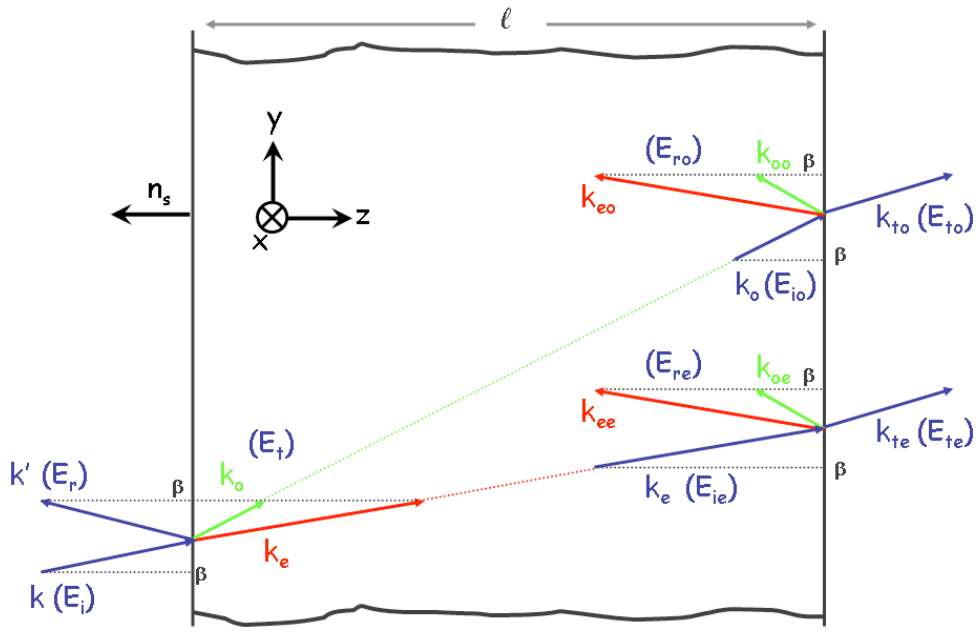

Figure A.3: Passage of a plane wave through an anisotropic uniaxial medium of thickness ℓ. The normal to the crystal plane is $\mathrm{n_s}$ and the reference frame $(\mathrm{x}, \mathrm{y}, \mathrm{z})$ is indicated.

The magnetic field associated to the reflected and refracted incident waves are obtained from (A.1) and (A.3):

$$\mathbf{H} \;=\; \frac{i}{\omega\mu}\,\nabla \times \mathbf{E} \;\; ,$$

and by using (A.20), one obtains:

$$\mathbf{H_i} \;=\; \frac{1}{\omega\mu}\,\mathbf{k} \times (\mathrm{A_s}\mathbf{s} \;+\; \mathrm{A_p}\mathbf{p})\; \mathrm{e}^{-i\mathbf{k}\cdot\mathbf{r}}\; \mathrm{e}^{i\omega t} \;\; ,$$

$$\mathbf{H_r} \;=\; \frac{1}{\omega\mu}\,\mathbf{k'} \times (\mathrm{B_s}\mathbf{s} \;+\; \mathrm{B_p}\mathbf{p'})\; \mathrm{e}^{-i\mathbf{k'}\cdot\mathbf{r}}\; \mathrm{e}^{i\omega t} \;\; ,$$

$$\mathbf{H_t} \;=\; \frac{1}{\omega\mu}\,\left(\, \mathrm{C_o}\mathbf{k_o} \times \mathbf{o}\; \mathrm{e}^{-i\mathbf{k_o}\cdot\mathbf{r}} \;+\; \mathrm{C_e}\mathbf{k_e} \times \mathbf{e}\; \mathrm{e}^{-i\mathbf{k_e}\cdot\mathbf{r}} \,\right)\; \mathrm{e}^{i\omega t} \;\; .$$

The tangential components of the fields $\mathbf{E}$ and $\mathbf{H}$ must be continuous at the interface $\mathrm{z} = 0$ between the isotropic medium and the crystal which leads to:

$$
\begin{aligned}
&(\mathbf{E_i}+\mathbf{E_r})\cdot\mathbf{x}=\mathbf{E_t}\cdot\mathbf{x} \quad , \quad (\mathbf{H_i}+\mathbf{H_r})\cdot\mathbf{x}=\mathbf{H_t}\cdot\mathbf{x} \quad , \\
&(\mathbf{E_i}+\mathbf{E_r})\cdot\mathbf{y}=\mathbf{E_t}\cdot\mathbf{y} \quad , \quad (\mathbf{H_i}+\mathbf{H_r})\cdot\mathbf{y}=\mathbf{H_t}\cdot\mathbf{y} \quad .
\end{aligned}
\tag{A.23}
$$

By using the following relations:

$$
\begin{array}{llll}
\mathbf{p}=\dfrac{k_z\mathbf{y}-\beta\mathbf{z}}{k} \quad , & \mathbf{p'}=\dfrac{k_z\mathbf{y}+\beta\mathbf{z}}{k} \quad , & \mathbf{p}\cdot\mathbf{y}=\mathbf{p'}\cdot\mathbf{y}=\dfrac{k_z}{k} \quad , \\
\mathbf{s}\cdot\mathbf{x}=1 \quad , & \mathbf{p}\cdot\mathbf{x}=0 \quad , & \mathbf{p'}\cdot\mathbf{x}=0 \quad , \\
\mathbf{s}\cdot\mathbf{y}=0 \quad , & (\mathbf{k}\times\mathbf{s})\cdot\mathbf{x}=0 \quad , & (\mathbf{k}\times\mathbf{s})\cdot\mathbf{y}=k_z \quad , \\
(\mathbf{k'}\times\mathbf{s})\cdot\mathbf{x}=0 \quad , & (\mathbf{k'}\times\mathbf{s})\cdot\mathbf{y}=-k_z \quad , & (\mathbf{k}\times\mathbf{p})\cdot\mathbf{x}=-k \quad , \\
(\mathbf{k}\times\mathbf{p})\cdot\mathbf{y}=0 \quad , & (\mathbf{k'}\times\mathbf{p'})\cdot\mathbf{x}=k \quad , & (\mathbf{k'}\times\mathbf{p'})\cdot\mathbf{y}=0 \quad ,
\end{array}
$$

the four relations (A.23) are written as:

$$
\begin{cases}
A_s+B_s &= C_o\,(\mathbf{x}\cdot\mathbf{o}) \;+\; C_e\,(\mathbf{x}\cdot\mathbf{e}) \\
k_z\,(A_p+B_p) &= k\,C_o\,(\mathbf{y}\cdot\mathbf{o}) \;+\; k\,C_e\,(\mathbf{y}\cdot\mathbf{e}) \\
k\,(B_p-A_p) &= C_o\,\mathbf{x}\cdot(\mathbf{k_o}\times\mathbf{o}) \;+\; C_e\,\mathbf{x}\cdot(\mathbf{k_e}\times\mathbf{e}) \\
k_z\,(A_s-B_s) &= C_o\,\mathbf{y}\cdot(\mathbf{k_o}\times\mathbf{o}) \;+\; C_e\,\mathbf{y}\cdot(\mathbf{k_e}\times\mathbf{e})
\end{cases}
\tag{A.24}
$$

General case

The resolution of the boundary equations (A.24) allows the four unknown quantities B_s, B_p, C_o and C_e to be obtained as function of the incident wave amplitudes A_s and A_p. The resolution of (A.24) leads to:

$$
\begin{aligned}
&C_o = A_s t_{so}+A_p t_{po} \quad , \quad B_s = A_s r_{ss}+A_p r_{ps} \quad , \\
&C_e = A_s t_{se}+A_p t_{pe} \quad , \quad B_p = A_s r_{sp}+A_p r_{pp} \quad ,
\end{aligned}
\tag{A.25}
$$

where:

$$
\begin{aligned}
t_{so} &= \frac{2k_z D}{AD-BC} \quad , \quad t_{se} = \frac{-2k_z C}{AD-BC} \quad , \\
t_{po} &= \frac{-2k_z B}{AD-BC} \quad , \quad t_{pe} = \frac{2k_z A}{AD-BC} \quad , \\
r_{ss} &= (\mathbf{x}\cdot\mathbf{o})\, t_{so} + (\mathbf{x}\cdot\mathbf{e})\, t_{se} - 1 \ , \\
r_{ps} &= (\mathbf{x}\cdot\mathbf{o})\, t_{po} + (\mathbf{x}\cdot\mathbf{e})\, t_{pe} \ , \\
r_{sp} &= \frac{k}{k_z}\left[(\mathbf{o}\cdot\mathbf{y})\, t_{so} + (\mathbf{e}\cdot\mathbf{y})\, t_{se}\right] \ , \\
r_{pp} &= \frac{k}{k_z}\left[(\mathbf{o}\cdot\mathbf{y})\, t_{po} + (\mathbf{e}\cdot\mathbf{y})\, t_{pe}\right] - 1 \ ,
\end{aligned}
\tag{A.26}
$$

and where the quantities A, B, C, D are defined by:

$$
\begin{aligned}
A &= \mathbf{o}\cdot(\mathbf{y}\times\mathbf{k}) + \mathbf{o}\cdot(\mathbf{y}\times\mathbf{k_o}) \ , \\
B &= \mathbf{e}\cdot(\mathbf{y}\times\mathbf{k}) + \mathbf{e}\cdot(\mathbf{y}\times\mathbf{k_e}) \ , \\
C &= k\ (\mathbf{o}\cdot\mathbf{y}) - \frac{(\mathbf{y}\times\mathbf{k})\cdot(\mathbf{k_o}\times\mathbf{o})}{k} \ , \\
D &= k\ (\mathbf{e}\cdot\mathbf{y}) - \frac{(\mathbf{y}\times\mathbf{k})\cdot(\mathbf{k_e}\times\mathbf{e})}{k} \ .
\end{aligned}
$$

We have introduced in (A.25) the so-called Fresnel coefficients describing the air-quartz transmission of an s or a p wave component in an ordinary or an extraordinary wave component, and the reflection in air of an s or a p wave component in an s or a p reflected wave component:

- t_{so} : transmission of an s wave component in an ordinary wave component,
- t_{po} : transmission of a p wave component in an ordinary wave component,
- t_{se} : transmission of an s wave component in an extraordinary wave component,
- t_{pe} : transmission of a p wave component in an extraordinary wave component,
- r_{ss} : reflection of an s wave component in an s wave component,
- r_{ps} : reflection of a p wave component in an s wave component,
- r_{sp} : reflection of an s wave component in a p wave component,
- r_{pp} : reflection of a p wave component in a p wave component.

Case where c belongs to the interface and the incident is normal

In the case of an incident wave of which the wave vector is perpendicular to the (xy) crystal plane, and in the case where moreover the optical axis **c** belongs to the interface plane, using relations (A.18) and (A.19) allows the Fresnel coefficient of expression (A.26) to be simplified as:

$$t_{so} = \frac{2\,n}{(n+n_o)}\,\mathbf{s}\cdot\mathbf{o} \quad , \quad r_{ss} = \frac{(n^2 - n_o n_e) - n\,(n_e - n_o)\,\cos 2\phi_c}{(n+n_o)\,(n+n_e)} \quad ,$$

$$t_{po} = \frac{2\,n}{(n+n_o)}\,\mathbf{p}\cdot\mathbf{o} \quad , \quad r_{ps} = -\,\frac{n\,(n_e - n_o)\,\sin 2\phi_c}{(n+n_o)\,(n+n_e)} \quad ,$$

$$t_{se} = \frac{2\,n}{(n+n_e)}\,\mathbf{s}\cdot\mathbf{e} \quad , \quad r_{sp} = r_{ps} \quad ,$$

$$t_{pe} = \frac{2\,n}{(n+n_e)}\,\mathbf{p}\cdot\mathbf{e} \quad , \quad r_{pp} = \frac{(n^2 - n_o n_e) + n\,(n_e - n_o)\,\cos 2\phi_c}{(n+n_o)\,(n+n_e)} \quad ,$$

where n is the index of the isotropic medium and n_o and n_e are the indices of the uniaxial medium.

We now want to determine the Fresnel coefficients corresponding to the passage of the wave at the interface between the anisotropic medium and the isotropic medium.

A.2.3 Electromagnetic propagation: quartz → air

To calculate the wave propagation at the second interface, we consider an incident wave propagating inside the crystal and arriving at the interface. We choose again to take the longitudinal coordinate z null at the interface. The electric field associated to this wave is written as:

$$\mathbf{E_i} = C_\epsilon \epsilon^+ \, e^{-i\mathbf{k}_\epsilon^+ \cdot \mathbf{r}} \, e^{i\omega t} \quad ,$$

where C_ϵ, ϵ^+ and $\mathbf{k}_\epsilon^+$ are quantities characteristic either of an ordinary wave (C_o, $\mathbf{o}^+$ and $\mathbf{k}_\mathbf{o}^+$), or of an extraordinary wave (C_e, $\mathbf{e}^+$ and $\mathbf{k}_\mathbf{e}^+$) propagating in the crystal, as shown in figure A.3. The electric fields associated to the reflected and refracted waves at the interface are called respectively $\mathbf{E_r}$ and $\mathbf{E_t}$. They are written as:

$$\mathbf{E_r} = (C_{ro}\mathbf{o}^- \, e^{-i\mathbf{k}_\mathbf{o}^- \cdot \mathbf{r}} + C_{re}\mathbf{e}^- \, e^{-i\mathbf{k}_\mathbf{e}^- \cdot \mathbf{r}}) \, e^{i\omega t} \quad ,$$

$$\mathbf{E_t} = (A_s\mathbf{s} + A_p\mathbf{p}) \, e^{-i\mathbf{k}\cdot\mathbf{r}} \, e^{i\omega t} \quad ,$$

where, as for the case of the passage from air to quartz, **s** and **p** are two unit vectors defined by equations (A.21) and (A.22). **s** is equal to **x**, **p** belongs to the (kz) plane, $\mathbf{o}^-$ and $\mathbf{e}^-$ are two unit vectors parallel to the electric field of the ordinary and extraordinary reflected waves respectively.

The magnetic fields associated to the incident reflected and refracted waves are written as:

$$\mathbf{H_i} \;=\; \frac{1}{\omega\mu}\,\mathrm{C}_\epsilon \mathbf{k}_\epsilon^+ \times \epsilon^+ \;\mathrm{e}^{-i\mathbf{k}_\epsilon^+\cdot\mathbf{r}}\;\mathrm{e}^{i\omega \mathrm{t}} \quad ,$$

$$\mathbf{H_r} \;=\; \frac{1}{\omega\mu}\left(\mathrm{C_{ro}}\mathbf{k_o^-} \times \mathbf{o^-}\;\mathrm{e}^{-i\mathbf{k_o^-}\cdot\mathbf{r}} \;+\; \mathrm{C_{re}}\mathbf{k_e^-} \times \mathbf{e^-}\;\mathrm{e}^{-i\mathbf{k_e^-}\cdot\mathbf{r}}\right)\mathrm{e}^{i\omega \mathrm{t}} \quad ,$$

$$\mathbf{H_t} = \frac{1}{\omega\mu}\,\mathbf{k} \times (\mathrm{A_s}\mathbf{s} \;+\; \mathrm{A_p}\mathbf{p})\;\mathrm{e}^{-i\mathbf{k}\cdot\mathbf{r}}\;\mathrm{e}^{i\omega \mathrm{t}} \quad .$$

General case

As for the calculation at the first interface, the continuity conditions of the tangential components allow the four unknown quantities $\mathrm{A_s}$, $\mathrm{A_p}$, $\mathrm{C_{ro}}$ and $\mathrm{C_{re}}$ involved in the field expressions to be obtained as a function of the amplitude of the incident wave in the crystal C_ϵ and as function of the wave vectors. Explicitly, the four continuity conditions are written as:

$$\left\{\begin{array}{rcl}
\mathrm{A_s} & = & \mathrm{C}_\epsilon\,(\mathbf{x}\cdot\epsilon^+) \;+\; \mathrm{C_{ro}}\,(\mathbf{x}\cdot\mathbf{o^-}) \;+\; \mathrm{C_{re}}\,(\mathbf{x}\cdot\mathbf{e^-}) \\
\mathrm{k_z\;A_p} & = & \mathrm{k\;C}_\epsilon\,(\mathbf{y}\cdot\epsilon^+) \;+\; \mathrm{k\;C_{ro}}\,(\mathbf{y}\cdot\mathbf{o^-}) \;+\; \mathrm{k\;C_{re}}\,(\mathbf{y}\cdot\mathbf{e^-}) \\
-\mathrm{k\;A_p} & = & \mathrm{C}_\epsilon\,\mathbf{x}\cdot(\mathbf{k}_\epsilon^+ \times \epsilon^+) \;+\; \mathrm{C_{ro}}\,\mathbf{x}\cdot(\mathbf{k_o^-} \times \mathbf{o^-}) \;+\; \mathrm{C_{re}}\,\mathbf{x}\cdot(\mathbf{k_e^-} \times \mathbf{e^-}) \\
\mathrm{k_z\;A_s} & = & \mathrm{C}_\epsilon\,\mathbf{y}\cdot(\mathbf{k}_\epsilon^+ \times \epsilon^+) \;+\; \mathrm{C_{ro}}\,\mathbf{y}\cdot(\mathbf{k_o^-} \times \mathbf{o^-}) \;+\; \mathrm{C_{re}}\,\mathbf{y}\cdot(\mathbf{k_e^-} \times \mathbf{e^-})
\end{array}\right. \tag{A.27}$$

An initial wave inside the crystal which is composed of its two components of ordinary and extraordinary fields is written as:

$$\mathbf{E_i} \;=\; \left(\mathrm{C_o}\mathbf{o}^+\;\mathrm{e}^{-i\mathbf{k_o^+}\cdot\mathbf{r}} \;+\; \mathrm{C_e}\mathbf{e}^+\;\mathrm{e}^{-i\mathbf{k_e^+}\cdot\mathbf{r}}\right)\;\mathrm{e}^{i\omega \mathrm{t}} \quad . \tag{A.28}$$

We therefore have to resolve two systems of four equations (A.27) where C_ϵ, ϵ^+ and k_ϵ^+ are replaced by the two sets of following coefficients:

$$\left\{\begin{array}{rcl}
\mathrm{C}_\epsilon & = & \mathrm{C_o} \\
\epsilon^+ & = & \mathbf{o}^+ \\
\mathbf{k}_\epsilon^+ & = & \mathbf{k_o^+}
\end{array}\right. \qquad \text{and} \qquad \left\{\begin{array}{rcl}
\mathrm{C}_\epsilon & = & \mathrm{C_e} \\
\epsilon^+ & = & \mathbf{e}^+ \\
\mathbf{k}_\epsilon^+ & = & \mathbf{k_e^+}
\end{array}\right.$$

The resolution of the continuity equations (A.27) leads to:

$$\begin{array}{rclcrcl}
\mathrm{C_{ro}} & = & \mathrm{C_o r_{oo}} + \mathrm{C_e r_{eo}} & , & \mathrm{A_s} & = & \mathrm{C_o t_{os}} + \mathrm{C_e t_{es}} \quad , \\
\mathrm{C_{re}} & = & \mathrm{C_o r_{oe}} + \mathrm{C_e r_{ee}} & , & \mathrm{A_p} & = & \mathrm{C_o t_{op}} + \mathrm{C_e t_{ep}} \quad ,
\end{array} \tag{A.29}$$

where:

$$
\begin{aligned}
r_{oo} &= \frac{E_o D - F_o B}{AD - BC} \quad , \quad r_{eo} = \frac{E_e D - F_e B}{AD - BC} \quad , \\
r_{oe} &= \frac{AF_o - E_o C}{AD - BC} \quad , \quad r_{ee} = \frac{AF_e - E_e C}{AD - BC} \quad , \\
t_{os} &= (\mathbf{x}\cdot\mathbf{o}^+) + (\mathbf{x}\cdot\mathbf{o}^-)\, r_{oo} + (\mathbf{x}\cdot\mathbf{e}^-)\, r_{oe} \ , \\
t_{es} &= (\mathbf{x}\cdot\mathbf{e}^+) + (\mathbf{x}\cdot\mathbf{o}^-)\, r_{eo} + (\mathbf{x}\cdot\mathbf{e}^-)\, r_{ee} \ , \\
t_{op} &= \left(\frac{k}{k_z}\right) \left[(\mathbf{y}\cdot\mathbf{o}^+) + (\mathbf{y}\cdot\mathbf{o}^-)\, r_{oo} + (\mathbf{y}\cdot\mathbf{e}^-)\, r_{oe} \right] \ , \\
t_{ep} &= \left(\frac{k}{k_z}\right) \left[(\mathbf{y}\cdot\mathbf{e}^+) + (\mathbf{y}\cdot\mathbf{o}^-)\, r_{eo} + (\mathbf{y}\cdot\mathbf{e}^-)\, r_{ee} \right] \ ,
\end{aligned}
\tag{A.30}
$$

and where the quantities A, B, C, D, E_o, E_e, F_o and F_e are defined by:

$$
\begin{aligned}
A &= \mathbf{o}^-\cdot(\ \mathbf{y}\times\mathbf{k}_\mathbf{o}^- \ - \ \mathbf{y}\times\mathbf{k}) \quad , \quad C = k\ (\mathbf{o}^-\cdot\mathbf{y}) + \frac{(\mathbf{y}\times\mathbf{k})\cdot(\mathbf{k}_\mathbf{o}^-\times\mathbf{o}^-)}{k} \ , \\
B &= \mathbf{e}^-\cdot(\mathbf{y}\times\mathbf{k}_\mathbf{e}^- - \mathbf{y}\times\mathbf{k}) \quad , \quad D = k\ (\mathbf{e}^-\cdot\mathbf{y}) + \frac{(\mathbf{y}\times\mathbf{k})\cdot(\mathbf{k}_\mathbf{e}^-\times\mathbf{e}^-)}{k} \ , \\
E_o &= \mathbf{o}^+\cdot[\ \mathbf{y}\times\mathbf{k} - y\times\mathbf{k}_\mathbf{o}^+] \quad , \quad F_o = -\ k\ (\mathbf{o}^+\cdot\mathbf{y}) - \frac{(\mathbf{y}\times\mathbf{k})\cdot(\mathbf{k}_\mathbf{o}^+\times\mathbf{o}^+)}{k} \ , \\
E_e &= \mathbf{e}^+\cdot[\ \mathbf{y}\times\mathbf{k} - y\times\mathbf{k}_\mathbf{e}^+] \quad , \quad F_e = -\ k\ (\mathbf{e}^+\cdot\mathbf{y}) - \frac{(\mathbf{y}\times\mathbf{k})\cdot(\mathbf{k}_\mathbf{e}^+\times\mathbf{e}^+)}{k} \ .
\end{aligned}
$$

In (A.29), Fresnel coefficients describing the reflection in the quartz of an ordinary or an extraordinary wave component in an ordinary or an extraordinary reflected wave component, and Fresnel coefficients describing the quartz-air transmission of an ordinary or an extraordinary wave component in an s or a p transmitted wave component have been introduced:

- r_{oo} : reflection of an ordinary wave component in an ordinary wave component,
- r_{eo} : reflection of an extraordinary wave component in an ordinary wave component,
- r_{oe} : reflection of an ordinary wave component in an extraordinary wave component,
- r_{ee} : reflection of an extraordinary wave component in an extraordinary wave component,
- t_{os} : transmission of an ordinary wave component in an s wave component,
- t_{op} : transmission of an ordinary wave component in a p wave component,

- t_{es} : transmission of an extraordinary wave component in an s wave component,
- t_{ep} : transmission of an extraordinary wave component in a p wave component.

Case where c belongs to the interface and the incidence is normal

If the incident wave inside the crystal has its wave vector perpendicular to the crystal plane and if moreover the optical axis **c** is in the interface plane, the Fresnel coefficient of expression (A.30) can be simplified as:

$$\begin{aligned}
r_{oo} &= \left(\frac{n_o - n}{n_o + n}\right) \mathbf{o}^+ \cdot \mathbf{o}^- \quad , \qquad t_{os} = \left(\frac{2\, n_o}{n_o + n}\right) \mathbf{o}^+ \cdot \mathbf{s} \quad , \\
r_{eo} &= 0 \qquad\qquad\qquad\quad , \qquad t_{es} = \left(\frac{2\, n_e}{n_e + n}\right) \mathbf{e}^+ \cdot \mathbf{s} \quad , \\
r_{oe} &= 0 \qquad\qquad\qquad\quad , \qquad t_{op} = \left(\frac{2\, n_o}{n_o + n}\right) \mathbf{o}^+ \cdot \mathbf{p} \quad , \\
r_{ee} &= \left(\frac{n_e - n}{n_e + n}\right) \mathbf{e}^+ \cdot \mathbf{e}^- \quad , \qquad t_{ep} = \left(\frac{2\, n_e}{n_e + n}\right) \mathbf{e}^+ \cdot \mathbf{p} \quad .
\end{aligned}$$

A.3 Calculation of the total transmitted field

Having determined all the transmission and reflection Fresnel coefficients at the air-quartz and quartz-air interfaces, the total electric field emerging from the crystal can now be calculated to obtain the expression of the total transmitted intensity. Introducing:

- the air-quartz transmission matrix $T_{aq} = \begin{pmatrix} t_{so} & t_{po} \\ t_{se} & t_{pe} \end{pmatrix}$,
- the air-quartz reflection matrix $R_{aq} = \begin{pmatrix} r_{ss} & r_{ps} \\ r_{sp} & r_{pp} \end{pmatrix}$,
- the quartz-air reflection matrix $R_{qa} = \begin{pmatrix} r_{oo} & r_{oo} \\ r_{oe} & r_{oe} \end{pmatrix}$,
- the quartz-air transmission matrix $T_{qa} = \begin{pmatrix} t_{os} & t_{es} \\ t_{op} & t_{ep} \end{pmatrix}$,

expressions (A.25) and (A.29) of the field amplitudes can be rewritten in matrix form. For the air-quartz passage, (A.25) becomes:

$$\begin{pmatrix} C_o \\ C_e \end{pmatrix} = T_{aq} \begin{pmatrix} A_s \\ A_p \end{pmatrix} \quad \text{and} \quad \begin{pmatrix} B_s \\ B_p \end{pmatrix} = R_{aq} \begin{pmatrix} A_s \\ A_p \end{pmatrix} \quad , \qquad \text{(A.31)}$$

and for the quartz-air passage (A.29) becomes:

$$\begin{pmatrix} C_{ro} \\ C_{re} \end{pmatrix} = R_{qa} \begin{pmatrix} C_o \\ C_e \end{pmatrix} \quad \text{and} \quad \begin{pmatrix} A'_s \\ A'_p \end{pmatrix} = T_{qa} \begin{pmatrix} C_o \\ C_e \end{pmatrix} \quad , \tag{A.32}$$

where A'_s and A'_p are the quantities A_s and A_p of equation (A.29) whose names have been changed to avoid confusion with the incident field. After only one passage of the wave through the medium, the transmitted wave (A'_s, A'_p) is the result of the incident wave (A_s, A_p) refracted by the first interface at $z = 0$, then propagated through the medium until the second interface at $z = \ell$ and refracted by the second face. Introducing the matrix:

$$P_{\pm} = \begin{pmatrix} e^{-i\ell \mathbf{k}_o^{\pm} \cdot \mathbf{z}} & 0 \\ 0 & e^{-i\ell \mathbf{k}_e^{\pm} \cdot \mathbf{z}} \end{pmatrix}$$

describing the wave propagation through the medium of thickness ℓ, the amplitude (C'_o, C'_e) of the field arriving at the second interface is written as:

$$\begin{pmatrix} C'_o \\ C'_e \end{pmatrix} = P_+ \begin{pmatrix} C_o \\ C_e \end{pmatrix} \quad .$$

Then, using (A.31) and (A.32), the amplitude of the field emerging from the crystal is written as a function of the incident field amplitude as:

$$\begin{pmatrix} A'_s \\ A'_p \end{pmatrix} = T_{qa}\, P_+\, T_{aq} \begin{pmatrix} A_s \\ A_p \end{pmatrix} \quad .$$

In the same way, the amplitude of the field transmitted after a double reflection on the first and the second crystal faces is written as:

$$\begin{pmatrix} A'_s \\ A'_p \end{pmatrix} = T_{qa}\, P_+ \left[\, R_{qa}\, P_-^{-1}\, R_{qa}\, P_+ \,\right] T_{aq} \begin{pmatrix} A_s \\ A_p \end{pmatrix} \quad .$$

After an infinity of internal reflections, the transmitted wave amplitude is written in the form:

$$\begin{pmatrix} A'_s \\ A'_p \end{pmatrix} = T_{qa}\, P_+ \sum_{n=0}^{\infty} \left[\, R_{qa}\, P_-^{-1}\, R_{qa}\, P_+ \,\right]^n T_{aq} \begin{pmatrix} A_s \\ A_p \end{pmatrix} \quad .$$

By using the fact that:

$$\sum_{i=0}^{\infty} M^i = [\, I - M \,]^{-1}$$

where I is the identity matrix, the amplitude of the total transmitted field through the crystal is written as:

$$\begin{pmatrix} A'_s \\ A'_p \end{pmatrix} = \mathcal{M}_{\mathcal{T}} \begin{pmatrix} A_s \\ A_p \end{pmatrix} \qquad \text{where :}$$
$$\mathcal{M}_{\mathcal{T}} \;=\; T_{qa}\, P_+ \left[\, I \;-\; R_{qa}\, P_-^{-1}\, R_{qa}\, P_+ \,\right]^{-1} T_{aq} \;\; . \tag{A.33}$$

Formula (A.33) provides the transmitted amplitude of a field passing through an anisotropic uniaxial medium of a given thickness ℓ, as a function of the amplitude of the initial field, and this by taking into account the multiple reflections which occur inside the medium. The calculation has been done in a (x, y, z) reference frame attached to the crystal and to the incident wave, and whose unit vectors $\mathbf{x}$, $\mathbf{y}$ and $\mathbf{z}$ are such as:

- $\mathbf{z} = -\mathbf{n_s}$ where $\mathbf{n_s}$ is the normal of the crystal surface,
- $\mathbf{x}$ is perpendicular to the incident plane defined by $(\mathbf{k_{in}}, \mathbf{n_s})$, $\mathbf{k_{in}}$ being the incident wave vector,
- $(\mathbf{x}, \mathbf{y}, \mathbf{z})$ is orthonormal.

In Chapters 4, 5 and 6, the generated ellipsometer intensity signals have been simulated by using formula (A.33) for the quartz quater wave plate transmission. The transmitted wave intensities simulated with this model and compared with experimental ellipsometer data recorded in photodiodes allow some parameters characteristic of the anisotropic uniaxial crystal as its thickness, its birefringence or some misalignments parameters, to be determined.

Bibliography

[1] G.-A. Voss and B. H. Wiik, *The electron-proton collider HERA*, Annu. Rev. Nucl. Part. Sci. 44 (1994) 413-452.

[2] I. Abt et al., *The H1 detector at HERA*, Nucl. Instr. and Meth. A 386 (1997) 310-347.

[3] I. Abt et al., *The tracking, calorimeter and muon detectors of the H1 experiment at HERA*, Nucl. Instr. and Meth. A 386 (1997) 348-396.

[4] Zeus Collabotation, *The ZEUS Detector Status Report*, Status Report 1993, DESY.

[5] G. Ingelman, A. De Roeck, R. Klanner, *Proceedings of Future Physics at HERA*, (1995/96).

[6] The Hermes Collaboration, *Hermes Technical Design Report*, DESY-PRC 93/06, MPIH-V20 1993.

[7] M. Walter, *An experiment to study CP violation using an internal target at the HERA proton ring*, Nucl. Instr. and Meth. A 360 (1995) 267-270.

[8] F. Willeke, *HERA Status and Upgrade Plans*, Proceedings of PAC'1997 conference, vol.1, 51-55.

[9] G.H. Hoffstaetter, *Future Possibilities for HERA*, Proceedings of EPAC 2000 conference, in Vienna 2000, EPAC 00, 13-17.

[10] J. Buon and J.P. Koutchouk, *Polarization of electron and proton beams*, Accelerator Physics (1995) 879-939.

[11] D. Sen et al., *Signifiance of Ehrenest theorem in quantum-classical relationship*, Current Science 80, 536 (2001).

[12] J. Buon, *Analytical approach to resonant depolarisation*, LAL-RT/82-06 (1982).

[13] J.S.Bell, *Polarized particles for accelerator physicists*, CERN report 75-11.

[14] B.W. Montague, *Polarized beams in high energy storage rings*, Phys. Rep. 113 (1984) 1.

[15] V. Bargmann, L. Michel, V.L. Telegdi, *Precession of the polarization of particles moving in a homogeneous electromagnetic field*, Phys. Rev. Lett. 2 (1959), 435-436.

[16] I.M.Ternov, Yu.M.Loskutov, L.I.Korovina, *Possibility of polarizing an electron beam by relativistic radiation in a magnetic field*, Sov. Phys. JETP, 14 (1962), 921.

[17] A.A.Sokolov and I.M.Ternov, *On polarization and spin effects in theory of synchrotron radiation*, Sov. Phys. Doklady, 8 (1964) 1203.

[18] A. W. Chao, *Polarization of a stored electron beam*, SLAC-PUB-2781 (1981).

[19] M. Sands, *The Physics of Electron Storage Rings: An Introduction*, SLAC-report 121 (1970).

[20] A. Piwinski, *Synchro-betatron resonances*, Lecture Notes in Physics 247 (1986) 104-120.

[21] D.P. Barber, *I. Electron and proton spin polarizsation in storage rings - An introduction*, proceedings of the 15th ICFA Advanced Beam Dynamics Workshop, Monterey (1998), also in DESY Report 98-096 (1998).

[22] A. Piwinski, *Beam instabilities and computer simulations*, Internal Report DESY M-83-21 (1983).

[23] J. Kewisch et al., *Nonlinear Spin Acceptance in Electron Storage Rings*, Phys. Rev. Lett. 62, 419-421, (1989).

[24] M. Böge, *The Status of Polarization Studies at HERA*, proceedings of PAC 1993, vol.1, 460-462 (1993).

[25] D.P. Barber, *The first attainment and the routine use of longitudinal spin polarization at a high energy electron storage ring*, Proceedings of the Particle Accelerator Conference (1995) 511-513.

[26] M. Böge, *Analysis of Spin Depolarizing Effects in Electron Storage Rings*, DESY 94-087 (1994).

[27] M. Böge and T. Limberg, *Calculation on depolarization in HERA due to beam-beam effects*, proceedings of PAC 1995, vol.5, 2901-2903 (1995)

[28] E. Gianfelice-Wendt et al., *Longitudinal positron polarisation in HERA-II*, Proceedings of EPAC 2004, Lucerne, Switzerland, 644-646.

[29] C. Montag and F. Stulle, *Simulation of orbit correction and synchrotron radiation aspects in the upgraded HERA interaction regions*, Proceedings of EPAC 2000, 370-372.

[30] E. Gianfelice-Wendt, *Vertical and Longitudinal Electron Polarization at HERA*, Proc. EPAC 94 (1994) 184-186.

[31] J.Buon and K. Steffen, *HERA variable-energy "mini" spin rotator and head-on ep collision scheme with choice of electron helivity*, Nucl. Instr. and Meth., A 245 (1986) 248.

[32] J.M. Grames et al., *Unique electron polarimeter analysing power comparison and precision spin-based energy measurement*, Phys. Rev. ST AB 7 (2004) 042802.

[33] T.J. Gay and F.B. Dunning, *Mott electron polarimetry*, Rev. Sci. Instrum. 63 (1992) 1635-1651.

[34] M. Steigerwald, *MeV Mott Polarimetry at Jeferson Lab*, AIP Con. Proc 570 935-942 (2001).

[35] B. Wagner et al., *A Møller polarimeter for CW and pulsed intermediate energy electron beam*, Nucl. Inst. and Meth. A 294 (1990) 541-548.

[36] D.P. Barber et al., *The HERA polarimeter and the first observation of electron spin polarization at HERA*, Nucl. Inst. and Meth. A 329 (1993) 79-111.

[37] U. Fano, *Remarks on the Classical and Quantum-Mechanical Treatment of Partial Polarization*, JOSA 39 (1949) 859.

[38] F.R. Arutyunyan et al., *Quasi-monochromatic and polarized high-energy gamma rays*, Sov. Phys. Usp 83 (1964) 339-357.

[39] C. Y. Prescott, *Spin dependent Compton scattering for use in analysing electron beam polarizations*, SLAC-TN-73-1 (1973).

[40] G. Bardin et al., *Conceptual design report of a Compton polarimeter for CEBAF Hall A*, note DAPNIA-SPhN-96-14 (1996).

[41] S. Escoffier, *Mesure précise de la polarisation du faisceau d'électrons à TJNAF par polarimétrie Compton pour les expériences G_E^p et $N-\Delta$*, Thesis (2001).

[42] V.N. Baĭer and V.A.Khoze, *Determination of the transverse polarization of high-energy electrons*, Sov. J. Nucl. Phys. 9 (1969) 238.

[43] J.R. Johnson et al., *Beam polarization measurements at the SPEAR strorage ring*, Nucl. Instr. and Meth. 204 (1983) 261.

[44] K. Long and K.P. Schüler, *Polarisation measurement on $e^{\pm}$ beams*, Nucl. Instr. and Meth. A 494 (2002) 75-80.

[45] D.P. Barber et al., *High spin polarization at the HERA electron storage ring*, Nucl. Inst. and Meth. A 338 (1994) 166-184.

[46] D.P. Barber et al., *The first achievement of longitudinal spin polarization in high energy electron storage ring*, Phys. Lett. B 343 (1995) 436-443.

[47] M. Beckmann et al., *The Longitudinal Polarimeter at HERA*, Nucl. Instr. and Meth. A 479 (2002) 334.

[48] J. Böhme, *Precision measurement with the transverse polarimeter at HERA II*, Eur. Phys. J. C 33, s01, s1067-s1069 (2004).

[49] W. Lorenzon et al., *Proposal to DESY for a Longitudinal Electron Polarimeter at HERA-East Section*, Internal Report HERMES-95-023 (1995).

[50] F.Zomer, *A high power Fabry-Perot resonator for precision Compton Polarimetry with the longitudinally polarised lepton beams at HERA*, LAL 03-12 (2003).

[51] K. Piotrzkowski, *Observation of the beam size effect at HERA*, hep-ex/9504003 (1995).

[52] Y. Tsai, *Pair production and bremsstrahlung of charged leptons*, Rev. Mod. Phys. 46 (1974) 815.

[53] M. Lomperski, *Compton scattering off black body radiation and other backgrounds of the HERA polarimeter*, DESY 93-045 (1993).

[54] E. Barrelet et al., *Letter of Indent to Upgrade the Longitudinal Polarimeter*, DESY PRC 00-02.

[55] C. Pascaud and F. Zomer, *Likelihood treatment of Polarisation Measurements*, Internal Report, Orsay, April 13, 1999.

[56] E. Barrelet et al., *Proposal to Upgrade the Longitudinal Polarimeter*, DESY PRC 00-02.

[57] H. Kogelnik and T. Li, *Laser Beams and Resonators*, Appl. Opt., Vol.5 (1996) 1550-1567.

[58] A.E. Siegman, *Hermite-gaussian functions of complex argument as optical-beam eigenfunctions*, J. Opt. Soc. Am. Vol.63 (1973) 1093-1094.

[59] A.E. Siegman, *Lasers*, University Science Books, 1986.

[60] R. Paschotta, *Encyclopedia of Laser Physics and Technology*, WILEY-VCH, 2008.

[61] N. Falletto, *Etude, conception et réalisation d'une cavité Fabry-Perot pour le polarimètre Compton de TJNAF*, Thesis Université Joseph Fourier-Grenoble 1, DAPNIA/SPhN-99-03T.

[62] J.P. Jorda et al., *A Fabry-Perot cavity for Compton polarimetry*, Nucl. Instr. and Meth. A 412 (1998) 1-18.

[63] N. Falletto et al., *Compton scattering off polarized electrons with a high-finesse Fabry-Perot Cavity at JLab*, Nucl. Instr. and Meth. A 459 (2001) 412-425.

[64] M. Baylac et al., *First electron beam polarization measurements with a Compton polarimeter at Jefferson Laboratory*, Phys. Lett. B 539 (2002) 8-12.

[65] S. Escoffier et al., *Accurate measurement of the electron beam polarization in JLab Hall A using Compton polarimetry*, Nucl. Instr. and Meth. A 551 (2005) 563-574.

[66] See `http://www.jdsu.com/product-literature/npro125126_ds_cl_ae_020606.pdf`

[67] R. Marie and A. Reboux from the LAL mechanical workshop.

[68] S.Y. Lee, Accelerator Physics, World Scientiic, 2004, p.216.

[69] Eun-San Kim, *Investigation of beam instabilities in PLS storage ring*, Proc. of EPAC 2002.

[70] S. Okubo, *Three-axis spherical Gimbal mount*, U.S. Patent, 4461463 (1984).

[71] See tt http://www.newport.com/servicesupport/Tutorials/images/fig02b.gif

[72] S. Baudrand, *Mesure de la polarisation longitudinale de faisceaux de positrons et d'électrons à HERA par effet Compton à l'aide d'une cavité Fabry-Perot de haute finesse*, PhD. Thesis (2007), Université Pierre et Marie Curie.

[73] P. Schuler private communication.

[74] V. Soskov from LAL Orsay.

[75] See `http://sales.hamamatsu.com/assets/pdf/parts_S/S1223_series.pdf`

[76] See `http://search.newport.com/?q=*&sku=CMA-12PP`

[77] Serge Huard, *Polarisation de la lumière*, Masson, Paris, 1993.

[78] Warren J. Smith, *Modern Optical Engineering*, McGraw-Hill, 2000.

[79] Jean-Louis Leroy, *La polarisation de la lumière et l'observation astronoqiue*, GIB.

[80] See `//www.ortodoxism.ro/datasheets/hamamatsu/G8370-02.pdf`

[81] See `http://search.newport.com/?sku=PR50PP`

[82] R.V. Pound, *Electronic Frequency Stabilization of Microwave Oscillators*, Rev. Sci. Instrum. 17 (1946) 490.

[83] R.W.P. Drever et al., *Laser Phase and Frequency Stabilization Using on Optical Resonator*, Appl. Phys. B 31 (1983) 97-105.

[84] E.D. Black, *An introduction to Pound-Drever-Hall laser frequency stabilization*, Am. J. Phys. 69, (2001) 79-87.

[85] G. Cantatore et al., *Frequency locking of a Nd:YAG laser using the laser itself as the optical phase modulator*, Rev. Sci. Instrum. 66 (1995) 2785.

[86] C. Scarlett and W. Lorenzon, *A New Sampling Calorimeter for the Longitudinal Polarimeter at HERMES*, Internal Report IPR-00-03 (2000).

[87] J. Raisanen et al., *DESY and CERN Calibrations of the New Sampling Calorimeter for the Longitudinal Polarimeter at HERMES*, Internal Report IPR-02-01 (2002).

[88] See `http://sine.ni.com/nips/cds/view/p/lang/en/nid/1527`

[89] See `http://www.ni.com/labview/`

[90] See `http://www.remote-anything.com/fr/index.htm`

[91] See `http://itcobe.web.cern.ch/itcobe/Services/Pvss/`

[92] See `http://newport.com/ESP300-3-Axis-Motion-Controller-Driver/140199/1033/catalog.aspx`

[93] See `http://www.micosusa.com/Con_5044.html`

[94] See http://www.analog.com/en/other/militaryaerospace/ad580/products/product.html

[95] See http://sine.ni.com/nips/cds/view/p/lang/en/nid/10972

[96] See http://www.adlinktech.cn/publications/manual/DAQ2000/NuDAQ-2010-05-06_50-11020-101.pdf

[97] See http://sine.ni.com/nips/cds/view/p/lang/en/nid/1880

[98] See http://digital.ni.com/manuals.nsf/websearch/8F46D333D49BB6268625697730076B09B

[99] A.M. Riva et al., *Very high Q frequency-locked Fabry-Perot cavity*, Rev. Sci. Intrum. 67 (1995) 2680-2684.

[100] See http://www.home.agilent.com/agilent/product.jspx?nid=-536902324.536881979.00&cc=US&lc=eng

[101] Chris Bowick, *RF Circuit Design*, Newnes (1997).

[102] M. Ait-Mohand, *Mise en œuvre d'un Polarimètre pour HERA: Système d'Acquisition et Application de Contrôle à l'aide de PVSS*, stage Ecole Doctorale Rayonnements et Environnement (2003).

[103] Ecole polytechnique, LAL-Orsay, Paris VI, *Proposal for a luminosity detector and its associated electronics*, Internal report, 3 march 1998 (preliminary version).

[104] T. Frisson, *Mesure de la luminosité pour l'expérience H1*, Thesis Université Paris-Sud (2006).

[105] See http://zone.ni.com/devzone/cda/tut/p/id/2710

[106] C. Dobrzynski, *Mise au point d'une procédure d'alignement d'un laser dans une cavité Fabry-Perot*, available on http://h1.web.lal.in2p3.fr/hardware/psfiles/rapport2_ceciledobrzynski.pdf.

[107] D.Z. Anderson et al., *Mirror reflectometer based on optical cavity decay time*, Appl. Opt. 23 (1983) 1238-1245.

[108] G. Rempe et al., *Measurement of ultralow losses in an optical interferometer*, Opt. Lett. 17 (1992) 363-365.

[109] J. Morville et al., *Effects of laser phase noise on the injection of a high-finesse cavity*, Appl. Opt. 41, 6980-6990 (2002).

[110] Paper in preparation, to be published in Nucl. Instr. and Meth.

[111] R. Clark Jones, *A New Calculus for the Treatment of Optical Systems. V, A More General Formulation, and Description of Another Calculus*, J. Opt. Soc. Am. 37, 107-110 (1947).

[112] G.Eppeldauer and J.E.Hardis, *Fourteen-decade photocurrent measurements with large-area silicon photodiodes at room temperature*, Appl. Opt. 30, 3091-3099 (1991).

[113] See `http://www.crystallaser.com/catalog.pdf`

[114] R.M.A. Azzam and N.M. Bashara, *Ellipsometry and polarized light* (Amsterdam, North-Holland, 1997).

[115] J. Poirson, T. Lanternier, J.C. Cotteverte, A. Le Floch, F. Bretenaker, *Jones matrices of a quater-wave plate for Gaussian beams*, App. Opt. 34 (1995) 6806-6818.

[116] F. Zomer, *Transmission and reflection of Gaussian beams by anisotropic parallel plates*, J. Opt. Soc. Am. A 20, 172-182, 2003.

[117] F. Zomer, *Transmission matrix of a uniaxial optically active crystal platelet*, Opt. Com. 252, 355-368 (2005).

[118] See `http://www.optiquefichou.fr`

[119] A. Carvallo, *Recherche de précision sur la dispersion infra-rouge du quartz*, Comptes rendus des scéances de l'académie des sciences, 126 (1989) 728.

[120] G.Ghosh, *Dispersion-equation coefficients for the refractive index and birefringence of calcite and quartz crystals*, Opt. Com. 163 (1999) 95-102.

[121] J.H. Shields and J.W. Ellis, *Dispersion of birefringence of Quartz in the near infrared*, J. Opt. Soc. Am. 46 (1956) 263.

[122] Newport company, Private communication.

[123] T. Toyoda and M. Yabe, *The temperature dependence of the refractive indices of fused silica and crystal quartz*, J. Phys. D: App. Phys., 16 (1983) 97-100.

[124] See `http://fr.wikipedia.org/wiki/Dilatation_thermique`

[125] P. Hello, *Couplages dans les détecteurs interférométriques d'ondes gravitationnelles*, LAL 96-93 (1996), page 70.

[126] D. Jacob et al., *Supermirror phase anisotropy measurement*, Opt. Lett. 20 (1995) 671.

[127] J.Y. Lee et al., *Measurement of ultralow supermirror birefringence by use of the polarimetric differential cavity ringdown technic*, Appl. Opt. 39 (2000) 1941.

[128] F. Brandi et al., *Measurement of the phase anisotropy of very high reflectivity interferential mirrors*, Appl. Phys. B 65 (1997) 351.

[129] R. Marie and A. Reboux from the LAL mechanical workshop.

[130] A.Reboux, private communication.

[131] J.E. Logan, N.A. Robertson, J. Hough, *Measurements of birefringence in suspended sample of fused silica*, Opt. Com. 107 (1994) 342-346.

[132] Measurement made by M. Linz from the Atomic Parity Violation group of the Laboratoire de l'Ecole Normale Supérieure, Paris.

[133] R. Clark Jones, *A new Calculus for the Treatment of Optical Systems. II. Proof of the Three General Equivalence Theorems*, J.O.S.A. 31 (1941) 493.

[134] R. Clark Jones, *A new Calculus for the Treatment of Optical Systems. I. Description and Discussion of the Calculus*, J.O.S.A. 31 (1941) 488.

[135] A. Delbart, DSM/DAPNIA 6-6112 R 2000 020 (1999).

[136] K.P. Schüler, *Polarimeter Studies for TESLA*, in Proceedings of the Linear Collider Workshop 2000, Fermilab, Batavia, IL, USA, 2001.

[137] G. Moortgat-Pick et al., *The role of polarized positrons and electrons in revealing fundamental interactions at the Linear Collider*, Phys. Rep. 460 (2008) 131-243.

[138] M. Birkinshaw, *The Sunyaev-Zel'dovich effect*, Phys. Rep. 310 (1999) 97-195.

[139] M. Birkinshaw et al., *The Sunyaev-Zeldovich effect toward three clusters of galaxies*, Nature 309 (1984) 34.

[140] `http://www.esa.int/science/planck/`

[141] A. Chamballu, *Sondages d'amas de galaxies par effet Sunyaev-Zed'dovich: Correlations et combinaison avec les observations X*, Thesis Université Paris 7 (2007)

[142] C. Ho and R.I. Epstein, *Inverse-Compton-Spectra for gamma-ray bursts: supressing the soft photons*, Astrophisical Journal, 343:277-291, 1989.

[143] Z.G. Dai et al., *GRB 060218/SN 2006aj: prompt emission from inverse-Compton scattering of shock breakout thermal photons*, arXiv:astro-ph 0604510v1, 2006.

[144] S. Kobayashi et al., *Inverse Compton X-Ray flare from gamma-ray burst reverse shock*, Astrophisical Journal 655, 391-395, 2007.

[145] L. Ball and J. Dodd, *Shock Geometry and Inverse Compton Emission from the Wind of a Binary Pulsar*, Astron. Soc. Austr., 2001, 18, 98-104.

[146] LIU Ji-feng et al., *Coherent Inverse Compton Scattering Responsible for Pulsar Polarized and Unpolarized Emission*, Chin. Phys. Lett. 16, 541 (1999).

[147] P. Pietrini and J.H. Krolik, *The inverse Compton Thermostat in Hot Plasmas near Accreting Black Holes*, Astrophisical Journal 447, 526 (1995).

[148] J. Malzac, *Accretion disc coronae in black hole binaries*, Mem. S.A.It. Vol. 75,382 (2007).

[149] M. Woods, *The scanning Compton polarimeter for the SLD experiment*, SLAC-PUB-7319 (1996).

[150] D. Doll et al., *A counting silicon microstrip detector for precision compton polarimetry*, Nucl. Inst. and Meth. A 492 (2002) 356-364.

[151] M. Wood, *Polarimetry at a future linear collider - How precise ?*, SLAC-PUB-8397 (2000).

[152] M. Woods et al., *Luminosity, Energy and Polarization Studies for the Linear Collider: Comparing e^+e^- and e^-e^- for NLC and TESLA*, SLAC-PUB 10353 (2004).

[153] M. Woods and K.C. Moffeit, *Studies of a downstream Compton polarimeter at the ILC*, SLAC-PUB 10669 (2004).

[154] I. Sakai et al., *Production of high brihtness γ rays through backscattering of laser photons on high-energy electrons*, Phys. Rev. ST Accel. Beams 6, 091001 (2003).

[155] T. Omori et al., *Efficient Propagation of Polarization from Laser Photons to Positrons through Compton Scattering and Electron-Positron Pair Creation*, Phys. Rev. Lett. 96, 114801 (2006).

[156] R. Brinkmann et al., *TESLA Technical Design Report*, PART II, March 2001.

[157] U.S. Linear Collider Steering Group, Accelerator Sub-committee, Linear Collider Option Task Forces, *U.S. Linear Collider Technology Options Study*, March 2004.

[158] I.F. Ginzburg et al., *Colliding ge and gg beams based on the single pass $e^\pm e^-$ colliders (VLEPP type)*, Nucl. Inst. and Meth. 205, 47 (1983).

[159] V. Telnov, *Principles of photon colliders*, Nucl. Instr. and Meth. A 335 (1995) 3-18.

[160] Douglas L. Borden et al., *Physics Possibilities at a Photon Linear Collider*, SLAC-PUB-5715.

[161] I.F. Ginzburg et al., *Colliding γe and $\gamma\gamma$ beams based on single-pass e^+e^- accelerators. II. Polarization effects, Monochromatization improvment*, Nucl. Inst. and Meth. 219, 5-24 (1984).

[162] V.G. Serbo, *Compton effect as a basic process in the conversion region*, Nucl. Instr. and Meth. A 472 (2001) 260-266.

[163] B. Grzadkowski and J.F. Gunion, *Using Back-Scattered Laser Beams to Detect CP Violating in the Neutral Higgs Sector*, UCD-92-18 (1992).

[164] M. Krämer et al., *Prospect of measuring the parity of Higgs particles*, Z. Phys. C 64 (1994) 21.

[165] G.J. Gounaris and G.P. Tsirigoti, *Signatures of CP-violating in $\gamma\gamma \to H$ using polarized beams*, hep-ph/9703446 (1997).

[166] R. Badelek et al., *TESLA Technical Design Report*, PART VI, March 2001.

[167] G. Klämke and K. Mönig, *Studies on chargino production and decay at photon collider*, Eur. Phys. J. C 42, 261-270 (2005).

[168] G. Cantatore et al., *Proposed measurement of the vacuum birefringence induced by a magnetic field on high energy photons*, Phys. Lett B 265 (1991) 418-424.

[169] C. Bamber et al., *Studies of nonlinear QED in collisions of 46.6 GeV electrons with intense laser pulses*, Phys. Rev. D 60, 092004.

[170] H. Elleaume et al., *Performance of computed tomography for contrast agent concentration measurement with monochromatic x-ray beams: comparison of K-edge versus temporal subtraction*, Phys. Med. Biol. 47 (2002) 3369-3385.

[171] P. Tafforeau et al., *Application of X-ray synchrotron microtomography or non-destructive 3D studies of paleontological specimens*, Appl. Phys. A 83 (2006) 195-202.

[172] J. Dik et al., *Visualization of a Lost Painting by Vincent van Gogh Using Synchrotron Radiation Based X-ray Fluorerscence Elementary Mapping*, Anal. Chem. 2008, 80, 6436-6442 (2008).

[173] W.J. Brown et al., *Experimental characterisation of an ultrafast Thomson scattering x-ray source with three-dimensional time and frequency-domain analysis*, Phys. Rev. ST-AB 7, 060702 (2004).

[174] D.J. Gibson et al., *PLEIADES: A picosecond Compton scattering x-ray source for advanced backlighting and time-resolved material studies*, Phys. Plasmas 11 (2004) 2857-2864.

[175] F.E. Carroll, *Tunable Monochromatic X Rays: A New Paradigm in Medicine*, AJR:179 (2002) 583-590.

[176] F.E. Carroll et al., *Pulsed Tunable Monochromatic X-Ray Beams from a Compact Source: New Opportunities*, AJR:181 (2003) 1197-1202.

[177] A.E. Vlieks et al., *Compton X-ray source*, Proceedings of EPAC 2004, Lucerne, Switzerland.

[178] S. Kashiwagi et al., *Compact soft x-ray source using Thomson scattering*, J. Appl. Phys. 98, 123302 (2005).

[179] K. Sakaue et al., *Recent progress of a soft X-ray generation system based on inverse Compton scattering at Waseda University*, Rad. Phys. Chem. 77 (2008) 1136-1141.

[180] K. Yamada et al., *A trial for fine and low-dose imaging of biological specimen using quasi-monochromatic laser-Compton X-rays*, Nucl. Instr. Meth. A 608 (2009) S7-S10.

[181] C.X. Tang et al., *A simulation study of Tsinghua Thomson scattering X-ray source*, CPC(HEP & NP), 33 (2009) 146-150.

[182] K. Sakaue et al., *Development of pulsed-laser super-cavity for Compact X-ray source based on laser-Compton scattering*, Proceedings of PAC07, Albuquerque, New Mexico, USA.

[183] M. Uesaka et al., *Monochromatic tunable Compton scattering X-ray source using X-band multi-bunch linac and YAG laser circulating system*, Nucl. Instr. and Meth. B 261 (2007) 867-870.

[184] F. Sakamoto et al., *Compton scattering monochromatic X-ray source based on X-band multi-bunch linac at the University of Tokyo*, Nucl. Instr. and Meth. A (2009), doi:10.1016/j.nima.2009.05.089.

[185] W.S. Graves et al., *MIT inverse Compton source concept*, Nucl. Instr. and Meth. A (2009), doi:10.1016/j.nima.2009.05.042.

[186] See `http://www.mxisystems.com/specifications.html`

[187] K. Sakaue et al., *Demonstration of multi-pulse X-ray generation via laser-Compton scattering using pulsed-laser super-cavity*, Proceedings of LINAC08, Victoria, BC, Canada.

[188] J. Urakawa, *The "Quantum Beam Project"*, FJPPL/Compton meeting, LAL Orsay, France, 1-2 December 2008.

[189] H. Toyokawa et al., *Recent progress in generation and application of AIST laser-Compton gamma-ray beam*, Nucl. Instr. and Meth. A (2009), doi: 10.1016/j.nima.2009.05.062.

[190] Z. Huang and R.D. Ruth, *Laser-Electron Storage Ring*, Phys. Rev. Lett 80 (1998) 976-979.

[191] See `http://www.lynceantech.com/sci_tech_cls.html`

[192] E. Bulyak et al., *Compact X-ray source based on Compton backscattering*, Nucl. Instr. and Meth. A 487 (2002) 241-248.

[193] C.X. Tang et al., *Tsinghua Thomson scattering X-ray source*, Nucl. Instr. meth. A, 608 (2009) S70-S74.

[194] P. Yu and W. Huang, *Lattice design and beam dynamics in a compact X-ray source based on Compton scattering*, Nucl. Instr. meth. A, 592 (2008) 1-8.

[195] C. Bruni et al., *The radiothomx project*, Proceedings of EPAC08, Genoa, Italy.

[196] J. Rifkin, *The Compact Light Source*, POSIPOL 2007 Worshop, LAL-Orsay, France, 23-25 May 2007.

[197] M. Bech et al., *Hard X-ray phase-contrast imaging with the Compact Light Source based on inverse Compton X-rays*, J. Synchrotron Rad. 16 (2009) 43-47.

[198] LAL drawing.

[199] See `http://www.rigaku.com/generators/fre-plus.html`

[200] Plot from M.E. Couprie and O. Marcouillé (from SOLEIL).

[201] P. Yeh, *Optical waves in layered media* (Wiley, New-York, 1988).

[202] P. Yeh, *Extended Jones matrix method*, J. Opt. Soc. Am. Vol.72, 507-513 (1982).

[203] C. Gu and P. Yeh, *Extended Jones matrix method. II*, J. Opt. Soc. Am. A/Vol.10, 966-973 (1993).

[204] P. Yeh, *Electromagnetic propagation in birefringent layered media*, J. Opt. Soc. Am. 69, 742-756 (1979).